ULTRA-THIN FILM TRIBOLOGY OF ELASTOMERIC SEALS IN PRESSURISED METERED DOSE INHALERS

By
David Grimble MSc BEng (Hons.)

Thesis submitted in partial fulfilment of the requirements for the degree of Doctor of Philosophy

Loughborough University

Wolfson School of Mechanical & Manufacturing Engineering

December 2009

Certificate of Originality

In printed version.

Abstract

Within pressurised Metered Dose Inhalers (pMDIs) the contact between the valve components and elastomeric seals is of major significance, representing the main contributory factor to the overall system frictional characteristics. Therefore, the seal performance is extremely important and must be optimised to meet the contradictory requirements of preventing leakage and allowing smooth actuation. The environmentally driven trend to HFA formulations as opposed to CFC based ones has deteriorated this problem due to poor lubrication conditions and it has, consequently, increased the frictional losses during the pMDI actuation (hysteresis cycle).

Research has been conducted into the key areas of the inhaler mechanism. As such, the contact pressure distribution and resulting reactions have been investigated, with emphasis on the correct treatment of the elastomer (seal) characteristics. The modelling of the device has been conducted within the environment of the multibody dynamics commercial software ADAMS, where a virtual prototype has been built using solid CAD geometries of the valve components. An equation was extrapolated to describe the relation between the characteristics of the ultra thin film contact conditions (sliding velocity, surface geometry, film thickness and reaction force) encountered within the inhaler valve and integrated into the virtual prototype allowing the calculation of friction within the conjuncture (due to viscous shear and adhesion).

The latter allowed the analysis and optimisation of key device parameters, such as seal geometry, lubricant properties etc. It has been concluded that the dominant mechanism of friction is adhesion, while boundary lubrication is the prevailing lubrication regime due to the poor surface roughness to film thickness ratio.

The multibody dynamics model represents a novel multi physics approach to study the behaviour of pMDIs, including rigid body inertial dynamics, general elasticity, surface interactions (such as adhesion), hydrodynamics and intermolecular surface interactions (such as Van der Waals forces). Good agreement has been obtained against experimental results at component and device level.

KEYWORDS: pMDI, Elastomeric Seals, Regimes of Lubrication, Friction, Adhesion, Boundary Lubrication

Acknowledgements

The author would like to acknowledge the support of Loughborough University and 3M throughout the duration of this work. Most notably, the author would like to thank Stephanos Theodossiades, Homer Rahnejat and Matt Wilby for all of their support and encouragement.

The author would also like to show his appreciation for the advice and support of Paul King, his friends and other colleagues without which the PhD experience would never have been so interesting or bearable.

Finally, a special note of thanks must go to my parents and family for their continued love, support and patience.

Contents

List of Figures

List of Tables

Nomenclature

A	Total contact area
A_a	Area of asperity contact
A_h	Hamaker constant
b	Hertzian half width
C	Fractional squeeze ratio
C_k	Constraint function
cw	Unloaded contact width
cwl	Pressure loaded contact width
D_e	Damping energy dissipation function
D	Inner seal diameter
d	Seal cross-sectional diameter
$D_{Current}$	Current calculated deflection
$D_{Desired}$	Desired deflection to fit seal to groove
D_{ERR}	Percentage error in deflection convergence
$D_{i,j}$	Influence coefficient
E	Elastic modulus of the seal
E_f	Elastic modulus of the housing
E'	Reduced elastic modulus
F	Contact load
F_n	Normal force
F_{nl}	Pressure loaded normal force
F_v	Viscous shearing force
$F_{\xi j}$	Generalised applied forces projected on ξ
g	Groove depth (Available space for seal)
G^*	Dimensionless material parameter
h	Lubricant film thickness
H	Lubricant film thickness
H^*	Dimensionless film parameter
h_0^*	Dimensionless film minimum
h_c	Central film thickness
H_{min}	Minimum film thickness
$H_{min,F}$	Minimum film thickness for fully flooded case
I	Mass moment of inertia
$\overline{J}_{i,k}$	Jacobian term
k	Ellipticity parameter of the contact
L	Centre line circumferential length of the seal
L_e	Lagrangian
L_0	Original seal centre line circumferential length
L_s	Length of actuation stroke
m_b	Body mass
m	The Pressure coefficient of boundary shear strength
m^*	Minimum Inlet distance for fully flooded conditions to prevail
M_q	Body momentum
P	Pressure value at a point
p	Canister Pressure
p^*	Dimensionless pressure

P’	Load per unit length
P_h	Hertzian peak pressure
P_{NEW}	Newly calculated pressure for an element
P_{vdw}	Additional contact force due to Van Der Waals effects
q	Leakage amount
$\overline{q}$	Net leakage for in and out strokes
Q	Rate of Leakage
$\vec{R}_G$	Location of the centre of mass
R_x	Effect radius of curvature
T	Kinetic energy
t	Time
u	Sliding velocity of the seal contact
U*	Dimensionless speed parameter
U_{av}	Average entrainment velocity
V	Potential energy
v	Velocity
W	Calculated contact Load
W*	Dimensionless load parameter
w_a	Load carried by asperities
W_{ERR}	Percentage error in load convergence
W_{Hertz}	Hertzian prediction of contact load
x	Degree of total seal cross-sectional compression/deflection
$\overline{x}_e$	Dimensionless film rupture point
$\overline{x}$	Dimensionless X-coordinate
Z	Hamrock deflection calculation variable

α	Pressure viscosity coefficient
β	Finite differencing parameter
β_{GWT}	Radius of curvature at asperity tip
γ	Adiabatic index
ΔL	Change in seal centre line circumferential length
δ_x	Deflection for an discretised element
$\overline{\delta}$	Dimensionless deflection
ΔX	Discretisation step size in X-coordinate
ε	Karaszkiewicz squeeze ratio
$\varepsilon_{x,y,z}$	Strain component
ζ	Surface density of asperity peaks
η	Dynamic viscosity
η_0	Ambient viscosity
θ	Euler angle
λ	Oil film parameter
λ_k	Lagrange multipliers
μ	Coefficient of friction
ξ	Generalised coordinates
ρ	Density of the lubricant
σ	Combined surface roughness (RMS)
$\overline{\sigma}$	Average contact pressure of the seal

$\overline{\sigma_p}$	Average contact pressure caused by the canister pressure loading
σ_0	Contact pressure of the seal for unloaded case
$\sigma_{x,y,z}$	Stress component
τ_0	Eyring shear stress
τ_{xy}	Shear component
υ	Poisson's ratio of the seal
υ_f	Poisson's ratio of the housing
φ	Euler angle
Φ	Vogpohl transformation coupling term
ψ_e	Euler angle
ψ	RMS value of the composite surface roughness of the contacting surfaces
ω	Rotational speed

1.0 Introduction to the Pressurised Metered Dose Inhaler

The pressurised Metered Dose Inhaler (pMDI) is a device designed to administer a therapeutic formulation dose to the human respiratory tract. This is achieved when the metering valve is actuated and the active drug substance (either in solution or suspension within the device) is released in the form of aerosol spray. This spray can then be directed using a suitable adaptor/actuator for either nasal or oral inhalation.

The pMDI is commonly used for the treatment of both asthma and Chronic Obstructive Pulmonary Disease (COPD). Asthma is a chronic airway condition, with the national Asthma campaign estimating that 1 in 8 children and 1 in 13 adults have current symptomatic asthma within the UK, with some 5.1 million people receiving treatment as of 2002 (MeRec *Briefing for the NHS, 2002*). COPD is a chronic, progressive disorder, again of the airways, but unlike asthma the obstruction is only partially reversible and is accompanied by an accelerated decline in lung function.

The two main categories of inhaled drugs are bronchodilators and corticosteroids. With bronchodilators relieving the symptoms of bronchoconstriction, while corticosteroids reduce inflammation of the airways in order to prevent asthma symptoms occurring (Wright *et al*, QSHC Online).

The annual cost of asthma drugs to the NHS is in excess of £500 million (Wright *et al*, QSHC Online), and while patient technique is crucial to effective treatment, the design and characteristics of the inhaler must be matched to the formulation to be used.

1.1 History of the pMDI

The pMDI was first introduced by what was then Riker laboratories in the 1950s (now part of 3M) (McDonald and Martin, 2000). It was initially based around CFC propellants such as CFC-11,12 or 114 (Noakes, 2002), but the industry was committed by signing the Montreal Protocol in 1987 to seek an alternative, non-CFC propellants (McDonald and Martin, 2000). Therefore, in recent years, considerable research has been devoted to the reformulation of the pMDI. The chosen propellants are usually Hydro-fluoro-alkanes (HFAs), specifically HFA-134a and HFA-227.

Reformulation has proven to be an arduous task, with the new propellants showing some incompatibility with valve gasket materials and also necessitating smaller spray orifices in the MDI actuators (Keller, 1999). These design changes were especially of importance as the propellant makes up 99% of most formulations (Noakes, 2002). The HFA formulations were found to have different solvency characteristics and, therefore, alternative surfactants had to be developed as without a co-solvent, they would not dissolve into the new formulations. This addition can then have an effect on the respirable dose created by the pMDI (<5μm particle diameter) and so the spray orifice was reduced in size to allow a finer aerosol to be produced. However, it must be noted that through use of excipients or canister coatings, the need for surfactants/co-solvents can be reduced/avoided. The HFA formulations were also found to produce different swelling characteristics of the rubber seals, and thus affect operation of the traditional metering valve designs (Colthorpe, 2003). In conjunction with tightening legislation from the Food and Drug Administration (FDA) for instance, regarding dose uniformity, the pMDI has received major redevelopments in recent years. HFA does have significant advantages over the traditional CFC MDI. However, in a recent study of a CFC and HFA Beclomethasone dipropionate MDI for example, the HFA MDI was found to deposit just 30% of the drug dose in the oropharynx (60% in the lung) where as the traditional CFC MDI deposited up to 90% of the dose within the oropharynx and just 10% in the lungs (Ibiapina *et al*, 2004).

1.2 Basic Operation and Components of an pMDI

A typical pMDI device includes the following parts/substances, as shown in Figure 1.1:

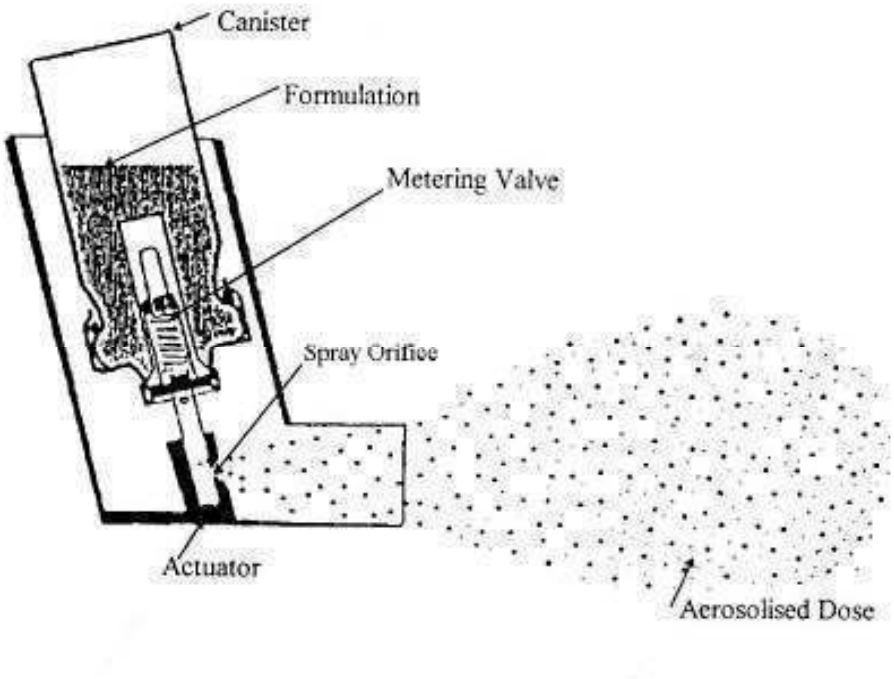

Figure 1.1: The metered dose inhaler (Purewal and Grant, 1998)

with a further breakdown of components shown in Figure 1.2:

- Canister
- Formulation (Nominally at 0.55 MPa in the case of 3M), including:
    - Active substance
    - Propellant
    - Surfactant
- Metering valve
- Actuator/adaptor

Each of these components can have an effect on the overall operation of the final device.

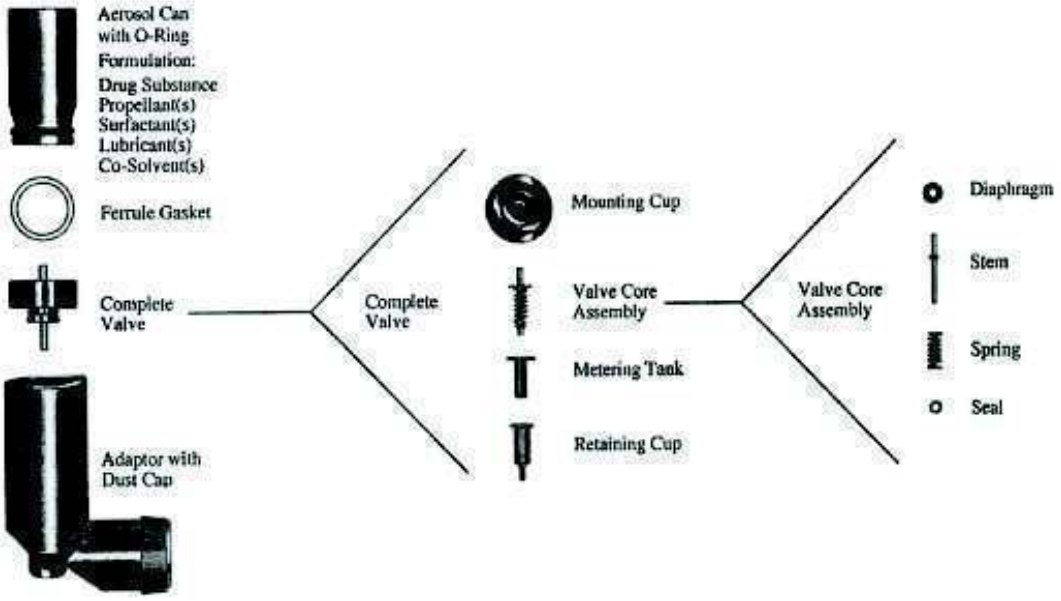

Figure 1.2: Component diagram of a typical pMDI (Fink, 2000)

1.3 The Canister

The canister is most commonly formed from aluminium alloy, although it may also be formed from glass with a PVC layer. This layer helps to protect the glass from impacts, UV light and also allows the slow release of any leakage from the glass container. In either case, the neck of the container is designed to suit the particular valve to be used. The surface roughness of the canister internal walls is also of importance as this presents an opportunity for drug deposition on any surface pits. With this in mind, the lining of the canister is crucial, and should be carefully considered in relation to the formulation to be contained. Recent testing of a salbutamol HFA formulation (Young *et al*, 2003) for example found that under examination, PTFE was the most suitable canister liner compared with borosilicate glass and aluminium. This conclusion was formed on the basis that PTFE exhibited the least amount of particle wall adhesion and thus potentially allowed a more efficient formulation.

1.4 Metering Valve

The majority of commercially available pMDIs are fitted with a 20mm ferrule type metering valve. In each case, the pMDI is designed to be operated with its valve pointing downwards. The valves used for commercial pMDIs are readily available in

four nominal metering volumes: 25µl, 50 µl, 63 µl, and 100 µl. In traditional designs, the sealing of the metering volume is maintained using either a flat gasket or an o-ring seal. In either case, the canister gasket seal (which should not be confused with the metering volume seals) is placed in the neck of the container and crimped into place during manufacture. The crimping conditions are critical to ensure a good seal is maintained, with careful checks of both crimp height and diameter required.

Figure 1.3 illustrates the basic operation of a metering valve through each stage of the actuation process. The valve can be simply thought as a series of taps, each allowing flow at the relevant time to allow the formulation to be administered in the required dose.

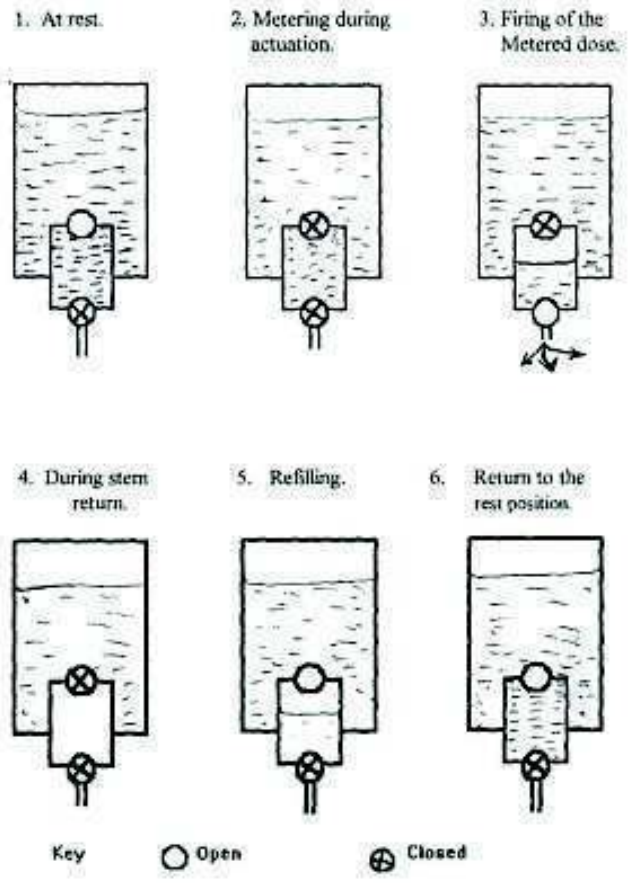

Figure 1.3: Metering valve operation (Purewal and Grant, 1998)

A usual practice in industry is to manufacture the valve stem and body by press forming in stainless steel (3M), although these can also be injection moulded in a suitable plastic material (such as the designs by Bespak or Valois), providing that the

chosen material is compatible with the formulation to be used within the device. The stem return spring is generally formed from stainless steel.

A typical metering design is shown in Figure 1.4, while the output throughout its life for such a device is shown in Figure 1.5.

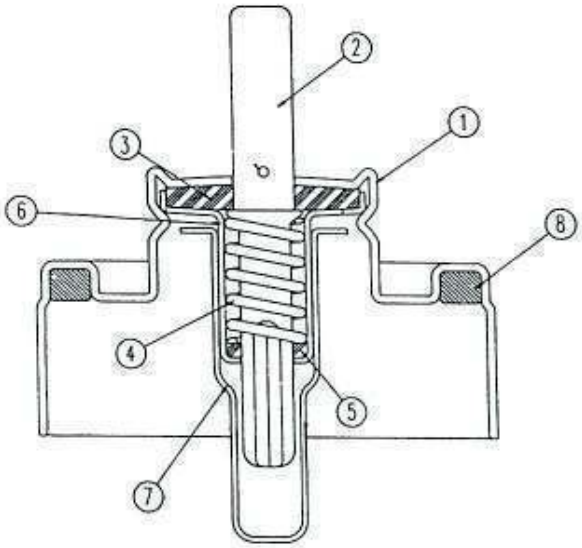

Ref	Description	Material
1	Ferrule	Aluminium
2	Stem	Stainless Steel
3	Diaphragm	Nitrile DB 218
4	Spring	Stainless Steel
5	Tank Seal	Nitrile DB 218
6	Tank	Stainless Steel
7	Bottle Emptier	Stainless Steel
8	Ferrule Gasket	Polyethylene DFDB 1085

Figure 1.4: 3M metering valve (Purewal and Grant, 1998)

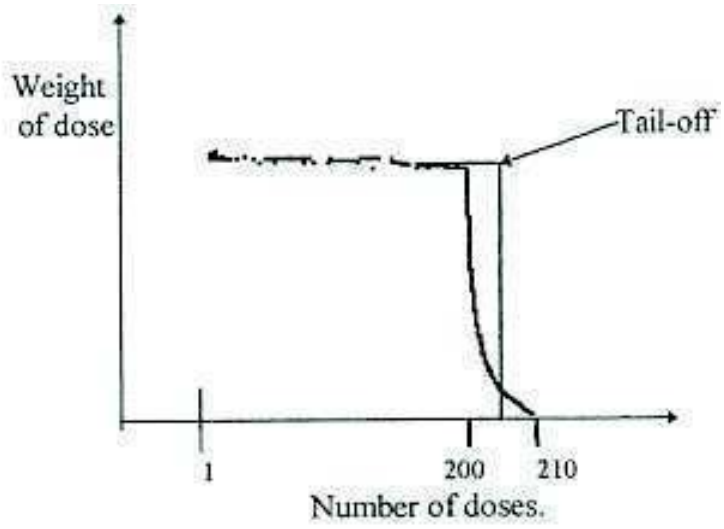

Figure 1.5: pMDI performance over time (Purewal and Grant, 1998)

As it can be seen, after the prescribed number of doses (in this case 200), the pMDI performance rapidly tails off, with the dose weight becoming progressively unreliable. This is to be expected as the pressure within the canister tails off. What is important, however, is that the dose weight is maintained over the indicated 'can life' and 'shelf life' of the inhaler. The 'shelf life' being that of a stored inhaler, and the 'can life' being the recommended number of metered doses that can be obtained from an inhaler during use.

The metering valve should meet the following basic requirements:

- The path from the valve seat to the spray orifice (See Figure 1.1) should be short. This condition minimises the space in which the drug substance can be accumulated. This also helps to prevent the valve from clogging or producing variations in dosage.
- The valve requires a high valve seating pressure, with a sharp shut-off to help prevent any leakage.
- The spray rate should be independent of the varying canister pressure. This will prevent any dose variation during the operational life of the inhaler.
- The valve components should not adversely affect the formulation and vice versa.
- The valve should ideally have a sharp tail off once the indicated canister life has been superseded. This not only prevents excessive waste of unused (but unreliable) formulation, but more importantly means that within a short

number of doses the patient senses a clear indication that their inhaler is exhausted, thus preventing them from continuing to administer varying dosages when really the canister requires replacement.

The performance of valve seals is determined by:

- The leakage rate occurring within the container. This is measured as the amount of leakage between the ferrule and the container, and the outer valve-stem seal, under static conditions.
- The dynamic sealing performance during actuation.

In the case of a breath actuated mechanism, the valve actuation forces are of critical importance and, therefore, the swelling of the rubber seals is of importance. During development, any swelling that will take place within the rubber must be taken into account as this will affect the dimensional tolerances of the finished inhaler, and thus the final operation of the device. Therefore, it is important to know how the chosen formulation will affect the rubber seals. The actuation forces are also affected by the surface finish of the components and the interactions at the mating surfaces. Therefore, these factors must also be taken into account at the design stage. In recent years, the main issues relating to inhaler design are as follows:

- Compatibility of valve components with the new, non-CFC formulations.
- Seal extractables.
- Loss of prime (device is not ‘primed’ for use as metered dose deteriorates), resulting from the formulation draining from the metering chamber during storage. This means that upon use, the initial shot has reduced drug content and, in order to overcome this, a number of shots (and therefore wasted formulation) must be fired into the air before the inhaler is used by the patient.
- Dose variability, which can be the result of loss of prime or from rapid flocculation of the suspension, or from flocculation of the drug, which can then drain from the metering chamber during storage.

1.5 The Actuator/Adaptor:

Although there are various types of actuators, the type discussed in this thesis will be that of the basic press and breathe actuator. This is simply an orifice through which the spray is aerosolised, and is then inhaled by the patient who must time their own breathe with the actuation. As previously mentioned, the actuators can be designed for either nasal or oral administration of the active drug substance (Figure 1.6).

Figure 1.6: Nasal and oral actuators (Berry *et al*, 2003)

The actuator holds the canister, allowing smooth actuation of the metering valve, with the metered dose passing through the final orifice and through either a nasal or oral adaptor. A simple diagram is provided in Figure 1.7, which shows a schematic outline of the actuator/adaptor for a press and breathe oral pMDI, the stem of which fits into the area labelled ‘X’.

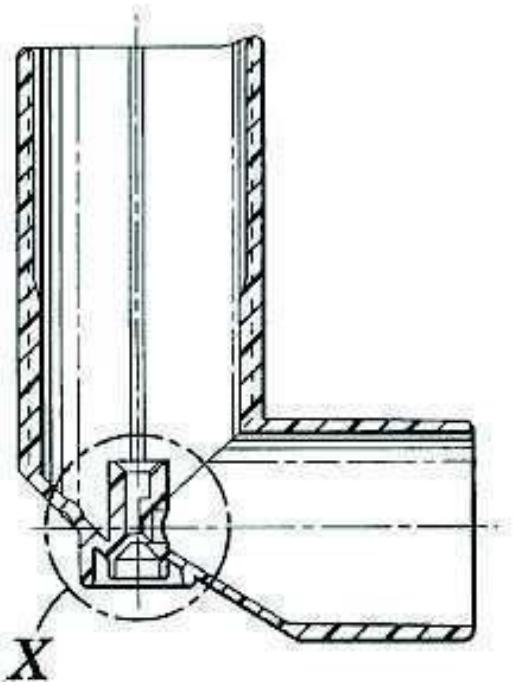

Figure 1.7: Press and breathe actuator design (US6120752)

For a 'press and breathe' type actuator, the following aspects of actuator design affect the pMDI performance:

- The diameter of the spray orifice affects the spray droplet size, with (in general) a smaller diameter producing a finer sprayed particle size.
- The valve stem must fit solidly within the housing in order to prevent any dose being fired back into the actuator upon motion.
- In order to allow sufficient air flow, large enough clearance must be maintained between the canister and adapter body.
- The resulting spray plume shape can be manipulated by varying the taper of the spray exit orifice.
- The volume of the space between the valve stem and spray orifice can also affect the spray plume, as it can act as an expansion chamber coupled with the volume of the metering chamber during the initial stages of vaporisation of the propellant.
- Minimisation of spray losses on the mouth-piece itself can be generally achieved through use of a round mouth-piece and a central orifice location.

1.6 Variations of actuators

A brief description of alternative actuators now follows.

1.6.1 Mechanical break-up actuators

These actuators can be useful when the proportion of volatile propellant is relatively low, for example, when a high proportion of ethanol is present. This type of actuator uses mechanical means to induce a swirling of the dose spray (Purewal and Grant, 1998). This motion encourages the expelled liquid to 'break-up' into finer particles over a shorter distance and, thus, aids inhalation.

1.6.2 Breathe-triggered actuators

It has been found that a significant percentage of patients (50%) fail to successfully synchronise their inhalation with the inhaler actuation, which reduces the effectiveness of the therapy. Therefore, a range of devices have been developed that automatically allow device actuation only in conjunction with sufficient breathe by the patient. This is achieved using a method such as that shown in Figure 1.8.

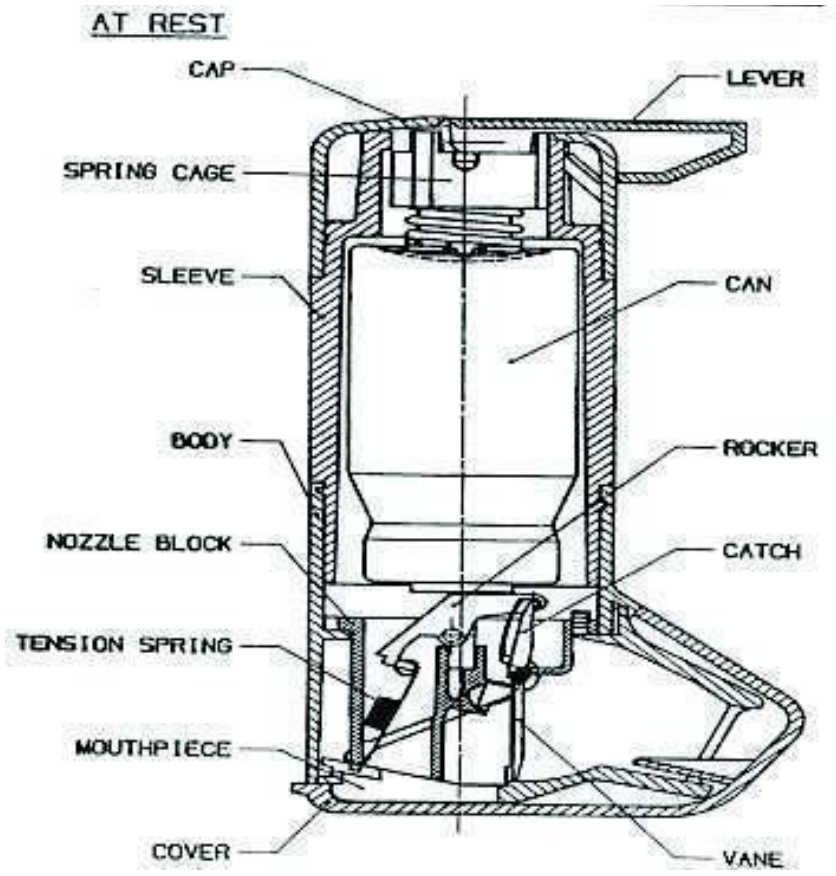

Figure 1.8: 3M Autohaler (Purewal and Grant, 1998)

This device operates by first priming the device by lifting the lever (the dust cap must also be removed and the device shaken prior to use). When the lever is raised, a spring is compressed which in turn pushes down on the base of the canister itself. The metering valve is prevented from actuating by the second lever mechanism in the nozzle. Only when the patient starts to breathe in is this lever allowed to move and the device actuates. This is achieved by the difference in pressure caused by patient's breath. This difference is detected as the airflow lifts the pressure vane; this in turn allows the lever preventing actuation to be released and, thus, the metered dose to be administered to the patient. Once the dose has been administered, the patient simply lowers the top lever and the device is automatically reset for the next actuation. This delivery system helps to maximise pulmonary drug delivery, which requires a deeper penetration into the lungs. An alternative to the autohaler system is that shown in Figure 1.9. The IVAX easi-breathe system is primed following shaking by removal of the cap with the inhaler in the upright position. Upon breathing, the device is triggered and the dose administered. Note in Figure 1.9 that the dose counter facility is not a feature of the currently marketed product.

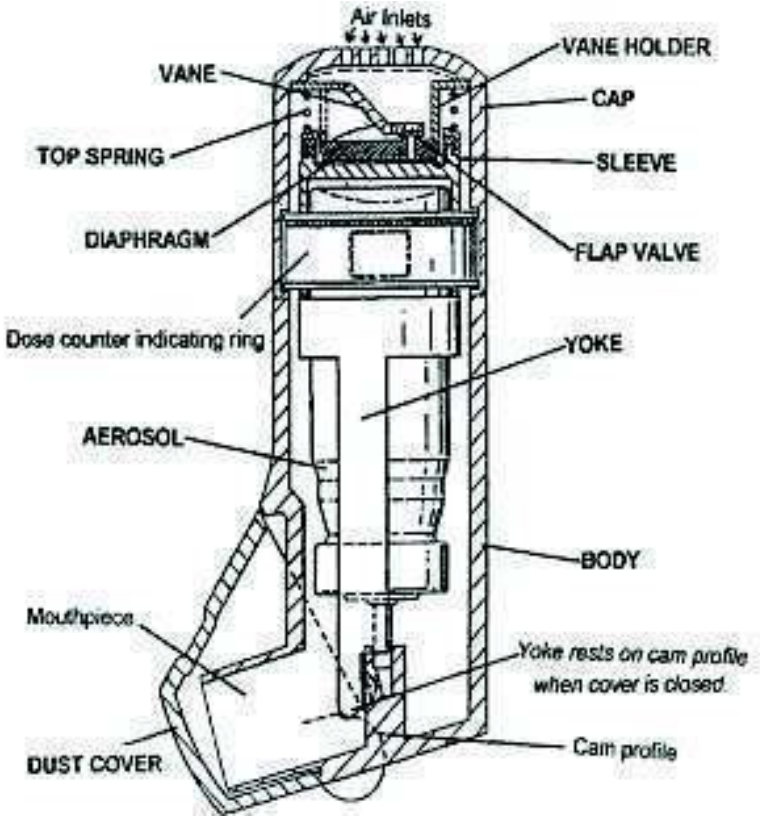

Figure 1.9: IVAX Easi-Breathe (Purewal and Grant, 1998)

In addition, companies such as KOS Pharmaceuticals, MAP Pharmaceuticals, Meridica and Chiesi all offer alternative actuator devices. Further information is available, but it has not been included in this thesis, as it was not felt necessary.

1.7 Alternative pMDI designs

What follows is a brief outline of the current valve/meter designs per manufacturer. For the purposes of this thesis, the information has been concentrated on the design of the metering valve.

1.7.1 3M

The basic pMDI design is detailed below as per patent US6120752. Figure 1.10 details the design of the metering valve.

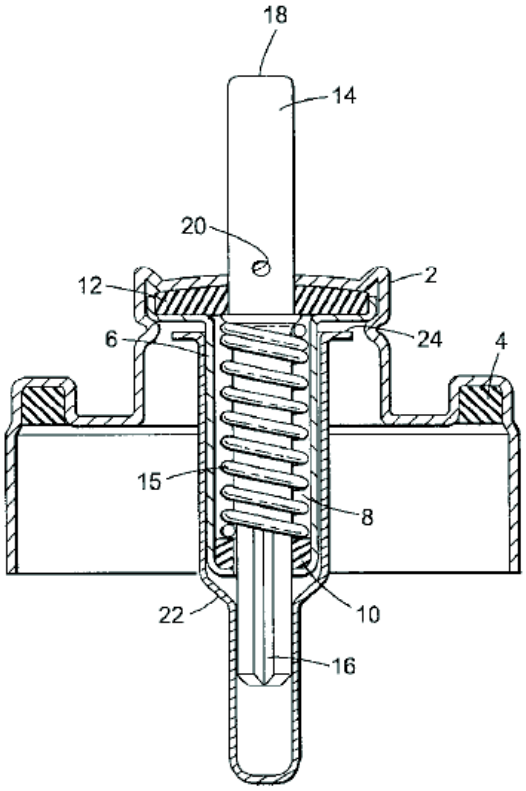

Figure 1.10: 3M metering valve (US6120752)

The device includes the following components:

- Valve Ferrule (2)
- Rim Gasket (4) for engaging the vial. This can comprise an ethylene-butylene co-polymer.

- Metering Tank (6) with walls defining the metering chamber (8). This chamber has an inlet end associated with a tank seal (10) and an outlet associated with a diaphragm (12). The tank seal and diaphragm can comprise a butadiene-acrylonite co-polymer.
- The valve stem (14) has a filling channel (16), a discharge end (18) and a discharge orifice (20), which extends through the valve ferrule and metering chamber.
- A bottle emptier (22) surrounds the metering tank (6) and valve stem in such a way that a capillary channel (24) is defined. This allows formulation to flow from the aerosol vial to the inlet of the metering chamber.
- The valve stem (14) is movable to an extended closed position which allows the vial contents to fill the metering chamber, but seals the outlet of the metering chamber. Alternatively, on actuation, the valve stem assumes a compressed open position. This position allows the contents of the metering chamber, but not the vial, to pass through the discharge orifice of valve stem. The spring (15) biases the valve stem (14) to the extended closed position.

Additional patented designs from 3M include:

- WO2004022143
- WO2004022142
- US2003127464
- US2002134376

1.7.2 Bespak

Bespak is a UK based manufacturer offering design, development and manufacture of a variety of respiratory products. Customers include Schering-Plough, Boehringer Ingelheim, Chiesi, GlaxoSmithKline, IVAX and Sanofi-Aventis (Bespak, www.bespak.co.uk).

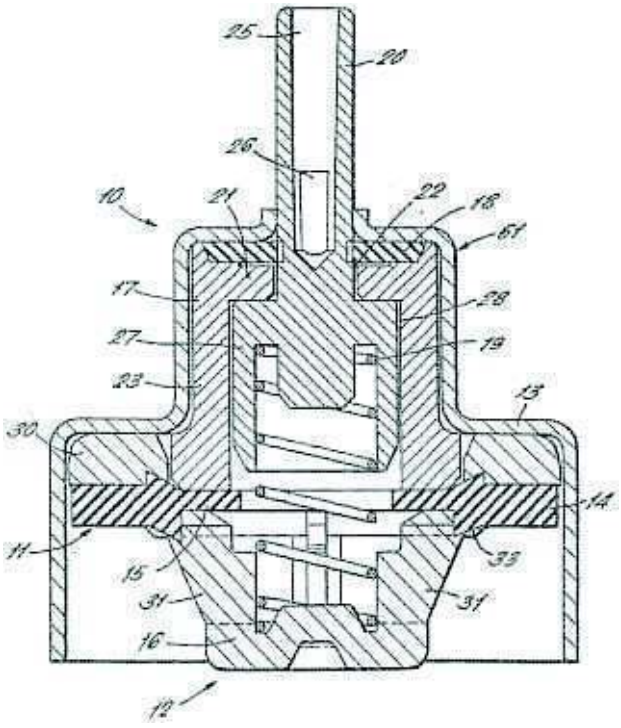

Figure 1.11: Bespak metering valve (WO0166439)

The metering valve design comprises of the following components (as taken from patent WO0166439, Figure 1.11):

- Valve stem (20) which slides within the valve body (16, 17), defining a metering chamber.
- Inner and outer seals (15, 18) are provided for sealing between the valve body and the valve stem (20). An additional gasket (14) is located on the valve body for sealing against the aerosol vial (not shown).
- At least one of the inner seal, outer seal or gasket is formed as a co-moulding with part of the valve body. This design is intended to reduce the potential for an elastomeric gasket being dislodged from its correct position on the valve body during assembly.

Bespak also offer patents on several other variations of the metering valve:

- WO2004096666
- GB2367809
- GB2345279
- GB2340477
- GB2338951
- US6006954
- GB2322847
- GB2298187
- GB2178398

1.7.3 GlaxoSmithKline

GlaxoSmithKline Plc forms a global healthcare group, active in the development of consumer healthcare products. While not a producer of valves as such, several designs are under patent by GlaxoSmithKline.

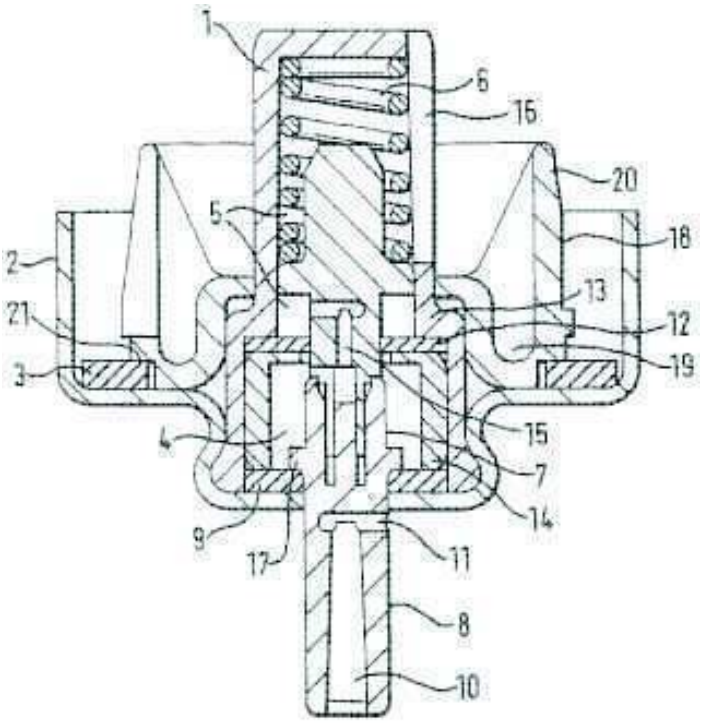

Figure 1.12: GlaxoSmithKline metering valve (US6170717)

The GlaxoSmithKline metering valve consists of the following components (as taken from patent US6170717, Figure 1.12):

- A valve designed specifically for non-CFC formulations, which features a liquid propellant suspension.
- The valve body (1) contains an orifice (16) to allow a measure of the formulation to pass from the vial into the metering volume.
- The ring (18) is positioned to reduce the volume of suspension that can be accommodated within the container, below the inlet orifice (16), when the valve is orientated down.
- The trough (19) is used to accommodate any drug sediment, thus ensuring that any metered dose is taken from the region of the vial above where sedimentation may have taken place. This, in conjunction with the ring (18) is intended to reduce the amount of wasted drug from within the vial, helping to allow the majority of the vial contents to be dispensed.

In addition, patent US6253762 describes an aluminium canister with a variety of fluorocarbon polymer coatings, with thickness of 1-25 μm. Coatings include PFA, FEP and blends of PTFE and polyethersulphone (PES). These coatings are used to reduce or eliminate the need for added surfactants/cosolvents to the formulation, which increases the stability and respirability of the drug over time.

Additional Patents relating to both valve and canister design include:

- WO2005023330
- WO2005016410
- WO2005011783
- MXPA03005697
- WO03049786
- WO0224552
- US6131566

1.7.4 Valois

Valois is a French company, with some 50 years experience in valve design. Along with 3M and Bespak, they are considered to be world leaders in valve development.

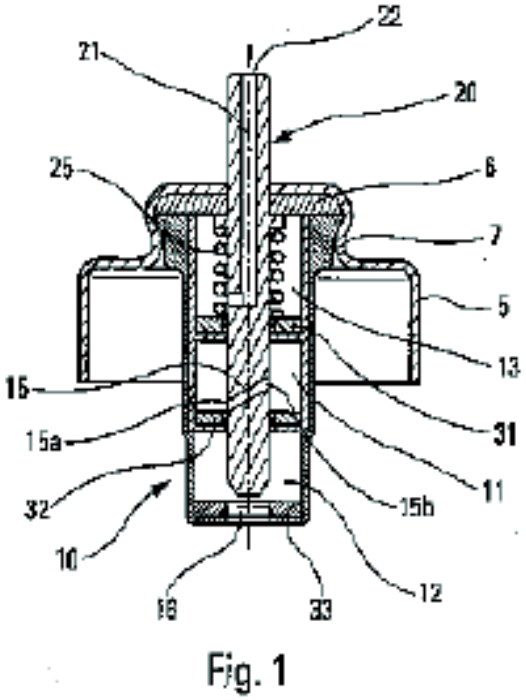

Figure 1.13: Valois metering valve (US2004226970)

The valve consists of the following components (as taken from patent US2004226970, Figure 1.13):

- The valve body (10) contains the valve member (20), which slides within the valve body. The member slides between a rest and actuated position, in much the same way as the traditional 3M design.
- The metering chamber (11) is at atmospheric pressure while the device is at rest. This allows the valve to be un-stressed during storage and prevents the spring from being exposed to the formulation, thus preventing any possible degradation or contamination.

Valois also offers the following valve designs:

- WO9950156
- GB2206099
- GB2206860
- FR2850166

1.8 Problems with the current designs

Several problems exist with the designs currently in production. Since the transition to HFA, dose uniformity has become an ever increasing problem as each inhaler required development to suit the new formulation.

During storage or periods where the device is not actuated, the drug can settle, hence the requirement for the device to be shaken by the patient. Once actuated this results in a non-uniform dose, which could contain either far too much or almost no active drug substance. In this instance, the device needs 'priming' before treatment can be carried out. This results in a waste of substance, and therefore a reduction in the life of the inhaler. This equates to a higher usage cost per useful treatment. To overcome this problem, the design of the metering valve must be carefully considered. Through the correct arrangement of metering chamber, elastomer seals and device operation, this problem can be largely eliminated (Cambridge Consultants Company, 2003). For example, the device operation can be moved away from metering at rest, to only metering upon actuation. This eliminates the problem of drug seeping/degradation within the metering chamber during storage.

Dose uniformity can also be affected by the storage orientation of the device (Berry *et al*, 2003). As one problem of the current designs is that through continual exposure to the drug (valve down orientation), leachable/extractable levels increase. This leads to a reduced respiratable drug output and thus a reduced dosage (Berry *et al*, 2003). Likewise, the actuator design can play an equally important role in ensuring the particle size of the emitted dose is within the respiratable range. HFA formulations require a reworked spray orifice to cope with the varying formulating properties in relation to traditional CFC inhalers (Berry *et al*, 2003).

The need for a priming dose also means that when a treatment is necessary, the recipient must be patient enough to fire one-to-several shots into the air before using the device to treat their attack, which is not convenient. Also, from texts available (Rubin and Durotoye, 2004) it is obvious that people do not always follow this procedure during general use. Quite often patients fail to clean, prime, store or even operate the devices properly. This can lead to problems with device actuation, as the

actuator may become blocked. The requirement for shaking can, however, be largely eliminated (Young *et al*, 2003) for HFA solution formulations through use of canister coatings intended to prevent the drug solution becoming unstable (Crowder *et al*, 2001). Additionally, by use of excipients, the need for surfactants/co-solvents can be reduced. This obviously affects the tribological characteristics of the elastomer/drug/stem interaction (University of Maryland School of Pharmacy, umaryland.edu).

The FDA has recently tightened its regulations for pMDIs. The inhaler must now be shown to deliver reproducible dosing throughout its intended shelf life, in representative temperature/humidity conditions. In addition, the dose must be shown to be of a stable respiratable range throughout the inhaler's life time (Byron, 2004). Therefore, the current designs must be carefully addressed, if the pMDI is to remain at the forefront of respiratory drug delivery systems.

1.9 Explanation of the new design

A new design has been presented by 3M, simplifying the current design by reducing the number of moving components. It also adopts a much simpler approach to the dose metering. In the new design, the pressure operated piston is the only moving component, with no requirement for a spring or other return mechanism (Figure 1.14).

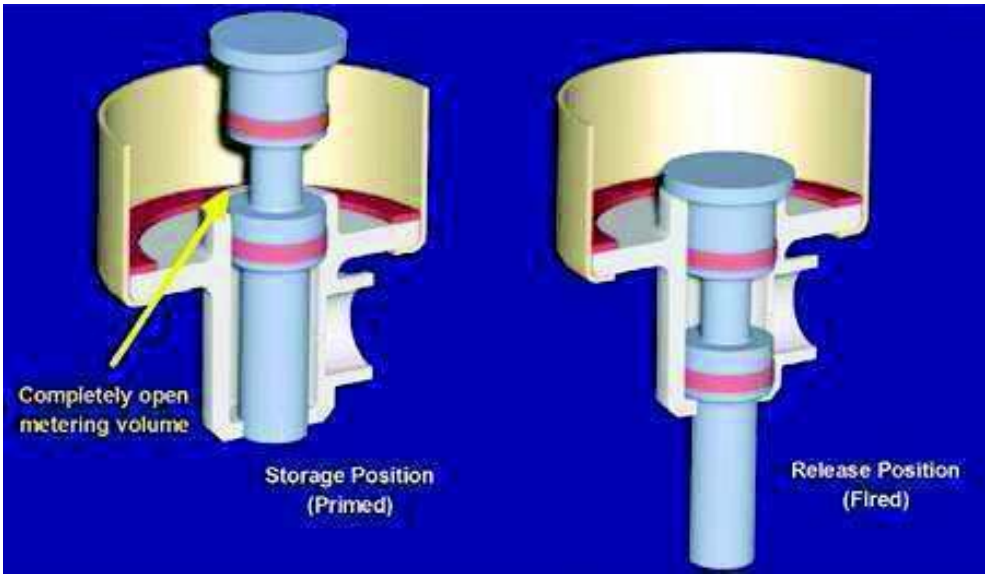

Figure 1.14: New inhaler design (Wilby, 2005)

In the new layout, the dosing chamber is fully exposed, but only at actuation. Therefore, it prevents any active drug from seeping from the metering chamber. This removes the need for a priming dose, and so reduces the usage costs, whilst also prolonging the life of the inhaler.

1.10 The Requirement for Optimisation

The concern with the new inhaler design is, however, a result of its simplicity. With no return spring, the actuation of the device is dependent on the pressure force within the container. This pressure, nominally 5.5 bar, must be able to overcome the friction forces preventing actuation, namely those of the seals against the housing bore. At the same time, appropriate sealing must be maintained in order to prevent leakage of formulation. An acceptable leakage rate must be achieved and, therefore, the design must be optimised to meet this requirement throughout its life. This is especially difficult, when considering that sufficient sealing must be maintained despite wear of the elastomeric components over the course of some 400 actuations. Furthermore, initial actuations must not be overly difficult during use. In order to optimise the inhaler design efficiently and cost effectively, a representative computer model is required, which must then be validated through experimental techniques. This is the main aim of this thesis.

1.11 Aims and Objectives

As already stated, the problem of optimising the pMDI device is of a complex nature, where various physical phenomena are interacting, requiring a multi-physics solution. Fundamentally, the investigation should ideally include:

- Mechanics of solids in contact
- Viscous action of the fluid in the contact of contacting solids through entraining action
- Physical interactions in vanishing conjunctions (The surface energy effects including adhesion forces and electrostatic interactions)
- Fluid diffusion and swelling of porous materials

The main objectives of this research are therefore:

- To develop fundamental understanding of the seal and formulation interactions with emphasis on system dynamics and physical effects within the mechanism.
- A fully-parameterised mathematical model simulating the system outlined above and allowing observations of key parameters, such as seal geometry.
- Validation of the final model through comparison with experimental measurements

Within this framework, it was intended that a key set of deliverables would be obtained and examined, namely:

- The mathematical model would be of parametric nature considering the following:
    - Seal material changes
    - Seal dimension changes
    - Seal geometry changes
    - Surface modification effects
    - Lubricant property changes
- Graphical output from the model to aid with communication of results, including, but not necessarily limited to graphs, diagrams and animations.

1.12 Structure of the Thesis

Within this chapter, the basic design, operation and composition of the pMDI has been discussed. The need for optimisation of the design was also highlighted, along with the key deliverables of the research. Each component was considered, along with issues of the current design. From this point the thesis is divided into a further 8 chapters.

Chapter 2 introduces the key concepts in tribology, with reference to the inhaler design and previous attempts at modelling similar phenomena. It starts with describing the regimes of lubrication before moving onto additional physical mechanisms, such as adhesion and swell, which can have an impact on the behaviour of the pMDI device.

Chapter 3 covers the experimental work that was carried out. This includes rig design and details of the methodology used. Additional testing of materials parameters is also included within this chapter and typical results are presented.

Chapter 4 presents dynamics' modelling of pMDI devices. The details of the ADAMS multi-body model are explained. This is with reference to both the general form and the inhaler valve design in particular, with the constraints and components used.

Chapter 5 continues the numerical work with details of the initial modelling approach, taken from some empirical equations. The additional phenomena and their implementation within the model are also discussed, including surface asperity interactions and inter-molecular forces. This chapter tackles the initial analytical approach and its integration within the ADAMS environment. The equations used for the lubricated conjunction, frictional forces and load distributions are outlined, with the results from the numerical model discussed further. Comparisons with physical testing of components are also highlighted.

Chapter 6 explains the further numerical work undertaken to investigate the contact conjunction and the conditions within the lubricant film in greater detail. Starting from an analytical solution, the chapter outlines the process by which the current solution was developed. Details of the numerical solution of Reynolds are provided, as well as the calculation of the seal fitment load and shape. Each part of the methodology is broken down in detail, and a program flow chart is shown to give a clear picture of how the numerical model is devised.

Chapter 7 presents a parametric analysis and discusses the main trends and findings. Studies have also been carried out using Hertzian theory and that due to Karaszkiewicz. Comparisons for various methods are also outlined.

Finally, chapters 8 and 9 discuss the final conclusions of the research and the suggestions for future work.

2.0 Introduction to Lubrication

A lubricant is regarded as any substance that reduces friction and wear characteristics of two solids in contact and in relative motion. In general, lubrication takes the form of a liquid. However, a lubricating solid, grease or gas can also be used in certain applications. For example, grease may be used in some roller or ball bearings or gas within a gas bearing (Hamrock B, 1994).

The benefit of successful lubrication in pMDIs is obvious. Friction is reduced within the mechanism, thus improving efficiency and the smoothness of the actuation process. Additionally, with reduction of wear, component life is prolonged and the risk of the patient inhaling debris minimised. The extent of benefit that lubrication offers is dependent upon the regime of lubrication, and thus the thickness of a lubricating film.

2.1 Lubrication regimes

The regime of lubrication within a contact can vary considerably depending on contact geometry, kinematics, applied load, lubricant rheology and the materials of the contacting solid surfaces. Depending on the aforementioned conditions lubrication can vary from boundary to fully hydrodynamic. The prevailing regime of lubrication can have a dramatic effect on the friction force caused by the reciprocation between the contacting surfaces. Boundary lubrication/dry contact conditions, for example, give a coefficient of friction value at least an order of magnitude greater than that of a hydrodynamic contact (Cameron, 1976).

Therefore, the regime of lubrication within the inhaler valve mechanism is extremely important, because depending on it, the resulting actuation motion may be smooth, or not. Likewise, if an excessive lubricant film is allowed to develop, leakage can occur. Therefore, in order to prevent wear of the seal and allow smooth actuation, while preventing leakage, the lubrication regime at the seal must be investigated. If necessary, the seal geometry, topography and material composition can then be

manipulated in order to encourage or - as the case may be - discourage a lubricating film.

Regimes of lubrication can be classified using the λ ratio (Hamrock, 1994) sometimes referred to as the oil film parameter, whereby:

$$\lambda = \frac{h}{\psi}$$

where:

h = lubricant film thickness (2.1)

ψ = rms value of composite surface roughness of the contacting surfaces

$$\psi = \sqrt{\psi_1^2 + \psi_2^2}$$

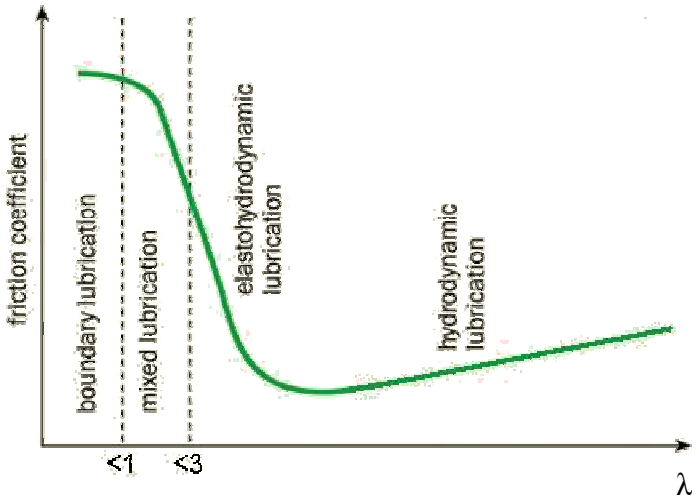

Figure 2.1: Regimes of lubrication (Stribeck, 1907)

In Figure 2.1, it can be seen that the classification of the lubrication regime comes under the following criteria:

$3 \leq \lambda$,Fluid film lubrication

$1 < \lambda < 3$,Partial or mixed lubrication

$\lambda < 1$,Boundary lubrication

The Stribeck curve in Figure 2.1 illustrates the variation of the coefficient of friction depending on the μ-λ relationship in a qualitative manner. It can be seen that there are four basic categories in which lubrication can be considered. What follows is a basic description of each of these regimes of lubrication.

2.1.1 Boundary Lubrication

Boundary Lubrication can be defined as the regime, where the average oil film thickness is less than the elastically deformed surface roughness. Therefore, the surface asperities come into contact with each other under relative motion (Hsu and Gates, 2005). This is a possible regime during the initial actuations of the device, where no fluid film has been previously established, and the elastomer surface has undergone no 'smoothing' of its asperities due to wear. Should a film of entrained fluid fail to lift or deform the seal, then boundary lubrication may be the case throughout the actuation cycle of the device.

In this region the contacting surfaces are not separated by lubricant film. Therefore, the lubricant does very little to reduce wear/friction - in comparison to full hydrodynamic lubrication - and a large amount of asperity contacts take place. The contact of the two surfaces is governed by the properties (both physical and chemical) of thin surface lubricant films. These films are no more than a few molecules, being no more than 1 – 10 nm in thickness (Grimble *et al*, 2008 (See Appendix) and Hamrock, 1994).

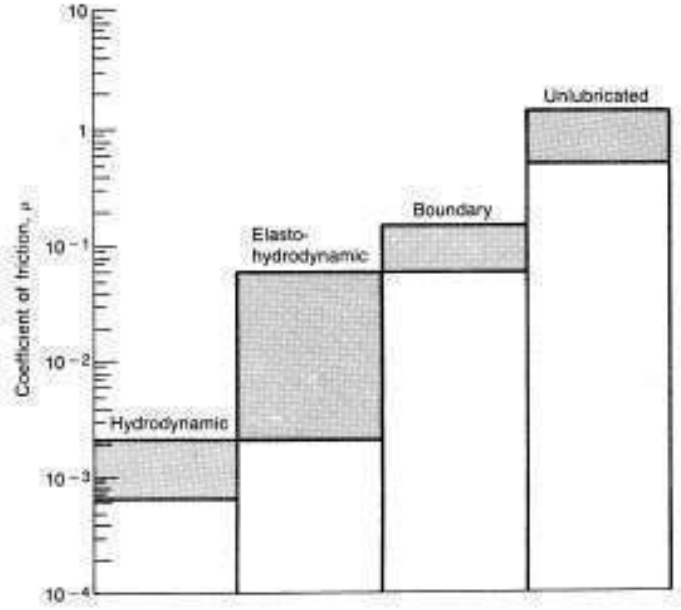

Figure 2.2: Coefficients of friction for different lubrication conditions (Hamrock B, 1994)

As it can be seen in Figure 2.2, boundary lubrication still represents a significant improvement in terms of reducing the coefficient of friction over totally dry contact.

This form of lubrication is mainly used for applications with heavy load and low running speeds (Hamrock, 1994). Therefore, machine elements that would otherwise be unable to operate due to excessive wear, such as scoring or seizure, can still be operational; for instance bearings, gears, cam and tappet interfaces (Hsu, 1997), where either a hard, wear resistant coating or a soft lubricating layer is used, depending on application. In the case of seals contact loads may not necessarily be high.

Depending on the materials in contact, there appears to be several different methods by which boundary lubrication functions. These include the presence of a sacrificial layer, a low shear interlayer, a friction modifying layer, a shear resistant layer and load bearing glasses (Hsu, 1997). Torrance (2005) has attempted to develop previous models of plastic-rigid sliding (Green 1954). The newly presented model utilises an elasto-plastic asperity sliding model to account for the over-estimation of surface strains when using the original rigid-plastic approaches and wedge approximation to describe the interaction of asperity and contacting surface (Torrance, 2005). A more chemically based investigation has been carried out to predict the formation and performance of boundary lubrication films (Hsu, 1997, Hsu and Gates, 2005). Taking note of friction and heat generated by the colliding, and possibly fracturing asperities with a view to the chemical reactions and the properties of the resulting boundary films that are formed. Although it is felt that the chemical reactions between the elastomer and the formulation would be of importance, their inclusion would unnecessarily complicate the research at this early stage of the investigation.

2.1.2 Mixed Lubrication

If the pressures within elastohydrodynamic (EHL) regime of lubrication are too high, or the operating speeds are too low, then the lubricant film will not be able to fully support the load and the film will be breached by surface asperities (Hamrock, 1994). Some film formation will, therefore, occur and partial or mixed lubrication would take place. The average film thickness is in the region of 0.01-1 μm (Hamrock, 1994).

The transition from fully developed EHL to mixed lubrication is not instantaneous, and is very much dependent on load and operating conditions. It is certain, however, that as the film becomes increasingly penetrated by the surface asperities, a greater proportion of the contact pressure will be supported by the asperities (Hamrock, 1994). This state of lubrication is, however, difficult to describe, since different lubrication regimes can appear at the same time (Luo and Liu, 2006). The hydrodynamic pressure will continue to obey Reynolds equation, while the asperity contact pressure follows the theory of elasticity (Hu et all, 2001). A large amount of investigation is still required in this area, particularly in the nano-scale conjunctions, as during mixed lubrication a detailed description of the lubrication regime present at any time is needed. While as the film thickness approaches that of the surface roughness, the effect of the surface roughness on the lubrication conditions becomes increasingly important (Luo and Liu , 2006).

Luo and Liu (2006) have used a relative optical interference intensity approach with a resolution of 0.5 nm vertically, and 1 μm horizontally. This allowed an investigation relating the contact width to factors such as surface roughness, Hertzian pressure and the combined effective elastic modulus. They concluded that the dynamic contact ratio is decreased by increasing the lubricant viscosity and speed. The addition of polar additives resulted in a decrease in pressure. Furthermore, surface asperity contact for a rough surface is found to take place at a higher speed than for a smoother surface (Luo and Liu, 2006). The resulting relationships correspond well to the measured phenomena for a steel plate/glass ball interaction. However, the paper does not cover polymer/rubber interactions.

Further research (Hu et al 2001) for point contacts has also been carried out, modelling asperity contacts as the result of a continuing decrease in film thickness. Therefore, there is no need for discontinuous conditional equations to model each aspect of mixed lubrication, but rather a single, continuous approach can be used. This is achieved through manipulation of Reynolds equation as the film thickness approaches zero (Patir and Cheng, 1979). The results obtained agree qualitatively with what would be expected for a point contact under both EHL and boundary lubrication regimes, with converged, stable solutions obtained by Hu et al (2001). However, no comparison to physical data was demonstrated. This approach was later

developed to include thermal effects by Wang et al (2005) and again, the model agreed qualitatively with what was expected by theory, although again, no comparison to physical data was demonstrated. In the analysis the thermal effects were found to be minor unless the thermo-elastic deformation of the surfaces were taken into account, which can cause increased thermal stresses, larger contact areas and higher contact pressures within a contact (Wang et al, 2005).

Another aspect of research concerns the useful life of a mechanism (Nogueira et al, 2002). This is obviously an important area to this investigation due to the changes the elastomer seals undergo during use, such as the smoothing of the surface and the possibility of wear particles being formed. It has been found that the surface roughness of the contacting surfaces must be chosen carefully to prevent excessive deterioration, but allowing the smoothing process of running-in (mechanism operation) to achieve an equilibrium (Nogueira et al, 2002). The running-in process alters the surface properties used in studies, such as in Hu Y et al (2001, Luo and Liu (2006). An attempt to model the parameters of the contacting materials with a view to reducing the necessary running-in period is provided in Nogueira et al (2006). The study does, however, concentrate on metallic contacts and not that of elastomers. Therefore, while a hydrodynamic parameter was developed in order to distinguish between regimes of lubrication, its applicability for this investigation is doubtful.

2.1.3 Elastohydrodynamic lubrication (EHL)

Elastohydrodynamic lubrication (EHL) is a variation of hydrodynamic lubrication, whereby the elastic deformation of a contacting surface has permitted the development of a supporting fluid film whose viscosity also alters with application of pressure in the case of hard EHL (For relatively hard contacting surfaces and therefore high pressures i.e. steel on steel). For relatively soft contacting surfaces however, such as those within the housing/seal conjuncture within this thesis, soft EHL prevails and it is the relative deformation of the surfaces for the given pressure distribution that is of importance rather than the absolute magnitude of the pressure itself. The magnitudes of which are in fact relatively low and therefore have little effect on the viscosity of the lubricant (i.e. MPa as opposed to GPa). While a hydrodynamic film may not be present, the elastic deformation of the pMDI valve seals may allow a thicker film than what would be predicted using conventional hydrodynamic theory to form within the deformed contact.

EHL has been a dominantly studied regime of lubrication during the second half of the 20th century (Dowson, 1998). Normally associated with non-conforming surfaces (Hamrock, 1994), there are two forms of EHL contact. These relate to a hard EHL contact, or a soft EHL contact (Gohar and Rahnejat, 2008).

Hard and soft EHL relate to materials of high elastic modulus and low elastic modulus respectively. Hard EHL usually permits maximum pressures of between 0.5 and 3 GPa, corresponding to Hertzian pressures. In contrast soft EHL typically operates with lower pressures and is sometimes referred to as iso-viscous elastic, where insufficient pressures do not significantly alter lubrication rheology (Gohar and Rahnejat, 2008).

Stephenson and Osterle (1962) numerically solved the problem of a line contact for a range of loads, from low load hydrodynamics to the heavily loaded full EHL case. This early work presented a simple numerical solution tailored to computational use, and illustrated the importance in selecting the correct weighting (damping) factors in order to achieve a successful converged solution. Due to initially not taking viscosity changes into effect, and in part due to the loading conditions examined, the EHL

pressure ‘spike’ was not found to be present during the course of the work. Therefore, while a very valid starting point, the work required further development in order to produce accurate results, particularly for the heavily loaded cases.

Other works, such as those by Cheng and Sternlicht (1965) introduced the element of temperature into the concept of the EHL solution. By coupling, not only the elasticity and Reynolds equations, but also those of energy within the system, thermal effects can be taken into account. The line contact of two infinitely long rollers (both rolling and sliding in motion) was considered under heavy loading, with the familiar EHL pressure ‘spike’ being found towards the exit of the film. Comparison was made to an identical case under isothermal conditions and the effect of temperature was found to be of moderate importance, although the peak pressure value was subjected to less than a 10% rise when taking into account thermal effects, with a similar level of effect visible in the film thickness. As such, and due to the complicated nature of thermal modelling the conditions within the pMDI valve, temperature effects were discounted. In fact thermal contributions during actuation would be negligible due to the very slow actuation speed and relatively low friction. Although it is recognised that the speeds are higher in use, the aerolisation of the formula also introduces a cooling effect similar to those noted for bearings by Cheng and Sternlicht (1965). This would no doubt be governed by the formulation of flow properties and, as such, are beyond the scope of this PhD.

Herrbrugh (1968) attempted to couple the hydrodynamic and elasticity equations into a single integral expression. This was then applied to a large range of load conditions assuming iso-viscous conditions. This approach was devised in order to overcome the iteration convergence problems of the traditional Reynolds approach when used with even moderate contact loads. While such a robust approach is desirable, the inclusion of viscosity variation is extremely important. Besides that, in the case of a pMDI, high loads are not present. Therefore, a more traditional approach is more applicable, and with modern computational capabilities no longer detrimentally slow or unstable, as a slower rate of convergence can be chosen to increase solution stability.

The analysis of an isothermal EHL contact was carried out with the numerical evaluation of a point contact by Hamrock and Dowson (1976) using a discretised

approach and the assumption that a uniform pressure could be applied across each individual element of the contact domain. In this way, the simultaneous solution of both the Reynolds and elasticity equations, were achieved. The pressure and film thickness variables were coupled using the additional variable Phi, where:

$$\phi = PH^{3/2} \tag{2.2}$$

This approach is referred to as solution of Reynolds equation using the Vogpohl transformation.

This allowed for a more stable solution under extremes of pressure, as a gentler curve is produced in relation to the gradient changes of pressure against X (domain position). By reducing the gradients values, a more stable relaxation method is achieved. This meant that convergence could be achieved at a faster rate, or indeed at larger load examples.

Following on from their initial work, the ellipticity parameters of the contact were explored (Hamrock and Dowson, 1976) in order to provide a range of validated results and also investigate the effects of the elasticity parameter on the resulting pressure profile and film shape. The parameter was varied from that of a ball on plate contact (i.e. circular) to that approaching a line contact condition. The analysis reproduced the findings of the optical interferometry and showed good agreement in terms of film thickness and profile (Hamrock and Dowson, 1976). It was also shown that, following a line contact analysis, the minimum film thickness for an elliptical contact could be ascertained using the simple formulation of:

$$H_{\min} = H_{\min,L}\left(1 - 1.6e^{0.62k}\right) \tag{2.3}$$

where k is the ellipticity parameter of the contact.

Finally, Hamrock and Dowson (1977) utilised their previous work in order to fully examine the influence of the ellipticity parameter, dimensionless speed, load and material parameters of the contact on the minimum film thickness within a fully

flooded point contact. The dimensionless speed was varied over two orders of magnitude, while the load was varied over a single order of magnitude. A range of materials and lubricants were also considered and in total 34 separate cases were examined. From this, a formula for the minimum film thickness was obtained as:

$$\widetilde{H}_{\min} = 3.63U^{0.68}G^{0.49}W^{-0.073}\left(1-e^{-0.68k}\right) \tag{2.4}$$

The presented analytical equation is extremely important as it allows a simple and fast analysis of elliptical Hertzian contacts. Negating the need for complex and slow numerical work, this approach is very beneficial to industry and as such represents a worthwhile route for the analysis of this thesis to take. Therefore, such an expression is sought, but with applicability to the soft EHL line contact conditions of the pMDI contact.

Mostofi and Gohar (1982) have also offered a numerical solution to the elastohydrodynamic point contact problem with the work being primarily for the investigation of metal to metal contacts in machinery. The applied theory in this case is very similar to the approach used in this thesis: the Reynolds equation was coupled with computational grid and a variation of Hamrock's deflection method to solve the elastohydrodynamic problem. In this instance the case of component rotation is also considered, as is that of differing geometries of a roller. Convergence was achieved for moderate loads and material parameters, but as with many research investigations on the subject, extremes of either were avoided due to the computational complications and convergence difficulties.

Pure entraining conditions for point contacts were further considered in work by Jalali-Vahid et al. (1998) for multi-grid solution of isothermal EHL circular contacts. In this work the use of multi-grid solutions allowed for a fast convergence to be achieved, while also allowing a large number of elements to be utilised so as to offer improved accuracy over a more conventional domain grid. Convergence was achieved for both high loads and low entrainment velocities and, therefore, this method can be regarded as a success in modelling terms.

In this work, a combination of backwards and central finite differencing was used to balance accuracy and stability, where by:

$$\frac{d\left(\frac{\bar{\rho}H^3}{\bar{\eta}}\frac{dP}{dX}\right)_i}{dX} = \frac{12U^*E'R_x^{\ 3}}{b^3P_h}\left\{(1-\beta)\frac{(\bar{\rho}H)_{i+1}-(\bar{\rho}H)_i}{\Delta X}+\beta\frac{(\bar{\rho}H)_i-(\bar{\rho}H)_{i-1}}{\Delta X}\right\} \qquad (2.5)$$

where β was chosen to be in the range 0.6-0.75. As such, this represents a potential approach to the implementation of the pMDI numerical model and the solution of the Reynolds equation.

The work by Hu and Zhu (2000) further explored the lubrication of point contacts, but with a view to the mixed lubrication condition as opposed to that of the fully flooded boundary condition within the work of Hamrock and Dowson (1976). In this instance the contact is assumed to be dry in areas of zero film thickness and hydrodynamically lubricated where a film thickness is present. Surface deflection is taken into account, providing an EHL solution. Most notably, the ability to take into account three-dimensional measured engineering rough surfaces is included within the model and as such the work represents an interesting addition to the previous works on the subject. In the case of the pMDI, however, it is not felt that such a method is the best route to take, since due to the nature of the components surface, it is difficult to obtain such data.

In an attempt to improve stability, the EHL problem was examined with the intention of coupling the process of solving the Reynolds equation with that of the elasticity and lubricant properties by Elcoate et al (1998). In this way, the instabilities of high loads and dominant surface deformations were avoided. A line contact Reynolds solution and comparable approach for the elastic deformation was used as a basis for the analysis, with the coupled solutions improving stability and allowing problems to be solved where the elastic surface deformation was key to the establishment of an EHL solution. This paper considers relatively high pressures and hard materials in comparison to those within this thesis. As such, while instabilities were encountered, it was not due to the high gradients of pressure as found in the work of Elcoate et al (1998). Therefore, such an approach was not deemed necessary.

The film thicknesses and pressures in EHL contacts were calculated by Houpert and Hamrock (1986) for line contacts by making use of the Roelands viscosity formula, a non-uniform discretised mesh and the three node approach to the deflection influence matrix. Although a two node approach proved more stable, the three node approach considerably reduced the number of required nodes for accurate calculation of the elastic deflections (Houpert and Hamrock, 1986). Almqvist and Larsson (2002) took a more conventional EHL solution approach for the Reynolds equation, by coupling it with thermal effects and also those of flow around the contact domain to give a more thorough picture of the phenomena within and around the EHL contact. This approach was also undertaken by Kushwaha and Rahnejat (2002) for roller bearings and Balakrishnan and Rahnejat (2005) for partially conforming contact of piston skirt to cylinder liner, both under isothermal conditions. Almqvist and Larsson (2002) concluded that the Navier-Stokes approach allowed successful solutions to thermal EHL problems up to moderate loads, however, the computational requirement was large and the convergence was very slow in order to avoid instability. This work, therefore, does not solve some of the inherent problems of EHL conjunctions but it does offer a more detailed solution.

A further attempt to improve both computational efficiency and stability was that of a non-uniform grid spacing. Within the contact region and where large pressure gradients are likely to be present, a large number of nodes are used, outside of which far fewer are found to be necessary. This technique was used in the work by Park and Kim (1998), who applied it to the EHL problem of a finite line contact and more specifically the case of an axially profiled roller, rolling over a flat plate surface. Although, in this instance, only moderate loads and material parameters were utilised, results were found to closely resemble those of. Johns and Gohar (1981) and Mostofi and Gohar (1982) who had previously reviewed the application of EHL theory to the study of roller bearings. In this instance the effects of temperature were ignored. However, a two dimensional numerical solution was employed, and roller misalignment effects were explored. The profile shape was shown to be extremely important and the numerical work was found to be useful in choosing the correct roller design for a given application with regard to axial profile edge blending, similar to the work of Kushwaha and Rahnejat (2002). With this in mind, geometry is a key

area that for investigation in this thesis, though due to the symmetry of the pMDI valve, a one dimensional analysis could be sufficient.

The lubrication of piston rings has also been a much analysed contact, being of particular importance in achieving efficient engine designs. Dowson, Ruddy and Economou (1983) examined this case to establish the contribution of EHL to the previously regarded hydrodynamic lubrication studies, in particular, during the high pressure conditions with the piston at the top dead centre in the power stroke of the combustion cycle. They concluded a four-fold increase in film thickness with the inclusion of deflection and pressure-viscosity effects, which represented a clear step forward in the modelling of piston ring-cylinder conjunctions. Such a result highlights the importance of accurately modelling the contact conditions. The pressures within the pMDI valve are much lower and the elastomer seal is also a great deal softer. It is, however, recognised that the work of Dowson, Ruddy and Economou (1983) puts forward a relatively simple representation of what is expected to be a complex contact scenario in pMDIs. Jeng (1992) also reviewed the case of a fully flooded piston ring-cylinder contact, by considering the conjunction as a one dimensional line contact along the ring face-width. In terms of piston ring analysis, the approach taken is somewhat simplistic compared to that of others, for example that of Dowson, Ruddy and Economou (1983). However, a very quick solution makes it an attractive approach with reasonable accuracy. This approach is in fact more applicable to that of a pMDI valve whose seal can readily be compared to that of a line contact scenario and so bears a resemblance to the modelling direction taken in this thesis.

The concept of partial lubrication, as opposed to full, was considered for a rough line contact case by Yujin and Linqing (1993). Of particular interest was the limit at which partial lubrication would take place, with that being at the point at which contact of surface asperities begins to appear, with the ratio of nominal film thickness to the root mean square composite surface roughness (i.e. the Stribeck oil film parameter) giving an indication of the contact conditions. It was also noted that the contacts of asperities are of great influence under lower loads, contributing significantly to the supporting contact pressure as a proportion of the overall load. Therefore, it was felt that in order to ascertain whether partial or full film lubrication was to be considered for pMDIs,

the load and surface asperity distributions must also be considered in addition to the film thickness-to-roughness ratio.

Akalin and Newaz (2001) analysed a piston ring-cylinder contact to provide an axis-symmetric, hydrodynamic/mixed lubrication model with a view to allowing potential wear calculations based on asperity pressure data. The results of the study showed good agreement with those of a measured piston ring-cylinder assembly by Furuhama and Sasaki (1983). An even closer agreement was obtained between the same measurements and two dimensional thermal-elastohydrodynamic analysis reported by Mishra, Rahnejat and King (2008). The one dimensional approach by Akalin and Newaz (2001) is however quite sufficient which is not too dissimilar to that taken in this thesis for the case of a seal against its retaining groove. The addition of cavitation at the exit boundary of the contact is also taken into account. Of importance to this thesis though, is that the inlet and outlet boundary conditions are known canister pressures at a certain point along the inlet/outlet domains. This can make the solution somewhat easier. In fact analytical approaches have been proposed for the case of o-ring seals by Hooke et al (1966) and Karaszkiewicz (1987). When considering a loaded seal within a pMDI, the canister pressure must be accounted for when considering the likely entrainment of lubricant within the contact.

The partial lubrication of a general EHL line contact was considered by Chang (1995). Taking a deterministic approach to the modelling of the surface asperity contact pressures, the work attempted to accurately calculate the interactions of asperities when compared with the more traditional models. The work represents a preliminary starting point with a number of assumptions requiring consideration. However, on the whole it is an interesting approach although stability and slow convergence is still an issue. It was not felt that this approach offered any benefit at this stage in terms of modelling the pMDI seal contact. Another work to consider the mixed lubrication model of a line contact is that of Faraon and Schipper, 2007. In this work the condition of a starved line contact was considered, using the resulting analysis to establish a λ parameter, where the surface roughness is a dominant factor over the film thickness and compare the case to the fully flooded contacts, where the thickness-to-roughness ratio was larger. Again, good agreement was found with the accompanying experimental analysis and importantly, the need to consider the film

thickness-to-roughness ratio for the pMDI case was highlighted. The lubrication conditions of the pMDI varying such that while initially the pressurised canister and therefore ample supply of lubricant aid fluid film formation, on the return stroke of the actuation the lubricant supply is dependant on the volume of lubricant that entrained past the seal and hasn't since evaporated following the initial in-stroke. Therefore a starved condition is likely to exist at this point. It is however shown later (see Chapter 7) that boundary lubrication prevails as entrainment is minimal during the entire actuation cycle suggesting lubricant supply is not the governing factor.

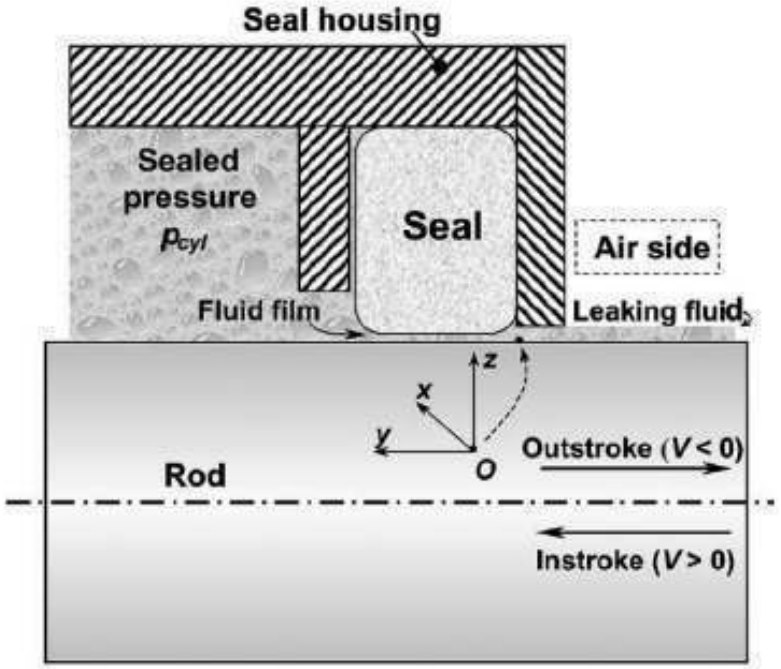

Figure 2.3: Basic seal assembly (Nikas G K and Sayles R S, 2005)

Research on reciprocating seals primarily considers rectangular seal cross sections (Nikas and Sayles, 2005), (Figure 2.3). A typical seal such as that shown belongs to the category of incompressible hyperelastic materials. What is of importance is the approach taken in relation to modelling the elasticity of the seal for global fitment deformation and under a differential applied pressure. It was found that for normal strains below 10%, the classical linear elasticity theory is applicable (Nikas and Sayles, 2005). Beyond this limit (Hookean limit), however, the Mooney-Rivlin model was applied. Using the elasticity models, the deformation of the seal was calculated

and this, along with roughness information was used to calculate the film thickness in the contact. The friction force due to the viscous shear (no asperity contact is assumed) was then calculated (Nikas and Sayles, 2005). Surface roughness effects were assumed to be an unnecessary addition due to the flattening of the asperities following running-in and under the operating pressures of the mechanism, with typical film thicknesses being in the region of 1 nm-1 μm, while asperities are in the region of 0.2-3 μm, depending on the state of running-in. Therefore, it was found that due to the minimum film thickness, the EHL contact pressure is almost equal to that of the dry contact pressure. It was also found that operating speeds greatly influenced film thickness, as does the seal profile. This work also concluded that an optimum operating speed exists in terms of film thickness and leakage, as does an optimum seal interference. This shows the requirement for theoretical modelling for inhaler valve seals rather than the inefficient current empirical approaches. A great deal of research on the subject is in place, from the basic numerical approach used (Nikas, 2003) and the computational procedure, to more developed schemes of modelling. Variations include the inclusion of transient parameters, such as the seal pressure and stroke velocity (Nikas, 2003). Also, the significance of back-up rings has been considered (Nikas, 2004), as has the configuration of tandem seals (Nikas and Sayles, 2005), although this would increase friction. Therefore, while results from the approach only achieved a similar order of magnitude to the experimental data taken, such an approach does, however, represent a comprehensive starting point for the current investigations.

Dowson has conducted a great deal of research on bio-tribology and synovial joints (Dowson, 1998, Dowson and Ehret, 1999, Jin and Dowson, 2005) in relation to the calculation of film thickness in both line and point contacts (Dowson and Ehret P, 1999). This work includes the introduction of an inverse procedure to allow the lubricant film thickness to be calculated for higher contact pressures without the risk of numerical instabilities, but with problems at low loads (Dowson, 1998). They suggest that a more basic model may be lacking in accuracy as Newtonian treatment of the lubricant, for instance, has been found in the past to over-estimate the resulting frictional forces of the contact (Dowson and Ehret, 1999). The limit of Newtonian flow is marked by the Eyring reference stress and is determined from the isothermal traction plots for a given lubricant at a given pressure, and therefore, must be taken

into account in order to improve accuracy (Evans and Johnson, 1986). Dowson, however, suggests that surface roughness is a relevant parameter (Dowson and Ehret , 1999), unlike Nikas and Sayles (2005) who point out that the flattening and running-in process negates the need for its inclusion. Therefore, it is unclear which approach is more valid. While surface roughness may be low, however, for the inhaler the likely scale of the lubricating layer would suggest that Dowson's conclusion of it being a necessary inclusion is of paramount importance.

Following their earlier work, Dowson and Hamrock (1976) investigated the elasto-hydrodynamic lubrication of low elastic moduli materials starting initially with fully flooded conditions (Dowson and Hamrock, 1978). The effects of material parameters, load and dimensionless speed were analysed, as was the effect of the ellipticity parameter in order to review conditions from a point contact to that approaching a line contact. Of key importance in this work was the changes that were necessary for the analysis of soft elastohydrodynamic lubrication. More specifically, the deflection was broken down into two parts: that of the dry Hertzian condition caused by static loading or fitment, and that of the pressure difference caused as a result of the Reynolds equation. In this way, convergence was achievable and code stability was maintained.

Following this initial success, elastohydrodynamic lubrication of low elastic moduli materials was investigated under starved inlet conditions (Hamrock and Dowson, 1979). This was achieved by moving the inlet of the conjunction further towards the centre of the contact region, allowing a relationship to be developed such that:

$$m^* = 1 + 1.07\left[\left(R_x/b\right)^2 H_{\min,F}\right]^{0.16} \qquad (2.6)$$

where, Rx is the effective radius of curvature, b is the Hertzian half width and $H_{min,F}$ is the dimensionless minimum film thickness for the fully flooded case. It can be shown that for the inlet distance (m) less than m*, starved conditions would exist, and when $m \geq m^*$, fully flooded inlet conditions prevail.

Calladine and Greenwood (1978) approached the deformation of an elastic surface through the use of an elastic half-space. An approach to model both line and point loads allowing for a change in the elastic modulus was determined using proportionality with the depth of the deflection.

2.1.4 Hydrodynamic Lubrication

Full fluid film lubrication represents a somewhat 'ideal' form of lubrication with the two surfaces being completely separated by the supporting lubricant. The supporting fluid wedge is formed by the relative surface motion. This means that both friction and wear are extremely low, allowing sufficient sealing to be maintained and the actuation to be smooth and consistent. In this regime, the minimum film thickness normally exceeds 1 μm (Hamrock, 1994). From a mathematical point of view, hydrodynamic lubrication is a particular form of the Navier Stokes equations, formulated as the Reynolds equation, a further explanation of which can be found in Pinkus and Sternlicht (1961). The film thickness is a function of the lubricant viscosity, the velocity of relative motion and also the load. As viscosity or velocity increases, so does the film thickness. Inversely as load increases, the film thickness decreases. Temperature is also an interrelated factor of viscosity and velocity (Pinkus and Sternlicht, 1961). Note that for elastohydrodynamic contacts, on the other hand, film becomes an amorphous solid and rather insensitive to load. Any increased load spreads the contact area, rather than affecting the film thickness.

It follows that for a hydrodynamic film to be formed, the fluid viscosity must be high enough to support the load, as must be the operating speed (Pinkus and Sternlicht, 1961). A more relevant area of research to this PhD is that of Karaszkiewicz (1985, 1987 and 1990) into hydrodynamic lubrication with specific consideration of O-ring seals.

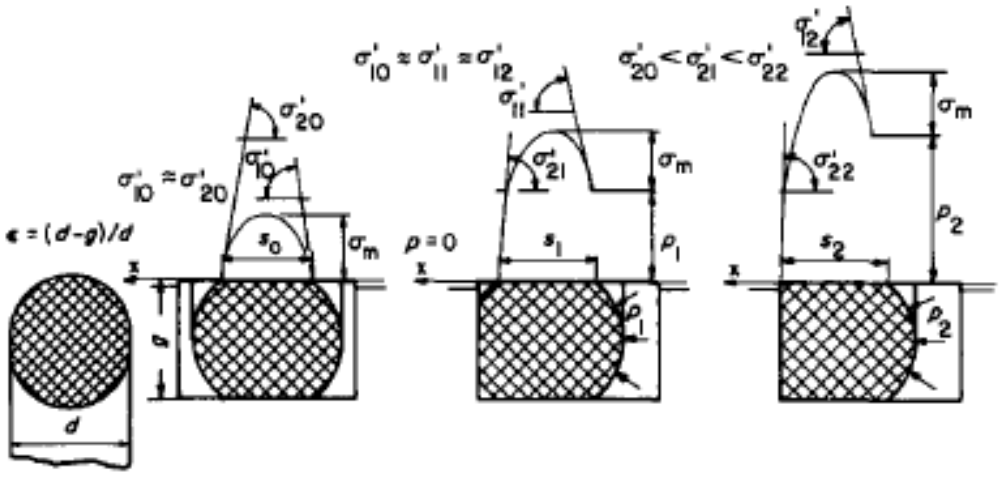

Figure 2.4: O-Ring pressure distribution, from left to right, O-ring: at sealed pressure P = 0, P = P_1, P = P_2 (Karaszkiewicz 1985)

Figure 2.4 shows the seal, housing and pressure case under consideration, where $P_1 < P_2$. Karaszkiewicz puts forth concepts, such as that a sliding distance twice the contact width is required to establish the film (Karaszkiewicz, 1985) and also that as the contact width is significantly smaller than the seal diameter, a line contact situation can be assumed (Karaszkiewicz, 1990). Using the work of Dowson on the film thickness of an elastohydrodynamic infinite line contact model, relevant equations for an O-ring were found (Karaszkiewicz, 1987). It has been shown experimentally that the contact pressure of an O-Ring is equal to that of Hertzian when fitted *in-situ* according to Karaszkiewicz (1979). This has allowed the calculation of pressure force per unit area of the O-ring, both for an un-pressurised and pressurised seal (Karaszkiewicz, 1987). In addition to the leakage rate, the contact width of both undeformed and deformed seals may be calculated using an analytical approach (Karaszkiewicz, 1990). When coupled with the equations for the friction force as a result of the viscous shear of the lubricant (see for example, Persson, 2000), the complete parameters of the O-ring seal can be modelled. The experimental verification of Karaszkiewicz (1987) shows reasonable agreement with the equations formed for film thickness and leakage. This, therefore, provides a useful, quick to implement starting point for the initial modelling of the inhaler valve mechanism.

2.2 Introduction to Rubber Characteristics and Modelling

In this thesis the terms ‘rubber’ and ‘elastomer’ are interchangeable for ease of reading. The review here concentrates on the literature relating specifically to O-ring seals, and also to the interaction of rubber components with the inhaler formulation. Of particular importance are those parameters of the rubber which relate to the inhaler performance, which are the wear rate, leakage and frictional characteristics (Nikas and Sayles, 2005).

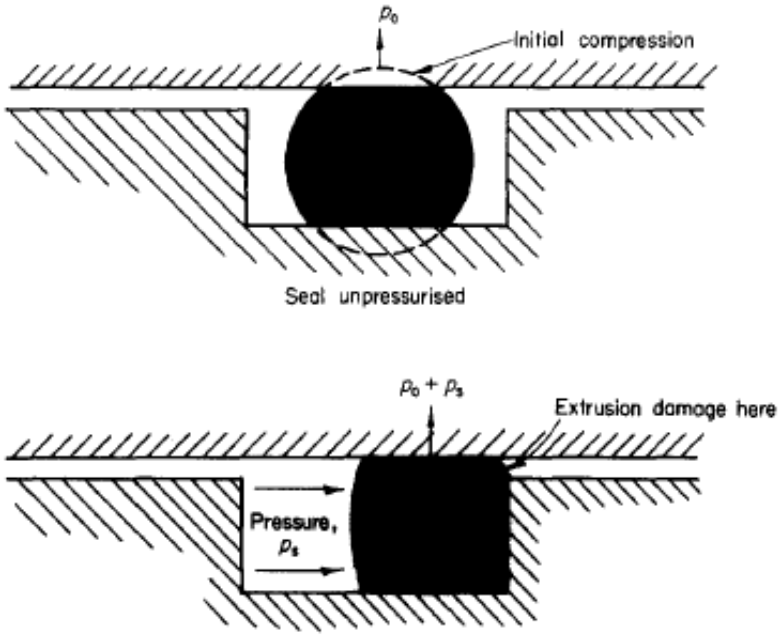

Figure 2.5: O-Ring seal in place (Flitney R K, 1982)

O-rings in particular offer an efficient means of sealing a number of mechanisms. They are economical and due to their production in a wide variety of materials they are suitable for sealing of almost all liquids and gases (Al-Ghathian et al 2005). The initial squeeze of the O-ring provides sealing under static conditions, in the axial or radial directions. When the pressure to be sealed is applied, the total sealing force is generated and provided the peak pressure exceeds that of the system pressure the O-ring will seal, and it is assumed that the pressure is transmitted uniformly over its surface (Figure 2.5). The O-ring is, therefore, capable of sealing a shaft undergoing both reciprocating and rotational motions (Roberts, 1977). Even with recent advances in computer modelling, there still remains the need to accurately calculate the frictional forces acting on the O-ring seals. Therefore, the majority of development

and design still depends on the use of empirical data and friction coefficient charts (Roberts, 1977 and Al-Ghathian et al, 2005).

2.2.1 Rubber sliding studies

A number of researchers have investigated the process by which rubber slides relative to a surface of different materials. Despite this, the sliding properties of rubber remain poorly understood (Chandrasekanren and Batchelor, 1997). When investigating the sliding of rubber over both smooth and rough/abrasive surfaces (Barquins and Roberts, 1986), the asperities of the rubber surface are usually assumed to be ideally hemispherical (Karaszkiewicz, 1987, Nikas and Sayles, 2005, Barquins, 1993, and Barquins and Courtel, 1975). However, it has been reported that due to deformation of the rubber a saturation point is reached at which the asperities form a solid 'block' surface (Barquins and Roberts, 1986). This results in a limiting value for the frictional force. Schallamach likened rubber sliding to the continual formation and destruction of molecular bonds, such that the rubber chains jump across the surface substrate (Barquins and Roberts, 1986). Grosch et al, (1963), found that sliding friction was a result of both the adhesion of the rubber and the counterface, but also the energy losses resulting from the deformation of the rubber asperities. A nominal 'jump' distance for the rubber chains was also found to be around 6 nm (Barquins and Roberts, 1986), with an applied stress directing the otherwise random jumps (Barquins, 1993).

Due to the 'soft' nature of rubber, 100% contact of the mating surfaces is achieved, as previously mentioned by the flattening of asperities. Therefore, as the load (pressure) is increased, the coefficient of friction effectively drops even though the frictional force is constant according to Flitney (1982). This means that modelling through use of friction coefficients is rather problematic (Nau, 1999). Experimentation into the area of rubber sliding consists mainly of a rubber hemisphere sliding on a hard surface (Roberts and Tabor, 1968) or vice versa (Barquins, 1993). From studies into the sliding of O-rings and seals in general Flitney (1982) noted that the profile of the seal is of importance. This has resulted in patent applications such as (United Sates Patent, Glaxo Group Limited, US6,926,178 B1), in which a variety of surface profiles and

seal compositions have been investigated with a view to improving inhaler valve performance.

2.2.2 Adhesion of Surfaces

When two contacting surfaces become separated by no more than a few molecular diameters of an intervening fluid, those surfaces are subject to attractive forces such as van der waals forces (Barquins, 1993). For example, under zero load Hertz would have predicted zero contact diameter. However, his original approach took no account of the short range surface forces, causing the surfaces to attract each other and thus create a finite contact area (Roberts and Thomas , 1974). The effect of short range forces was investigated by placement of a glass cover slip onto the surface of a rubber hemisphere, a microscope was then used to measure the attractive forces present in terms of the contact area generated (Roberts and Thomas, 1974). In addition, the attraction and peeling forces were considered for a rubber cylinder rolling down an inclined plane. Further research has also been conducted by Hui et al (2000) and Moore and Geyer (1972). Attempts were made to extend the contact of elastic asperities into the viscoelastic regime and allow for the 'real' contact area when calculating the adhesive forces (Hui et al, 2000). This is related to the load of the contact and also the time over which contact occurs. The loading history is, therefore, of importance as the asperities of different heights will be under different states of relaxation (Hui et al, 2000). Therefore, it is important to have knowledge of previous states of the rubber, as with slow sliding velocity the adhesive properties of the rubber can become influential (Moore and Geyer, 1972). When considering adhesion, however, a roughness of just 1 μm is enough to reduce the adhesion to a fraction of that of a smooth surface (Fuller and Tabor, 1975). This is an important observation which significantly affects the approach to modelling of inhaler seal contacts.

2.2.3 Schallamach Waves

An area to which the adhesion theories of elastomers lead is that of the Schallamach waves. This is illustrated in Figure 2.6, which shows the wave forming, and travelling

back across the contact. These ‘waves of detachment’ are visible when a hard material and rubber are sliding relative to each other (Schallamach, 1971).

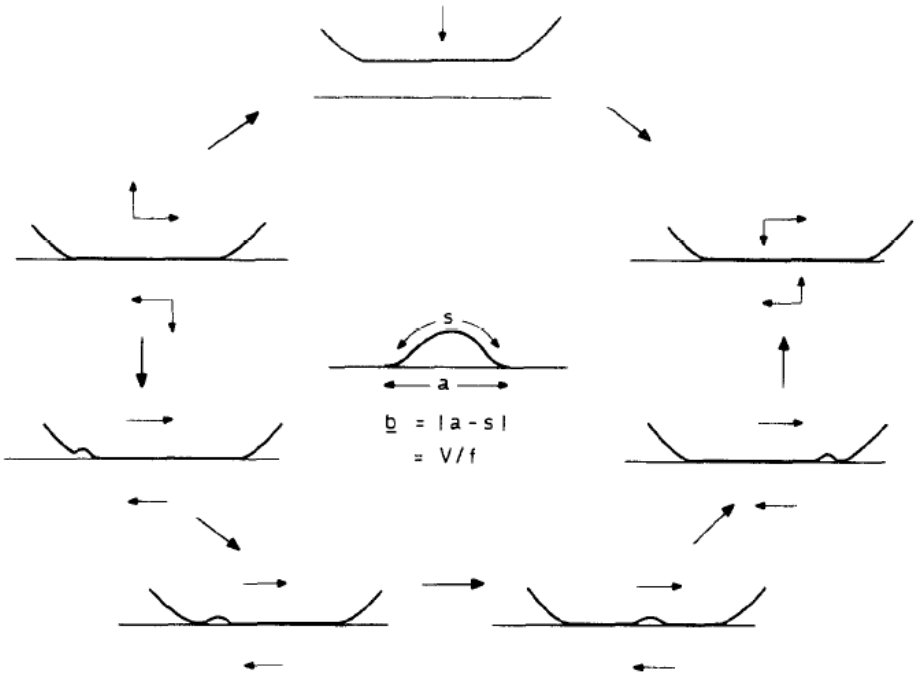

Figure 2.6: Schematic of energy dissipation during Schallamach wave propagation (Briggs and Briscoe, 1979)

These waves propagate across the surface of the rubber at a velocity exceeding that of the sliding velocity (Schallamach, 1971) with the overall sliding displacement attributable to these waves. The adhesion/contact force was calculated for the surface of the wave, although Schallamach was not able to determine if true sliding took place at any point in the contact. This phenomenon is of importance when considering the operation of seals in engineering applications (Barquins and Courtel, 1975). With Schallamach waves forming above a critical sliding velocity, which depends on the interface characteristics (adhesion properties), the geometry of the contact and also on the temperature of the mechanism, it has been found that the critical velocity can be anything from 40 to 800 μm/s (Barquins and Courtel, 1975). The higher the temperature, the higher the critical velocity becomes. The wave frequency also increases so that the number of waves in a contact remains constant (Koudine et al, 1997). What is also noteworthy is that when lubrication was present Schallamach waves could not be observed, although it must be noted that the experiments of Barquins and Courtel (1975) were limited to one configuration of sliding interface

and, therefore, the findings may not apply to all situations. The rubber, for instance, must be sufficiently 'soft', with Schallamach waves not normally observed on harder rubber compounds as the adhesion and shear stresses are not large enough (Best et al, 1981). Any elasticity model used for the seals in pMDIs should, therefore, keep account of such stresses with a view to inhibit Schallamach waves. However, any lubricant would reduce these stresses (reduced adhesion) and therefore the presence of Schallamach waves may be avoided.

2.2.4 O-Ring Parameters

Experiments have shown that while the presence of lubricant reduces the coefficient of friction due to the chemical alteration of the rubber, an increase in wear can result (Chandrasekanren and Batchelor, 1997). Therefore, it is important to be able to characterise the operating conditions the seal would be expected to perform under and understand the effects that such conditions would have on its performance. Research has, therefore, been conducted into the prediction of the life time of an O-ring in service (Gillen and Bernstein Wilson, 1987) by relating the initial compression of the seal to the resulting sealing force and, thus allowing a failure point to be calculated for static seals.

The groove the seal is housed within is also of importance, as this can have an effect on the sealing properties due to contact conformance.

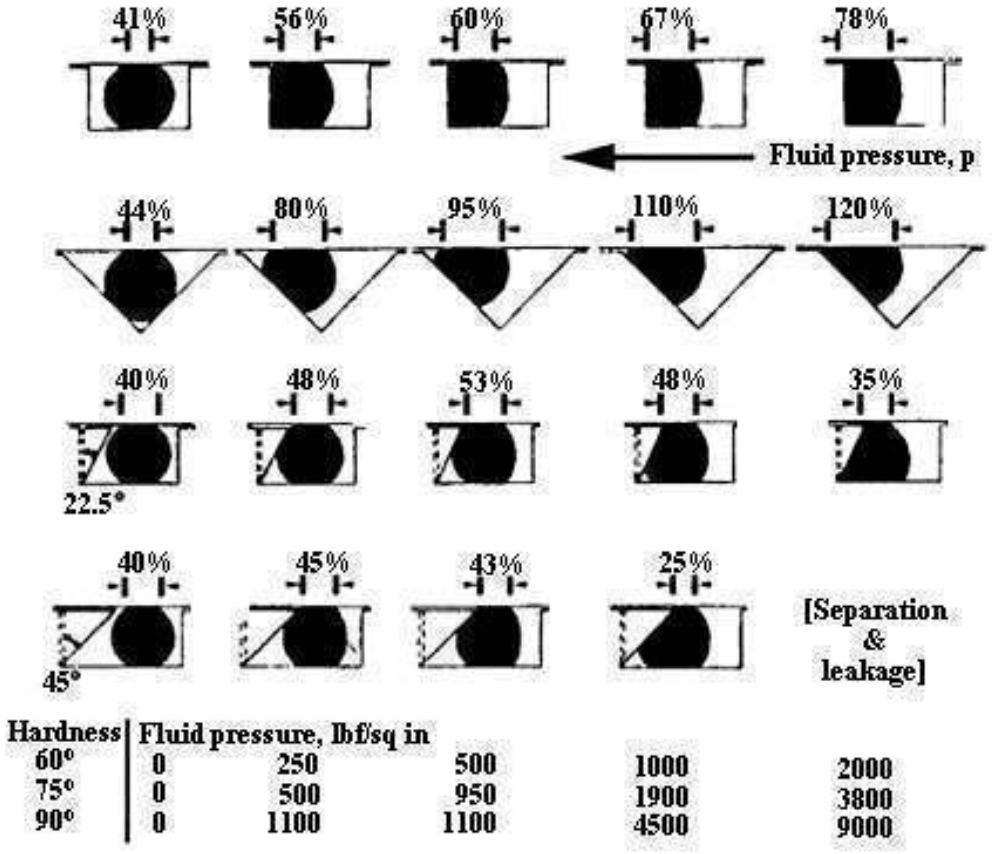

Figure 2.7: Effects of housing shape on contact width (Nau, 1999)

As illustrated in Figure 2.7, appropriate design of the groove profile shape can increase the contact width at higher pressures, or reduce it depending on what is required within the system. Experiments have also shown that it is only with the most viscous lubricant that a seal geometry featuring bevelled edges becomes possible to establish full fluid film lubrication (Nau, 1999), although no account was taken of the seal deformation and the effect of sealed pressure. Modelling techniques have been attempted to determine the mechanical behaviour of a seal. Dragoni and Strozzi (1989) used a linear elastic approach to model an un-pressurised O-ring seal contained within a rectangular groove. With reasonable success for calibrated but not over-sized grooves, insensitivity to modification of Poisson's ratio was noted. Therefore, while this work was an interesting attempt, further research is required to establish a direct repercussion from the model results to the sealing properties.

Lindley (1967) reviewed the contact conditions and load-compression characteristics of toroidal seals with a view to improving engineering design. This was achieved

using a Hertzian representation coupled with an empirically determined modification to account for larger compressions.

$$F = \pi dDE\left(1.25\left(\frac{x}{d}\right)^{3/2}\right) \tag{2.7}$$

Equation (2.7) shows the initial approach, while Equation (2.8) shows the relationship with an additional term for higher strains. In this manner, the equation is said to be of relevance for strains up to 25%.

$$F = \pi dDE\left(1.25\left(\frac{x}{d}\right)^{3/2} + 50\left(\frac{x}{d}\right)^{6}\right) \tag{2.8}$$

Alternatively, the force required for a given compression can be found based upon the contact width, such that:

$$F = \frac{\pi^2 b^2 DE}{6d} \tag{2.9}$$

with the contact width, b, being:

$$b = d\sqrt{\frac{6}{\pi}\left(1.25\left(\frac{x}{d}\right)^{3/2} + 50\left(\frac{x}{d}\right)^{6}\right)} \tag{2.10}$$

This was found to result in a very simple approximation of contact width as:

$$b = 2.4x \tag{2.11}$$

where x is the amount of compression/deflection the cross-section undergoes in total, when fitted into position, as shown in Figure 2.8.

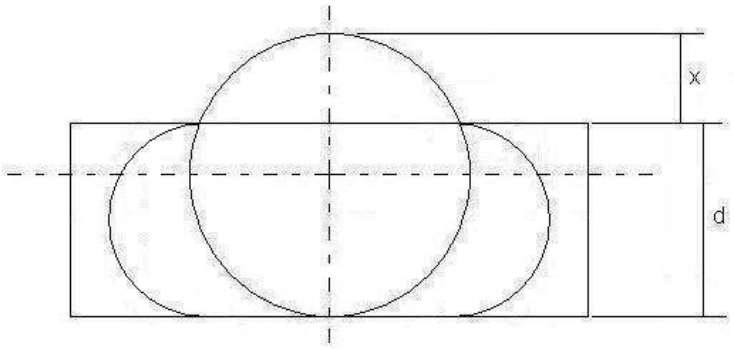

Figure 2.8: Lindley deflection example (Lindley, 1967)

Further sealing characteristics were reviewed by Lindley, including those of peak contact pressure and the resulting sealing capability. The work shows reasonable agreement to experimental results for moderately deformed seals, although, as shown by George et al. (1987) as the strain levels increase, the results of Lindley increasingly underestimate the contact conditions.

Green and English (1992) expanded the work of Lindley and that of Dragoni and Strozzi (1988) using FEA studies. They developed a simple equation and a table of coefficients to analytically calculate the contact force for a restrained/unrestrained o-ring under both axial and radial load conditions. The equation for the non-dimensional force given as:

$$\overline{F} = \frac{F}{\pi dDE} = a\delta^b + c\delta^d \qquad (2.12)$$

where the coefficients a, b, c and d are shown for each contact condition in Table 2.1:

Type of Loading	a	b	c	d
Axial Unrestrained Lubricated	0.74602	1.25282	3.09259	3.38757
Axial Unrestrained Unlubricated	0.97275	1.29292	6.93373	3.55385
Radial Unrestrained	1.03792	1.2871	7.77994	3.534
Plane Strain Unrestrained	0.97184	1.29093	7.1014	3.55262
Axial Restrained	1.63328	1.38463	683.984	5.1869
Radial Restrained	1.7673	1.38755	948.475	5.32269
Plane Strain Restrained	1.55365	1.38072	530.577	5.13163

Table 2.1: Contact equation coefficients (Green and English, 1992)

Although the plane strain approach showed reasonable agreement with experimental work on O-rings (Green and English, 1994), the axisymmetric condition was predominantly utilised for ease of modelling. It was noted that under restrained conditions, the plane strain assumption proved less agreeable beyond compressions of around 10%.

The work of Green and English (1992) was expanded further for axisymmetric studies and comparisons to plane strain (Green and English, 1994). The conclusions were similar to those arrived at before, but with the further explanation that the seal was shown to provide differing contact stresses on each contact region. In this work, the seal fitment characteristics of the radially restrained loaded case could cause inaccuracies within the plane strain approach and further work would be required to improve the method. Some results, such as contact width, were inconclusive and, therefore, it was decided that a more established approach should be followed in this thesis.

FEA was applied to the O-ring contact problem by George et al (1987), using a neo-Hookean approach and details of the materials elastic and bulk moduli to achieve similar results to the analyses using more detailed elastic properties. However, the results up to 20% compression differed little from Lindley's approach (Lindley, 1967), suggesting a good basis for comparison without the need to resort to a full FEA solution.

Kuran et al (1995) found that for low pressure o-ring cases, the seal modulus was not as important as the degree of squeeze present. Suggestions for the calculation of leakage were also made. The contact width is found to be similar to that of Lindley's (Lindley, 1967), i.e. Equation (2.11): but with 2.5 instead of 2.4 as the constant of proportionality:

$$W / D = 2.5C \tag{2.13}$$

where C is the fractional squeeze (reduced diameter/the original diameter). The results for contact pressure also showed reasonable agreement with Lindley (1967) and suggested that in low pressure examples, it is certainly the squeeze that dominates the sealing potential of a given o-ring.

The problem of O-ring sealing and deformation was revisited by Kim et al (2007), using a mixture of experimental verification and finite element analysis, coupled with Lindley (1967). In this work it was confirmed that Lindley underestimates the compressive forces for large strains. However, it was shown that the application of a Hertzian pressure distribution profile on seal contacts is valid. The finite element analysis is reviewed and it was observed that such work requires careful validation. It is also accepted that FEA is somewhat undeveloped for use with elastomeric seals due to the difficulty to accurately consider the properties of rubber. Further difficultly is encountered in the case of a laterally restrained or pressurised O-ring, such as within the inhaler system. It was shown that the concept of a linear elastic simplification was valid for fractional compressions of up to 30% and providing the ratio of the seal cross-section and contact width does not exceed a value of 5. Overall, the application of linear FEA was found to be relatively accurate, but was deemed too intensive for this research.

Öngün et al. (2008) carried out an axisymmetric FEA of the o-ring contact problem under the mixed lubrication regime. In this instance arbitrary non-linear material properties were utilised. It was concluded that further work is needed to validate the contact model. Stupkiewicz and Marcinisyn (2008) used an FEA approach to model an elastomeric o-ring, incorporating a hyperelastic (Mooney-Rivlin) solid to represent the seal behaviour. Friction within the contact was accounted for by incorporating lubricant shear and an attempt was also made to model a rectangular cross-section seal. Surface roughness was not taken into account and only elastohydrodynamic lubrication conditions were considered in the study. The soft mixed EHL problem has also been applied to alternative sealing situations, such as a rotary lip seals (Shen and Salant, 2007). The supporting load, film thickness and contact area were calculated. It was shown that rectangular seals form appreciably thinner films than o-ring type seals (Ruskell, 1980).

In addition, Dragoni and Strozzi (1988) reviewed the case of a laterally restrained o-ring under un-pressurised conditions. Again, a rectangular groove was used and an o-ring was examined under compressive loads. An FEA approach was taken and a suitable mesh was applied to the o-ring cross-section, regarding it as a disk of unit thickness. A Hertzian pressure distribution at the contact surfaces was assumed and it was found to give reasonable agreement with that determined experimentally. A comparison was made to the analytical work of Lindley (1967) and a modification was presented to account for the restraining walls of the groove. While the method highlights a lack of tensile stresses within a restrained o-ring and a significant increase in surface contact pressures as a result of the restraint, there are still factors missing that prevent the application of such an approach to the inhaler system, namely that of pressure and also that of fitment conditions arising from the seal being radially stretched around the stem, while simultaneously being compressed in terms of the seals cross-section in the available groove space between the inhaler stem and the housing.

A theoretical solution without the need to resort to a full FEA solution was presented by Hooke et al (1967) for the modelling of an isotropic elastic o-ring seal in a radial sealing orientation. This was achieved through an approach for the elastic distortion of a circular cross-section.

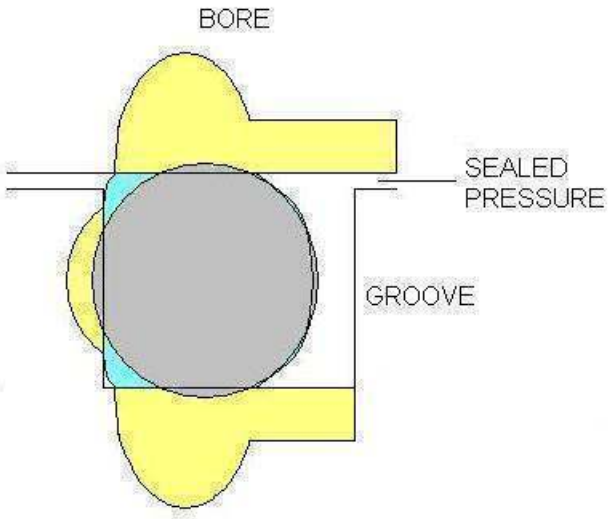

Figure 2.9: Contact conditions of an o-ring within a groove

The contacting conditions of a disk of unit thickness were described (see Figure 2.9). The deflection was modelled using the general elasticity theory from Milne-Thompson (1960). This approach has some potential, assuming a plane strain simplification, negating the need for full FEA. As such it represents a potentially computationally quick solution. Development for the inclusion of fitment stresses is necessary. However, despite this, the method gives reasonable agreement for results with a static seal, suggesting that this is an approach to be potentially adopted. The global ring deformation is something that has been covered in the past. Timoshenko and Roark both give details on the ring deformation due to a uniformly distributed radial loading for instance (Timoshenko, 1965, Young and Budynas, 2001).

It is not uncommon for a linear approach to be considered when modelling the elasticity of rubber, assuming the normal strain is below 10% (Nikas and Sayles, 2005, Bou-Saidand Fantino, 2001). In the latter, a linear (Hooke's) formulation has been used as part of a finite element approach to represent the static problem of a sealing element using the Hellinger-Reissner mixed formulation approach, in which both displacements and stresses are independently varied. This numerical approach was chosen to avoid restrictive assumptions. The large deformations of the elastic bodies were stabilised by linearising the mixed formulation. This approach showed good agreement with the respective test data from literature. A common, but computationally intensive approach is that of finite element analysis (George et al, 1987). Analytical methods include that of Lindley (compressions < 20%) (George et al, 1987) and Mooney-Rivlin (Nikas, and Sayles, 2005). In George et al (1987) the Finite Element Mechanical Analysis of Large Elastic Strains (FEMALES) package was used to investigate the compression of an o-ring between two flat plates with the aim of extracting useful information for the design and assessment of a seal. This approach was taken due to the general lack of development in standard FEA programs for large elastic deformations and strains. Also, the incompressible nature of elastomers and non-linear elastic behaviour cause numerical instabilities within traditional FEA packages (George et al, 1987). Quadratic elements, each formed using four triangular elements were used, a known displacement is inputted, and the remaining nodes could move iteratively until the strain energy is minimised. The final positions of the nodes are then used to calculate the stresses within each element, which are then averaged for each node location. It was found that, for several basic

approaches considered for the governing elasticity (i.e. Lindleys, Hookes and so forth) no discernable difference was found until the compression exceeded 20%. The output of the modelling approach proved useful in estimating the contact width, compression loads, contact stress distributions and deformed geometry of the seal.

The finite element approach has shown good agreement with the test data for an unconstrained o-ring, although it has been conceded that in many cases a simpler analytical approach is perfectly adequate (George et al, 1987). Modelling of rubber contact has been based around that of a single asperity contact, or through the modelling of a complete rough surface. Reasonable agreement has been found in each case, although this is more quantitative in the single asperity case (Peng and Bhushan, 2001). A more analytical approach can be worthwhile, since for a rough, 3D surface with many arbitrary shaped asperities the use of FEA requires a huge number of elements. With a thin layer approach (layer thickness less than or comparable to the contact area) and use of Gaussian distribution of asperity heights the computation effort can be reduced (Peng and Bhushan, 2001). Contacting asperities were represented as concentrated point contacts, with the seal surface discretised for analysis. Limits were applied to ensure than no tension was created at the contacting points, nor was the resulting contact pressure allowed to exceed the hardness of the softer surface. As such, the contact was solved by minimising the potential energy. The presence of a thin film was allowed for by considering meniscus ‘bridge’ forces. These forces depend on the surface tension, meniscus area, thickness and the contact angles of the two surfaces (Peng and Bhushan, 2001).

A model was developed, using the ADAMS commercial software. This approach has shown good agreement in all cases but in torsion (Le Guen, 2001) (Figure 2.10).

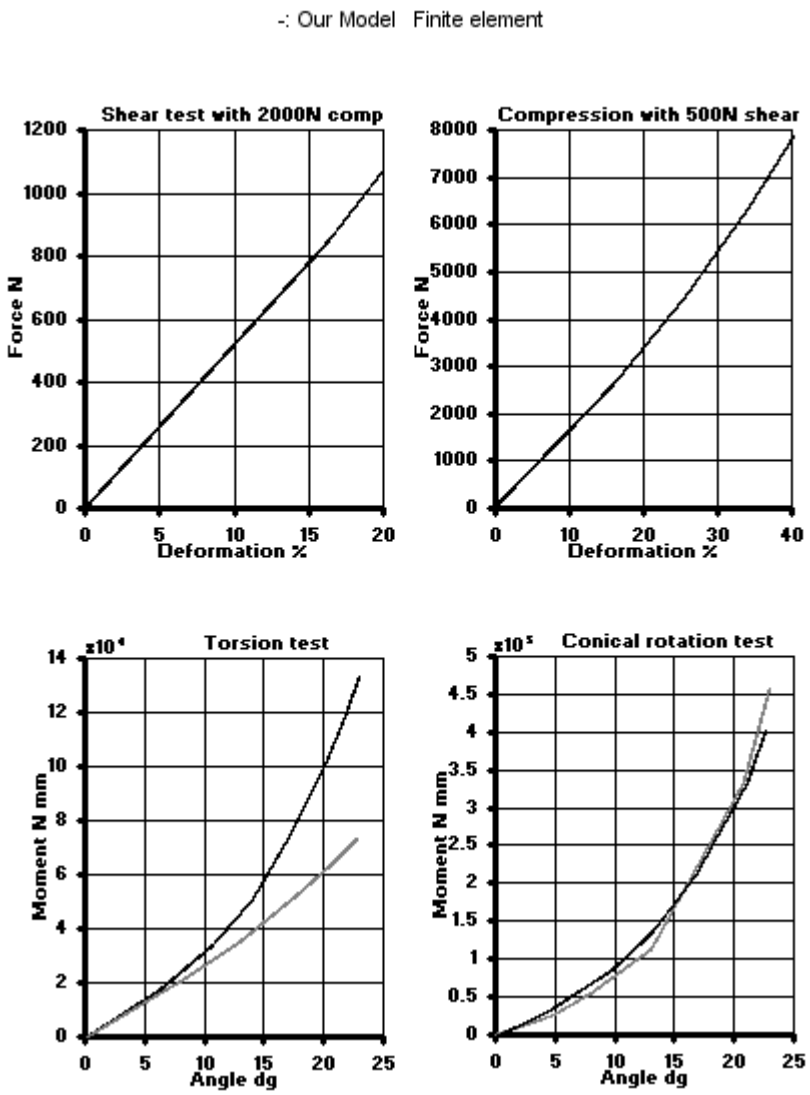

Figure 2.10: ADAMS elastomer model test correlation results (Le Guen et al, 2001)

This approach (Le Guen et al, 2001) is relatively simple to implement. The forces within the model are simply a function of the displacement and velocity of the ADAMS model, using an energy equation basis to the kinematics of the displacement within the model. The approach was tested on two different elastomer bush geometries and as it can be seen in the results shown in Figure 2.10, the model provides good agreement. However, the model is not directly applicable to the o-ring geometry. From the aforementioned it is clear that very little has been done in the case of the o-ring within inhalers, although a lot of work has been done to model elastomeric seals. The particular circumstances of an inhaler are quite special. The fine particulates of the formulation, the low sealing pressures, sliding velocity and

irregular usage mean that the current elastomeric models can only be directly applied with serious compromises.

2.2.5 Friction and Wear

The contact of two nominally flat surfaces was reviewed by Greenwood and Williamson (1966) for metallic surfaces, taking into account not only the load, but also the contact conditions. In this way, the contact deformation was shown to be dependent on surface topography and friction of the real area of contact.

The total friction in the contact described by Greenwood and Tripp (1971) is:

$$\text{Friction}_{\text{Total}} = \text{Friction}_{\text{Lubricant}} + \text{Friction}_{\text{Asperities}} \qquad (2.14)$$

It is, therefore, necessary to establish the proportion of load supported by the asperities (the real area of contact, Figure 2.11) and, thus, the frictional contribution.

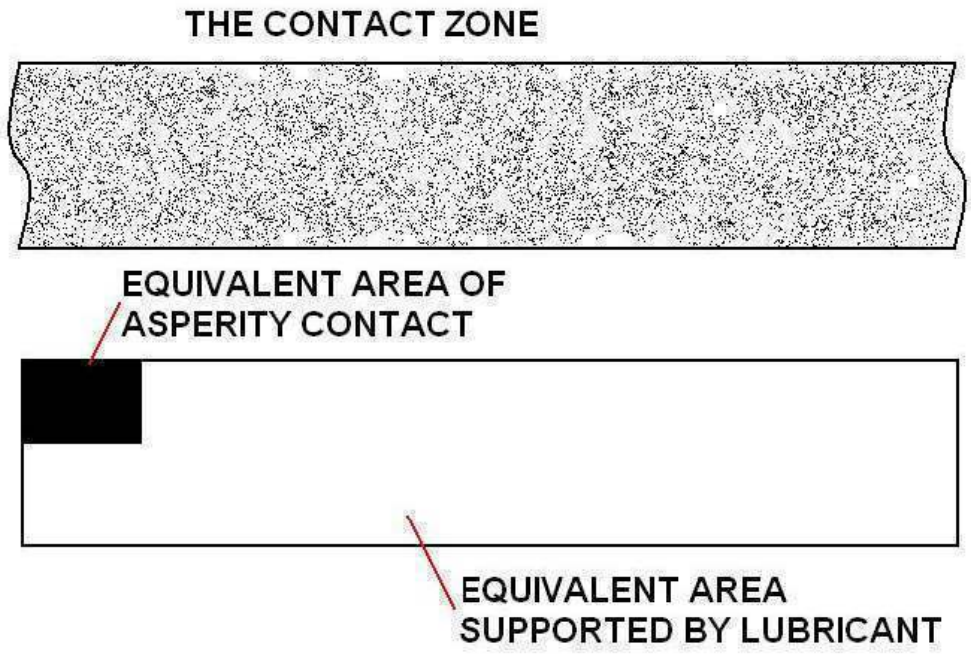

Figure 2.11: Surface asperity contact area

Surface asperities were measured and their radii were found to be orders of magnitude greater than that of their heights (Greenwood and Williamson, 1966). It was also shown through experimental measurements that a Gaussian distribution of asperity

heights is a very good approximation. The results shown (load and area of contact) seemed to be unaffected by the contact roughness modelled using an equivalent single plane or using both the contacting planes (Greenwood and Tripp, 1971). The standard deviation of surface roughness was also shown to be comparable to that of the centre line average deviation of the surface used to model the asperity interactions (Fuller and Tabor, 1975).

Elastomers are soft in nature, generally undergoing a flattening of surface roughness in contact in the order of 20 μm (Fuller and Tabor, 1975). The wear of a component can also have dramatic effects on the surface roughness of an elastomeric seal. Rana et al. (2001) found that even a relatively smooth seal which exhibited an initial surface roughness of 1.7 μm prior to operation became smoothed following brief testing to just 0.2 μm. Friction is reduced through use of higher actuating speeds, higher pressure gradients to encourage entrainment or the use of more viscous fluids (Rana et al., 2001). The reciprocating surface must be smooth enough to prevent seal wear leading to leakage and poor overall performance. A rough surface interacting with a smooth elastomer increases the degree of friction within the contact (Rana et al., 2001).

At low sliding speeds friction becomes almost independent of speed and temperature, indicating static friction as a key aspect according to Roberts (1992). This was also found by Rana et al.(2001), when reciprocating a smooth surface against that of a rough seal at low speeds. There is, however, large variation of the static friction coefficient value, as rubber modulus and contact geometry both dictate the friction conditions (Roberts, 1992).

In cases of absorption of fluids into the rather porous seal structures, friction is known to increase, even beyond that of the original dry contact. This phenomenon may be attributed to the softening of the rubber surface and also the swelling of the contact geometry. Surfactant liquids on the other hand give low friction due to operating as boundary lubricant layers in the case of very thin films (Roberts, 1992). Briscoe et al. (1973) studied the effects of pressure and temperature on the shear strength of very thin lubricant layers including polymeric films.

2.2.6 Swell

Another characteristic that requires consideration is that of swelling. Due to absorption of the propellant (HFA 134a) and moisture, the rubber seal can swell. This is because of the polymer inability to dissolve when cross-links are present. As such, any exposure to solvent takes place through absorption, leading to swelling. A swollen elastomer is in fact a solution, but one which exhibits an elastic as opposed to viscous response to loading in relation to its material properties. The addition of solvents causes the polymer chains to extend. Conversely, the resulting refractive force opposes the swelling. A point of equilibrium is eventually reached, being the point of maximum swelling. The extent of swelling depends on the thermal conditions, chemical nature and degree of cross-linking of the polymer and penetrant (Bouvier and Gelus, 1986). The main parameter of interest perhaps is that of the rate of absorption, which dictates the swelling mechanism. The relaxation characteristics and the diffusion characteristics also play roles, the process of swelling being that of elastic diffusion, viscous diffusion or a combination of the two (viscoelastic) (Bouvier and Gelus, 1986).

Seal performance is reduced (United Sates Patent, Glaxo Group Limited, US6,926,178 B1) as the increased interference of the seal and bore means an increase in the actuation or the return force required. Solvent absorption within an elastomer can also reduce the physical properties such as hardness, strength and resistance to tearing. In some cases just 20% absorption by volume can reduce such properties of an elastomer by 60% (Westbrook and French, 1999). It has been found that swelling of up to 17% can take place within just twenty four hours due to exposure to HFA propellant (United States Patent, Virginia Commonwealth University, US5,190,029), details of which are shown in Table 2.2, giving an extension of 8% in addition to the weight increase detailed for Nitrile rubber (United States Patent, Virginia Commonwealth University, US5,190,029).

Propellant	% of Initial Weight After 24h Immersion in Propellant						
	LDP	Nitrile	Black Buna	White Buna	Chloro-butyl	Butyl	Neoprene
HFC-134a	101	117	112	114	100	101	101

Table 2.2: Percentage of initial weight after 24 hours immersion in propellant (United States Patent, Virginia Commonwealth University, US5,190,029)

From literature it is clear that there are significant differences between the out and in strokes of the seal (see Figure 2.3 for a definition of out/in stroke direction). While the out stroke gives contact stresses and film pressures almost equal to that of the sealed pressure, the in-stroke gives very high contact stresses and negligible hydrostatic pressure. In this case, quite large hydrostatic pressures are required to lift the seal and allow formation of a fluid film (Nau, 1999). There have been attempts to prove the absorption characteristics and, thus, model the absorption of trapped lubricant over time (Field and Nau, 1975). The absorption is not, however, linked to swelling of the rubber and, therefore, more work is required to formulate a modelling approach. The available data on the elastomer swelling is also generally for exposure to pure solvent components and not mixtures, which can cause difficulty in modelling and design (Westbrook and French, 1999).

2.2.7 Electrostatics

Following the replacement of CFC propellants with HFA, conventional surfactants were found to be in many cases insoluble in HFA formulations without the addition of co-solvents (Vervaet and Byron, 1999). While the ethane or similar variants provide comparable boiling points and vapour pressures to those of CFC 12, there is a resulting increase in polarity. The largely empirical nature of the pharmaceutical industry and the comparative lack of database information in the area further compounds the problems when it comes to design of formulations (Vervaet and Byron, 1999).

Due to the asymmetrical spatial arrangement of Fluorine atoms on the carbon backbone of HFA-134a, a polarity exists. HFA-134a is more negatively charged than HFA-227, and as such it features a higher dipole moment and dielectric constant.

Upon exiting the pMDI, the negatively charged droplets evaporate. The charge remains until the electrostatic repulsive force overcomes the surface tension, causing the droplet integrity to break down. The resulting 'daughter droplets' continue this same cycle until only the non-volatile particles remain.

2.3 Knowledge transfer from previous work

The following summarises the findings and relevance of the previous work conducted on the testing of an inhaler design within Loughborough University (Mavros et al., 2003).

- The current test rig does allow comparison of the friction characteristics of rubber samples for both dry and lubricated sliding conditions. However, it is not representative of the actual contact conditions within the valve.
- The previous results showed a great dependence on possible crimping/O-ring retaining features, see Figure 2.12. In the new model, the o-ring apertures may vary in size.

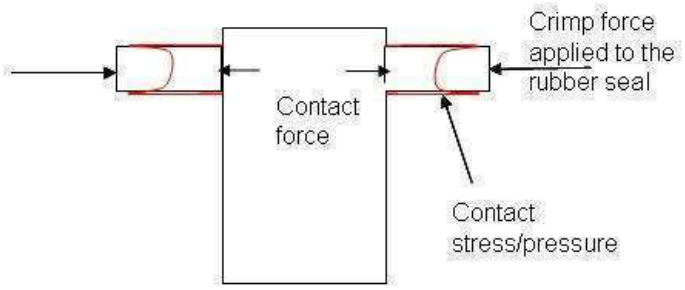

Figure 2.12: Additional contact force due to crimping (Mavros et al., 2003)

- In-situ testing of the valves suggests that effective lubrication does not take place:
    - Little contribution due to lubrication is suggested during the inward stroke
    - Although there is potential for lubrication on the outward stroke, this could equally be explained by the pressure effects on the initial deformation of the rubber.

- When lubricated sliding was examined within the test rig, some contribution was found to be made. However:
    - The film developed slowly (as expected) and the corresponding reduction in μ suggests that hydrodynamic lubrication is not present, with asperities still coming into contact along the contact length, see Figure 2.13.

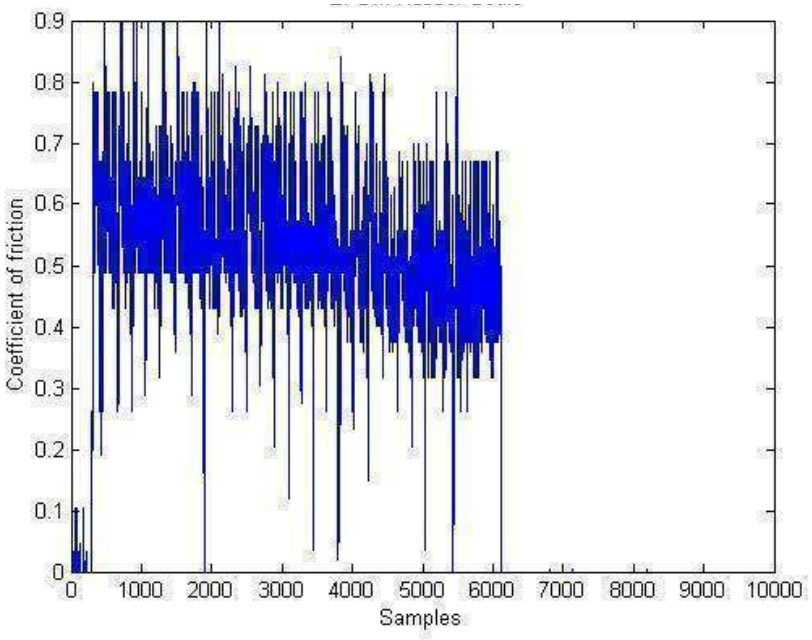

Figure 2.13: Resulting frictional coefficient reduction during film formation during sliding of EPDM rubber seals (Mavros et al., 2003)

- The previous model approach appears valid for initial investigations i.e.
    - Rigid Stem
    - Deformable seals, with viscoelastic representation
    - Flexible Ferrule/canister

The following developments are seen as essential for the investigations:

- The kinetic friction between the seal/polymer surfaces should be estimated from the tribological contact conditions.
- The inclusion of the correct lubrication regime is necessary within the new model, in order to accurately take into account the effects of the formulation (mixture).
- Further research is needed for the new design to establish whether a mixed regime of lubrication can be encouraged, and if so, what modifications are necessary to achieve this objective.

3.0 Experimental Methodology

3.1 Introduction

Experimental studies were conducted in order to validate the numerical results of the models developed and also provide information on the more readily determinable material parameters under examination. As such, the experimentation fell into two main categories.

1. Materials Parameters
    a. Surface roughness
    b. Asperity density, shape and distribution
2. Device representative testing
    a. Parametric studies of inhaler components
    b. Determination of friction coefficient for contacting surfaces

3.2 Objectives of the Experiments

The objectives of the experiments were:

- To ensure that correct material parameters are used in modelling of the inhaler components
- To validate the model by correlating its predictions with the experimental findings and provide confirmation of model accuracy.

3.3 Experimental Rig Design

In order to validate the numerical predictions, an experimental rig was developed with the aim of measuring the coefficient of friction, both under static and kinetic conditions. Fully flooded lubricated sliding conditions were considered. In principle both the static and kinetic coefficients of friction could be measured quite simply by following the procedure that for a given normal force N, a tangential force T would be required to slide the contacting plate relative to the stationary surface (the main plate). This required tangential force accounts for the prevailing friction and was therefore measured. This allowed the coefficient of friction to be evaluated from the relationship (Equation 3.1) first suggested by Amontons for onset of motion (static coefficient of friction) and later verified by Coulomb for kinetic conditions.

$$\mu = \frac{TangentialForce}{NormalForce} \tag{3.1}$$

For dry contact conditions the measurement is quite simple. However, the nature of the lubricant in the case of an inhaler prevents this from being the case. Both the propellant and the ethanol content of the formulation contained within the canister are quite volatile under ambient pressures. Therefore, a means of keeping the formulation under pressure was required. This required the test bed to be contained within a pressurised chamber, whilst flooding the contact with the fluid.

3.3.1 Pressure Cell

In order to accommodate the desired pressurised conditions a pressure vessel was built, containing the sliding friction test bed (Figure 3.1). The vessel was pressurised to a pressure of 5.5 bar by means of a high pressure air line, which was monitored by a simple pressure gauge on the rear of the pressurised cylinder. The formulation (the fluid) was delivered from an inhaler canister to the moving plate. Thus, evaporation of the mixture was avoided. The following features were taken into account:

- Safe operation was possible with an internal pressure of 7 bar, with a maximum of 12 bar as a precaution against failure. (A working pressure of 5.5 bar is required to replicate conditions within an inhaler valve).
- External control of the sliding friction rig was made possible by use of a motor and external control switch
- Accurate delivery of the lubricant to the pre-specified positions of the contact region was ensured using feed tubes
- Visual observations of the sliding motion taking place during the testing was possible by incorporating a high strength polycarbonate window

The pressure vessel incorporates the following to ensure operation and safety during experimentation:

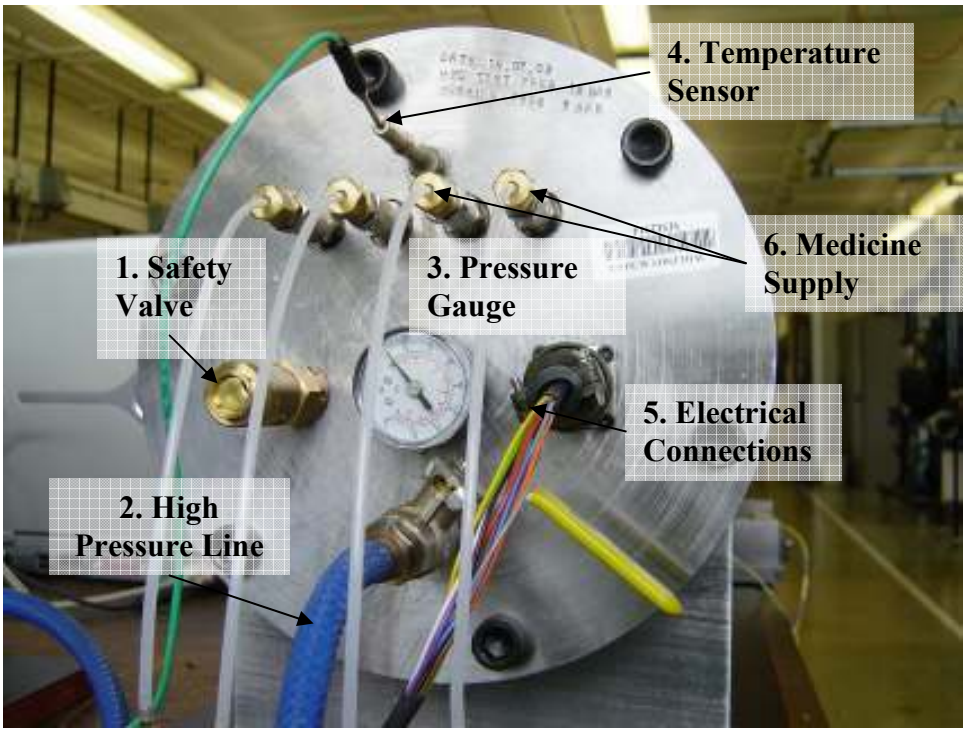

Figure 3.1: The pressure vessel

Electrical connections feed into the vessel to allow operation of the motor and provide power/signal to/from the strain gauge, the complete experimental rig being pictured in Figure 3.2.

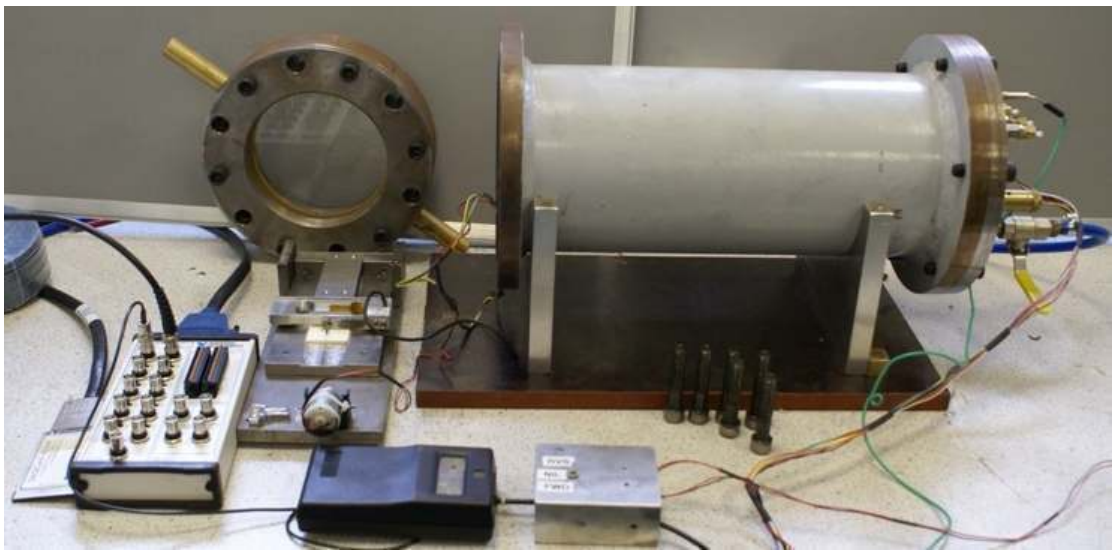

Figure 3.2: Complete rig assembly

A safety valve prevents the internal pressure from exceeding 8 bar, whilst the pressure gauge allows measurement of the internal pressure. This was set using a high pressure

air line. A temperature sensor allowed measurement of the conditions within the test cell during a sliding friction test. Finally, the four lubricant feed tubes allowed lubricant filled pMDIs to be connected and the lubricant to be fed into the contact (As labelled Medicine supply, Figure 3.1). At the front of the pressure vessel, a high strength polycarbonate window panel was secured such that the operation of the sliding plate can be viewed. This window also allowed a laser vibrometer to be targeted at the sliding friction plate so that the sliding velocity during actuation could be observed.

3.3.2 DC Motor

In order to actuate the sliding plate, a DC motor was attached to one end of the sliding plate (Figure 3.3). This is powered and operated externally by means of a universal power supply and a simple switch for forward/reverse/stop. The motor drives a gearbox which reduces its rotational speed and allows an inelastic thread to be wound up, pulling the sliding plate in the process.

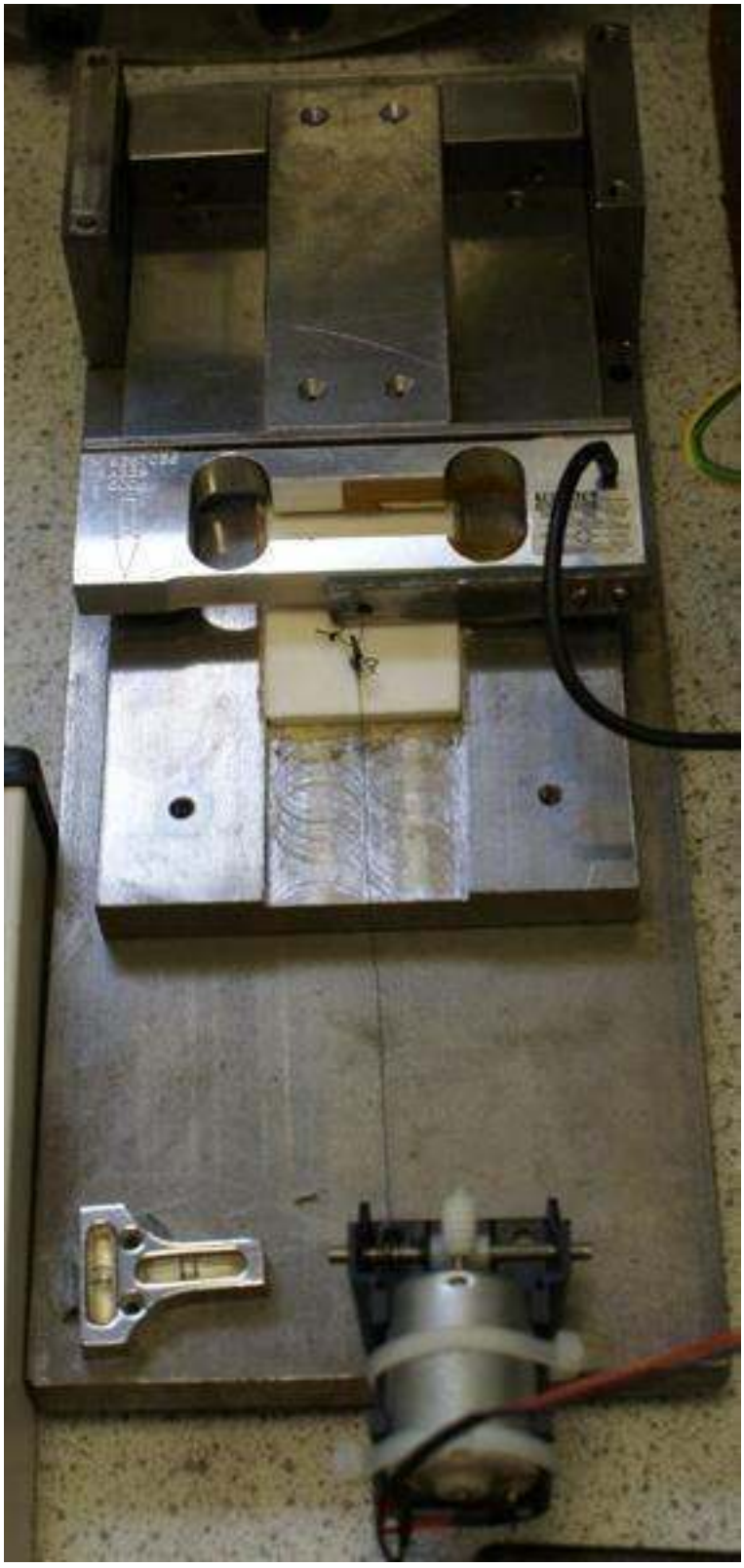

Figure 3.3: DC motor assembly

3.3.3 Load Cell

The inelastic thread from the motor is mounted to a load cell, the other side of which is mounted to the sliding plate (Figure 3.3). The force required from the motor

assembly to slide the plate is, therefore, recorded and transmitted via the strain gauge amplifier to the computer software (Labview programme – http://www.ni.com/labview).

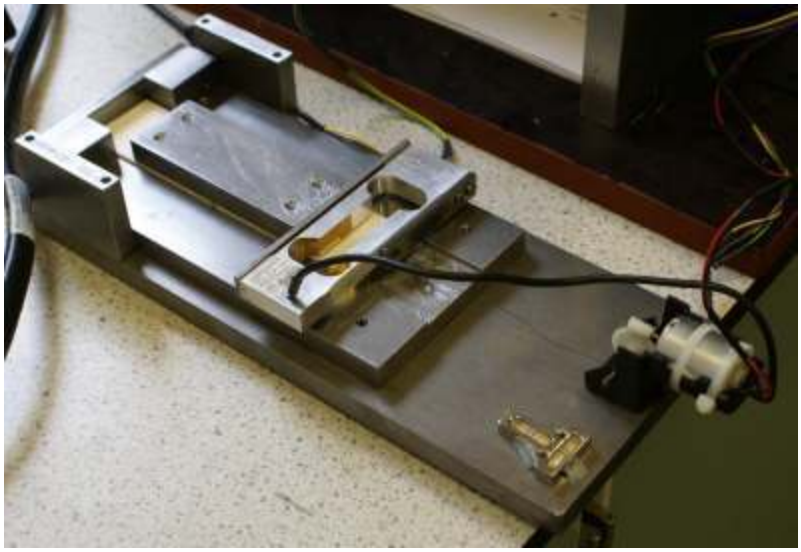

Figure 3.4: The sliding test bed

The specification of the Vishay Model 1004 load cell (Figure 3.4) is given below:

- 0.6 Kg Load Capacity
- Maximum cumulative error < 0.0067% of the rated output

3.3.4 Laser Vibrometer

In order to obtain velocity data for the sliding plate a laser vibrometer wa used (Figure 3.4). This is a non-interfering non-contact measurement method and allows the measurement to be conducted from outside the pressure cell, the laser itself being targeted on the sliding plate through the window on the front end of the vessel. As such, any packaging issues with containing a measurement method within the pressure cell were thus eliminated.

Figure 3.5: Laser vibrometer

A Polytec Vibrometer OFV 3000 controller with an OFV 302 sensor head was used, the specification of which is given below:

- Velocity decoder:
  - Measurement sensitivity range: 1 - 1000 mm/s
  - Signal bandwidth: 35 – 150 kHz
  - Output swing: +/- 10 Volts (Therefore a range of +/-10mm/s to +/-10m/s is possible depending on the chosen measurement sensitivity)
- Laser:
  - Laser type: Helium neon (He-Ne)
  - Wavelength: 633nm
  - Cavity length: 205mm
  - Laser output power: 2.3mW / class IIIa
  - System output power: <1mW / class II
- OFV 302 sensor head:
  - Range of standoff distances: 30cm – 30m

3.3.5 Sliding Friction Plate

The sliding friction plate was mounted on four o-ring seals using epoxy glue. These were mounted such that the lubricant feed wells deposit into the centre of each o-ring (Figure 3.6). The aim was to attain, as far as possible, fully flooded inlet conditions. The sliding plate was then actuated along the bottom plate which consists of a polymer bed of the same material and surface roughness as that of the housing bore within the inhaler mechanism.

3.3.6 Lubricant Feed

Injection of the lubricant was achieved through the use of non-return valves coupled with feed tubes to direct the flow of lubricant to the contacts.

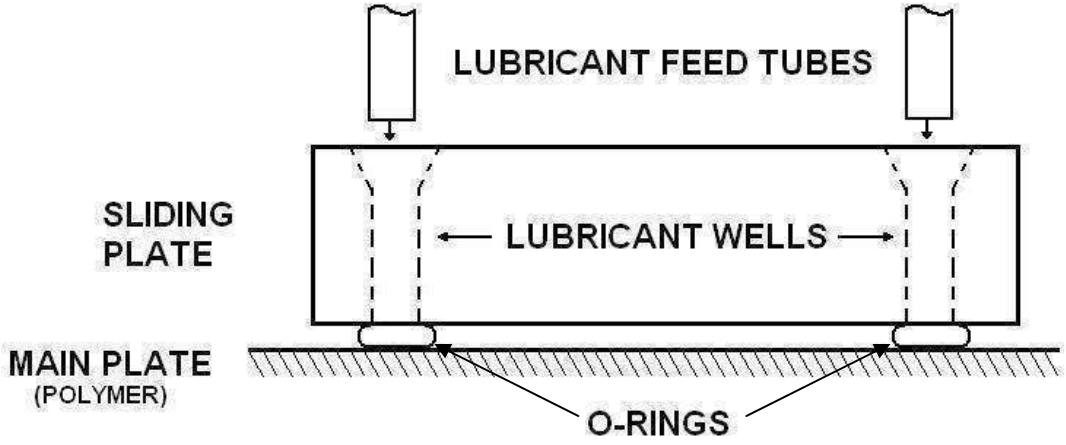

Figure 3.6: Lubricant feed system

Upon flowing through the tubing, the lubricant enters/flows into the four wells within the sliding plate. These then discharge into the centre of the o-ring seal contact allowing the seal-polymer contact to become fully flooded.

3.3.7 Strain Gauge Amplifier Circuit

A strain gauge amplifier of type RS846-171 (Figure 3.7) was used in order to amplify the signal from the Model 1004 load cell.

Figure 3.7: Strain gauge amplifier circuit

Once amplified, both this signal and that of the laser vibrometer were recorded using a type BNC-2110 connector block (Figure 3.8) to provide signal shielding and allow simultaneous sampling of both strain gauge and vibrometer data channels.

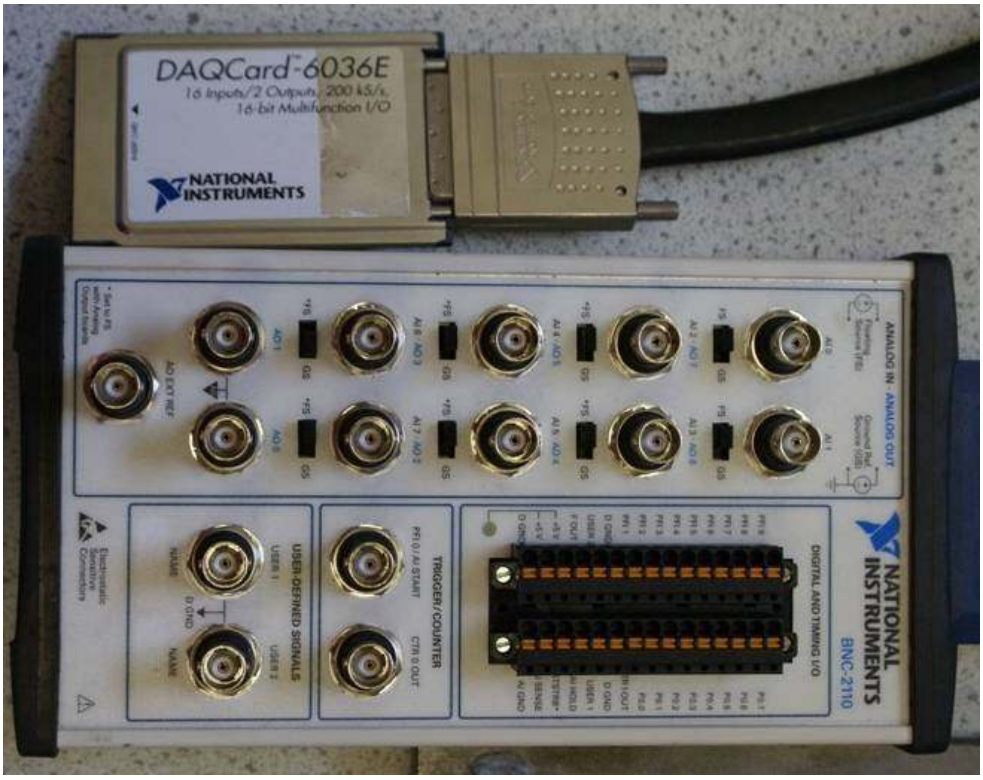

Figure 3.8: BNC connector block and DAQCard - 6036E

A national instruments DAQ card 6036E (Figure 3.8) was used to sample the data. The specifications of DAQ are as follows:

DAQ Card 6036:

- 16 Analogue Input (AI) Channels
- 8 differential AI channels
- 8 digital I/O channels
- 16 bit resolution
- Type II PC card slot interface

3.4 Experimental Procedure

3.4.1 Preparation of the Rig

Before conducting a set of measurements, the load cell was calibrated using a series of known weights. The polymeric plate is also cleaned using compressed air and four polymeric seals attached to the sliding plate using tweezers to handle them and prevent any potential contamination. A thin layer of glue was used to attach the seals to the sliding plate. The complete block assembly, including seals, wires and the attached load cell was then weighed in order to accurately determine the normal load

present on the rubber seals for the ensuing measurement. Then, the sliding plate was positioned at its starting location on the stationary surface as shown in Figure 3.3.

3.4.2 Measurement Procedure

During tests, the procedure shown in Figure 3.9 is followed.

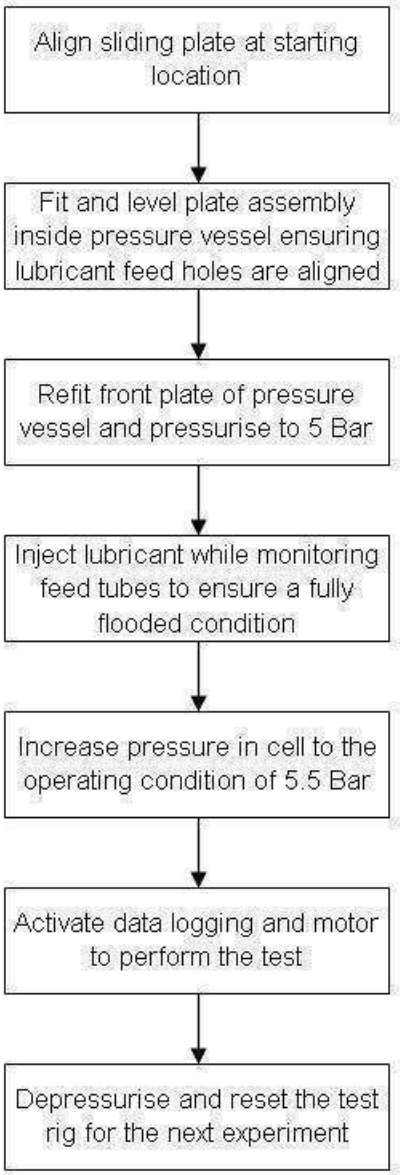

Figure 3.9: Test rig procedure

Prior to any measurement, the ambient temperature was recorded. The sliding block was aligned and the pull thread attached from the motor to the sliding plate (Figure 3.11).

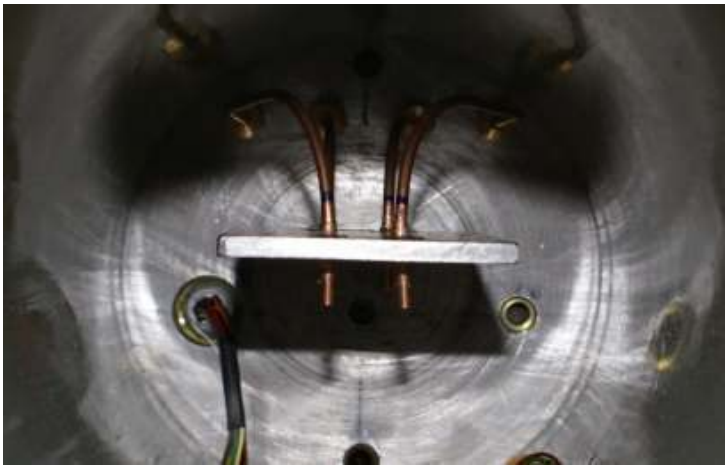

Figure 3.10: Lubricant feed tubes

The assembled rig was then placed in the pressure cell, taking care to align the fluid feed tubes (Figure 3.10) with the sliding plate. Once positioned, the pressure vessel was sealed and pressurised to 5 bar. At this stage the fluid was injected and the feed tubes were monitored to ensure that sufficient amount of fluid was distributed to the contact areas. The pressure vessel was then pressurised to 5.5 bar. The Labview program was then initialised to collect the data, sampling at 1000 Hz to ensure that no aliasing took place (Figure 3.11).

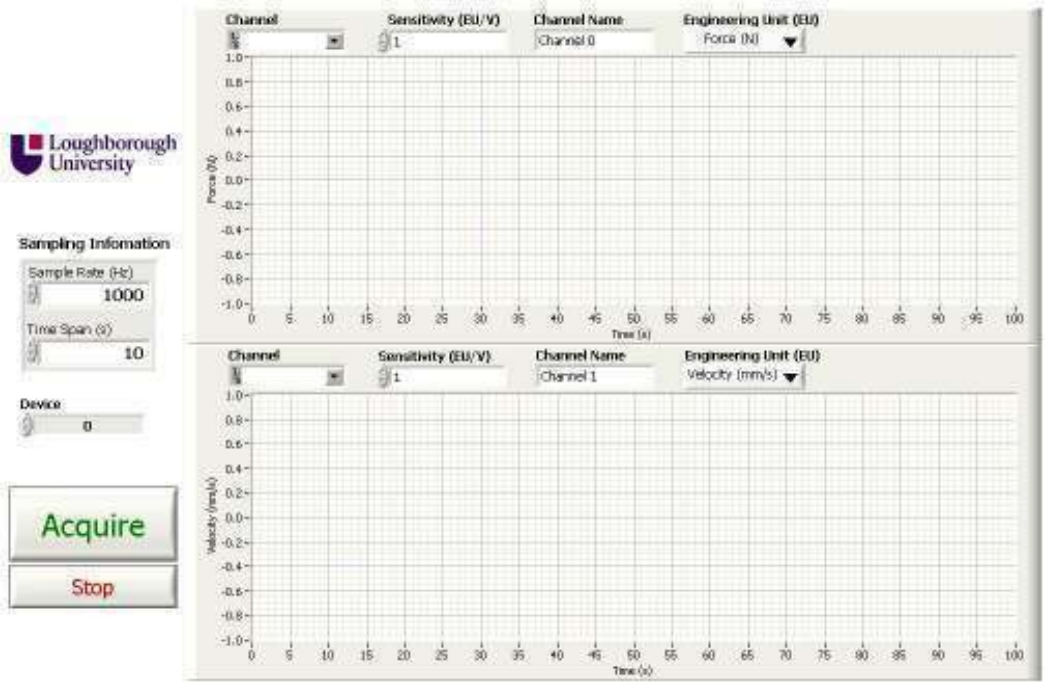

Figure 3.11: Labview screenshot

The motor was then activated and the sliding plate pulled over the surface of the polymer. At this point the pressure cell could be depressurised and reset ready for another test to take place.

3.4.3 Calculation of Friction Coefficient

When testing commences, the thread applies a pull force to the sliding plate in the tangential direction. At the onset of motion, the horizontal force drops momentarily as the velocity reaches a peak. Information on both the peak load and velocity is captured and recorded to be processed. Following the initial peak, the proceeding peaks that form the dynamic motion (stick-slip) are also recorded and saved. In order to calculate the static and kinetic coefficients of friction, the data is split. The static (initial) peak was determined, and an average of the dynamic peaks was calculated as shown in Figure 3.12.

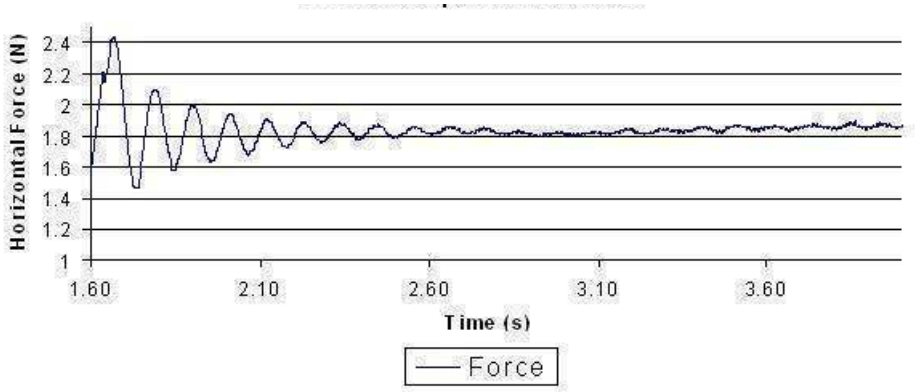

Figure 3.12: Static and dynamic sliding force peaks

Each of these was then divided by the normal applied force (weight carried) in order to calculate the respective coefficients.

3.5 In-situ Experimental Rig Design

A further set of tests were conducted using inhaler components assembled as they would be during normal device operating conditions. Sample inhalers were tested in a tensile testing machine used in compression to record the force necessary to actuate an inhaler and thus calculate the frictional force of a seal while fitted within an inhaler and in contact with the polymeric housing bore. This testing was carried out using two inhaler configurations:

1. Complete inhaler valve with two seals and metered dosing
2. Non-actuating single seal inhaler valve configuration
    a. Varying interference fitments of seal to housing
    b. Varying housing bore manufacturing technique

In each case, the inhaler is mounted securely to the machine and a force is applied to ensure a motion of ±20 mm/min. The force required is then recorded allowing the friction contribution of each seal to be determined. Prior to testing, each inhaler was weighed using a four place balance over a period of several days to determine whether any leakage was taking place. Each inhaler was also allowed a period of at least seven days to rest and allow the seals to fully settle. Example results for configurations 1 and 2 are shown in Figure 3.13 and Figure 3.14 respectively. As can be seen, as the second seal comes into contact in Figure 3.13 between 0 and 5 mm the frictional force is increased as expected over that of a single seal. Further comparisons to this data with the numerical results can be found in Chapter 7.

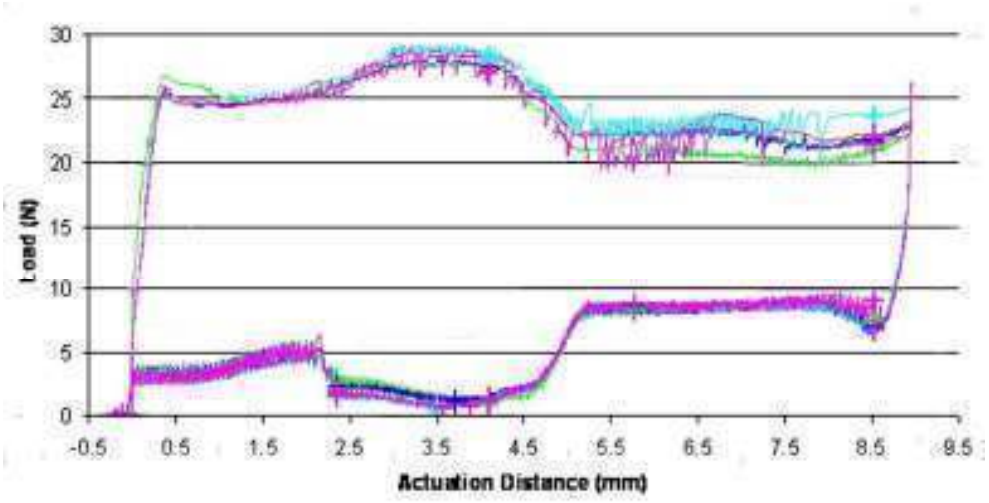

Figure 3.13: Example 3M results (multiple runs for illustration of repeatability) for the complete seal assembly

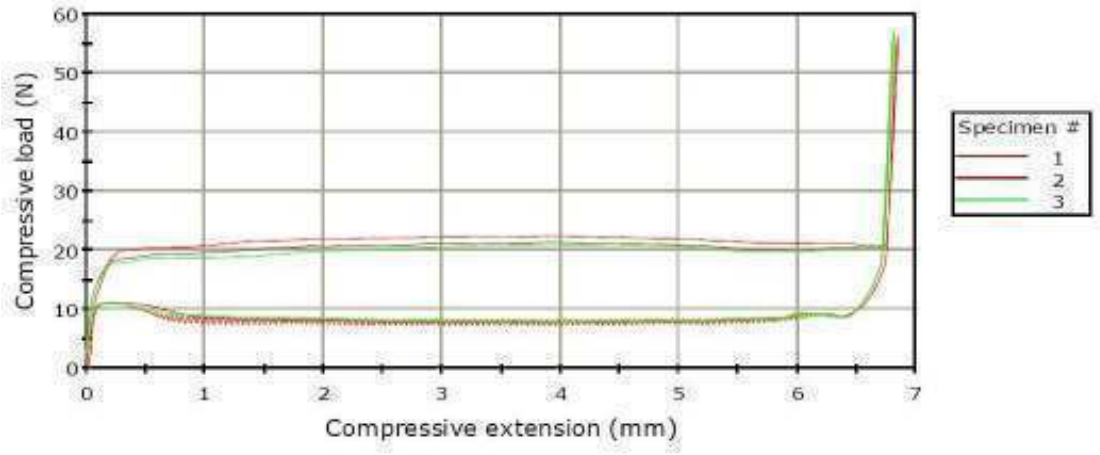

Figure 3.14: Example 3M results for single seal assembly

3.6 Materials Parameter Testing

3.6.1 Polymer Surface testing (Talysurf)

A Taylor Hobson Talysurf 4 was used to measure surface roughness of the polymeric bore and also that of the polymeric plates used in the friction sliding rig tests, a typical result of which is shown in Figure 3.15. The polymer plates used to represent the bore of the inhaler valve were machined so as to produce comparable roughness values to that of the housing bore. Each time the surface finish was examined using the Talysurf in a number of random locations. These results determined whether the surface finish was comparable to that of the bore.

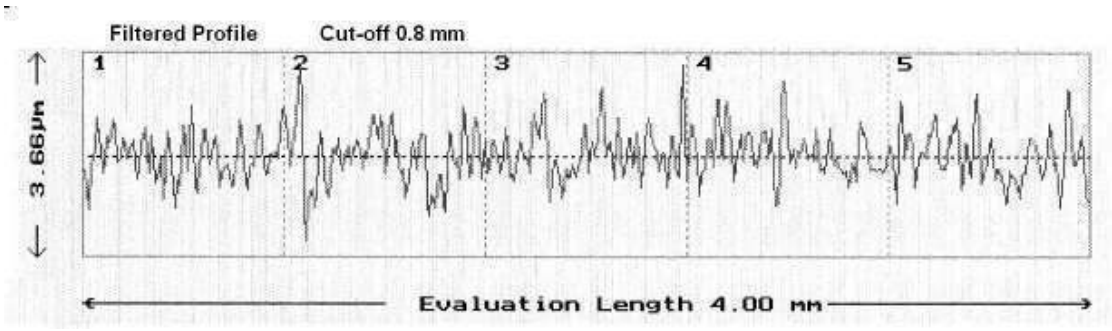

Figure 3.15: Example Taylsurf trace

3.6.2 Polymer Surface Testing (Zygo Interferometric Scanner)

A Zygo New View 5000 interferometric scanner was utilised to determine the surface properties of the contacting housing bore for use in the Greenwood and Tripp model

(roughness and asperity density). Specifically the aim is to determine the product: $\varsigma\beta_{GWT}\sigma$

Where:

ς = Surface density of asperity peaks

β_{GWT} = Radius of curvature at asperity tip

σ = Combined surface roughness

This was achieved by assuming a constant initial value of the radius of curvature based on the scan results from the surface tests. From this the density within a given area could be calculated, while the combined surface roughness was readily measurable.

In order to ensure that the correct values were used within the developed code (see Chapter 5), samples of the inhaler housing bore were machined to allow examination using an interferometric scanning machine. Typical results of which are shown in Figure 3.16, Figure 3.17 and Figure 3.18.

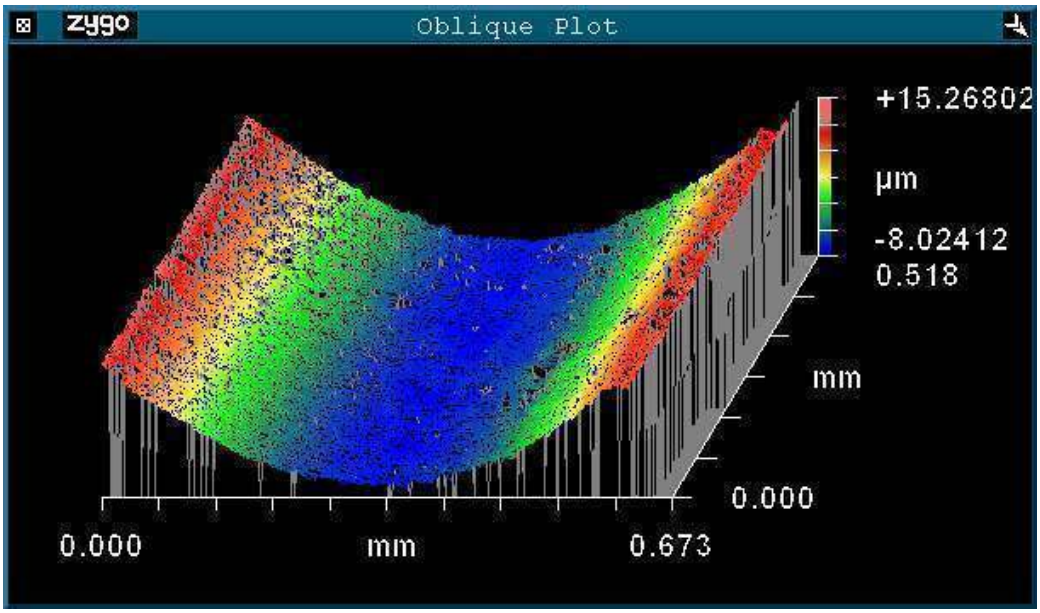

Figure 3.16: Example surface profile scan

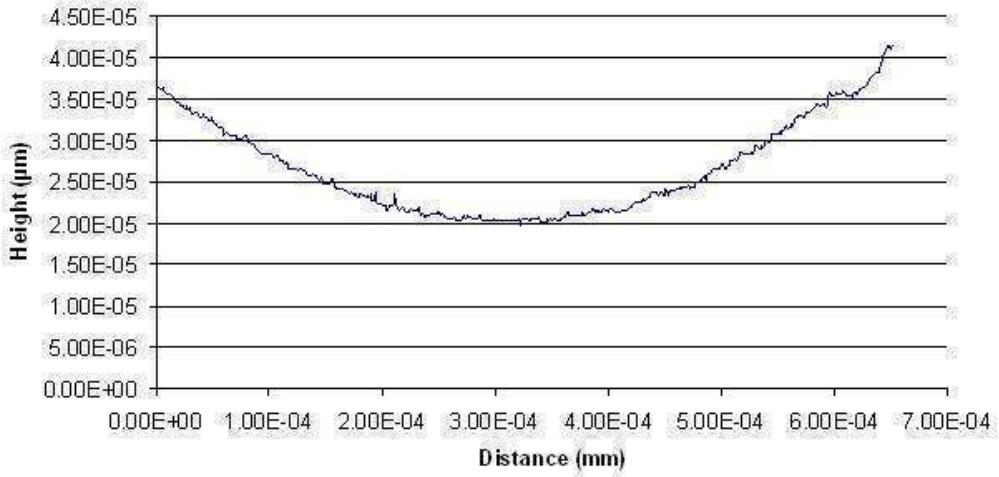

Figure 3.17: Example surface profile

The individual terms ζ, β_{GWT} and σ are difficult to obtain. However, the product of the three terms is readily obtainable from surface profile measurements. Greenwood and Tripp state a value between 0.042 and 0.07 for metallic contacts (Greenwood and Tripp, 1971), the average being 0.055. However, Fuller and Tabor, 1975 found that for polymer-elastomer contacts a result in the range of 0.09-0.15 is more applicable. Following the surface analysis of the bore, a result of 0.12 was calculated.

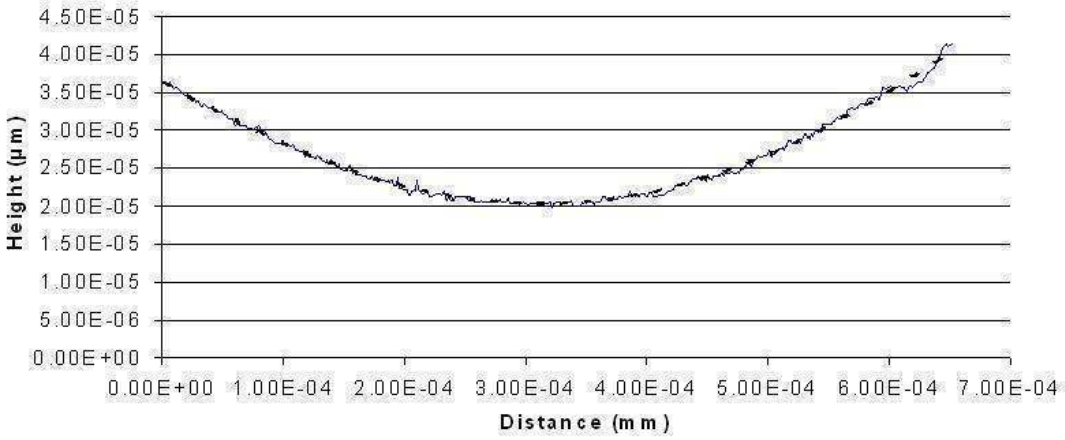

Figure 3.18: Surface profile and polynomial fit

This value is in agreement with the range suggested by Fuller and Tabor, 1975 and was calculated using a simple approach based on the following assumptions and calculations:

- The surface profile was approximated using a 6th order polynomial

- The difference between asperity heights was then calculated from this smooth surface approximation.
- The radius and asperity area was calculated by assuming each asperity has a uniform base and no larger than the resolution of the scanner.
- The volume of each asperity could then be calculated based on its height above the smooth surface and its assumed base size. The radius at the tip could also be calculated.
- The total asperity volume and number of asperities was then calculated, allowing the final product to be determined.

4.0 Numerical Work

4.1 Introduction

The pMDI valve under investigation in this thesis consists of a stem, two elastomeric seals and a housing bore as shown in Figure 4.1.

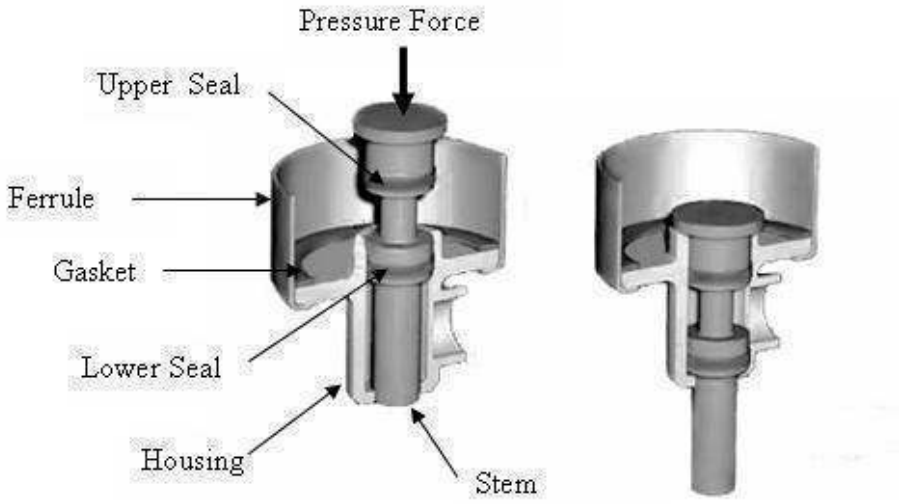

Figure 4.1: pMDI valve design

Each of these elements is subjected to internal pressure-induced forces and those generated due to valve actuation such as friction. The fundamental requirements of the inhaler dictate that the sealing mechanism must prevent leakage of the formulation and also ingression of any contaminants from the external environment. Simultaneously, the device must ensure that smooth actuation takes place and the frictional force does not prevent the complete actuation of the device. Therefore, prediction of friction of the elastomeric seals in contact with the housing bore is very important.

To date, the design and development of pMDI valves has been of an empirical nature. Therefore, both time and experimental resources are usually invested in order to develop and test a particular design concept. As such, a move towards a virtual prototype simulation approach is invaluable to the pharmaceutical industry. This approach depends on the use of appropriate assumptions to recreate the operating conditions of the mechanism. This requires careful consideration and justification.

The result is that a design can be evaluated in shorter periods than through the traditional empirical approach and also at a fraction of the cost.

The elastomeric seals are extremely flexible in comparison to the relatively rigid stem and housing bore. This flexibility must be represented properly within the inhaler model. During actuation the inertial effects, friction and changes in canister pressure also affect valve operation.

It is, therefore, necessary to develop a fundamental model of the interacting components. The recognised approach for mechanism dynamics is constrained Lagrangian dynamics. For slow moving bodies, the rigid-body approach is acceptable and therefore used throughout this study to represent the non-elastomeric components of the inhaler. The elastomeric components of the model are handled using external subroutines written in the Fortran programming language. These are responsible for evaluation of deflection, surface interaction and friction force of each seal across the contact width of the seal. The multi-body dynamics model then handles the resulting force balance at any instant of time during valve motion.

The multi-body model is formed using component geometry and physical characteristics from CAD part data to represent those within the real inhaler system. These are connected using constraint functions, represented in defined joints and joint primitives as is usual in the multi-body approach. The numerical model is, therefore, a mathematical formulation by a set of differential-algebraic equations. The former are the equations of motions of parts, whilst the latter represent holonomic constraints.

4.2 Multi-body Dynamics

Analysing the dynamics of a system involves determining the motion and associated forces for the number of degrees of freedom, as these are determined by the introduced constraints (mechanism physical assembly). For a multi-degree of freedom system, the Lagrange's approach simplifies the task of deriving the differential-algebraic equation set. This approach is explained below.

4.2.1 Model Description

The multi-body dynamic analysis is based around constrained Lagrangian dynamics, the solution being found for a set of differential-algebraic equations, where the system equations of motion are represented by partial differential equations and the physical constraints are specified by means of algebraic expressions. The set of equations is then solved and the results of the analysis are given in the form of displacement, velocity, acceleration and reaction forces or torques. In this instance, the friction force output from the system allows for improved component design by improving the actuation in terms of wear, smooth motion and good sealing.

The work highlighted in this thesis is a model of a medical inhaler valve system developed within a commercial software environment, referred to as ADAMS (Automatic Dynamic Analysis of Mechanical Systems). This software is based on constrained Lagrangian dynamics, the formulation and solution procedure for which is outlined later in this chapter.

The model is formed using an assembly of individual component parts, each having relative degrees of freedom with respect to others and with associated constraints, in order to ensure that the model is an accurate representation of the inhaler valve ideal function. The resulting differential equations of motion, algebraic functions (constraints) and applied forces/torques can then be arranged in matrix form (referred to as the Jacobian matrix) to allow for a simultaneous solution of the components' dynamics (Rahnejat H, 1998). Due to the complexity of the system model, a suitable solution method is required, such that the system response is obtained using small, discrete steps of time. Each part can be created to both rotate and translate about a set of Cartesian axes X, Y and Z. However, as a particular response is desired from any

multi-body system, the parts must be constrained relative to one another so that the intended mechanism function is simulated. By restraining the system in its entirety, all possible degrees of freedom can be removed. In this case, for a given input to the mechanism, only a prescribed output would be possible and, therefore, a kinematic system would result. However, by allowing one or more degrees of freedom, a dynamic system would be obtained.

As mentioned, within the ADAMS software, the Lagrange's equations for a constrained system are utilised in order to simplify the procedure. The method utilises the ground as a fixed reference datum, upon which all the equations of motion are referenced using a global coordinate system. Therefore, the position and orientation of any rigid part with respect to the global coordinate system can be expressed as:

$$\{\xi_j\}_{j=1\to 6} = \{x, y, z, \psi_e, \theta, \varphi\}^T \tag{4.1}$$

where, $j = 1,...,6$ corresponds to each co-ordinate in the vector set.

Lagrange's equation for a constrained system generates six differential equations of motion for each defined part within a given mechanism. The governing equations of motion for a body are derived from Lagrange's equation, as:

$$\frac{d}{dt}\left(\frac{\partial L_e}{\partial \dot{\xi}_j}\right) - \frac{\partial L_e}{\partial \xi_j} + \frac{\partial D_e}{\partial \dot{\xi}_j} - F_{\xi_j} + \sum_{k=1}^{n} \lambda_k \frac{\partial C_k}{\partial \xi_j} = 0 \tag{4.2}$$

In the above equation, the following quantities are represented:

- Applied kinetics (such as applied forces and torques)
- Kinematic relations (in terms of position and orientation)
- Constraint functions (which formulate the reaction forces due to the constraints)
- Energy (both the rotational and translation kinetic energy)
- Body forces arising from potential energies
- Momenta

where $L_e = T - V$ is the Lagrangian: the difference between Kinetic and Potential energies.

4.2.2 Kinetic energy

Breaking the formulation down into sections, firstly the total kinetic energy, *K*, of a body in motion is given by its translational and rotational kinetic energy components. The translation components of kinetic energy are given by:

$$\begin{bmatrix} T_x \\ T_y \\ T_z \end{bmatrix} = \frac{1}{2} m_b \begin{bmatrix} v_x & v_y & v_z \end{bmatrix} \begin{Bmatrix} v_x & v_y & v_z \end{Bmatrix}^T \tag{4.3}$$

where, m_b is the mass of a body (part) and $\begin{bmatrix} v_x & v_y & v_z \end{bmatrix} = \begin{bmatrix} \dot{x} & \dot{y} & \dot{z} \end{bmatrix}$. The resultant kinetic energy can, therefore, be defined as:

$$T = \frac{1}{2} m_b v^2 = \frac{1}{2} m_b \begin{bmatrix} \dot{x}^2 & \dot{y}^2 & \dot{z}^2 \end{bmatrix} \tag{4.4}$$

With the rotational components of the kinetic energy given by:

$$\begin{bmatrix} T_{rx} \\ T_{ry} \\ T_{rz} \end{bmatrix} = \frac{1}{2} \begin{bmatrix} I_{xx} & 0 & 0 \\ 0 & I_{yy} & 0 \\ 0 & 0 & I_{zz} \end{bmatrix} \begin{bmatrix} \omega_x & \omega_y & \omega_z \end{bmatrix} \begin{Bmatrix} \omega_x & \omega_y & \omega_z \end{Bmatrix}^T \tag{4.5}$$

Finally, the total angular kinetic energy can be shown to be:

$$\begin{bmatrix} T_r \end{bmatrix} = \frac{1}{2} I \omega^2 = \frac{1}{2} \left(I_{xx} \omega_x^2 + I_{yy} \omega_y^2 + I_{zz} \omega_z^2 \right) \tag{4.6}$$

where *I* is the mass moment of inertia matrix and ω is the overall angular velocity of a part.

4.2.3 Momenta

The general momentum of a body is given by the term $\frac{\partial T}{\partial \dot{q}_j}$ in the Lagrange equation (4.2), and is denoted by M_{q_j}, giving:

$$M_{q_j} = \frac{\partial T}{\partial \dot{q}_j} \tag{4.7}$$

By breaking down the momenta further, the translational and rotational components can be expressed individually. Taking the translational components first, by differentiation of the translational kinetic energy equation (4.4), the following equations are formed with respect to the generalised vector set:

$$M_x = \frac{\partial T}{\partial \dot{x}} = m_b \dot{x} \tag{4.8}$$

$$M_y = \frac{\partial T}{\partial \dot{y}} = m_b \dot{y} \tag{4.9}$$

$$M_z = \frac{\partial T}{\partial \dot{z}} = m_b \dot{z} \tag{4.10}$$

Similarly, the rotational components of momenta are obtained. The angular velocity components in the rotational kinetic energy equation (4.6) are replaced by their respective components in terms of $\left[\dot{\psi}_e \quad \dot{\theta} \quad \dot{\phi}\right]$, resulting in the following expressions for the angular momentum of a component in motion relative to a fixed reference coordinate system (Rahnejat H, 1998):

$$M_{\psi} = \frac{\partial T}{\partial \dot{\psi}_e} = I_{xx}\ddot{\psi}_e S\theta S\phi + I_{yy}\dot{\psi} S\theta C\phi + I_{zz} C\theta \tag{4.11}$$

$$M_{\theta} = \frac{\partial T}{\partial \dot{\theta}} = I_{xx}\dot{\theta} C\phi - I_{yy}\dot{\theta} S\phi \tag{4.12}$$

$$M_{\phi} = \frac{\partial T}{\partial \dot{\phi}} = I_{zz}\dot{\phi}^2 C\phi \tag{4.13}$$

where: $C \equiv \cos$ and $S = \sin$.

4.2.4 Kinetics

Starting with Lagrange's equation, the terms relating to the applied kinetics can be utilised to describe the forces acting on a component, such as contact forces or body forces. Taking a generalised force F acting on a body, the components of this force can then be expressed for any coordinate direction as:

$$F_{q_j} = \left[\frac{\partial \vec{R}_G}{\partial q_j}\right].F \tag{4.14}$$

Where, $\left[\frac{\partial \vec{R}_G}{\partial q_j}\right]$ is the differential with respect to a co-ordinate in the generalised vector co-ordinate set (known as the Euler's equation). The unit vectors (i.e. $\left[\vec{i} \quad \vec{j} \quad \vec{k}\right]$) specify the direction the applied force acts with respect to the global reference frame. For instance taking the force to be applied in the *x* direction, the generalised force component would be given by a vector dot product operation as:

$$F_x = \left[\frac{\partial \vec{R}_G}{\partial x}\right].F = F.\vec{i} \tag{4.15}$$

A similar method can be applied to account for the generalised forces in the other co-ordinate directions. The scalar product in equation (4.15) equates to zero if the applied force does not have a component in a given direction.

Based on the above formulation, a set of equations of motion are established using the Lagrange's equation (4.2) for constrained systems for each component of the multi-body inhaler valve model.

4.2.5 Constraint Functions

The final term of Lagrange's equation (4.2) accounts for the reaction forces on the joints within the mechanism. These constraint functions, Ck, must be determined for every joint in each instance, where a degree of freedom is removed from a part. The number of constraint functions required varies dependent on the joint chosen. For example, a translational joint removes five degrees of freedom and specifies five constraint functions. The n constraint functions for the different joints in the inhaler valve model are represented by a combination of holonomic and non-holonomic functions as (Rahnejat H, 2000):

$$\begin{bmatrix} C_k \\ \dot{\xi}_j \dfrac{\partial C_k}{\partial \xi_j} \end{bmatrix} = 0, \ (j = 1 \rightarrow 6), \ (k = 1 \rightarrow n) \qquad (4.16)$$

4.3 Description of the multi-body inhaler valve model

4.3.1 Inhaler Background

The inhaler mechanism consists of a damped non-linear system with several degrees of freedom. Three interconnected components make up the valve stem, onto which two highly elastic o-ring seals are fitted. The seals interact with the contacting inhaler bore and the applied canister pressure. The relationship for the response of the seals is quite complex, resulting from a number of tribological reactions. For testing purposes the actuation velocity is restricted to 20 mm/min, thus, providing a slow variation of load with time during the actuation process. The constant actuation velocity also means that inertial forces (as the result of acceleration) are ignored. The successful actuation of an inhaler valve is sensitive to many factors, as it can be seen from the

experimental data, where seals with nominally same geometric properties and produced with the same manufacturing process, present very different behaviour during operation as can be seen in Chapter 6.

In terms of the development of a virtual prototype model, a simplified approach was deemed suitable in order to represent the fundamental motions of the inhaler valve. CAD geometry components were imported into ADAMS and the model was formulated in order to provide a direct comparison to a corresponding test rig and, therefore, allow a means of validation.

The inhaler valves used for the experimental testing consist of the following:

- Three individual stem components assembled using an interference fit and a measured and controlled applied force
- Two elastomeric o-ring seals of known dimensions both before and immediately after fitment into their retaining grooves.
- An outer housing (bore) of known dimensions to which the canister is firmly sealed
- A compression testing machine secures the housing and canister, while providing a driving force to the inhaler stem in order to maintain a constant velocity
- Sensors within the machine capture the force required to maintain the motion during an actuation test, both for in-stroke and out-stroke cycles

4.3.2 Multi-body model constraints and definitions

4.3.2.1 Component Parts

Each component (or rigid body/part) has six degrees of freedom. Therefore, six equations of motion are required to define its motion as described earlier in this chapter. In order for a multi-body dynamic analysis to be carried out, each component part is modelled using the Lagrangian approach. Joints between neighbouring components are described by means of constraints.

4.3.2.2 Constraints

An imposed constraint removes a relative degree of freedom (or several depending on the type) of a given component and its neighbouring part. Constraints are in the form of joints, each representing an ideal case where no unwanted movement is possible. Types of constraints include:

Fixed Joint - A fixed joint is used to lock two parts together. As such it removes all the six relative degrees of freedom between the two parts.

Revolute Joint - A revolute joint permits the rotation of one part relative to another about a single coordinate axis. It is effectively a hinge joint.

Translational Joint - A translational joint allows a part to translate relative to another along a single defined axis.

4.3.2.3 Applied Forces

A force or torque can be applied to a part. It can also arise from the interactions of parts within the multi-body system. In this instance it is used to represent the force applied to the stem components by the canister internal pressure force.

4.3.2.4 Degrees of freedom within the inhaler valve model

The degrees of freedom within a multi-body system represent the minimum number of independent coordinates required to accurately describe the position of each component within the system. For each degree of freedom an additional equation of motion is required in order to solve the dynamic response of the system. With a free body in a 3D space, there are six degrees of freedom initially present. These may be

constrained as previously stated using a joint to constrain the motion in a particular direction or about a particular axis. With this in mind, it can be seen that the total number of degrees of freedom within a mechanical system can be shown to be the total number of coordinates that form the system less the total number of imposed constraints. The number of degrees of freedom of the multi body inhaler model is obtained using the Gruebler-Kutzbach expression as:

$$DOF = 6(\text{number of parts} - 1) - \sum \text{Constraints} \quad (4.17)$$

Note that the number of parts count is reduced by one as within the multi-body model the ground contributes to the total number of parts. However, the ground is a fixed reference and does not contribute to the overall number of degrees of freedom; as such it is discounted from the calculation.

For a rigid body multi-body system, the number of degrees of freedom represents a measure of the type of system being investigated such that:

- If the number of DOF < 0, then the system is over-constrained and, therefore, it cannot be resolved. If the system is over-constrained, then there usually exists some degree of redundancy in the system model.
- If the number of DOF $= 0$, then the system is kinematic. Kinematics is the description of a body's motion without consideration of the causes of motion (i.e. applied forces and moments). Although simpler to resolve than a dynamic solution, the inertial and damping effects within the system are ignored.
- If the number of DOF ≥ 0, then the system is dynamic, as is the case used to model the inhaler valve mechanism. Dynamics consider both the kinetics and kinematics of a system and, therefore, take account of both the motion and the causes of motion. The fundamental principles are based on Newton's three laws of motion.

For the inhaler valve the model consists of 8 individual parts and 41 constraints. As a result, the system has a single degree of freedom when the Gruebler-Kutzbach calculation (4.17) is used. This single degree of freedom corresponds to the translational movement of the rigid stem assembly with respect to the housing bore. In

this way, no allowance of stem 'rattle' or rotation during its motion is made. When a constant velocity is defined inertial dynamics are disregarded (uniform motion, Newton's first law of motion). The force acting on the seals is in equilibrium with canister pressure and seals' friction. This approach forms the basis of the current analysis and is justified at low actuation speeds. If the speed of actuation is fast, inertial effects come in to play.

4.4 Description of the modelled parts

4.4.1 Components of the modelled system

The individual components and the final assembly are illustrated in Figures 4.2-4.8 below for reference.

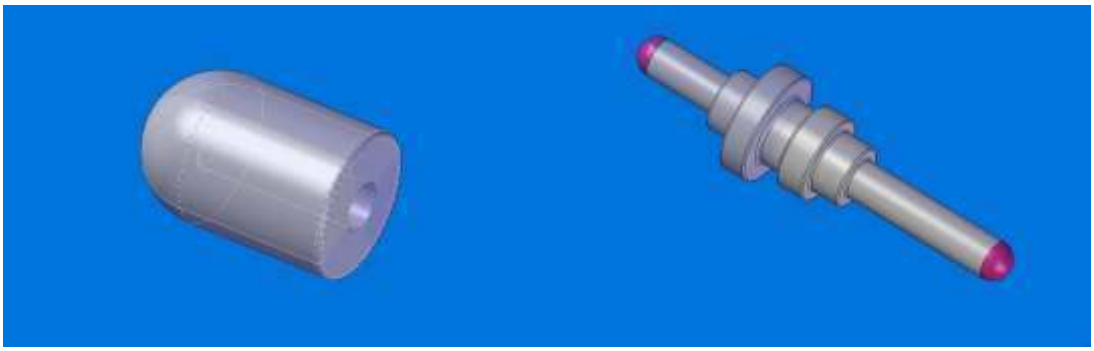

Figure 4.2: Stem top

Figure 4.3: Stem centre

Figure 4.4:Stem bottom

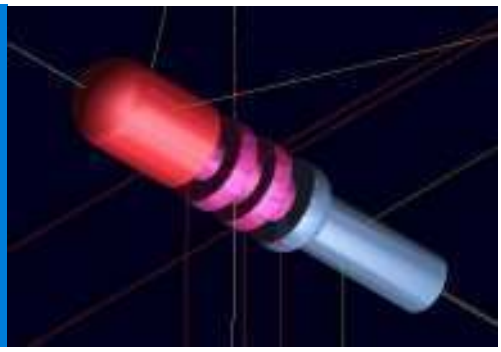

Figure 4.5: Stem assembly

Figure 4.6: Example seal

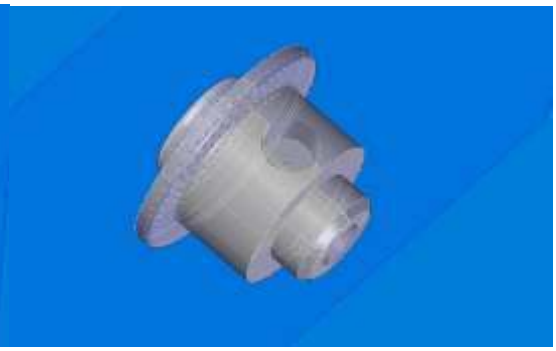

Figure 4.7: Housing bore

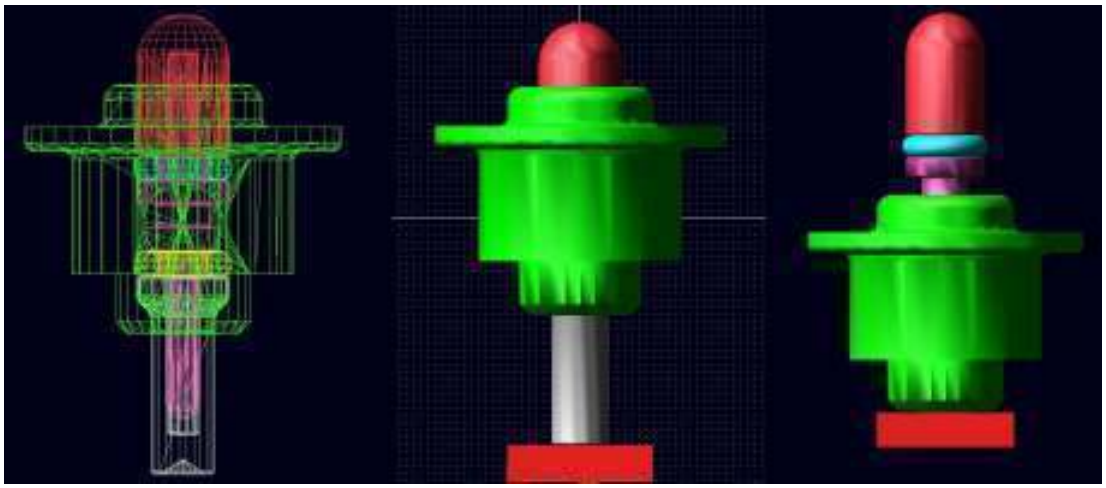

Figure 4.8: The completed assembly

4.4.2 Rigid component properties

The mass and inertial properties of each component part within the inhaler mechanism are listed in Table 4.1 below.

			Moments of Inertia (Kg mm²)		
Number	Part Name/Description	Mass (Kg)	Ixx	Iyy	Izz
1	Valve Housing	1.25E-02	0.416015	0.380506	0.367929
2	Stem Centre	1.12E-03	2.43E-02	2.43E-02	2.27E-03
3	Stem Top	1.47E-03	1.15E-02	1.15E-02	6.45E-03
4	Stem Bottom	1.14E-03	1.93E-02	1.93E-02	3.45E-03
5	Inner Seal	3.23E-06	1.90E-05	1.00E-05	1.00E-05
6	Outer Seal	3.23E-06	1.90E-05	1.00E-05	1.00E-05
7	Actuating Block	1.00E-10	1.00E-10	1.00E-10	1.00E-10
8	Ground	—	—	—	—

Table 4.1: Mass and inertial properties of the valve model

4.4.3 Applied Forces (Restraints)

Table 4.2 lists the magnitude and duration of each force acting on the bodies within the multi-body dynamic model mechanism. The location, where each force is imposed on the respective geometry is also indicated.

Number	Type	Posistion	Magnitude	Duration
1	Actuation Force	Actuating Block	Dependant on Contact Conditions	Through Out Simulation
2	Inner Seal Friction Force	Stem Centre	Dependant on Motion/Pressure Gradient	Through Out Simulation
3	Outer Seal Friction Force	Stem Centre	Dependant on Motion/Pressure Gradient	Through Out Simulation
4	Pressure Force	Stem Top	14.5 N	Through Out Simulation

Table 4.2: Applied forces

4.4.4 System Constraints

Table 4.3 defines the constraint type and number of degrees of freedom removed for each component part within the inhaler mechanism.

Number	Part I	Part J	Constraint Type	Number of Constraints
1	Valve Housing	Ground	Fixed	6
2	Stem Centre	Stem Top	Fixed	6
3	Stem Bottom	Stem Centre	Fixed	6
4	Inner Seal	Stem Centre	Fixed	6
5	Outer Seal	Stem Centre	Fixed	6
6	Actuating Block	Stem Bottom	Fixed	6
7	Actuating Block	Ground	Translational	5

Table 4.3: Constraints between connected components in the multi-body valve model

4.4.4 Tribological Parameters

Table 4.4 defines the key material and tribological parameters from within the inhaler mechanism model.

Parameter	Value
Stem Modulus of Elasticity (1)	2.6 GPa
Seal Modulus of Elasticity (1)	2.5 MPa
Stem Poisson's Ratio (1)	0.35
Seal Poisson's Ratio (1)	0.49
Nominal Canister Pressure (1)	0.55 MPa
Pressure-Viscosity Coefficient (2)	2.8×10^{-9} Pa-1
Ambient Viscosity (2)	0.211×10^{-3} Pa.S
Eyring Shear Strength (3)	3.5 Mpa
Hamaker Constant (4)	1.35×10^{-19}

(1) Obtained from 3M data
(2) Solvay Fluor Datasheet (www.solvaychemicals.com)
(3) Roberts (1992)
(4) Israelachvili (1992)

Table 4.4: Tribological properties of the model

Simulation studies with the model described here are reported in Chapter 5.

5.0 Tribology of inhaler valve seals

5.1 Introduction

This chapter outlines the fundamentals of tribology applied to the inhaler valve mechanism, and more specifically to the conjunction between the elastomeric seals and the polymeric housing bore. The investigation begins by presenting approaches to similar research problems found in literature, before moving onto more in-depth solutions. Analytical and numerical models are considered, including features, such as surface roughness and intermolecular forces.

5.2 Initial Modelling

The findings of the papers such as those by Nikas (2005) and Karaszkiewicz (1987) were chosen as a suitable starting point to begin development of a lubrication model. The formulae outlined by Karaszkiewicz (1985, 1987) have been developed specifically for O-ring sealing and present the case of simple hydrodynamics. The initial model has followed this approach. The multi-body dynamics valve model (see Chapter 4 for a detailed explanation of the model structure in ADAMS) supplies to the lubrication model the necessary information of the stem displacement and of the sliding velocity between the two surfaces in contact. This is then relayed to a FORTRAN subroutine (lubrication model), which calculates in real time the sliding friction force using the procedure outlined in Figure 5.1.

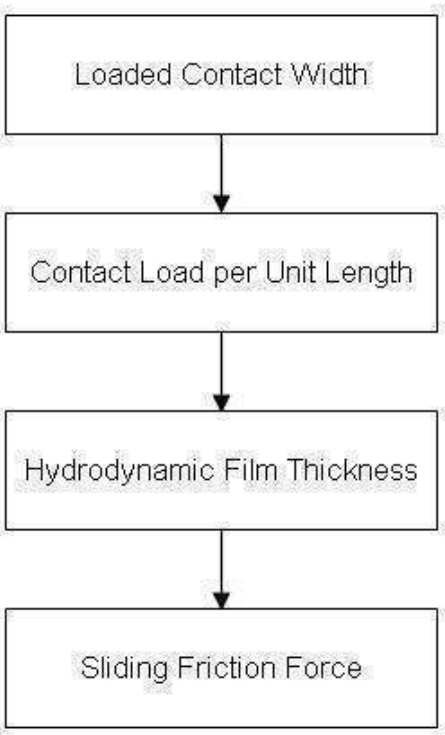

Figure 5.1: Calculation procedure of the friction force

Prior to the calculation of the contact width, the pressure gradient across the seal is determined. This is calculated based on the displacement of the stem within ADAMS, with the friction of the inner seal being completely turned off when not in loaded contact with the housing bore. A static coefficient of friction is also included for the onset of motion at the start of the actuation. This was found following tests on the sliding conditions of rubber samples (provided by 3M).

The contact width of the seal/bore interaction can be calculated based on the dimensions of the groove which are known, as are those of the seal. This allows the determination of the contact area of the seal and, thus, the squeeze ratio as indicated in Equation (5.2) (Karaszkiewicz, 1987). The applicability of the chosen equations is for seals with a squeeze ratio of $0.07 \leq \varepsilon \leq 0.25$.

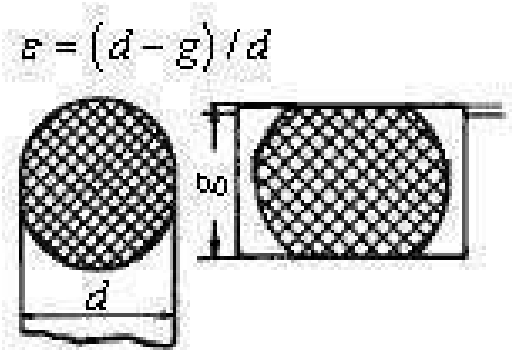

Figure 5.2: O-ring seal squeeze ratio diagram (Karaszkiewicz, 1987)

The resulting squeeze ratio (ε) in this instance for the novel valve design being within the range (Dimensions taken from 3M test data):

$$\varepsilon = \frac{(d-g)}{d} = \frac{(1.61-1.36)}{1.61} \qquad (5.1)$$
$$\underline{\underline{\varepsilon = 0.155}}$$

Initially this approach was undertaken for an unloaded seal as that studied by Karaszkiewicz's initial work (1979, 1985 and 1987). However, this method was later modified to use the formula given for the contact width of a seal loaded with a pressure P (Karaszkiewicz, 1990) as:

$$cwl = \left((2\varepsilon + 0.13) + \left[0.39(1-\varepsilon)^{-1} - 0.5(2\varepsilon + 0.13) \right] \left[1 - \exp\left(-\frac{4.6p}{E} \right) \right] \right) d \qquad (5.2)$$

This then allows the contact force of the seal on the bore to be calculated. Again, this formula was taken from Karaszkiewicz (1990). This force will later be used in conjunction with Barus' law (Cameron, 1976) to calculate the viscosity of the lubricant within the seal/bore contact area.

$$Fn = \left(\left(\frac{\pi}{6} \right) (2\varepsilon + 0.13)^2 \right) (ELd) \qquad (5.3)$$

The above formula (Karaszkiewicz, 1990) is in fact that of an unloaded seal, while the

case of a loaded (by pressure p) seal is given below (Karaszkiewicz, 1990):

$$\overline{\sigma_0} = \left(\frac{\pi}{6}\right)(2\varepsilon + 0.13)E$$
$$\overline{\sigma_p} = \frac{\upsilon}{1-\upsilon} p$$
$$\overline{\sigma} = \sigma_0 + \overline{\sigma_p} \qquad (5.4)$$

$$Fnl = \pi Lcwl\overline{\sigma}$$

This relationship allows a tribodynamic model to be constructed using friction coefficients, although it has been shown that this is not a very accurate way of tackling the modelling of rubber lubrication (Nau, 1999). Therefore, while it was useful to have the contact force for the seal to gain an understanding of its sealing properties, modelling of the lubricant action is necessary.

What has also been found necessary is the inclusion of pressure gradient changes during the actuation motion. This is because, depending on the displacement of the stem within the bore, the seals may have zero, positive or negative pressure gradients acting across them. The inner seal also loses contact completely during metering of the dose and, therefore, does not contribute to the system friction during approximately 50% of the actuation process.

5.2.1 O-ring Lubrication

Lubrication within the initial model assumes fully developed hydrodynamic conditions with no direct contact of the rubber and housing bore, whilst it is admitted from the previous reports provided by 3M and also from the current analysis of the compression tests that this is not true in reality. This was chosen as a suitable starting point, as it represents the most simple regime of lubrication to model and also literature relating to O-rings under these conditions was readily available (Karaszkiewicz, 1985).

The lubricating film thickness was, therefore, calculated using the following extrapolated film thickness formula (Karaszkiewicz, 1987):

$$h_c = 4.4(\eta u)^{0.65}(R)^{0.56}(W)^{-0.21}(E')^{-0.44} \tag{5.5}$$

Where W, the force per unit length (N/mm) of an unloaded seal is calculated by (Karaszkiewicz, 1987) as:

$$W = \frac{(\pi E c w^2)}{6d} \tag{5.6}$$

or by the following formula for a seal loaded by pressure p (Karaszkiewicz, 1985) as:

$$W = cwl\overline{\sigma} \tag{5.7}$$

E´ is the reduced modulus of elasticity for the rubber-polymer contact and is calculated as (Hamrock, 1994):

$$E' = 2\left(\frac{1-\upsilon_a{}^2}{E_a} + \frac{1-\upsilon_b{}^2}{E_b}\right)^{-1} \tag{5.8}$$

Finally, the frictional sliding force can be evaluated by assuming no asperity contact using the formula below due to Persson (2000), which calculates the force resulting from the viscous shearing of a lubricant, in the case of this PhD predominately

modelled as pure HFA 134a for simplicity unless stated otherwise due to it representing the bulk of the formulation in reality.

$$F_V = \left(\frac{D\pi\eta c w_L u}{h_C} \right) \beta$$

Where :

$$\beta = \left(\frac{1}{\xi - 1} \right) \left((4 \ln \xi) - \left(6 \left(\frac{\xi - 1}{\xi + 1} \right) \right) \right) \tag{5.9}$$

$$\xi = \frac{h_C}{h_M}$$

5.2.2 Findings of the initial model

The calculated film thickness, however, has been found to be ultra-thin, and is in the region of just 0.3 nm. However, the rubber itself is likely to have asperities in the region of just 0.2 μm after its initial running in 'smoothing runs' (Rana et al, 2001). Therefore, while the presence of a film is theoretically still possible, further work is required to prove the existence of such a film and its contribution towards reducing system friction due to the extremely low thickness calculated.

What has been shown so far is that while the magnitudes of the calculated friction are incorrect at this stage, the qualitative shape of the actuation force plot matches that of the test data supplied by 3M.

Figure 5.3 shows an example plot of consecutive actuations of an inhaler valve. The line indicated with the arrow being the initial run, hence the static (dry) peak at the onset of motion. The extremes at either end of the plot are due to the compression testing machine leaving the stem entirely (when plot reaches zero) and when the machine reaches the housing as the stem is fully depressed (when plot exceeds 30N). The remaining variations are due to changes in the pressure gradients across the seals, as each seal becomes loaded or unloaded depending on the instantaneous position of the stem.

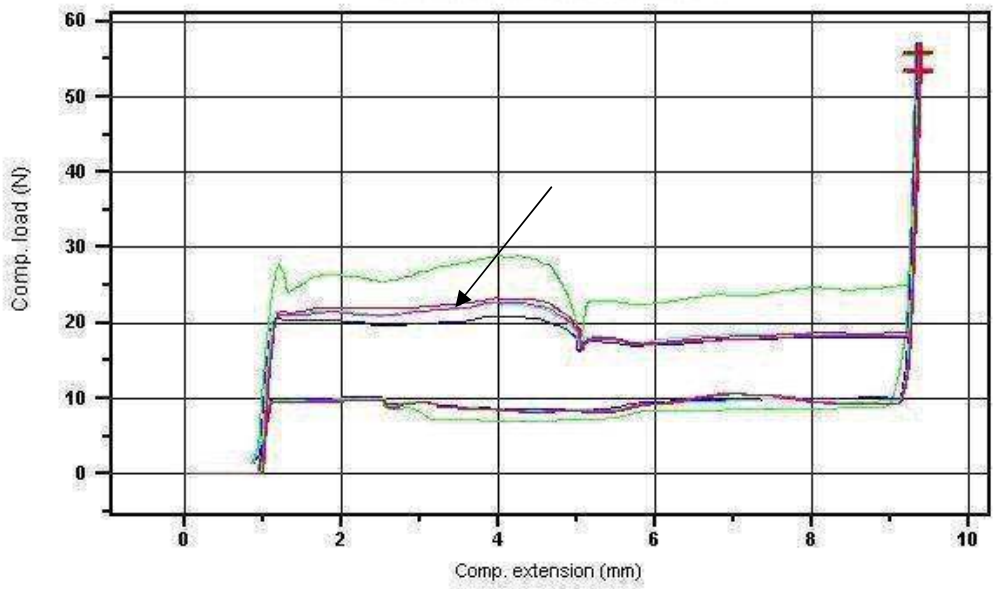

Figure 5.3: 3M test data actuation forces for multiple 20 mm/min tests (Multiple runs demonstrating repeatability of consecutive tests on a single pMDI over time, with the initial run indicated)

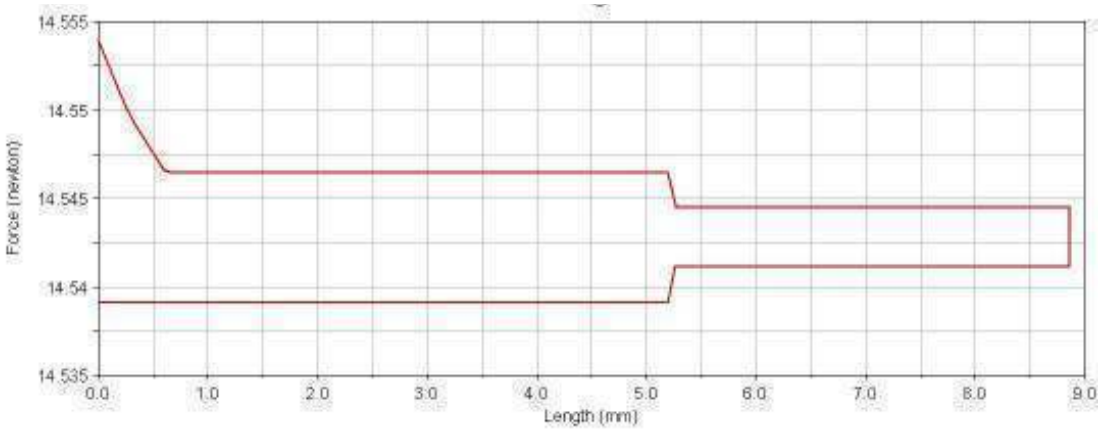

Figure 5.4: Model actuation force result for a 20 mm/min simulation

The overall shape of the test data actuation plot can be compared with that of the model predictions shown in Figure 5.4 which were obtained using the parameters indicated in Table 5.1.

Parameter	Value
d	1.61 mm
D	6 mm
E_f	2.6 GPa
E	2.5 MPa
g	1.36 mm
p	0.55 MPa
R_x	0.805 mm
u	10 mm/min
α	2.8×10^{-9} Pa^{-1}
η_0	0.211×10^{-3} Pa s
τ_0	3.5 MPa
υ_f	0.35
υ	0.49

Table 5.1: Model parameters

Qualitatively, each of the stages of the test plot is present. However, further work is required to represent them in a more realistic manner.

At this stage, it is felt that errors result from the erroneous film thickness calculation and the ensuing viscous friction calculation. The inclusion of asperity contact modelling and a numerical approach validating the current analytical is intended to trace the inaccuracies and form a more accurate model.

5.3 Addition of Surface Asperity Forces

Following the initial work which assumed full hydrodynamic lubrication in the contact, it was found that the calculated friction was unrealistic and there was no resemblance to the test data. The magnitudes of the recorded and calculated friction values were found to be several orders of magnitude apart. Therefore, it was concluded that full hydrodynamic lubrication could not be present, the calculated film thickness being insufficient to prevent the contact of surface asperities.

It was deemed necessary to include an element of boundary lubrication. Based on the initial film thickness calculations, it was apparent that direct contact of surface asperities was possible and likely to take place. In order to account for this, the asperity contact model of Greenwood and Tripp (1971) was chosen.

5.3.1 Greenwood and Tripp Surface Asperity Model

The total friction in the contact is described as (Greenwood and Tripp, 1971):

$$\text{Friction}_{\text{Total}} = \text{Friction}_{\text{Lubricant}} + \text{Friction}_{\text{Asperities}} \tag{5.10}$$

It is necessary to establish the proportion of load carried by the asperities and, thus, the frictional contribution. In order to do this, a Gaussian distribution of asperity heights was assumed and as such, the equivalent area of asperities making direct contact through the lubricant film can be calculated.

Figure 2.11 shows the equivalent area of asperity contacts formed from the summation of the asperities penetrating the lubricant film. The equivalent area is found according to:

$$A_a = \pi^2 \left(\varsigma \beta_{GWT} \sigma\right)^2 AF_2\left(\lambda\right) \tag{5.11}$$

Where:
A = Herztzian contact area
ς = Surface density of asperity peaks
β_{GWT} = Radius of curvature at asperity tip
σ = Combined surface roughness
λ = Seperation parameter $\left(= \frac{\mathrm{h_o}}{\sigma}\right)$

The load supported by the asperities in direct contact is:

$$\mathrm{W_a} = \frac{8\sqrt{2}}{15} \pi \left(\varsigma \beta_{GWT} \sigma\right)^2 \sqrt{\frac{\sigma}{\beta_{GWT}}} E^* AF_{5/2}\left(\lambda\right) \tag{5.12}$$

where the composite elastic modulus $\left(\mathrm{E}^*\right)$ is given by:

$$\frac{1}{E^*} = \frac{1}{2}\left[\frac{1-\upsilon_1^{\,2}}{E_1} + \frac{1-\upsilon_2^{\,2}}{E_2}\right]$$

The Gaussian distribution of asperity heights is represented in the above equations as the statistical terms F_2 and $F_{5/2}$, which are defined as:

$$F_n(\lambda) = \frac{1}{\sqrt{2\pi}} \int_{\lambda}^{\infty} (s-\lambda)^n e^{-s^2/2} ds \tag{5.13}$$

This is then represented using a polynomial fit as outlined in Figure 5.5 below:

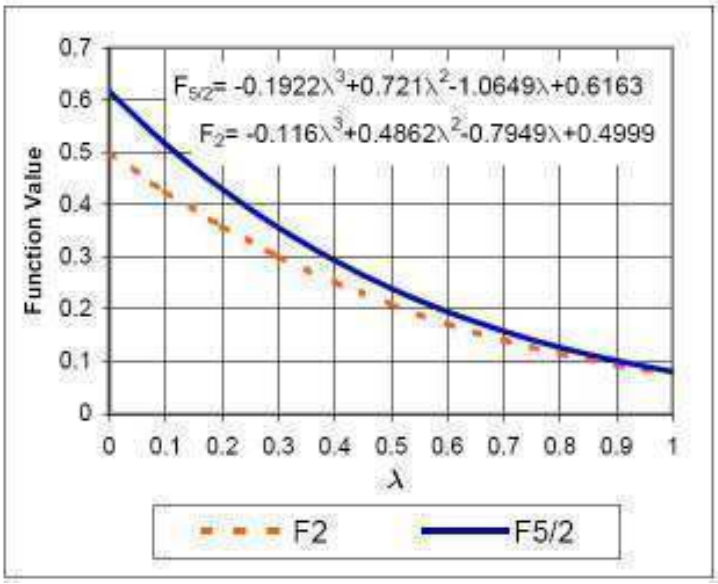

Figure 5.5: Statistical approximation of surfaces (Teodorescu and Bryzik, 2003)

5.3.2 Implementation of the Asperity Model

In order to implement the Greenwood and Tripp asperity model in the tribological routine, an additional iteration was introduced into the code. In the analytical model (Karaszkiewicz approach), an additional step was added, as outlined in Figure 5.6.

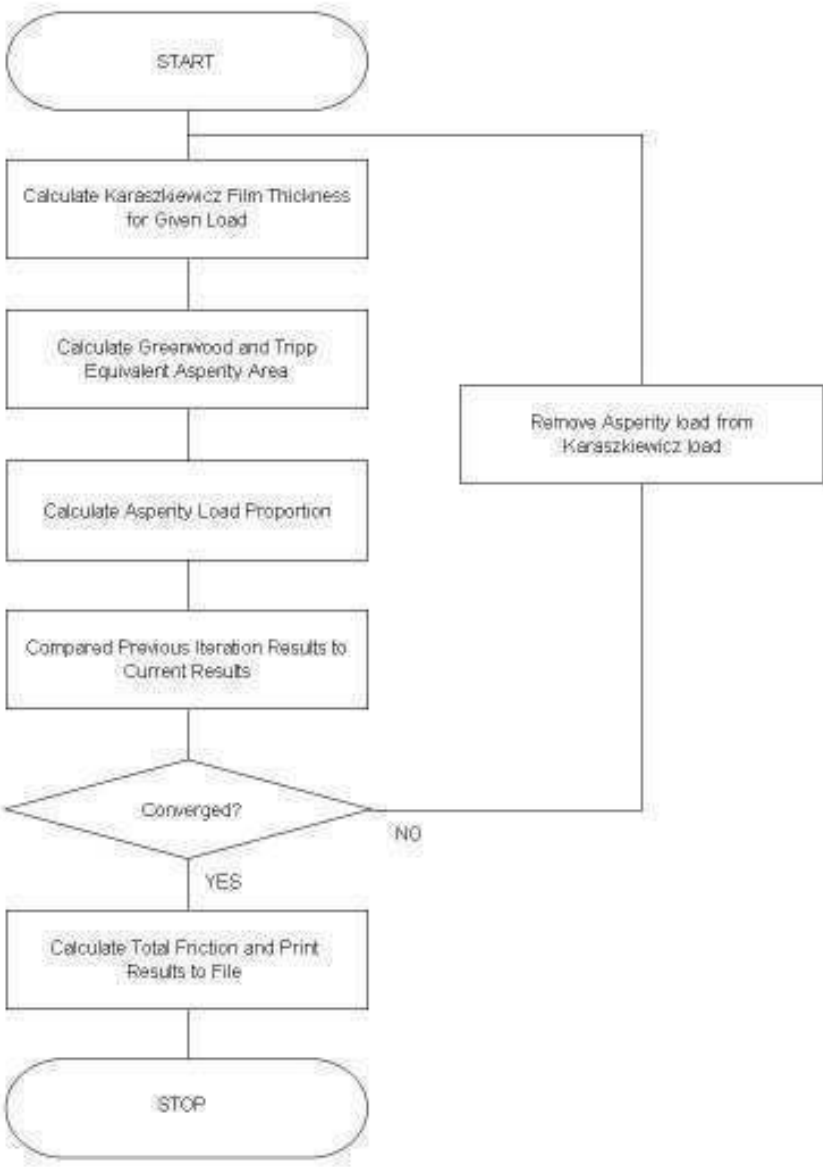

Figure 5.6: Karaszkiewicz-Greenwood and Tripp program flowchart

The proportion of load carried by the asperities is removed from the overall load value that a lubricant film would support. In this way, a thicker film can be formed. The equivalent area of asperity contact and, thus, load is then readjusted and the process continues until the changes within the iterations is below a predetermined error level. At this point the code is considered to have converged on a solution. Once converged, the overall friction of the system is calculated. The friction on the asperity contact is given by:

$$F_{Asperities} = \tau_0 A_a + m W_a \tag{5.14}$$

Friction due to lubricant viscous shear can be calculated using the following formulae (Greenwood and Tripp, 1971):

$$\tau = \frac{\eta V}{h_0} \text{ Providing } \frac{\eta V}{h_0} < \tau_0 \text{ else: } \tau = \tau_0 + \gamma W^* \tag{5.15}$$

where:

$W^* = \frac{W - W_a}{A_a}$

$\eta = \eta_0 e^{\alpha P^*}$

α = Pressure viscosity coefficient

And finally, the lubricant friction is given by:

$$F_{\text{Lubricant}} = \tau \left(A - A_a \right) \tag{5.16}$$

5.3.3 Van der Waals Forces

When close proximity of molecules takes place, a potential attractive force is generated due to a temporary imbalance of the molecular dipoles of each molecule and while small, the total effect in the contact can be significant. In order to account for Van der Waals effects due to the close proximity of the contacting surfaces, the following equation was utilised (Israelachvili, 1992 and Gohar and Rahnejat, 2008):

$$p_{vdw} = -\frac{A_h}{6\pi h^3} \tag{5.17}$$

where:

P_{vdw} = Additional contact force due to Van Der Waals Effects

A_h = Hamaker constant

h = Seperation of bodies (film thickness)

Using this formula, the additional contact force can then be established and added to that caused by both the fitment and canister pressures on the seal contact:

$$p_{Total} = p_{Fitment} + p_{Canister} + p_{vdw} \tag{5.18}$$

This additional step is integrated as shown in Figure 5.7, in order to allow the effect of Van der Waals force on the overall system friction.

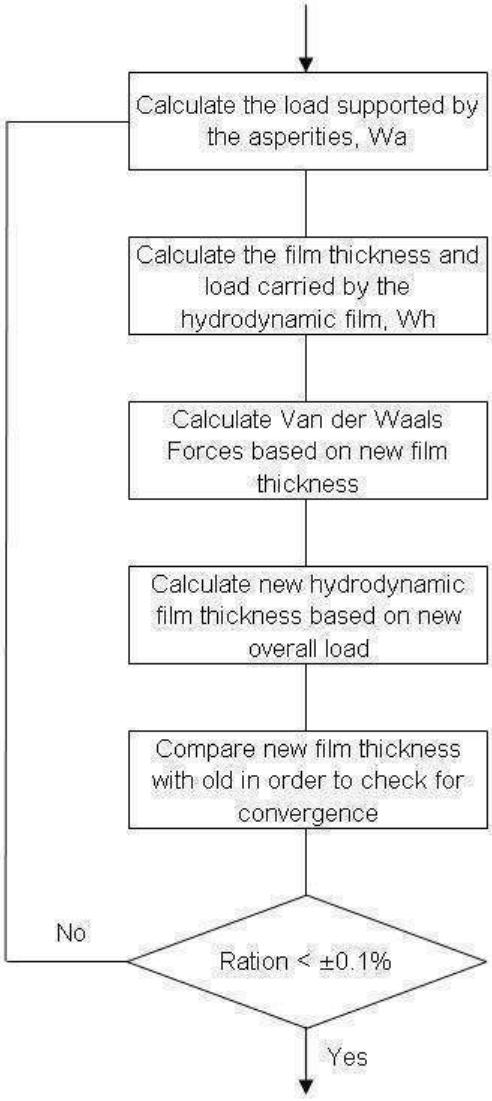

Figure 5.7: Flow chart including Van der Waals effects

5.4 Measurements and model validation

Following the inclusion of the Greenwood and Tripp asperity model, coupled with Van der Waals effects, model predictions were compared with a series of compression tests carried out for the pMDIs, at a constant rate of 20 mm/min (a sliding velocity of 0.34 m/s). The valves were then released to return under the action of canister pressure. Figure 5.8 shows the typical characteristics obtained experimentally in full line plots. This is the hysteretic behaviour of the device; its force-extension/deflection characteristics. Compression force is applied at point A (see also Figure 5.9) and follows the steep curve AB.

The force along this part of the characteristic plot is that of the combined seals' friction force and that due to the canister pressure. Motion commences at point B, where the static friction peak at the onset of motion is visible. Thereon, steady uniform motion dictates no significant inertial effect.

From point B, the characteristics follow the pressure gradients across the two seals (shown in Figure 5.9) and the kinetic friction during the compression phase.

As the actuation continues, the inner-most seal leaves contact with the housing bore at point C, resulting in a sharp drop. By point D, the valve cannot be compressed further and the compression testing machine reaches the housing, causing a sharp increase in the measured force. At this point the transition to valve release begins. From D (see also Figure 5.9) the return force is the net difference between the pressure induced force and the friction in the outer seal contact. In the region BD, the resultant force shown in Figure 5.8 is that necessary to overcome the opposing forces of the combined seals' friction force and that of the canister pressure. As point E is reached, and in the region EA, the existing force attempts to prevent valve return at a rate faster than specified. The force is due to canister pressure.

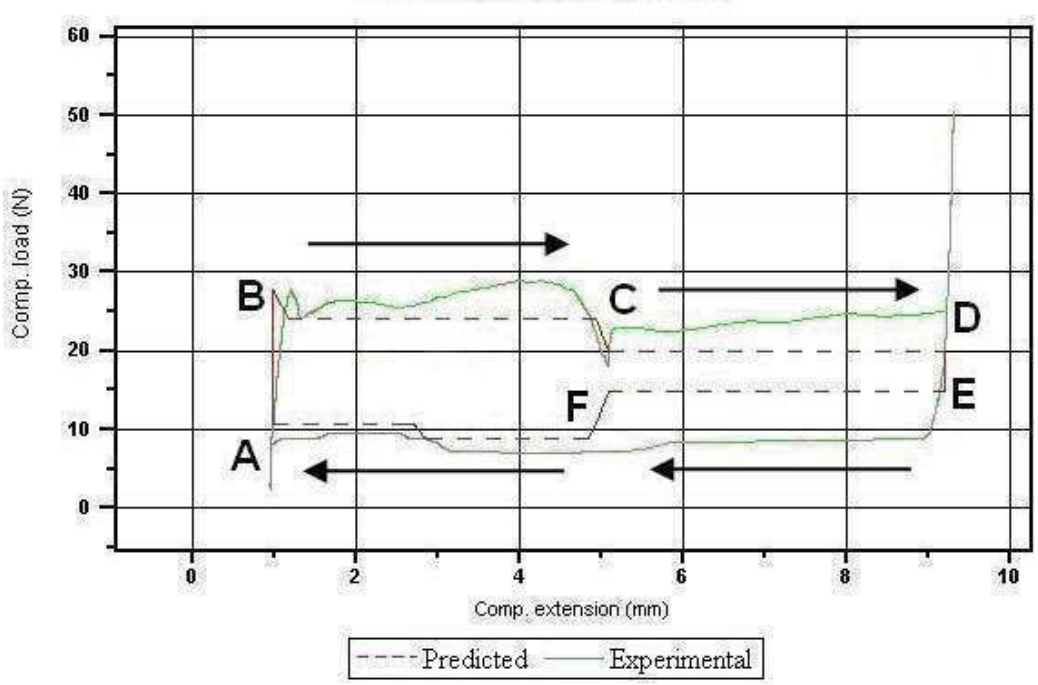

Figure 5.8: Measured and predicted valve actuation characteristics at 20 mm/min

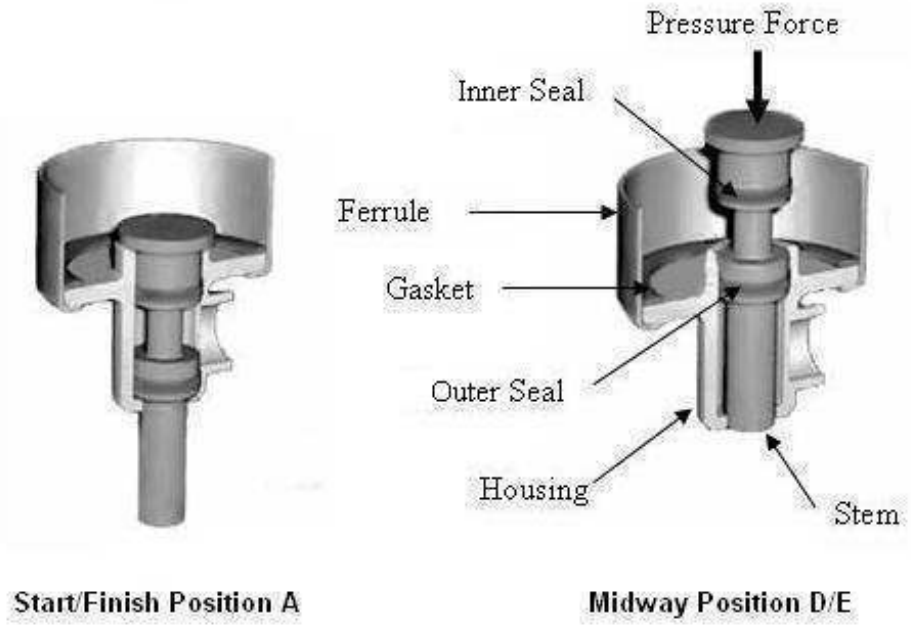

Figure 5.9: Schematic representation of an inhaler valve

At point E the valve stem begins to move again and the pressure return force, discounting friction due to one seal, is recorded. Point F indicates an increase in system friction as the inner-most seal re-enters the housing, resulting in a reduction in

the return force of the overall device. Finally, the characteristics return to point A as the valve is entirely released and comes to rest.

The dotted line in Figure 5.8 represents the predicted characteristics using the described friction model applied at both seal-to-housing contacts in the multi-body dynamic model, where the stem is moving at the constant sliding speed of 20 mm/min. As it can be observed, reasonable agreement is found with the measured data. The predicted film thickness from Equation (5.6) for both seals is in the range of 2-4 nm, which indicates that contribution due to viscous friction is very small compared to the boundary contribution. The variation in the outer seal film thickness is shown in Figure 5.10.

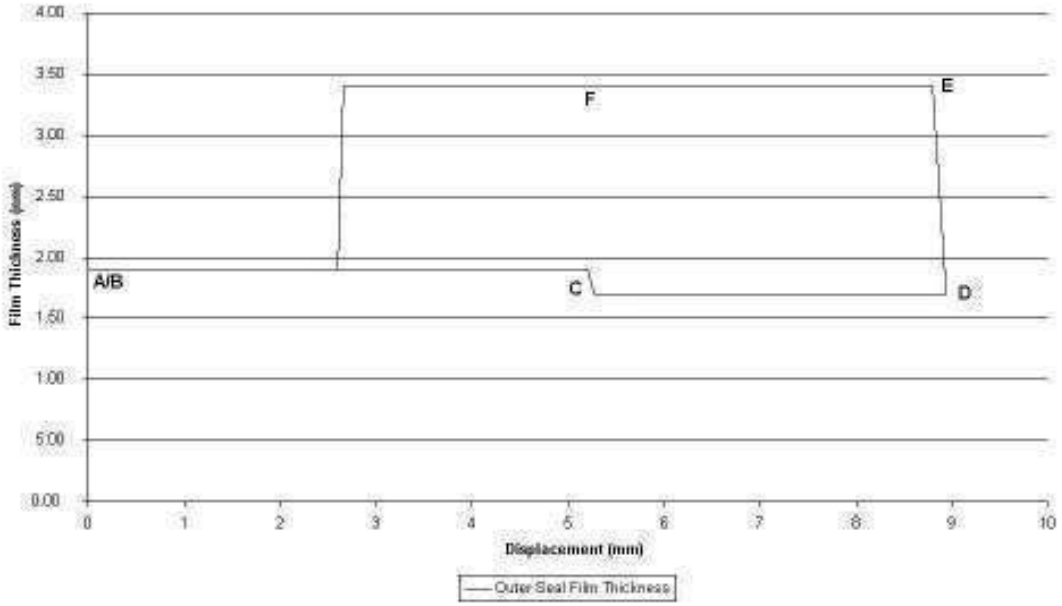

Figure 5.10:Cyclic variation of outer seal-to-housing film thickness

As it can be observed, throughout the compression-release cycle the film thickness is very small, indicating that contribution due to viscous friction is almost negligible. This is verified by the predicted inner seal friction shown in Figure 5.11 and Figure 5.12 for the boundary/total friction and viscous contribution respectively. While the predicted boundary/total friction and viscous contribution for the outer seal is shown in Figure 5.13and Figure 5.14 respectively.

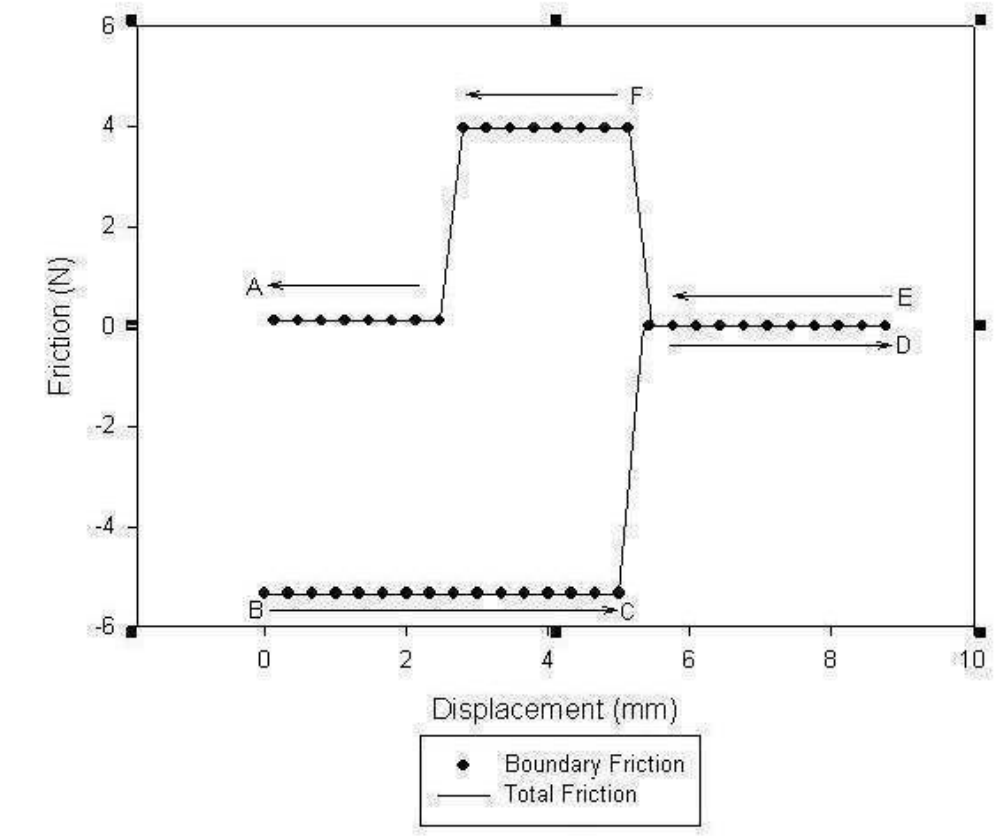

Figure 5.11:Inner seal boundary and total friction

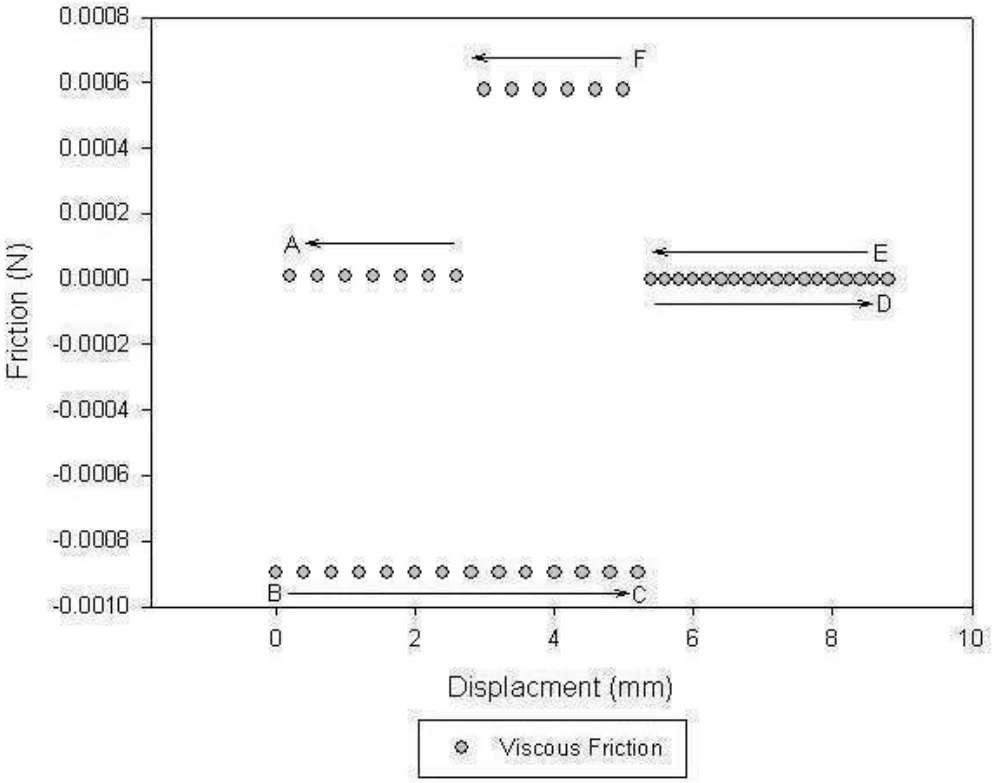

Figure 5.12: Inner seal viscous friction

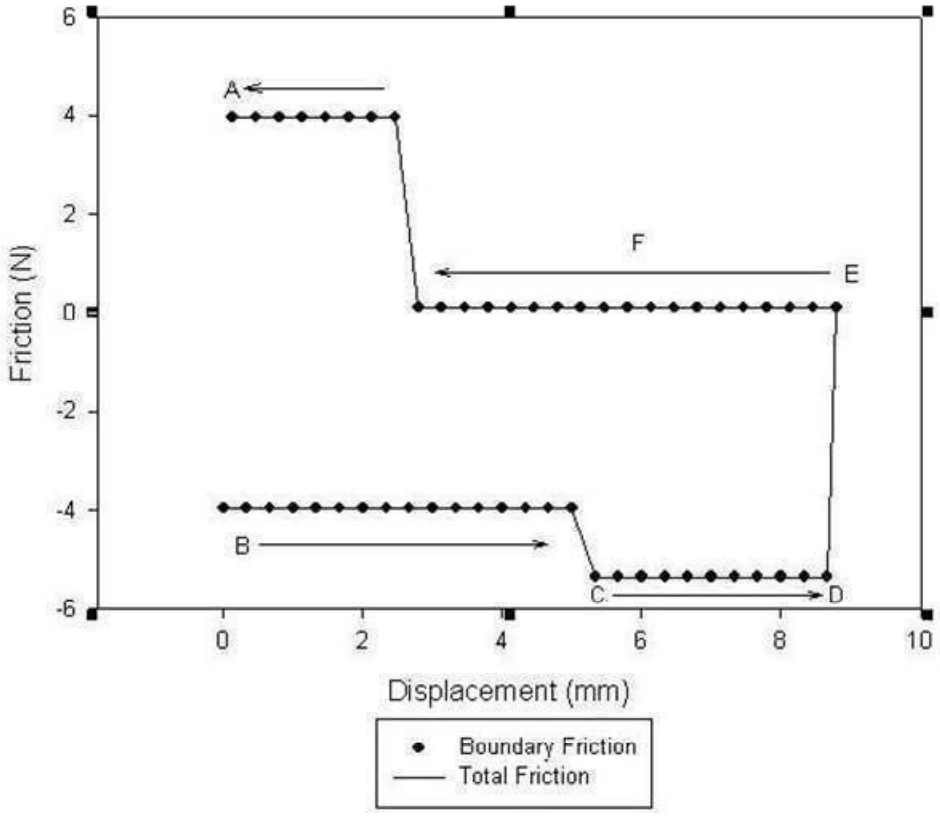

Figure 5.13: Outer seal boundary and total friction

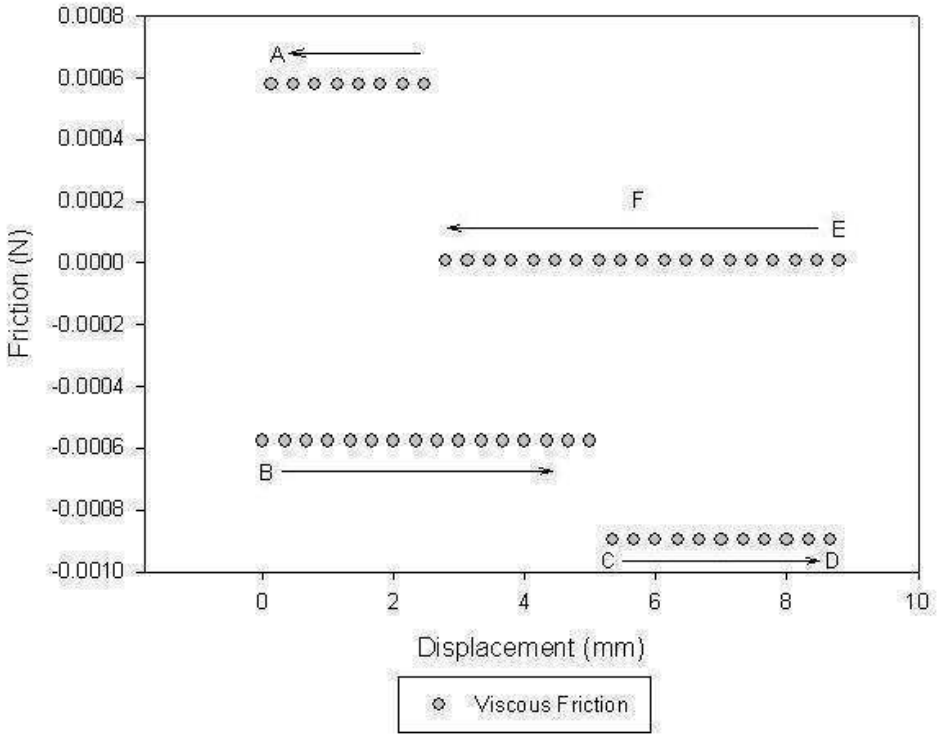

Figure 5.14: Outer viscous friction

Note that boundary friction is dominant, accounting for more than 95% of the overall friction. In all the figures the lettering A-F corresponds to the same instances as already described for Figure 5.8. The static friction is represented by the ordinate value corresponding to AB. This indicates an inner seal friction of approximately 5N and a corresponding value of 8N for the outer seal, which represent the effort AB on Figure 5.8. This static friction is entirely contributed by boundary interactions, given by Equation (5.15) (note that there would be no contribution due to any viscous action with cessation of entraining motion). Seals' friction remains almost unaltered for valve motion corresponding to BC, because of the uniform nature of the motion (see Figure 5.11 and Figure 5.13). At C the inner seal leaves contact and because of the pressure differential acting across the outer seal, a larger area of asperity contact develops, resulting in increased friction. The outer seal friction remains almost unaltered due to the uniform motion of the valve up to point D (end of compression stroke), whilst the inner seal is still out of contact. The return action begins immediately. At F the inner seal comes into contact with dramatically increased friction, therefore causing a reduction in the return force in Figure 5.8. The pressure differential across the outer seal drives it until aerosol release in the interval FA, whilst the inner seal comes to rest.

The differences between the predicted results and the experimental measurements are because of a number of factors, unaccounted for in the model. Firstly, the rubber seals digest a certain amount of formulation and swell, thus altering the contact area. Secondly, the boundary friction model employed here presumes dominance of adhesive friction between asperity tip-pairs, thus the effect of deformation (ploughing) friction in their potential oblique interactions is ignored. Finally, small menisci are expected to form between the asperity tips of the seals and those of the housing, which have been ignored in this initial analysis. Another important contributor to friction is Van der Waals forces which can contribute significantly to static friction under dry contact condition. Under "wet" conditions Van der Waals interactions are considerably reduced. Point E in Figure 5.8 seems to suggest this effect in transition from a momentarily drying contact to a wet case. These considerations form the basis for more in-depth future research.

5.5 Conclusions

The hysteretic characteristics of the pMDIs determine the required effort in valve actuation which is an important performance measure due to the range of users from the very young to the very elderly. This requirement together with the need for proper sealing of volatile formulations, assurance of precise dosage delivery and robustness for many actuations govern the design of pMDI devices. Unfortunately, these pre-requisites result in conjunctions that are tribologically poor due to environmental and bio-compatibility constraints imposed on the use of propellants with poor rheology in tribological terms. Thus, excessive friction can lead to a greater actuation effort and poor stem return repeatability (effected by canister pressure overcoming the conjunctional friction). This may result in unrepeatable and inaccurate successive actuations leading to poor drug delivery characteristics. The work has shown the importance of developing a parametric friction model, which can be expanded to include other previously mentioned phenomena, thus acting as a predictive tool in the development of a new generation of pMDIs.

5.6 Leakage

Finally, Leakage can occur when the O-ring starts to slide during actuation of the inhaler valve, any coherent film that is formed due to lubricant entrainment. For the central film thickness where dp/dx =0, the rate of leakage, Q, is given by (Karaszkiewicz, 1987):

$$Q = \pi D h_c U / 2 \tag{5.19}$$

Where D is the diameter of the sealing conjuncture

U is the sliding velocity

During a stroke of length L_s and time t the leakage is given as:

$$q = Qt = 0.5\pi D h_c L_s \tag{5.20}$$

If q is calculated for both the in-stroke and out-stroke of the inhaler, the net leakage is given as:

$$\overline{q} = q_O - q_I \tag{5.21}$$

The results of which are shown for comparison in Chapter 7, section 7.7.4.

6.0 General Reynolds Approach

Karaszkiewicz (1979,1987) has considered the contact of O-ring seals (also see Koudine *et al*, 1997). It was found that seals allowed a hydrodynamic film to be developed within the contact area. A limitation, however, is usually that the film formation is not discretised over the entire contact width but given as an overall value for either the minimum or central film thickness within the contact. In these studies, inclusion phenomena such as adhesion or electrostatic effects was not necessary due to the gap size and a hydrodynamic film. With quite thin and potentially interrupted films, it was deemed necessary to move away from the work of Karaszkiewicz (1979, 1987) and develop a solution based on a more fundamental approach, based on soft EHL, and inclusion of near surface effects, where necessary.

Reynolds equation can be derived by considering the equilibrium of a small element of fluid (Cameron, 1976). Considering the equilibrium of such an element in the x-direction (the direction of entraining motion), the shear stresses acting on the top/bottom faces can be established, along with the pressure forces on the opposing face (see Figure 6.1).

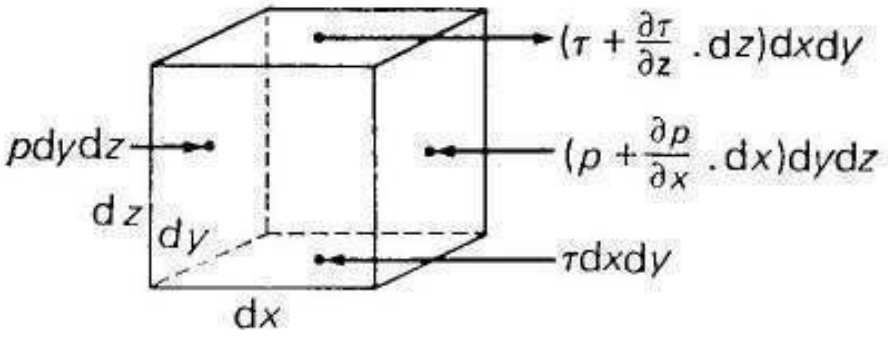

Figure 6.1: Equilibrium of a fluid elementary volume (after Cameron, 1976)

The following assumptions are made:

- Body and inertial forces are ignored (the element of fluid has insignificant inertial properties). Also the flow velocity is considered not to vary in direction with a constant velocity due to the elements size.
- Pressure does not vary across very thin films, thus: $\frac{\partial P}{\partial z} = 0$.

- The principal radii of bodies at the point of contact are considered to be large in comparison to the thickness of the lubricating film. Therefore, the surface velocities are regarded as constant and the flow is laminar.
- The lubricant is considered to be Newtonian
- No slip takes place at the boundaries of the contacting elements and the outermost lubricant layers (this is the basis of the Newtonian slow viscous model).
- Fluid inertia is negligible.
- The viscosity is assumed to remain constant across the thickness of the film. It is admitted this is a somewhat a crude assumption, but it was chosen initially to allow simplification of the problem.

The full Reynolds equation in all directions can, therefore, be formulated. For an incompressible fluid: (Cameron, 1976, Hui *et al*, 2000, and Gohar and Rahnejat, 2008)

$$\frac{\partial}{\partial x}\left(\frac{h^3}{\eta}\frac{\partial P}{\partial x}\right)+\frac{\partial}{\partial y}\left(\frac{h^3}{\eta}\frac{\partial P}{\partial y}\right)= 6\left\{\frac{\partial}{\partial x}\left(U_1+U_2\right)h+\frac{\partial}{\partial y}\left(V_1+V_2\right)h+2\left(W_{S1}+W_{S2}\right)\right\} \quad (6.1)$$

The terms in Reynolds equation can be thought of as those on the right hand side, being the flow terms due to surface velocities (Couette terms) and those on the left hand side as induced by pressure or resistance to flow. The individual terms being as follows:

P = Pressure
h = Film Thickness
η = Viscosity
w = Speed of approach/seperation of the components
x = Direction/Co-ordinate of entraining motion
y = Direction/Co-ordinate of side leakage
z = Direction/Co-ordinate of approach/seperation

In order to simplify the analysis, and in line with previous research (Keller, 1999, and Pinkus and Sternlicht, 1961) a line contact was assumed, thus allowing an infinitely long bearing approach to be taken with respect to the Reynolds equation. This means that the contact conjunction is considered along the face-width of the seal along the sliding axial direction of the seal (i.e. *x*-direction). This approach was also used by Karaszkiewicz (1979,1987) and by Hooke *et al* (1966). It must be regarded as an approximation as the contact is actually conforming between the seal and the polymeric canister.

6.1 Analytical Iso-Viscous Rigid Solution

As previously stated, the full Reynolds solution can be simplified using an infinitely long bearing assumption. It is also assumed that no side leakage takes place (i.e. in the *y*-direction). Hence, the contact can be represented by the reduced Reynolds equation:

$$\frac{\partial}{\partial x}\left(\frac{h^3}{\eta}\frac{\partial P}{\partial x}\right)=6\left\{\frac{\partial}{\partial x}\left(U_1+U_2\right)h\right\} \tag{6.2}$$

This form of the equation also disregards the effect of squeeze film, thus it may be regarded as steady-state, as pointed out by Gohar and Rahnejat (2008).

Pressures in the seal conjunction with the canister wall are relatively low as can be seen later. Thus, viscosity variation with pressure is ignored (i.e. Iso-viscous condition). Therefore:

$$\frac{\partial}{\partial x}\left(h^3\frac{\partial P}{\partial x}\right)=6\eta_0\left\{\frac{\partial}{\partial x}\left(U_1+U_2\right)h\right\} \tag{6.3}$$

Now, letting U = U_1+U_2, then:

$$\frac{\partial}{\partial x}\left(h^3\frac{\partial P}{\partial x}\right)=6U\eta_0\frac{\partial h}{\partial x} \tag{6.4}$$

This form of Reynolds equation can be integrated with respect to *x* to obtain the pressure gradient within the lubricant as:

$$h^3\frac{\partial P}{\partial x}=6U\eta_0 h+C_1 \tag{6.5}$$

In order to obtain the constant of integration C_1, it is necessary to employ a boundary condition. For insufficient loads, a hydrodynamic condition is assumed, where at the point of maximum pressure:

$$\frac{\partial P}{\partial x} = 0 \qquad x = -x_a$$
$$h = h_a \qquad P = P_{\max}$$

Resulting in $C_1 = -6U\eta_0 h_a$ as found by Rahnejat (1984) and Sasaki and Mori (1963). Thus:

$$h^3 \frac{\partial P}{\partial x} = 6U\eta_0 h - 6U\eta_0 h_a \tag{6.6}$$

Equation (6.6) can then be rearranged to obtain:

$$\frac{\partial P}{\partial x} = 6U\eta_0 \left[\frac{h - h_a}{h^3} \right] \tag{6.7}$$

Now, assuming a parabolic profile for the film thickness in accord with the hydrodynamic film assumption, Reynolds equation is transformed into:

$$\frac{\partial P}{\partial x} = \frac{6U\eta_0 \left(h_0 \left(1 + \frac{x^2}{2Rh_0} \right) - h_0 \left(1 + \frac{x_a{}^2}{2Rh_0} \right) \right)}{\left(h_0 \left(1 + \frac{x^2}{2Rh_0} \right) \right)^3} \tag{6.8}$$

Where a parabolic relationship between the film and x-coordinate is assumed as:

$$h = h_0 \left(1 + \frac{x^2}{2Rh_0} \right) \text{ and the reduced radius, } R = \frac{r_1 r_2}{r_1 + r_2} \tag{6.9}$$

Grouping and cancelling terms gives:

$$\frac{\partial P}{\partial x} = 6\eta_0 \frac{\frac{U}{2R}\left(x^2 - {x_a}^2\right)}{\left(h_0\left(1+\frac{x^2}{2Rh_0}\right)\right)^3} \tag{6.10}$$

The Reynolds equation can now be solved using the dimensionless groups given as (Rahnejat, 1984):

$$Tan\bar{x} = \frac{x}{\sqrt{2Rh_0}}$$

$$Tan\bar{x}_a = \frac{x_a}{\sqrt{2Rh_0}}$$

$$p^* = \frac{{h_0}^2}{\sqrt{2Rh_0}\,6U\eta_0} P \tag{6.11}$$

$$W^* = \frac{W_S}{U}$$

$$h_0{}^* = \frac{h_0}{R}$$

Therefore: $dx = \sqrt{2Rh_0}\sec^2\bar{x}d\bar{x}$

$d\bar{x}_a = 0$

Also:

$$h = h_0\left(1+\tan^2\bar{x}\right) = \frac{h_0}{\cos^2\bar{x}} = h_0\sec^2\bar{x}$$
$$h_a = h_0\left(1+\tan^2\bar{x}_a\right) = \frac{h_0}{\cos^2\bar{x}_a} = h_0\sec^2\bar{x}_a \tag{6.12}$$

$$dP = \frac{6U\eta_0\left(h_0\sec^2\bar{x} - h_0\sec^2\bar{x}_a\right)}{{h_0}^3\sec^6\bar{x}}\sec^2\bar{x}\sqrt{2Rh_0}\,d\bar{x} \tag{6.13}$$

Rearranging and implementing the substitution for P* gives:

$$\frac{h_0}{\sqrt{2Rh_0}}\frac{\partial P}{6U\eta_0}=\frac{d\bar{x}}{\sec^2\bar{x}}\frac{\sec^2\bar{x}_a d\bar{x}}{\sec^4\bar{x}} \tag{6.14}$$

The following integrals are, therefore, needed:

$$\int\cos^2\bar{x}d\bar{x}=\int\left(\frac{1+\cos 2\bar{x}}{2}\right)d\bar{x}=\frac{\bar{x}}{2}+\frac{\sin 2\bar{x}}{4} \tag{6.15}$$

$$\begin{aligned}&\int\cos^4\bar{x}d\bar{x}=\int\left(\frac{1+\cos 2\bar{x}}{2}\right)^2 d\bar{x}=\int\frac{1}{4}+\frac{\cos 2\bar{x}}{2}+\frac{1}{8}+\frac{\cos 4\bar{x}}{8}d\bar{x}\\&=\frac{3}{8}\bar{x}+\frac{\sin 2\bar{x}}{4}+\frac{\sin 4\bar{x}}{32}\end{aligned} \tag{6.16}$$

Upon substitution:

$$\begin{aligned}&P^*=\frac{\bar{x}}{2}+\frac{\sin 2\bar{x}}{4}-\frac{1}{\cos^2\bar{x}_a}\left(\frac{3}{8}\bar{x}+\frac{\sin 2\bar{x}}{4}+\frac{\sin 4\bar{x}}{32}\right)+C2\\&\textit{where}:\\&P^*=\frac{h_0{}^2}{\sqrt{2Rh_0}\,6U\eta_0}P\end{aligned} \tag{6.17}$$

The constant C_2 is dependent on the seal boundary conditions which change during actuation as shown in Figure 6.2.

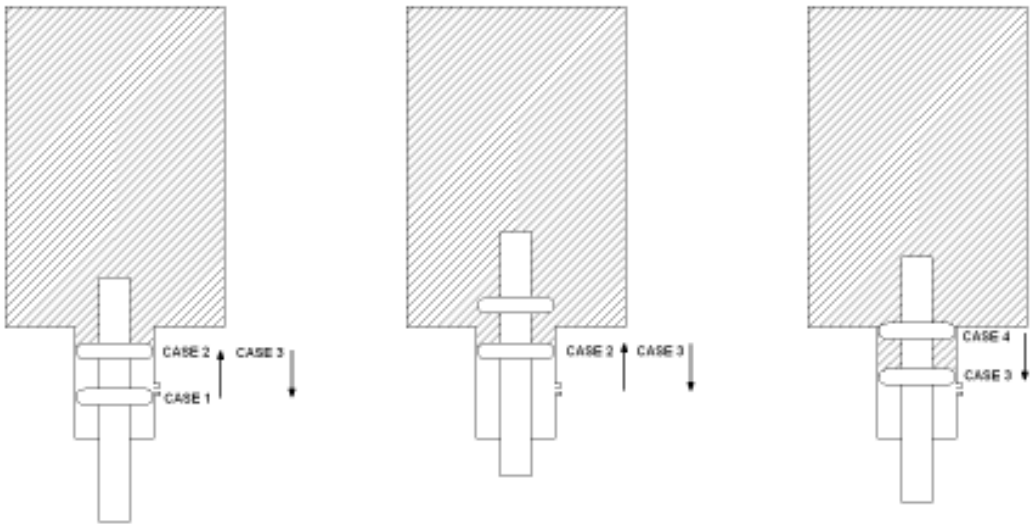

Figure 6.2: Seal boundary condition changes

Case 1: Zero pressure at both inlet and exit

$$P^* = 0 \quad where \quad \bar{x} = -\frac{\pi}{2} \text{ and } P^* = \frac{dP^*}{d\bar{x}} = 0 \quad at \bar{x} = \bar{x}_e$$

This is the usual Reynolds or Swift-Steiber outlet boundary condition, which specifies the point of film rupture.

Thus:

$$0 = \frac{\pi}{4} + \frac{\sin 2\left(-\frac{\pi}{2}\right)}{4} - \frac{1}{\cos^2 \bar{x}_a}\left(\frac{3\pi}{16} + \frac{\sin 2\left(-\frac{\pi}{2}\right)}{4} + \frac{\sin 4\left(-\frac{\pi}{2}\right)}{32}\right) + C2$$

Therefore: (6.18)

$$C2 = \frac{\pi}{4} - \sec^2 \bar{x}_a \left(\frac{3\pi}{16}\right)$$

And:

$$0 = \frac{\bar{x}_e}{2} + \frac{\pi}{4} + \frac{\sin 2\bar{x}_e}{4} - \sec^2\left(\bar{x}_e\right)\left(\frac{3\pi}{16} + \frac{3\bar{x}_e}{8} + \frac{\sin 2\bar{x}_e}{4} + \frac{\sin 4\bar{x}_e}{32}\right) \quad (6.19)$$

Then, finally the non-dimensional pressure is given by:

$$P^* = \frac{\bar{x}}{2} + \frac{\pi}{4} + \frac{\sin 2\bar{x}}{4} - \sec^2\left(\bar{x}_e\right)\left(\frac{3\pi}{16} + \frac{3\bar{x}}{8} + \frac{\sin 2\bar{x}}{4} + \frac{\sin 4\bar{x}}{32}\right) \tag{6.20}$$

Case 2: 0.55MPa at inlet and zero pressure at outlet

$$P = 0.55MPa \quad where \quad \bar{x} = -\frac{\pi}{2}$$

Therefore:

$$P^* = \frac{{h_0}^2}{\sqrt{2Rh_0}\,6U\eta_0}0.55MPa$$

Giving:

$$P^*_{0.55} = \frac{\pi}{4} + \frac{\sin 2\left(-\frac{\pi}{2}\right)}{4} - \frac{1}{\cos^2 \bar{x}_a}\left(\frac{3\pi}{16} + \frac{\sin 2\left(-\frac{\pi}{2}\right)}{4} + \frac{\sin 4\left(-\frac{\pi}{2}\right)}{32}\right) + C2$$

Therefore: (6.21)

$$C2 = P^*_{0.55} + \frac{\pi}{4} - \sec^2 \bar{x}_a\left(\frac{3\pi}{16}\right)$$

and:

$$0 = P^*_{0.55} + \frac{\bar{x}_e}{2} + \frac{\pi}{4} + \frac{\sin 2\bar{x}_e}{4} - \sec^2 \bar{x}_e\left(\frac{3\pi}{16} + \frac{3\bar{x}_e}{8} + \frac{\sin 2\bar{x}_e}{4} + \frac{\sin 4\bar{x}_e}{32}\right) \tag{6.22}$$

Finally, the non-dimensional pressure is given by:

$$0 = P^*_{0.55} + \frac{\bar{x}}{2} + \frac{\pi}{4} + \frac{\sin 2\bar{x}}{4} - \sec^2\left(\bar{x}_e\right)\left(\frac{3\pi}{16} + \frac{3\bar{x}}{8} + \frac{\sin 2\bar{x}}{4} + \frac{\sin 4\bar{x}}{32}\right) \tag{6.23}$$

Case 3: Zero pressure at the inlet and 0.55Mpa pressure at the outlet, the non-dimensional pressure is given by:

$$P^* = -P^*_{0.55} + \frac{\bar{x}}{2} + \frac{\pi}{4} + \frac{\sin 2\bar{x}}{4} - \sec^2\left(\bar{x}_e\right)\left(\frac{3\pi}{16} + \frac{3\bar{x}}{8} + \frac{\sin 2\bar{x}}{4} + \frac{\sin 4\bar{x}}{32}\right) \tag{6.24}$$

Case 4: 0.55Mpa at both inlet and outlet the non-dimensional pressure is given by:

$$P^* = \frac{\bar{x}}{2} + \frac{\pi}{4} + \frac{\sin 2\bar{x}}{4} - \sec^2\left(\bar{x}_e\right)\left(\frac{3\pi}{16} + \frac{3\bar{x}}{8} + \frac{\sin 2\bar{x}}{4} + \frac{\sin 4\bar{x}}{32}\right) \qquad (6.25)$$

For a converging-diverging wedge, such as that illustrated in Figure 6.3 the film across the contact is continuous, with no discontinuity in the gap between the bounding contiguous surfaces (Cameron, 1966).

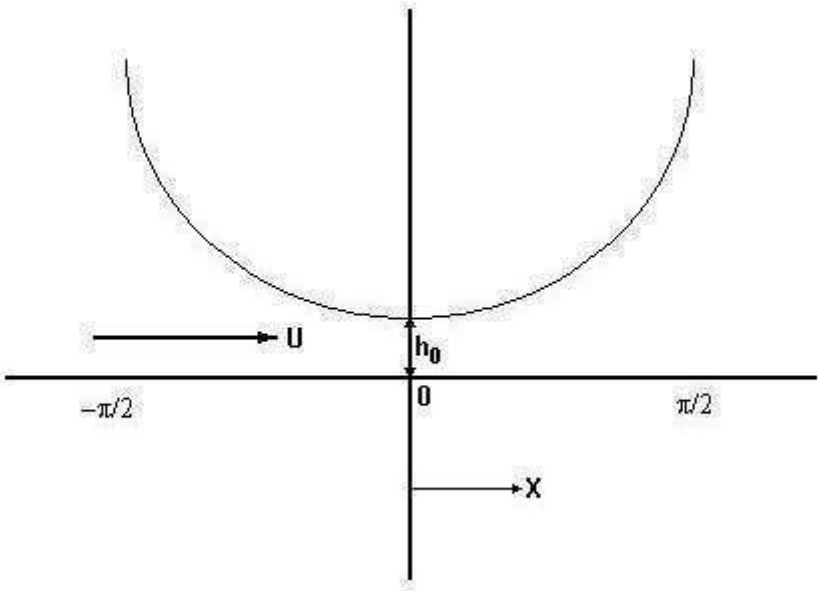

Figure 6.3: Contact region of a lubricated conjunction

The pressure across the contact can, therefore, be modelled using an equation with the inlet pressure being zero at -π/2 and the outlet pressure also being zero at π/2. The *x*-coordinate boundaries are shown in Figure 6.4. When the *x*-coordinate takes values ±R, the film thickness is infinitely large.

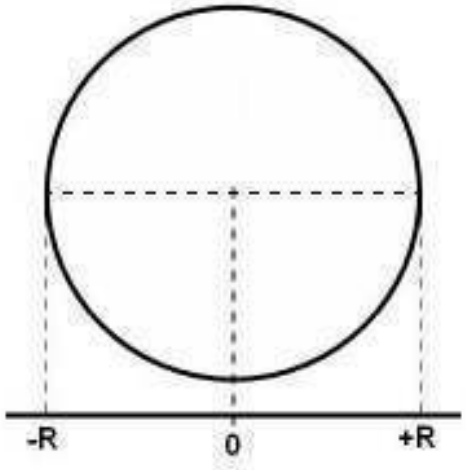

Figure 6.4: Contact extremities

However, the film thickness is being modelled by a parabola with the non-dimensional relationship shown in Equation (6.26) below:

$$Tan\bar{x} = \frac{x}{\sqrt{2Rh_0}} \tag{6.26}$$

As a result the film thickness can only approach infinity when the *x*-coordinate equals to ± ∞. Therefore, the non-dimensional *x*-coordinate must be equal to ± π/2 when the film thickness is infinity, and thus the pressure becomes zero. In reality the pressure reaches an extremely low value long before the *x*-coordinate is equal to ±R and, therefore, the practical difference of setting the pressure to zero at ±R or ±∞ is negligible according to Rubin and Durotoye (2004). The pressure being zero at ± ∞ is known as the Full Somerfield condition, with the resultant pressure distribution as shown in Figure 6.5.

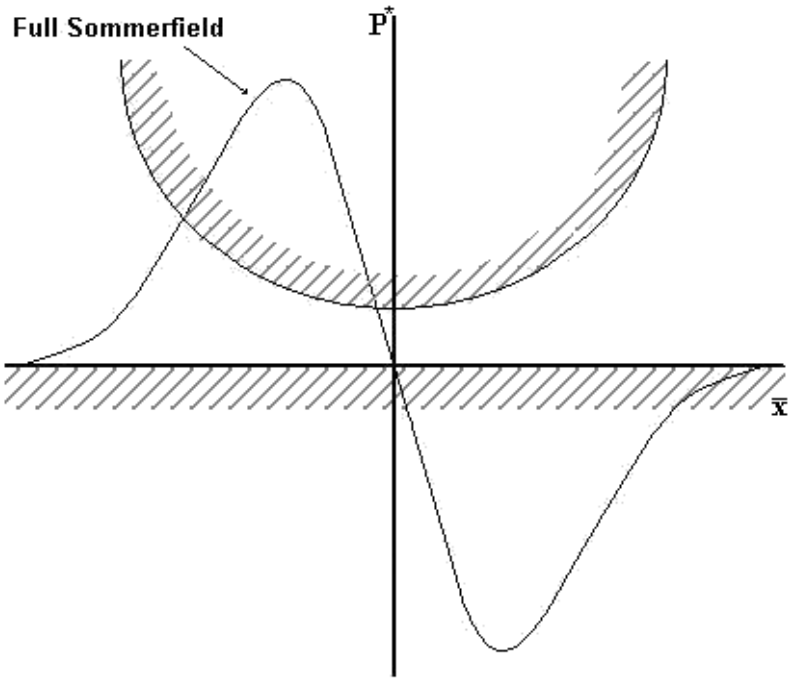

Figure 6.5: Full Sommerfeld condition

Whilst this condition allows for the continuity of flow across the contact, it becomes apparent that the net load carried by the lubricant is in fact zero, as any positive pressure is counterbalanced by the negative distribution. Therefore, the Half Somerfield condition is often utilised with the pressures within the contact beyond the zero point on the grid (the centre of the contact) set to zero. This creates a profile as that shown in Figure 6.6.

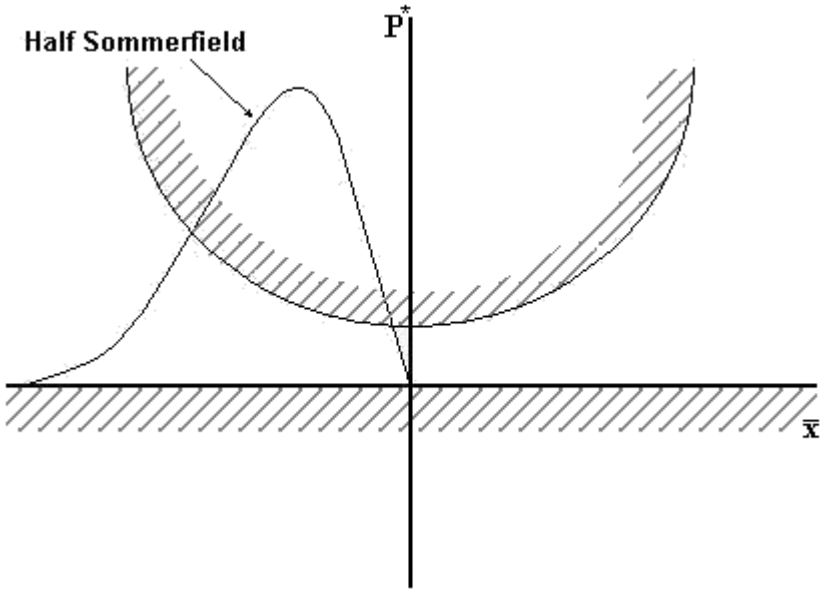

Figure 6.6: Half Sommerfeld condition

Whilst this solves the problem of the contact being mathematically unable to support any load, there is a resultant discontinuity of flow rate (see Cameron, 1966). Therefore, the most widely accepted case is that of Reynolds' or Swift-Steiber boundary condition. Under this condition, the point at which the pressures become negative (film rupture point) is determined based upon the inflow. This results in a profile as shown in Figure 6.7.

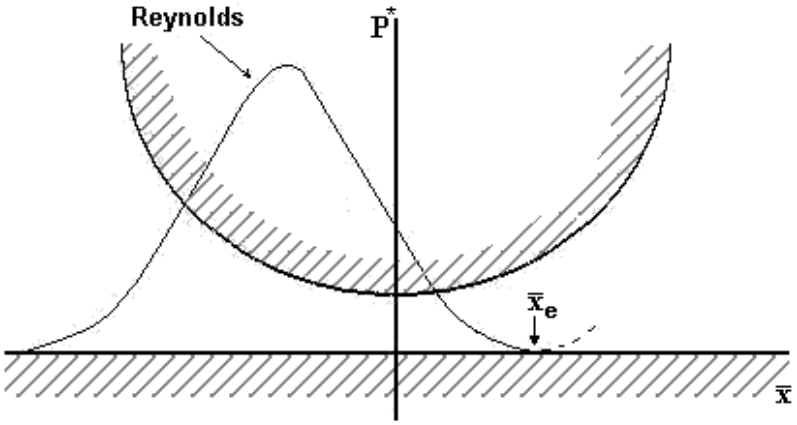

Figure 6.7: Reynolds condition

In this instance, the flow of lubricant is maintained across the contact, while a load is also able to be calculated to represent that supported by the film.

6.1.1 Domain approach

Although mathematically, as previously stated, there is very little difference in modelling the contact across the region of ±R (the radius of the seal) and ± π/2 (Cameron, 1966), the substitution of terms is simplified through adopting the contact domain of ± π/2. This approach was followed in order to establish the *x*-coordinate system utilised during the modelling procedure. The grid itself is non-uniform, in order to place more nodes within the contact region, which is obviously the area of most interest. Within this, a parabolic shape is used to represent the profile of the contacting seal.

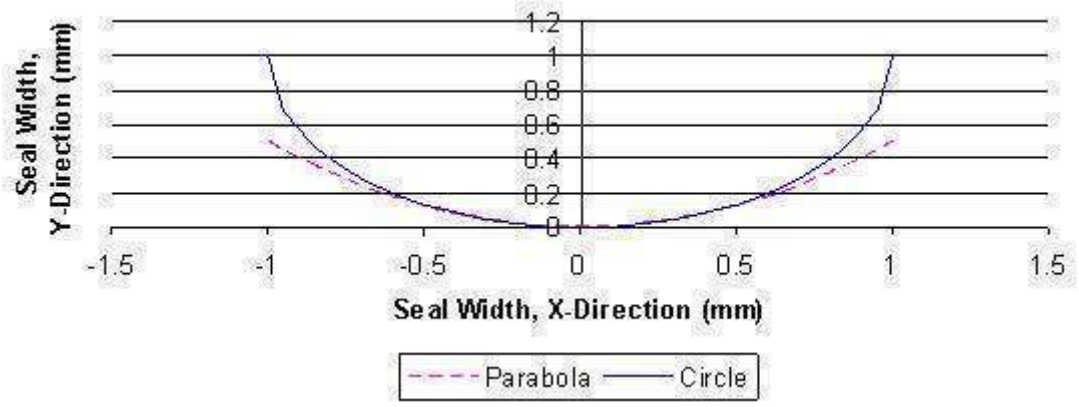

Figure 6.8: Parabola surface approximation verification

The resulting profile is shown in Figure 6.8. As it can be seen, the parabola represents a simple but sufficiently accurate representation for the contact domain.

6.1.2 Computational Procedure

The program algorithm functions as outlined in the flow charts of Figure 6.9 and 6.10. As it can be seen, the program is iterative and adjusts the minimum film thickness within the contact which supports the required contact load. At each instance that the minimum film is adjusted the resulting film/pressure profiles are calculated.

Once the computational grid is determined, using the non-dimensional equations and the $\pm\ \pi/2$ x-coordinates previously described, the film thickness profile can be established, based upon an initial guess for the minimum film thickness value. The rupture point of the Reynolds condition can then be ascertained using an iterative process. At the point where a substituted x-coordinate produces a negative pressure result, the exit boundary is found by interpolating between this point and the previous x-coordinate. Once the exit point is found, the pressure distribution can be solved using the equations for the non-dimensional pressure already outlined previously (Equations (6.19), (6.22), (6.23) and (6.24). The resulting load can then be calculated using a simple numerical integration of the pressure profile as:

$$W = \sum_{i=1}^{n} P\left(X_{i+1} - X_i\right) \tag{6.27}$$

If the calculated load is within a preset tolerance compared with the initially defined load, then the procedure is deemed to have converged:

$$W_{ERR} \leq \frac{|W_{Hertz} - W|}{W_{Hertz}} \tag{6.28}$$

Otherwise, the minimum film thickness is reduced based on the difference between the current load and the defined applied load. This process is referred to as relaxation. The process is then repeated. The correction in film thickness is given by:

$$H_m^n = H_m^{n-1} - \left(\alpha \frac{W_{Hertz} - W}{W_{Hertz}} \right) \tag{6.29}$$

where α is a preset damping factor to prevent numerical errors arising from severe changes in the minimum film thickness value.

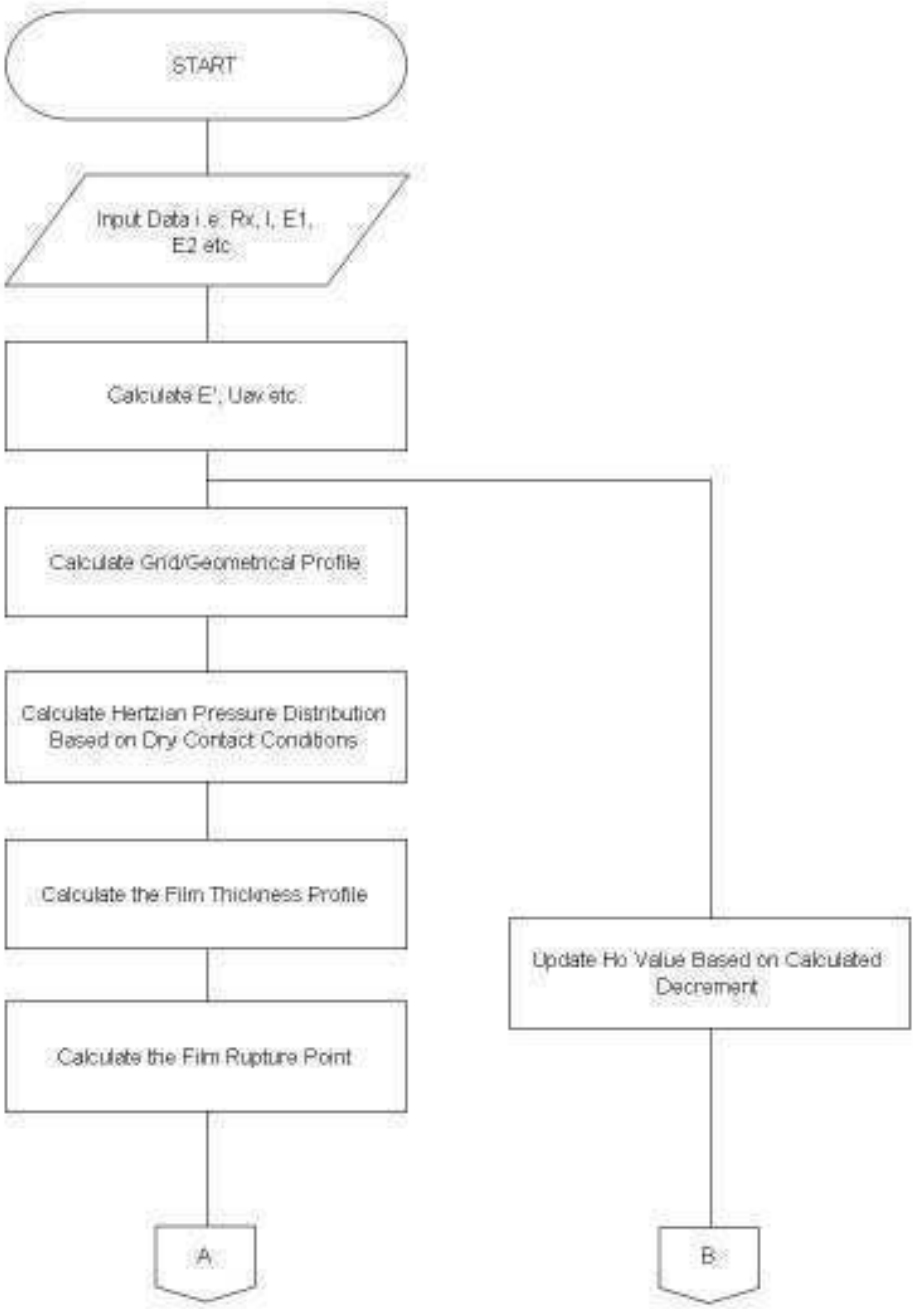

Figure 6.9: Solution flow chart part 1

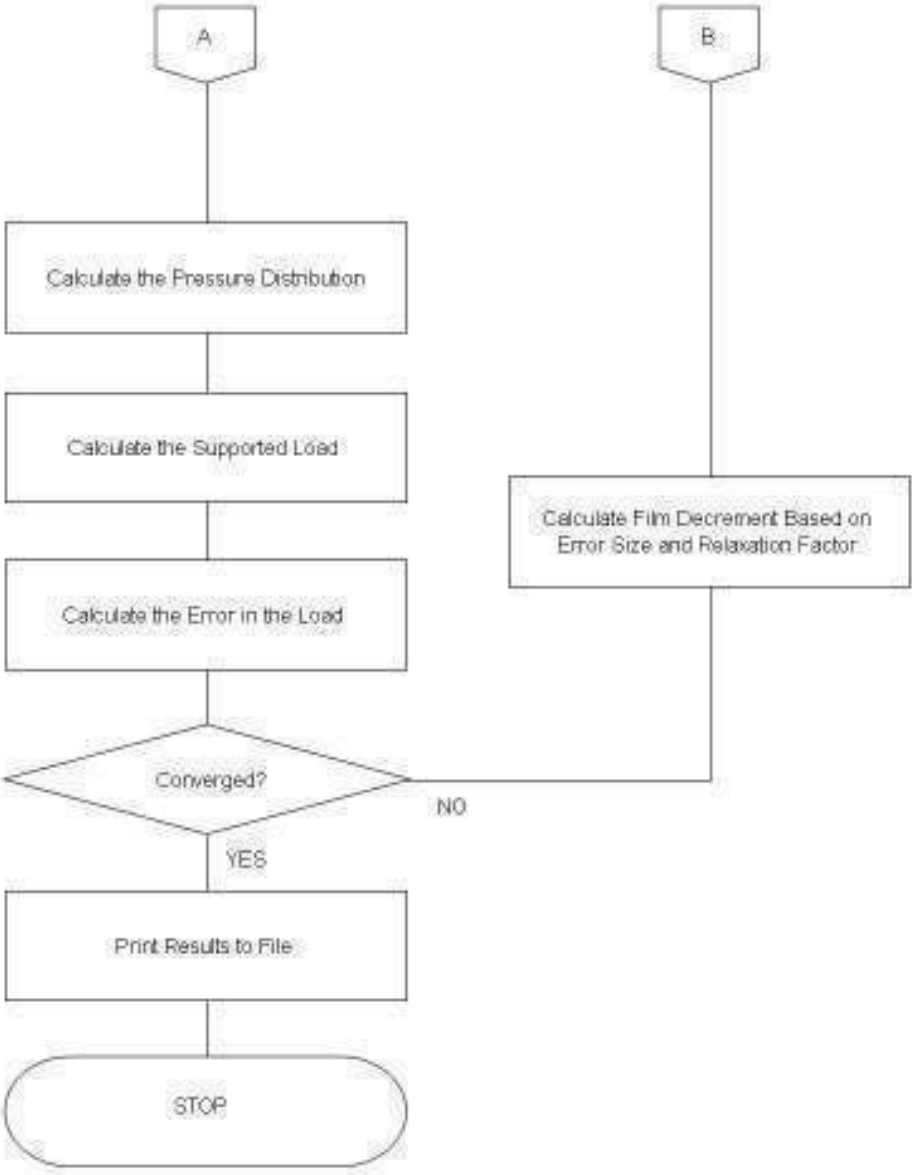

Figure 6.10: Solution flow chart part 2

6.1.3 Program Verification

In order to validate the procedure, it was proposed to test it against a case of known solution available in literature. The work of Economou (1976) was chosen, as due to the soft EHL nature of the inhaler contact, any attempted analysis of the housing/seal conjunction at this stage would fail to converge and, thus, comparison of results would be impossible. It is accepted that Economou's work was for a hard EHL case and so the result from the developed program would never represent an exact match at this stage, although the conforming nature of piston ring contact means that similar

low pressures would be expected. The program was, therefore, set using the parameters below from (Economou, 1976) for a steel piston ring contact:

R_x = Ring face radius = $2.540m$
Rw = Ring width=$0.00476m$
l = Ring length = $0.6379m$
$U_{av} = \left(\frac{U_1 + U_2}{2} \right) = 2.115ms^{-1}$
W = Ring load = $607.2808N$

As the current program is for iso-viscous conditions, an exact match to the literature results cannot be achieved. This can be seen in a comparison of test cases carried out by Hamrock (1994), shown in Figure 6.11.

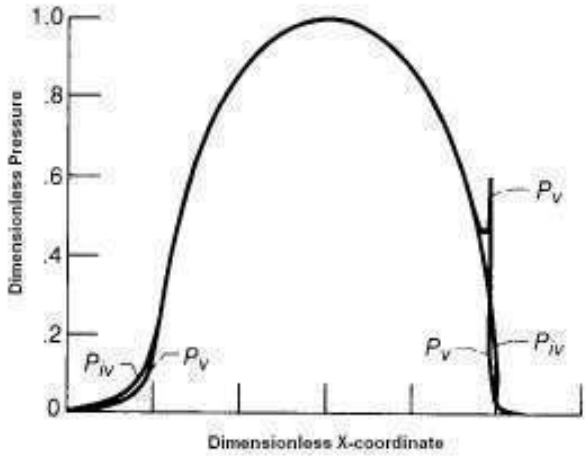

Figure 6.11: Effect of viscosity on a test case (after Hamrock 1994)

As it can be seen, without the viscosity changes the EHL spike does not occur. More importantly, it must be noted that the current method at this stage does not take into account the deflection within the contact. It is, therefore, only a hydrodynamic iso-viscous rigid result and so a certain level of inaccuracy would be expected.

The results of Economou show a film thickness of between 5.7 and 6.2 nm, as can be seen in Figure 6.12.

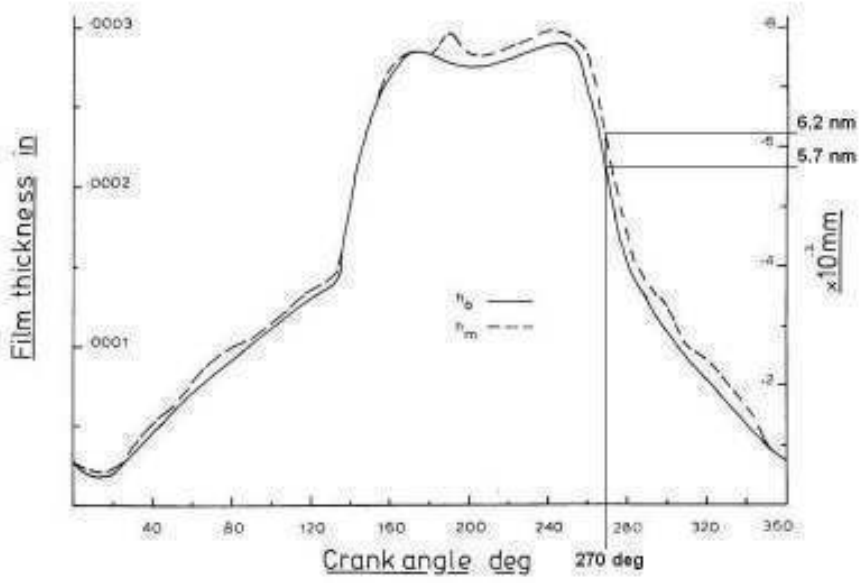

Figure 6.12: Film thickness in a piston ring conjunction (after Economou, 1976)

In comparison, the analytical approach described above calculates a film thickness of 3.87nm, which can be seen in Figure 6.13 under the same conditions.

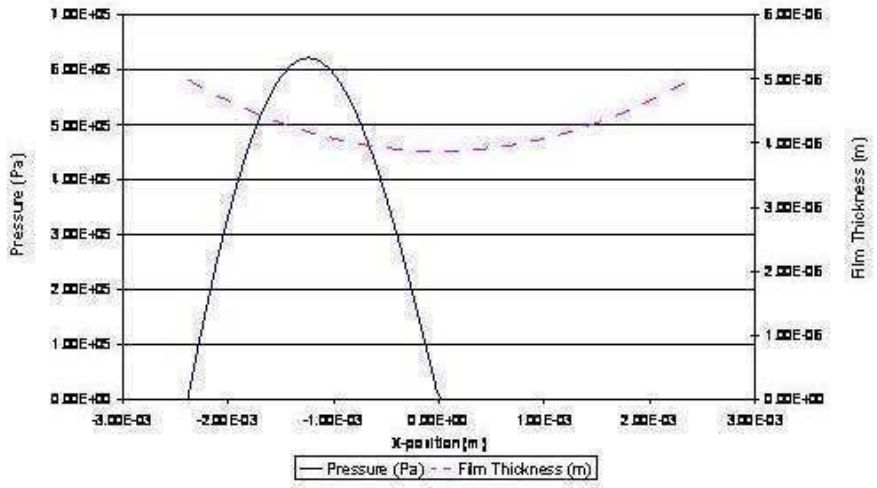

Figure 6.13: Results of analytical method using Economou's approach

This result is as expected, since without the piezo-viscous effect and contact deformation the resulting iso-viscous rigid film would have a lower load carrying capacity. Thus, at the same load the film thickness would be thinner. Following on from this comparison, it was decided that the program was functioning appropriately. However, before continuing on the modelling of the inhaler mechanism, the

deflection at contact must be taken into account, since without this feature, not only the model would be a poor representation of the soft elastohydrodynamic contact, but it also would demonstrate convergence problems. In order to do this, however, fundamental changes to the analytical method would be required due to the way the methodology was derived. As previously stated, a parabolic variation of the film thickness was assumed. This takes the form:

$$h = h_0 + \frac{x^2}{2R} \tag{6.30}$$

In order to account for the contact deflection:

$$h = h_0 + \frac{x^2}{2R} + \delta_x \tag{6.31}$$

Therefore, the derivation for the analytical approach would change. The difficulty incurred, however, is that the deflection term δ_x is a function of the generated pressures. Therefore, it can be noted that on substitution, the pressure becomes an integral function of itself. This creates a complex situation and constitutes that a simple analytical approach is no longer possible. Therefore, in order to progress, solution of Reynolds equation numerically would be necessary.

6.2 Numerical Reynolds Solution

Following on from the analytical approach it was deemed necessary that the pressure distribution across the contact should be obtained. This would allow the desired additional parameters such as adhesion to be incorporated into the program, since a detailed description of the contact domain would be available. In order to achieve this, Reynolds equation (6.1) should be discretised and solved numerically. For the steady state condition with no side leakage and squeeze effect:

$$\frac{\partial}{\partial x}\left(\frac{\rho h^3}{12\eta}\frac{\partial p}{\partial x}\right)=\frac{\partial}{\partial x}\left[\frac{\rho h\left(u_A+u_B\right)}{2}\right] \tag{6.32}$$

6.2.1 Contact geometry

The contact itself is regarded as an infinitely long bearing. Therefore, the contact profile is considered not to vary along its contact width and along the seal circumference, so that the problem becomes one dimensional (per unit length). Thus, the seal edge effect is also ignored. The resulting contact, therefore, can again be regarded as that shown in Figure 6.3, one of a roller of infinite length (seal width dimension) and of an equivalent radius against a flat elastic half-space.

6.2.2 Hertzian Contact load

The contact profile of the seal with the stem, however, is not parabolic as it is deformed due to its fitment into the seal groove. This contact is in fact conforming, but with the assumption of a single dimension made in the previous section (similar to that made by Karaszkiewicz, 1985, 1987 and 1990) a Hertzian contact assumption for line contact can be made for the seal-groove interface. The use of Hertzian theory implies the following assumptions:

- The radius of curvature of the contacting bodies is considerably larger than the contact footprint dimensions.
- The deformation of the contacting bodies is within the elastic limit
- The surfaces of the contacting bodies are smooth in order for the resulting reaction forces to be considered normal to the surfaces with no friction. Although the assumption of friction is relaxed for many Hertzian-type analyses.

- The profile of the undeformed bodies in contact can be represented by ellipsoidal solids of revolution.

Using the above assumptions and Hertzian theory, it is possible to calculate the contact conditions between the O-ring seal and the inhaler housing bore.

6.2.3 Hertzian Contact Parameters

By following the assumptions described above, the width of the component contact area can be established. If the two components in contact are subject to a given load, a flattened contact area according to Hertz is created due to localised elastic deformation.

This contact width for the seal is a function of the load applied, the mechanical properties of the contiguous solids and their principal radii in contact. Therefore, the Hertzian half-width is given as:

$$H_W = \text{b (In Reynolds Derivation)} = \sqrt{\frac{4WR_x}{\pi E' l}} \tag{6.33}$$

As a result of this, a pressure profile is formed over the area, referred to as the elastostatic Hertzian pressure distribution (Hertz, 1881):

$$P_x = P_h \sqrt{1 - \frac{x^2}{H_w^2}} \tag{6.34}$$

where P_h is the maximum Hertzian pressure for line contact geometry as:

$$P_h = \frac{2W}{\pi H_w l} \tag{6.35}$$

For contact of a parabola against a surface of infinite radius (a practically flat surface), this results in a pressure distribution of the form shown in Figure 6.14.

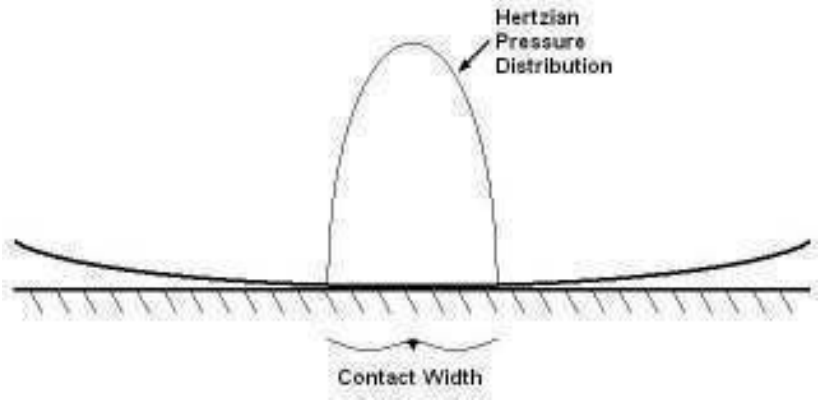

Figure 6.14: Hertzian pressure distribution

6.2.4 Computational grid setup

The computational grid can then be established based upon Hertz using the contact half-width as a means of discretising the contact domain. The inlet meniscus is considered to be N times the contact half-width away from the leading edge of the Hetzian contact, with N depending on the size of the contact conditions being examined. It must be ensured that a sufficient inlet is established as without it, a starved contact may result with increasing sliding speed, particularly under lightly loaded hydrodynamic or soft EHL conditions. Due to the rate at which the pressure drops once the divergent portion of the contact is reached, the outlet needs only to be a fraction of the inlet size, say M times larger than the Hertzian half-width, where N>>M. A typical computational grid is shown in Figure 6.15 below.

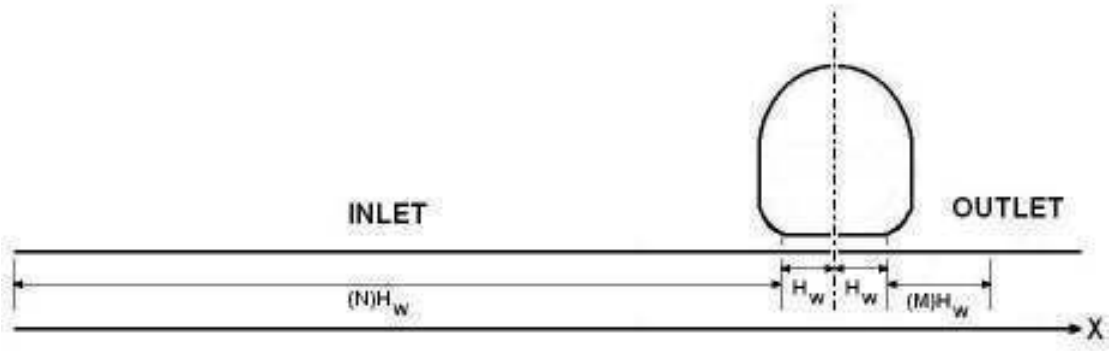

Figure 6.15: The computational domain

The inlet distance and the contact half-width are then used to determine the number of computational nodes within the program. For instance, allowing ten nodes within the

half-width, and knowing the inlet and outlet distances permits the total number of nodes to be calculated within the program. An additional difference to the numerical grid, in addition to the enlarged domain considered, is that the grid position is not zero at the centre of the contact. Instead, the zero x-coordinate is located at the far left location at the edge of the conjunction (lubricated domain) (see Figure 6.15).

6.2.5 Non-Uniform Grid Domain

In order to enhance computational accuracy, the previous uniform grid was further broken down into the Hertzian contact domain and the inlet and outlet regions. The area of contact is assigned a greater number of nodes, while also permitting the overall number of nodes to be reduced. For example, around 85 nodes can be assigned to each half-width within the Hertzian region. At the same time, just 55 nodes are utilised to the inlet and outlet regions as shown in Figure 6.15.

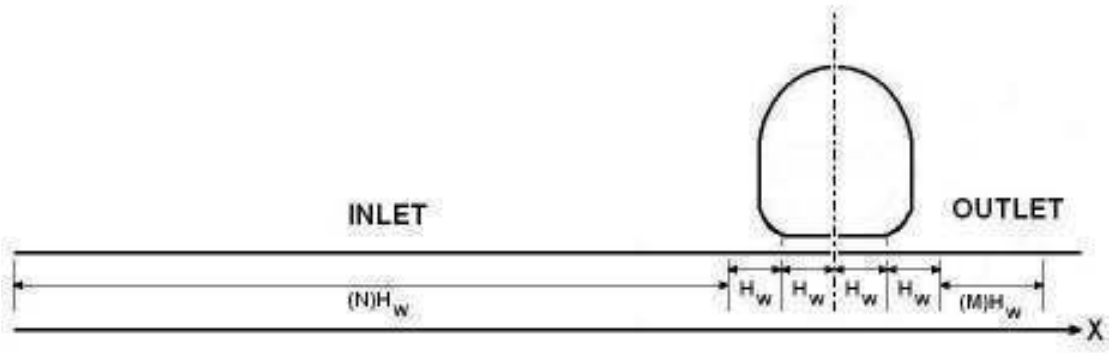

Figure 6.16: The modified non-uniform grid

Following further testing and investigation numerical stability still proved to be a problem. As such, the non-uniform grid concept was further expanded. The areas with the greatest pressure changes are those within the contact region and also at the edges of the contact region. It is the gradient of these changes that can cause the computational iterations to become unstable and prevent convergence. With this in mind, the number of nodes was increased not only for the Hertzian contact region, but also for the adjoining half-widths as shown in Figure 6.16. Once again, this allowed a higher number of nodes within and around the contact region where the greatest pressure changes occur, but with a reduced overall grid size to aid computational efficiency and reduce demand on system memory.

6.3 The Numerical Reynolds Equation

As with the previously described analytical approach (see section 6.2), the numerical approach commences with use of Reynolds equation for an incompressible fluid in all directions as shown in Equation (6.1).

This is simplified for the line contact conjunction under steady-state condition and with no side leakage to:

$$\frac{\partial}{\partial x}\left(\frac{\rho h^3}{12\eta}\frac{\partial p}{\partial x}\right)=\frac{\partial}{\partial x}\left[\frac{\rho h\left(u_A+u_B\right)}{2}\right]$$

where $u_{av}=\dfrac{u_A+u_B}{2}$. Therefore:

$$\frac{\partial}{\partial x}\left(\frac{\rho h^3}{\eta}\frac{\partial p}{\partial x}\right)=12\left\{\frac{\partial\left(\rho h u_{av}\right)}{\partial x}\right\} \tag{6.36}$$

Assuming $u_{av}=constant,$ then the Reynolds equation becomes:

$$\frac{\partial}{\partial x}\left(\frac{\rho h^3}{\eta}\frac{\partial p}{\partial x}\right)=12u_{av}\left\{\frac{\partial\left(\rho h\right)}{\partial x}\right\} \tag{6.37}$$

The Reynolds equation can then be non-dimensionalised for ease of computation using the following non-dimensional groupings:

$$\begin{cases} X=x/b \\ \overline{\rho}=\rho/\rho_0 \\ \overline{\eta}=\eta/\eta_0 \\ H=hR_x/b^2 \\ U^*=\left(u_{av}\eta_0\right)/\left(R_xE'\right) \\ P=p/P_h \\ W^*=W/\left(E'R_xl\right) \end{cases} \rightarrow \begin{cases} x=bX \\ \rho=\rho_0\overline{\rho} \\ \eta=\eta_0\overline{\eta} \\ h=Hb^2/R_x \\ u_{av}=U^*R_xE'/\eta_0 \\ p=P_hP \\ W=W^*E'R_xl \end{cases} \rightarrow \begin{cases} dx=bdX \\ d\rho=\rho_0 d\overline{\rho} \\ d\eta=\eta_0 d\overline{\eta} \\ dh=\left(b^2/R_x\right)dH \\ du_{av}=\left(R_xE'/\eta_0\right)dU^* \\ dp=P_hdP \end{cases} \tag{6.38}$$

Upon substitution of the above, the Reynolds equation becomes:

$$\frac{d}{bdX}\left(\frac{\rho_0\bar{\rho}(Hb^2/R_x)^3}{\eta_0\bar{\eta}}\frac{P_h dP}{bdX}\right)=12u_{av}\left\{\frac{d\left(\rho_0\bar{\rho}(Hb^2/R_x)\right)}{bdX}\right\} \tag{6.39}$$

Expanding $(Hb^2/R_x)^3$ terms leads to:

$$\frac{d}{bdX}\left(\frac{\rho_0\bar{\rho}H^3b^6}{\eta_0\bar{\eta}R_x^{\ 3}}\frac{P_h dP}{bdX}\right)=12\frac{U^*R_xE'}{\eta_0}\left\{\frac{d\left(\rho_0\bar{\rho}Hb^2\right)}{bR_xdX}\right\} \tag{6.40}$$

Taking constant terms out of differentials gives:

$$\frac{\rho_0b^6P_h}{b^2R_x^{\ 3}\eta_0}\frac{d}{dX}\left(\frac{\bar{\rho}H^3}{\bar{\eta}}\frac{dP}{dX}\right)=12\frac{U^*R_xE'\rho_0b^2}{\eta_0bR_x}\left\{\frac{d\left(\bar{\rho}H\right)}{dX}\right\} \tag{6.41}$$

Cancelling ρ_0 and η_0, and simplifying the remaining terms gives:

$$\frac{b^4P_h}{R_x^{\ 3}}\frac{d}{dX}\left(\frac{\bar{\rho}H^3}{\bar{\eta}}\frac{dP}{dX}\right)=12U^*E'b\left\{\frac{d\left(\bar{\rho}H\right)}{dX}\right\} \tag{6.42}$$

Multiplying both sides by $\frac{R_x^{\ 3}}{b^4P_h}$ yields:

$$\frac{d}{dX}\left(\frac{\bar{\rho}H^3}{\bar{\eta}}\frac{dP}{dX}\right)=\frac{12U^*E'R_x^{\ 3}}{b^3P_h}\left\{\frac{d\left(\bar{\rho}H\right)}{dX}\right\} \tag{6.43}$$

Or, with u_{av} on the right side of the equation:

$$\frac{d}{dX}\left(\frac{\bar{\rho}H^3}{\bar{\eta}}\frac{dP}{dX}\right)=\frac{12u_{av}\eta_0R_x^{\ 2}}{b^3P_h}\left\{\frac{d\left(\bar{\rho}H\right)}{dX}\right\} \tag{6.44}$$

Before discretisation and solution of Reynolds equation, the elastic film shape (i.e. film thickness at any point in the contact, H) must be obtained. This is due to any initial gap due to conformability of the seal to the canister wall, global deformation of the seal in fitment and localised deformation due to generated hydrodynamic pressures. Therefore, calculations of global and local deformation of the seal are very important to evaluate the film thickness (H) required for the solution of Reynolds equation.

6.3.1 The Deflection of the Contact

The deflection within the contact is of extreme importance, especially in the case of a soft elastohydrodynamic contact like that within the inhaler seals' conjunctions. In the case of soft EHL, the elastic deformation is large, even with relatively light loads. This limits the pressure within the contact to typically within the order of MPa, as opposed to GPa for hard EHL (Hamrock, 1994). These relatively low pressures generally have a negligible effect on the viscosity of the lubricant. However, the lubricant film thickness is more dependent on the contact load than in hard EHL contacts (Hamrock, 1994) (this is shown in the current analysis by the derived extrapolated oil film thickness equation in Chapter 7). The pressures are also considered to be quite low to have any significant effect on the fluid density.

As shown in Figure 6.17, the deflection of a parabola has a dramatic increase on the contact geometry of the seal.

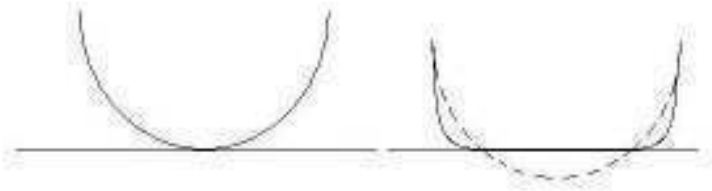

Figure 6.17: Deflection illustration

This has a significant effect upon friction due to an increased contact area in conformance of surfaces. Hence, it is important to take into account this deflection. It was decided that the column approach would provide a simple starting point for the deflection calculation, using a Hertzian contact width and pressure distribution

approximation. The equation for the column method deflection is given below: (Rahnejat, 2000)

$$\delta_x = \frac{(1-2\nu)(1+\nu)d}{E(1-\nu)}P \tag{6.45}$$

It is important to note that this approach is not ideal and it was only hoped to provide a rough approximation. An explanation for this is shown in Figure 6.18.

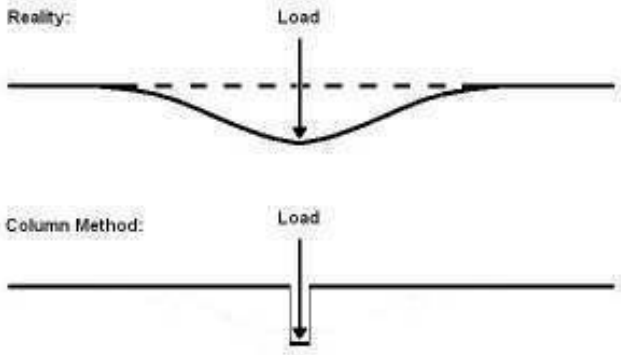

Figure 6.18: Column method deflection compared to reality

Due to the simplicity of the approach, the deflection caused at a point by a given load is assumed not have any effect on neighbouring points. As is shown in Figure 6.18, a point on the surface of the material only reacts to a normal load acting directly upon it, effectively meaning that each discretised point becomes its own 'column' of material unrelated to those around it. This means that any stress/strain induced within a column due to a given load does not influence the remainder of the material. Each column is therefore unsupported by its neighbouring columns and so deflection is over estimated in the case of an elastomeric material. Therefore, the result is not very representative of a true soft EHL contact. Despite the approach initially being felt sufficient to provide an approximate solution and to be a suitable starting point for modelling the deflection of the contact the results were extremely poor. As such, it was quickly dropped and an alternative approach sought.

6.3.2 Hamrock Deflection Approach

The deflection within the contact caused by the lubricant entrainment was initially determined using (Hamrock, 1994). However, within this thesis, the basic approach with regard to rectangular conjunctions is outlined.

For two surfaces of different materials, the elastic deformation at any point *x* on the surface is given as:

$$\delta = -\frac{2}{\pi E'}\int_{x_{\min}}^{x_{end}} p \ln\left(x - x'\right)^2 dx' \tag{6.46}$$

where *p* is the pressure as a function of x, in the range x_{min} to x_{end} and E' is the reduced elastic modulus of the contact. Using the following substitutions:

$$\begin{aligned} x &= bX & \frac{1}{R_x} &= \frac{1}{r_{ax}} + \frac{1}{r_{bx}} \\ x' &= bX' & & \\ p &= p_H P & \frac{R_x}{D_x} &= \frac{1}{4}\left(\frac{\pi}{2W^*}\right)^{1/2} \\ \delta &= \frac{b^2\bar{\delta}}{R_x} & W^* &= \frac{w}{E' R_x} \end{aligned} \tag{6.47}$$

where p_H is the maximum Hertzian pressure. Substitution into Equation (6.46) gives:

$$\bar{\delta} = -\frac{1}{2\pi}\left[\int_{X_{\min}}^{X_{end}} P \ln\left(X - X'\right)^2 dX' + \ln\left(R_x^2 \frac{8W^*}{\pi}\right)\int_{X_{\min}}^{X_{end}} P dX'\right] \tag{6.48}$$

Since the normal load per unit width can be found by integrating the pressure from inlet to outlet, it can be shown that:

$$\begin{aligned} & w = \int p dx \\ & \therefore \\ & \int P dX' = \frac{\pi}{2} \end{aligned} \tag{6.49}$$

Substitution of which into Equation (6.49) gives:

$$\overline{\delta} = -\frac{1}{2\pi}\left[\int_{X_{\min}}^{X_{end}} P \ln\left(X - X'\right)^2 dX' + \frac{1}{4}\ln\left(R_x^2 \frac{8W^*}{\pi}\right)\right] \tag{6.50}$$

The constant term on the right hand side of Equation (6.50) represents up to 90% of the total deformation within the contact. While, integrating by parts the overall equation gives:

$$\overline{\delta} = -\frac{1}{2\pi}\left|PI\right|_{X_{\min}}^{X_{end}} + \frac{1}{2\pi}\int_{X_{\min}}^{X_{end}} \frac{dP}{dX'} I dX' - \frac{1}{4}\ln\left(R_x^2 \frac{8W^*}{\pi}\right)$$

where (6.51)

$$I = \int \left(X - X'\right)^2 dX' = -\left(X - X'\right)\left[\ln\left(X - X'\right)^2 - 2\right]$$

Taking the pressure at both X_{min} and X_{end} to be zero, this can be reduced to:

$$\overline{\delta} = -\frac{1}{2\pi}\int_{X_{\min}}^{X_{end}} \frac{dP}{dX'}\left(X - X'\right)\left[\ln\left(X - X'\right)^2 - 2\right] dX' - \frac{1}{4}\ln\left(R_x^2 \frac{8W^*}{\pi}\right) \tag{6.52}$$

Finally, taking the region $[X_{j-1}, X_{j+1}]$ to be described by a polynomial fit, an analytical solution is possible such that:

$$\overline{\delta_i} = \sum_{j=1}^{N} D_{i,j} P_j - \frac{1}{4}\ln\left(R^2 \frac{8W^*}{\pi}\right) \tag{6.53}$$

The resulting dimensionless deflection $\overline{\delta}_i$ at node I is, therefore, a function of the dimensionless pressure P_j and influence coefficients D_{ij}, the calculation of which will now be explained.

6.3.3 Influence Coefficients

The interval [X_{min} , X_{end}] can be divided into small intervals [X_{j-1} , X_{j+1}] so that the deformation $\delta_{i,j}$ at a node i is the sum of all the elementary deformations $d\bar{\delta}_{i,j}$ calculated at node I and due to the pressure in the interval [X_{j-1} , X_{j+1}].

$$\bar{\delta}_{i,j} = \sum_{j=2,4,....}^{N} d\delta_{i,j} \tag{6.54}$$

An illustration of this principle is shown in Figure 6.19.

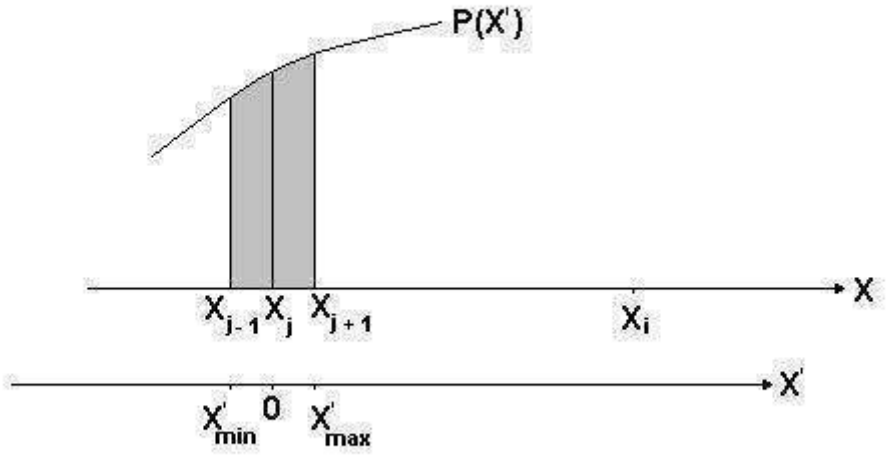

Figure 6.19: Discretisation principle

Assuming dP/dX' to vary linearly within these small intervals, the following linear expression is obtained:

$$\frac{dP}{dX'} = (a_1 X' + a_2)P_{j-1} + (a_3 X' + a_4)P_j + (a_5 X' + a_6)P_{j+1}$$

Where:

$$a_1 = \frac{2}{d_1}$$

$$a_2 = -\frac{(X_j + X_{j+1})}{d_1} + a_1 X_j$$

$$a_3 = \frac{2}{d_2}$$

$$a_4 = -\frac{(X_{j+1} + X_{j-1})}{d_2} + a_3 X_j$$

$$a_5 = \frac{2}{d_3}$$

$$a_6 = -\frac{(X_j + X_{j-1})}{d_3} + a_5 X_j$$

$$d_1 = (X_{j-1} - X_{j-1})(X_{j-1} - X_{j+1})$$

$$d_2 = (X_j - X_{j-1})(X_j - X_{j+1})$$

$$d_3 = (X_{j+1} - X_{j-1})(X_{j+1} - X_j) \qquad (6.55)$$

Therefore:

$$d\bar{\delta}_{i,j} = -\frac{1}{2\pi} \int_{Xj-1 \to X_j}^{Xj+1 \to X_j} \frac{dP}{dX'} \left(X_i - X_j - X'\right) \left[\ln\left(X_i - X_j - X'\right)^2 - 2 \right] dX' + \text{Constant} \qquad (6.56)$$

It can be seen that:

$$d\bar{\delta}_{i,j} = dD_{i,j-1} P_{j-1} + dD_{i,j} P_j + dD_{i,j+1} P_{j+1} + \text{Constant} \qquad (6.57)$$

where $dD_{i,j}$ are the elementary influence coefficients calculated as:

$$dD_{i,j-1} = -\frac{1}{2\pi} \int_{X_{j+1} - X_j}^{X_{j+1} - X_j} (a_1 X' + a_2)(X_i - X_j - X') \times \left[\ln(X_i - X_j - X')^2 - 2 \right] dX' \qquad (6.58)$$

Adopting a change of variables to:

$$
\begin{aligned}
&Z = (X_i - X_j - X') \\
&Z_{\min} = X_i - X_{j-1} \\
&Z_{\max} = X_i - X_{j+1} \\
&b_2 = a_1(X_i - X_j) + a_2 \\
&dZ = dX'
\end{aligned}
\tag{6.59}
$$

which gives:

$$
dD_{i,j-1} = -\frac{1}{2\pi}\int_{Z_{\min}}^{Z_{\max}} -(a_1 Z + b_2) Z (\ln\ Z^2 - 2)\, dZ \tag{6.60}
$$

Using the imposed variable of M, N and K it gives the following:

$$
\begin{aligned}
dD_{i,j-1} &= -\frac{1}{2\pi}(a_1 K + a_2 \frac{M}{2}) \\
dD_{i,j} &= -\frac{1}{2\pi}(a_3 K + a_4 \frac{M}{2}) \\
dD_{i,j+1} &= -\frac{1}{2\pi}(a_5 K + a_6 \frac{M}{2})
\end{aligned}
\tag{6.61}
$$

where:

$$
\begin{aligned}
&M = Z_{\min}^2(\ln Z_{\min}^2 - 3) - Z_{\max}^2(\ln Z_{\max}^2 - 3) \\
&N = Z_{\max}^3(\ln\left|Z_{\max}\right|^3 - 4) - Z_{\min}^3(\ln\left|Z_{\min}\right|^3 - 4) \\
&K = M\frac{X_i - X_j}{2} + \frac{2N}{9}
\end{aligned}
\tag{6.62}
$$

The final deflection is obtained as:

$$\bar{\delta}_i = \sum_{j=2,4,\ldots}^{N-1} d\bar{\delta}_{i,j}$$
$$\bar{\delta}_i = \sum_{j=1}^{N} D_{i,j} P_j - \frac{1}{4}\ln\left(R^2 \frac{8W^*}{\pi}\right) \tag{6.63}$$

So, for an even node:

$$D_{i,j} = dD_{i,j} \tag{6.64}$$

However, if j is odd, the influence coefficient term is given by:

$$D_{i,j} = dD_{i,j-1} + dD_{i,j+1} \tag{6.65}$$

The resulting influence coefficient matrix is shown in Figure 6.20. As it can be seen, the greatest influence is when $i = j$, as it would be expected, with reducing amounts of deflection when i ≠ j.

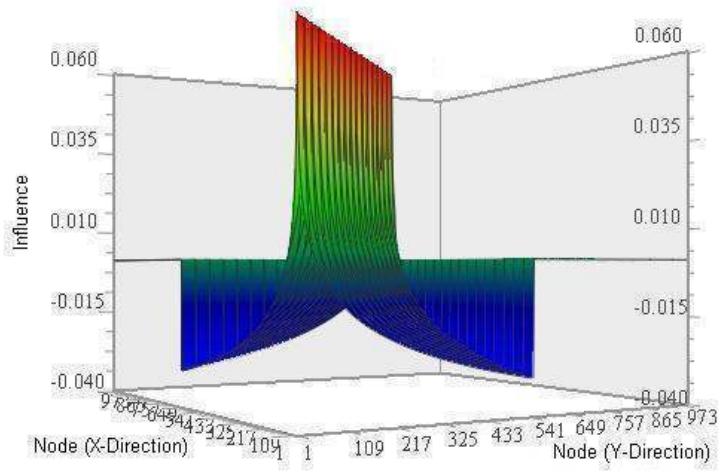

Figure 6.20: Influence plot

This means that the deflection at node i is mostly influenced by the pressure acting at node j when j = i. Likewise, as shown in the plot above, the influence on node i by j = i ± 1 is slightly less than when j = i but more than when j = i ± 2. This trend continues for the entire array.

An alternative suggestion is that of Teodorescu and Bryzik (2003) in which, $D_{i,j}$ are allowed to be directly calculated for each node. This aids the program speed and numerical stability.

$$\bar{\delta}_i = \sum_{j=1}^{N} D_{i,j} P_j - \frac{1}{4} \ln\left(R^2 \frac{8W^*}{\pi} \right) \tag{6.66}$$

However, the resulting deflection magnitude marginally exceeds that predicted by the Hertzian theory. A comparison of the deflection methods is shown in Figure 6.21 below for a steel on steel, mineral oil filled conjuncture (See Table 6.1):

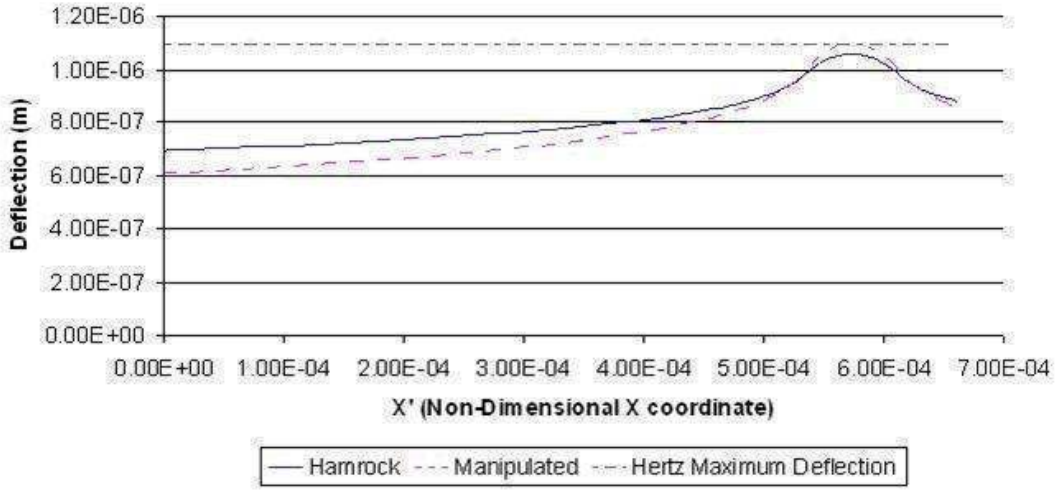

Figure 6.21: Deflection approach comparison

Parameter	Value (1)
Modulus of Elasticity	211 Gpa
Poisson's Ratio	0.3
Ambient Viscosity	0.0411 Pa.S
Contact Load	2256 N

(1) Arbitrary values for a steel on steel contact with mineral oil

Table 6.1: Parameters for initial deflection trials

This discrepancy would become more pronounced with an elastomer material. Therefore, this method was abandoned as, although it improved program stability, the resulting profile for a given Hertzian pressure distribution gave a resultant geometry profile which overestimated the deflection in the central region and therefore resulted

in an erroneous film profile. As such, the traditional Hamrock method was employed as a starting point for determining the local deflection within the contact.

6.3.4 Diametral Loading Approach

The Concept behind Hamrock's approach using the elasticity integral (referred to as the potential equation) was further expanded to allow for the opposing contact's influence coefficients, caused by the opposite side of the seal cross-section. This loaded pair of contacts were initially taken as reacting directly on the vertical axis of the seal as illustrated in Figure 6.22.

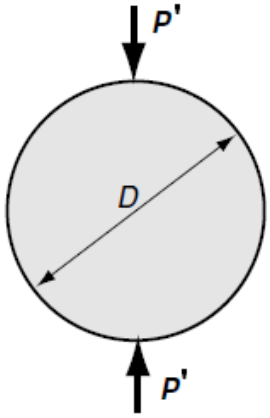

Figure 6.22: Diametral loading pair

In this instance, the extra contact load caused by the force on the opposite side of the seal is taken into account, with the load being assumed to be applied over a small width in relation to that of the cross-sectional diameter, D (Figure 6.22). The stress at any point must then be calculated. In order to do this, the Flamant solution (Flamant 1892, and Sadd, 2005), as utilised by Hamrock (Hamrock, 1994) for a load acting on a point on a semi-infinite elastic half-space (see Figure 6.23) is applied.

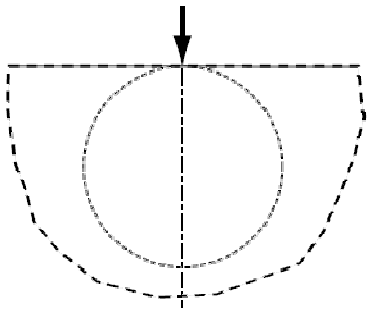

Figure 6.23: Flamant contact solution

The principle of superposition is then utilised to form the rest of the solution. This involves the superposition of two Flamant solutions, and also an induced uniform

radial tension necessary to remove the boundary traction caused by the point loads acting on the imaginary disk within the half space (Sadd, 2005).

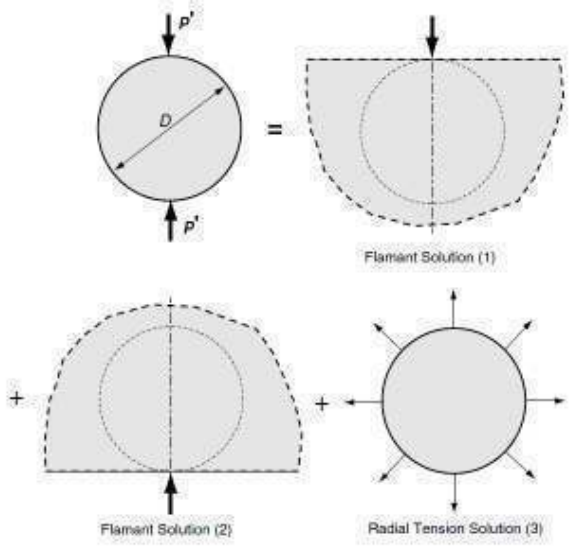

Figure 6.24: Principal of superposition

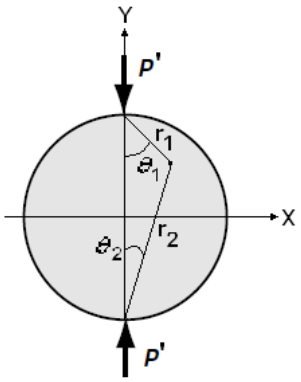

Figure 6.25: Stress field representation

Observing both Figure 6.24 and Figure 6.25, the stress components for the two Flamant solutions are:

$$\sigma_x^{(1)} = -\frac{2P'}{\pi r_1}\cos\theta_1 \sin^2\theta_1 \quad \sigma_x^{(2)} = -\frac{2P'}{\pi r_2}\cos\theta_2 \sin^2\theta_2$$

$$\sigma_y^{(1)} = -\frac{2P'}{\pi r_1}\cos^3\theta_1 \qquad \sigma_y^{(2)} = -\frac{2P'}{\pi r_2}\cos^3\theta_2 \tag{6.67}$$

$$\tau_{xy}^{(1)} = -\frac{2P'}{\pi r_1}\cos^2\theta_1 \sin\theta_1 \quad \tau_{xy}^{(2)} = -\frac{2P'}{\pi r_2}\cos^2\theta_2 \sin\theta_2$$

Each Flamant solution produces a constant radial stress on the circular boundary (periphery) of the disk. In order to match the desired problem the boundary forces must be removed by the addition of a uniform radial load, defined as:

$$\begin{aligned} T_n &= -\sqrt{\left(\sigma_r^{(1)}\cos\theta_1\right)^2 + \left(\sigma_r^{(2)}\sin\theta_1\right)^2} \\ &= -\sqrt{\left(-\frac{2P'}{\pi D}\cos\theta_1\right)^2 + \left(-\frac{2P'}{\pi D}\sin\theta_1\right)^2} \\ &= -\frac{2P'}{\pi D} = \sigma_x^{(3)} = \sigma_y^{(3)} \end{aligned} \tag{6.68}$$

Applying the theory of superposition for states 1, 2 and 3 (Figure 6.24) gives:

$$\begin{aligned} \sigma_x &= -\frac{2P'}{\pi}\left[\frac{(R-y)x^2}{r_1^4} + \frac{(R+y)x^2}{r_2^4} - \frac{1}{D}\right] \\ \sigma_y &= -\frac{2P'}{\pi}\left[\frac{(R-y)^3}{r_1^4} + \frac{(R+y)^3}{r_2^4} - \frac{1}{D}\right] \\ \tau_{xy} &= -\frac{2P'}{\pi}\left[\frac{(R-y)^2 x}{r_1^4} + \frac{(R+y)^2 x}{r_2^4}\right] \end{aligned} \tag{6.69}$$

where $r_{1,2} = \sqrt{x^2 + (R \mp y)^2}$

This solution gives the stress pattern for that of a concentrated point load on the boundary. However, the reality of the problem in the case of an O-ring is that of a distributed load where by, observing Figure 6.26:

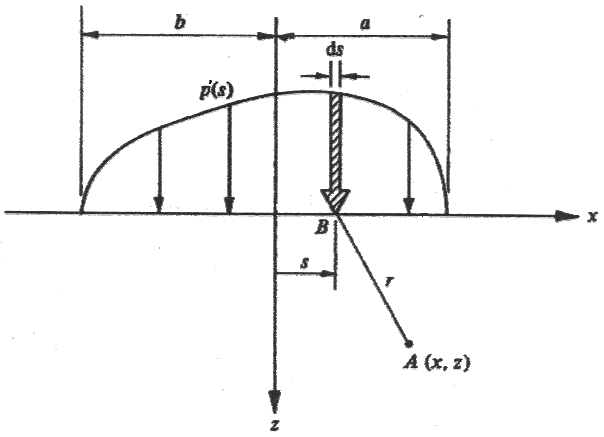

Figure 6.26: Load distribution

For a distributed load, the displacements are determined in the same manner as for a point load, but carrying the principle of superposition to perform the integration of the pressure distribution acting on an elastic surface (Johnson, 2005). Figure 6.26 shows a distributed load, P'(s), acting over a contact of width (–b<x<a). The stress components at any point A are desired. This is achieved by taking, for example, the normal pressure acting on the surface at B over an elemental width ds at a distance s from the origin. This can, therefore, be regarded as a concentrated force of magnitude P'×ds acting normal to the surface at a distance s from the origin. The equations for stress at a given point (such as A) therefore become (Johnson, 2005):

$$\sigma_x^{(1)} = -\frac{2z}{\pi}\int_{-b}^{a}\frac{p'(s)(x-s)^2\,ds}{\left\{(x-s)^2+z^2\right\}^2}$$

$$\sigma_y^{(1)} = -\frac{2z^3}{\pi_1}\int_{-b}^{a}\frac{p'(s)ds}{\left\{(x-s)^2+z^2\right\}^2} \qquad (6.70)$$

$$\tau_{xy}^{(1)} = -\frac{2z^2}{\pi}\int_{-b}^{a}\frac{p'(s)(x-s)ds}{\left\{(x-s)^2+z^2\right\}^2}$$

Once again, the summation of the displacements caused by each of the concentrated forces results in the final deformation of the surface. However, one drawback of this

approach is that, while a distributed load is modelled, it is still assumed that the contact width is much smaller than that of the radius of the cross-section (Johnson, 2005). This presents a problem as no account is taken of the load being applied along the curvature of the surface, as any error is small in the case of (-b<x<a)<<R. However, when of comparable size the result is that of Figure 6.27:

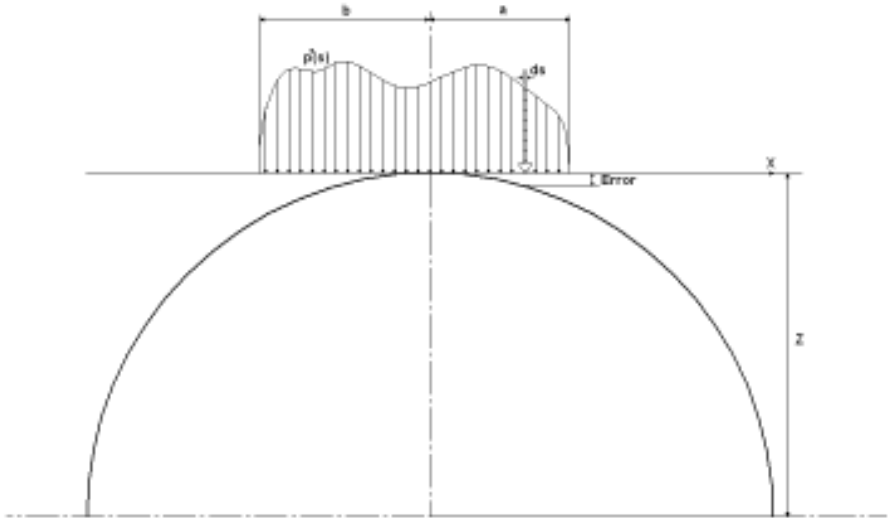

Figure 6.27: Distribution error

As the stresses are summed within the circular domain, those closest to the surface are not included, as no account is taken of the shortening distance to the centre of the circle (Z, Figure 6.27). As such the deflection is increasingly misrepresented the further the point of application is from the central axis.

6.4 Enhanced Deflection Method

In order to remedy the previous issues of unrepresentative deflection values, an alternative method was developed. Based upon the work of (Muskhelishvili, 1953), the condition of a circular disk under concentrated forces acting upon its boundary was considered, as illustrated in Figure 6.28.

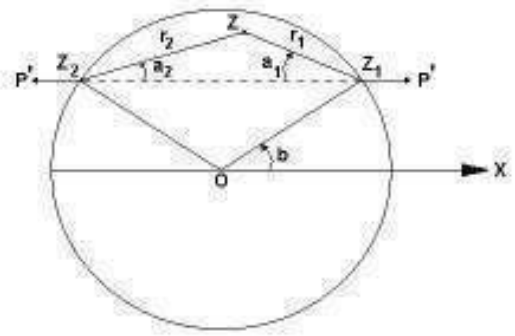

Figure 6.28: Concentrated forces acting on a circular disc

In the case of Figure 6.28, two equal and opposite forces are acting in parallel to the Ox axis. Each force acts at points Z1 and Z2, respectively, and as such the stress components at an arbitrary point, Z, are given as:

$$\sigma_x = \frac{2P'}{\pi}\left(\frac{\cos^3 a_1}{r_1} + \frac{\cos^3 a_2}{r_2}\right) - \frac{P'}{\pi R}\cos b$$

$$\sigma_y = \frac{2P'}{\pi}\left(\frac{\sin^2 a_1 \cos a_1}{r_1} + \frac{\sin^2 a_2 \cos a_2}{r_2}\right) - \frac{P'}{\pi R}\cos b \qquad (6.71)$$

$$\sigma_{xy} = \frac{2P'}{\pi}\left(\frac{\sin a_1 \cos^2 a_1}{r_1} + \frac{\sin a_2 \cos^2 a_2}{r_2}\right)$$

The superposition of the distributed load was then carried out using a pre-determined grid domain.

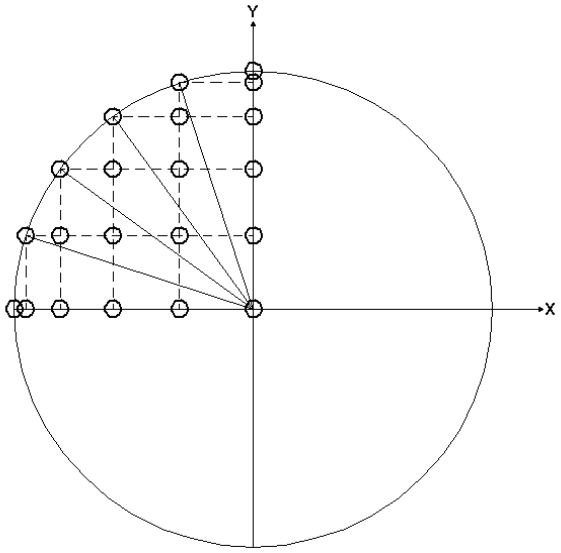

Figure 6.29: Grid domain diagram

Initially nodes are placed on the boundary of the circular domain at regular intervals, for instance at 1° intervals. These points are then used as the basis for forming a non-uniform dimensional grid over the seal cross section. Figure 6.29 shows an example of this grid procedure for a 90° segment of the cross-section.

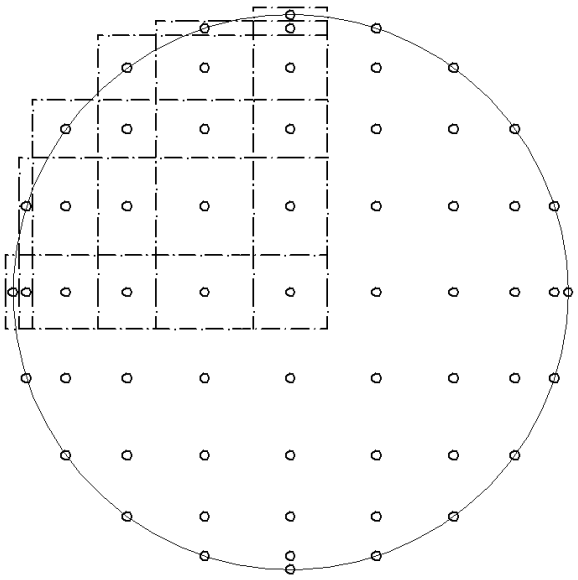

Figure 6.30: Node boundaries

Starting at the outer edges, the boundaries of the elements were calculated such that each node location was central within its element as illustrated in Figure 6.30.

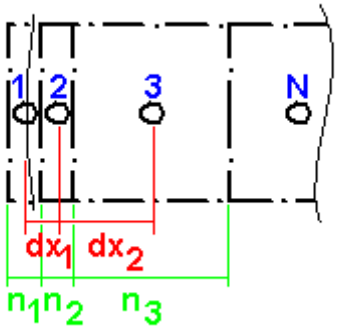

Figure 6.31: Nodal positioning

Initially, the distance dx_1 (see Figure 6.31) is taken for the element widths n_1 and n_2. The value of $n_2/2$ is then taken from the distance dx_2 and doubled to give n_3. This process continues until the centre of the contact is reached, with the opposite side being a mirror of the original.

6.4.1 Tension Fitment and Seal Elongation

The contribution due to fitment from the stretching of the seal over the stem is first calculated. This is achieved by starting with the undeformed length of the central axis around the seal. Based on the stem and groove dimensions, the final length is then calculated for the central axis to fit within the centre of the groove space (G) available. This allows the calculation of the desired deflection resulting from the cross sectional squeeze (See Figure 6.32, d1,2) which is also determined once the change in initial diameter is found from the tensile component.

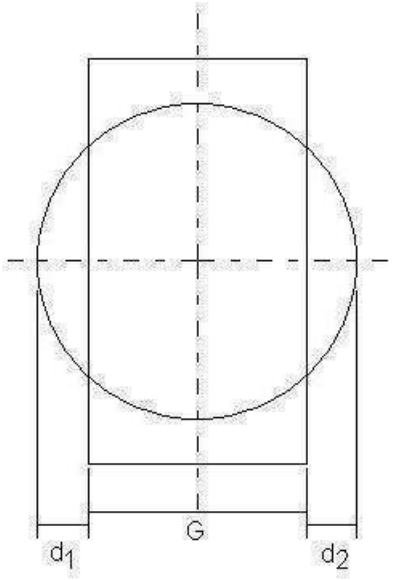

Figure 6.32: Assumed initial fitment

The strain is calculated as:

$$\text{Strain}_Z, \varepsilon_z = \frac{\Delta L}{L_o}$$

The stress from the stretch (in the direction of the stretch, z) is then given by:

$$\sigma_z = E\varepsilon_z$$

Where E is the elastic modulus of the seal elastomer. The cross sectional strain in the x/y direction is then given by:

$$\varepsilon_{x,y} = -\frac{(\upsilon\sigma_Z)}{E}$$

Where υ is the poisons ratio of the seal elastomer, which at 0.49 is treated as basically incompressible and therefore any change to the geometry shape must maintain the original volume of the seal material.

This strain is then multiplied by each element size and summed within the seal boundary in order to calculate the total deflection and the resulting profile change, as illustrated in Figure 6.33, where the original radial radius and cross sectional radius (R1 and RCS1, respectively) are transformed to the stretched fitment dimensions (R2 and RCS2) with R2 falling inline with the central position of the groove dimension, G.

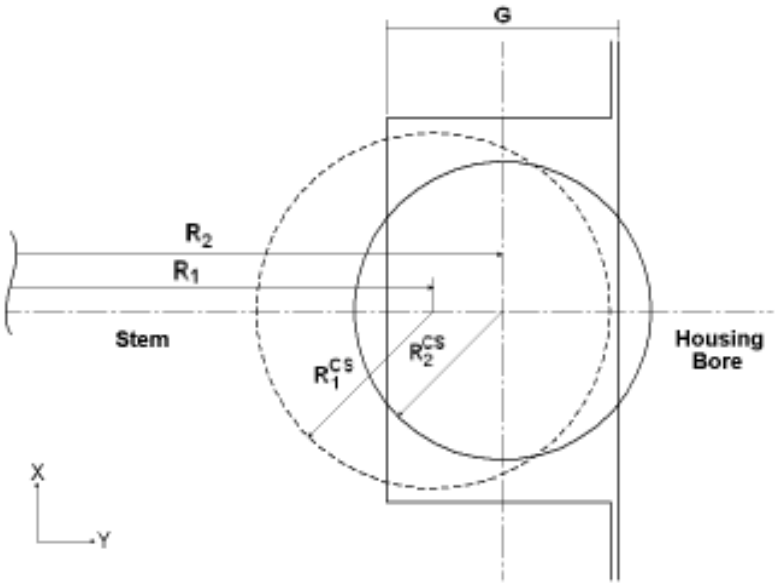

Figure 6.33: Tension effects

6.4.2 Pressure Loading Component

Once the tension and elongation of the seal are calculated, it is necessary to determine the additional loading on the contact face, resulting from the application of canister pressure. For reasons of simplicity, this was applied using an equivalent contact load as opposed to a uniformly distributed pressure on the seal face. This assumption was used in order to allow a simple fitment case, whereby the pressure force acting on the side of the seal at any point in the actuation cycle was exactly balanced by the interference fit and, therefore, the contact force acting on the opposing seal side. This procedure is illustrated in Figure 6.34:

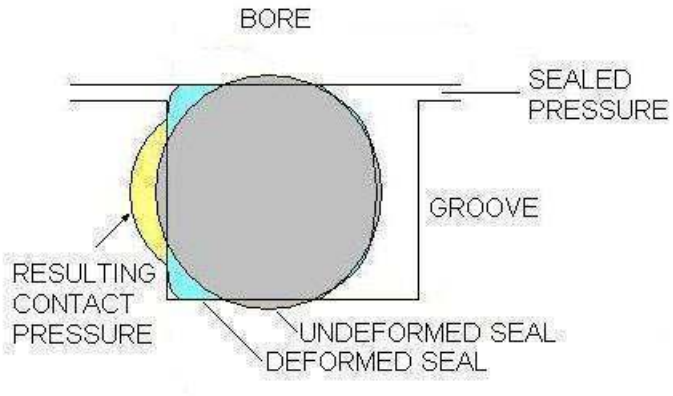

Figure 6.34: Pressure loading approach

In this manner, the stress was calculated using loading pairs, such that the magnitude and distribution of the canister pressure is the same as that on the opposing contacting side. In such a case Equations (6.71) for stress can be used. Once again, this can then be transformed to strain and, therefore, deflection using the individual elements within the cross-section of the seal.

6.4.3 Final Fitment Component

The final additional component is that of the contact conjunction. In this instance the exact contact width and load should be calculated in order for the seal to correspond to the boundary of the Stem-bore conjunction. Once again Equations (6.71) are utilised to calculate the corresponding stresses and, thus, strains and deflections of each element. Superposition of all of these components determines the final seal shape. The applicability of superposition depends on several assumptions:

- The material is homogeneous and isotropic
- The rules of linear elasticity may be applied
- Small strain analysis may be assumed

The applicability of such conditions may not appear immediately obvious. However, it has been shown by Kim *et al* (2007) that compressions of up to 30% can be reasonably approximated for a rubber conjunction using such assumptions.

In order to fit the seal to the groove boundary, the contact width must be determined. In this instance, Hertzian calculations do not hold true, so the contact width must be determined using the interference of the seal with the boundary. This is achieved by initially basing the width on the chord length of the interference between the seal and the boundary as shown in Figure 6.35.

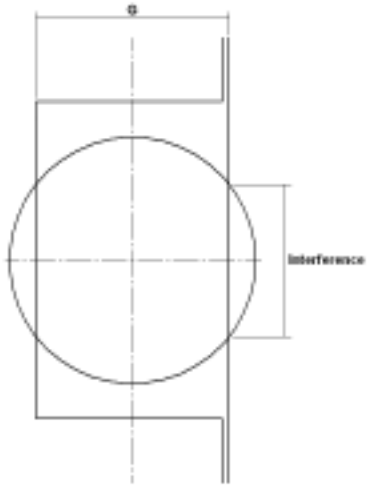

Figure 6.35: Initial contact width estimate

This initial estimate encompasses the true contact width. An initial estimate of the conjunctional load is then applied over this width and the resulting deformation calculated. The error between the calculated deflection and the desired amount required to achieve a correct fitment is then obtained. The load is then iterated on a node by node basis until each edge node within the contact width complies with the boundary of the bore. Should the pressure at any node become negative in an attempt to reach the boundary condition, it is set to zero and the contact width reduced so that it no longer includes this node. Likewise, should a node outside the contact width attain a positive pressure, the contact width is extended to include it. This procedure is carried out based on the difference between the adjacent nodes, such as that for the inlet for example, as shown in Figure 6.36:

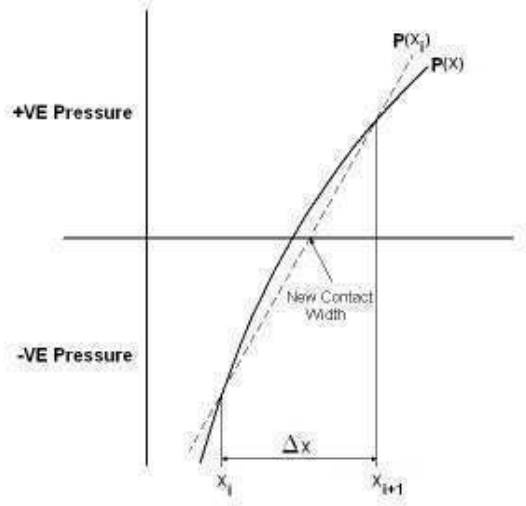

Figure 6.36: Contact width interpolation

A linear interpolation approximation was used for the point at which the pressure profile would indeed be zero. The pressure profile was then modified on this node by node basis using a damping factor in order to stabilise the variations and prevent oscillatory behaviour, leading to the collapse of the pressure distribution. This means that the error due to deflection for any given node is found by:

$$D_{ERR} \leq \frac{\left| D_{Desired} - D_{Current} \right|}{D_{Desired}} \tag{6.72}$$

If the error for any node within the contact width is greater than what would be expected, each and every node is iterated through:

$$P_{New} = P_{New} + \alpha \left[\left(\frac{D_{Desired} - D_{Current}}{D_{Desired}} \right) \Big/ N_{Width} \right] \tag{6.73}$$

This new pressure distribution is then used to calculate deflection and the process continues. The overall flow chart is shown in Figure 6.37. It is important to note, that a unit pressure is initially applied over the contact area in order to create an influence coefficient matrix similar to that in the approach highlighted by Hamrock (1994). This can then be utilised within the numerical solution of Reynolds equation, as well as for fitment loading.

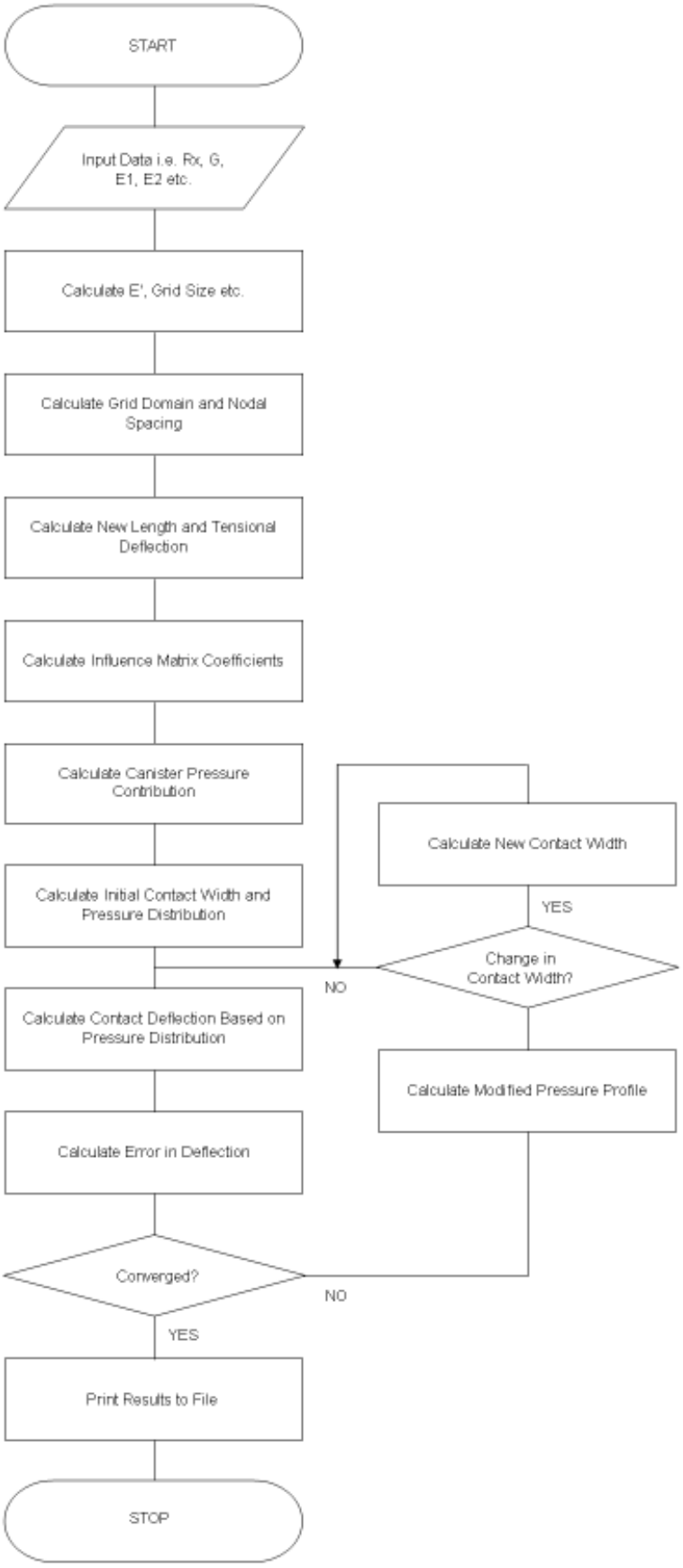

Figure 6.37: Fitment operation flow chart

6.5 Solving the Reynolds Equation

In order to solve Reynolds equation numerically, a finite differencing technique was employed. This technique provides an approximate solution for a given instant of time. The solution is achieved by taking the complete solution domain and discretising it into a series of grid points. Solution values are then found for each grid point (Hamrock and Dowson (1976), Jalali-Vahid *et al*. (2000) and Rao (2004))**.**

There are three possible approaches for solving a differential equation with finite differencing techniques: central, forward and backward differencing schemes. The basic premise of each scheme is illustrated in Figure 6.38 and for a thorough explanation see either Dowson and Higginson (1966), Gohar (2001), Venner and Lubrecht (2000), Jalali-Vahid (2000) or Rao (2004).

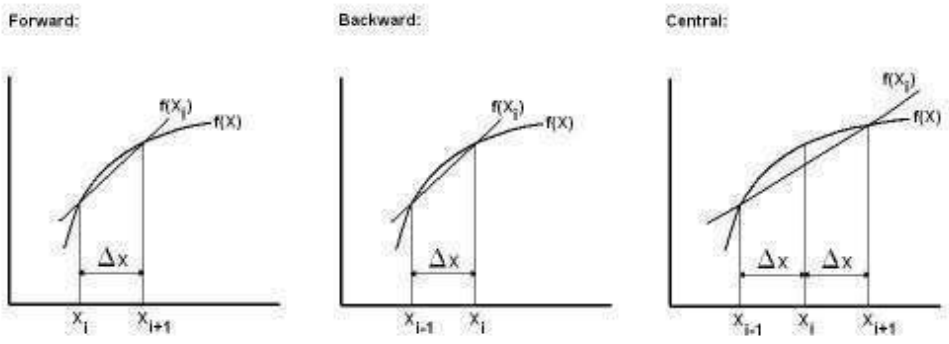

Figure 6.38: Finite differencing technique

The central differencing technique was employed for discretisation of the left hand terms of Reynolds equation, with the terms on the right hand side set out with an additional β variable (Jalali-Vahid *et al*, 2000). This allows the right hand side terms to be calculated, based upon either forward, backward or central differencing methods without the need to change the program other than the β value **(**Jalali-Vahid *et al* (2000) and Gohar (2001)). This was made in order to help convergence should one method prove problematic.

Whereby:

- $\beta = 0$ = Forward dif. scheme.
- $\beta = 1$ = Backwards dif. scheme.
- $\beta = 0.5$ = Central dif. scheme.

6.5.1 Implementation within Reynolds Equation

Implementing the above approach for Reynolds equation results in:

$$\frac{\left(\frac{\bar{\rho}H^3}{\bar{\eta}}\frac{dP}{dX}\right)_{i+\frac{1}{2}}-\left(\frac{\bar{\rho}H^3}{\bar{\eta}}\frac{dP}{dX}\right)_{i-\frac{1}{2}}}{\Delta X}=\frac{12U^*E'R_x{}^3}{b^3P_h}\left\{(1-\beta)\frac{(\bar{\rho}H)_{i+1}-(\bar{\rho}H)_i}{\Delta X}+\beta\frac{(\bar{\rho}H)_i-(\bar{\rho}H)_{i-1}}{\Delta X}\right\} \quad (6.74)$$

The left hand side terms become:

$$\begin{aligned}\left(\frac{\bar{\rho}H^3}{\bar{\eta}}\frac{dP}{dX}\right)_{i+\frac{1}{2}}&=\left(\frac{\bar{\rho}H^3}{\bar{\eta}}\right)_{i+\frac{1}{2}}\frac{P_{i+1}-P_i}{\Delta X}\\ \left(\frac{\bar{\rho}H^3}{\bar{\eta}}\frac{dP}{dX}\right)_{i-\frac{1}{2}}&=\left(\frac{\bar{\rho}H^3}{\bar{\eta}}\right)_{i-\frac{1}{2}}\frac{P_i-P_{i-1}}{\Delta X}\end{aligned} \quad (6.75)$$

With:

$$\begin{aligned}\left(\frac{\bar{\rho}H^3}{\bar{\eta}}\right)_{i+\frac{1}{2}}&=\frac{\left(\frac{\bar{\rho}H^3}{\bar{\eta}}\right)_{i+1}+\left(\frac{\bar{\rho}H^3}{\bar{\eta}}\right)_i}{2}\\ \left(\frac{\bar{\rho}H^3}{\bar{\eta}}\right)_{i-\frac{1}{2}}&=\frac{\left(\frac{\bar{\rho}H^3}{\bar{\eta}}\right)_i+\left(\frac{\bar{\rho}H^3}{\bar{\eta}}\right)_{i-1}}{2}\end{aligned} \quad (6.76)$$

Grouping these terms and re-arranging as necessary, the left hand side of the equation results in:

$$\left(\frac{\bar{\rho}H^3}{\bar{\eta}}\frac{dP}{dX}\right)_{i+\frac{1}{2}} = \frac{\left[\left(\frac{\bar{\rho}H^3}{\bar{\eta}}\right)_{i+1} + \left(\frac{\bar{\rho}H^3}{\bar{\eta}}\right)_i\right]P_{i+1} - P_i}{2\Delta X}$$
$$\left(\frac{\bar{\rho}H^3}{\bar{\eta}}\frac{dP}{dX}\right)_{i-\frac{1}{2}} = \frac{\left[\left(\frac{\bar{\rho}H^3}{\bar{\eta}}\right)_{i} + \left(\frac{\bar{\rho}H^3}{\bar{\eta}}\right)_{i-1}\right]P_{i} - P_{i-1}}{2\Delta X} \tag{6.77}$$

Then, finally:

$$\frac{\partial}{\partial X}\left(\frac{\bar{\rho}H^3}{\bar{\eta}}\frac{dP}{dX}\right)_i = \frac{\frac{\left[\left(\frac{\bar{\rho}H^3}{\bar{\eta}}\right)_{i+1} + \left(\frac{\bar{\rho}H^3}{\bar{\eta}}\right)_i\right]P_{i+1} - P_i}{2\Delta X} - \frac{\left[\left(\frac{\bar{\rho}H^3}{\bar{\eta}}\right)_{i} + \left(\frac{\bar{\rho}H^3}{\bar{\eta}}\right)_{i-1}\right]P_{i} - P_{i-1}}{2\Delta X}}{\Delta X}$$
$$= \frac{\left[\left(\frac{\bar{\rho}H^3}{\bar{\eta}}\right)_{i+1} + \left(\frac{\bar{\rho}H^3}{\bar{\eta}}\right)_i\right]P_{i+1} - P_i - \left[\left(\frac{\bar{\rho}H^3}{\bar{\eta}}\right)_{i} + \left(\frac{\bar{\rho}H^3}{\bar{\eta}}\right)_{i-1}\right]P_{i} - P_{i-1}}{2\Delta X^2} \tag{6.78}$$

Dealing with the right hand side of the original equation, as ΔX remains constant (uniformly spaced grid), it can be moved outside the differential, yielding:

$$\frac{12U^*E'R_x^{\ 3}}{b^3P_h\Delta X}\left\{(1-\beta)\left[(\bar{\rho}H)_{i+1} - (\bar{\rho}H)_i\right] + \beta\left[(\bar{\rho}H)_i - (\bar{\rho}H)_{i-1}\right]\right\} \tag{6.79}$$

The rearranged left and right hand sides of the original Reynolds equation can now be gathered and, where applicable, multiplied out to give:

$$\frac{1}{2\Delta X^2}\left\{\left[\left(\frac{\bar{\rho}H^3}{\bar{\eta}}\right)_{i+1}+\left(\frac{\bar{\rho}H^3}{\bar{\eta}}\right)_i\right]P_{i+1}-\left[\left(\frac{\bar{\rho}H^3}{\bar{\eta}}\right)_{i+1}+2\left(\frac{\bar{\rho}H^3}{\bar{\eta}}\right)_i+\left(\frac{\bar{\rho}H^3}{\bar{\eta}}\right)_{i-1}\right]P_i+\left[\left(\frac{\bar{\rho}H^3}{\bar{\eta}}\right)_i+\left(\frac{\bar{\rho}H^3}{\bar{\eta}}\right)_{i-1}\right]P_{i-1}\right\} \quad (6.80)$$
$$=\frac{12U^*E'R_x{}^3}{b^3P_h\Delta X}\left\{(1-\beta)\left[(\bar{\rho}H)_{i+1}-(\bar{\rho}H)_i\right]+\beta\left[(\bar{\rho}H)_i-(\bar{\rho}H)_{i-1}\right]\right\}$$

As previously stated, the equation is solved by numerical approximation. Therefore, the left hand side never exactly equals the right hand side. A residual value (F_i^R) will always remain (Kushwaha *et al,* 2000*)*:

$$F_i^R=\left[\begin{array}{c}\frac{1}{2\Delta X^2}\left\{\left[\left(\frac{\bar{\rho}H^3}{\bar{\eta}}\right)_{i+1}+\left(\frac{\bar{\rho}H^3}{\bar{\eta}}\right)_i\right]P_{i+1}-\left[\left(\frac{\bar{\rho}H^3}{\bar{\eta}}\right)_{i+1}+2\left(\frac{\bar{\rho}H^3}{\bar{\eta}}\right)_i+\left(\frac{\bar{\rho}H^3}{\bar{\eta}}\right)_{i-1}\right]P_i+\left[\left(\frac{\bar{\rho}H^3}{\bar{\eta}}\right)_i+\left(\frac{\bar{\rho}H^3}{\bar{\eta}}\right)_{i-1}\right]P_{i-1}\right\}\\ -\frac{12U^*E'R_x{}^3}{b^3P_h\Delta X}\left\{(1-\beta)\left[(\bar{\rho}H)_{i+1}-(\bar{\rho}H)_i\right]+\beta\left[(\bar{\rho}H)_i-(\bar{\rho}H)_{i-1}\right]\right\}\end{array}\right] \quad (6.81)$$

6.5.1.1 The Modified Newton-Raphson Method

An established method for solving non-linear differential equations is the Newton-Raphson technique. This was employed to solve for the residual function and it can be formulated as:

$$f\left(X_{n+1}\right)=f\left(X_n\right)+f'\left(X_{n+1}-X_n\right)+Err \quad (6.82)$$

With the real solution:

$$\overline{F}_i^R=f\left(\overline{P}_{i+1},\overline{P}_i,\overline{P}_{i-1}\right)=0 \quad (6.83)$$

The approximate solution by Newton-Raphson method is:

$$F_i^R=f\left(P_{i+1},P_i,P_{i-1}\right)\neq 0 \quad (6.84)$$

This allows the function to be rewritten in Taylor series expansion in the form:

$$\overline{F}_i^R = F_i^R + \frac{\partial F_i}{\partial P_{i+1}}\Delta P_{i+1} + \frac{\partial F_i}{\partial P_{i-1}}\Delta P_{i-1} + \frac{\partial F_i}{\partial P_i}\Delta P_i + Err = 0$$
$$where: \Delta P_i = \overline{P}_i - P_i \tag{6.85}$$

The first order differentials can then be replaced by a Jacobian matrix [J], containing the derivatives set of the function with respect to all the dependent variables. Thus, assuming the truncation error is small enough to be ignored, then:

$$-F_i^R = \overline{J}_{i,i+1}\Delta P_{i+1} + \overline{J}_{i,i-1}\Delta P_{i-1} + \overline{J}_{i,i}\Delta P_i$$
$$where: \overline{J}_{i,k} = \frac{\partial F_i}{\partial P_k} \tag{6.86}$$

which can then be re-arranged in the form of a Gauss-Seidel iteration as:

$$\Delta P_i^n = \frac{-F_i^R - \overline{J}_{i,k-1}\Delta P_{i-1}^n - \overline{J}_{i,k+1}\Delta P_{i+1}^{n-1}}{J_{i,k}} \tag{6.87}$$

(where n denotes the current iteration and n-1 the previous iteration). For each iteration, the new pressure is then given by:

$$P_i^n = P_i^{n-1} + \Omega\Delta P_i^n \tag{6.88}$$

where Ω represents a relaxation factor on the pressure change to prevent drastic changes, causing numerical convergence errors. This factor is typically 0.01 for the cases considered in this research (Grimble *et al.,* 2008 (See Appendix)).

6.5.1.2 The Jacobian Terms

The first order differentials are solved using a Jacobian of the form (Dowson and Ehret, 1999):

$$\overline{J}_{i,k} = \frac{\partial F_i}{\partial P_k} \tag{6.89}$$

which are then used to determine both the residual (F_i^R) and the pressure difference terms (ΔP_i^n). Therefore, the Jacobian values for the current, previous and following node positions must all be established.

(a) Current Node Position

$$\overline{J}_{i,k} = \frac{\partial F_i}{\partial P_k}$$

But, k = i, so: (6.90)

$$\overline{J}_{i,k} = \frac{\partial F_i}{\partial P_i}$$

Upon substitution into the residual equation:

$$= \frac{\partial}{\partial P_i}\left[\begin{array}{c} \frac{1}{2\Delta X^2}\left\{\left[\left(\frac{\overline{\rho}H^3}{\overline{\eta}}\right)_{i+1}+\left(\frac{\overline{\rho}H^3}{\overline{\eta}}\right)_i\right]P_{i+1}-\left[\left(\frac{\overline{\rho}H^3}{\overline{\eta}}\right)_{i+1}+2\left(\frac{\overline{\rho}H^3}{\overline{\eta}}\right)_i+\left(\frac{\overline{\rho}H^3}{\overline{\eta}}\right)_{i-1}\right]P_i+\left[\left(\frac{\overline{\rho}H^3}{\overline{\eta}}\right)_i+\left(\frac{\overline{\rho}H^3}{\overline{\eta}}\right)_{i-1}\right]P_{i-1}\right\} \\ -\frac{12U^*E'R_x^3}{b^3P_h\Delta X}\left\{(1-\beta)\left[(\overline{\rho}H)_{i+1}-(\overline{\rho}H)_i\right]+\beta\left[(\overline{\rho}H)_i-(\overline{\rho}H)_{i-1}\right]\right\} \end{array}\right] \tag{6.91}$$

Finally, by multiplying out brackets and upon collection of terms:

$$\bar{J}_{i,i} = \left[\frac{1}{2\Delta X^2} \left\{ \left[\frac{\partial\left(\frac{\bar{\rho}H^3}{\bar{\eta}}\right)_{i+1}}{\partial P_i} + \frac{\partial\left(\frac{\bar{\rho}H^3}{\bar{\eta}}\right)_i}{\partial P_i} \right] P_{i+1} - \left[\left(\frac{\bar{\rho}H^3}{\bar{\eta}}\right)_{i+1} + 2\left(\frac{\bar{\rho}H^3}{\bar{\eta}}\right)_i + \left(\frac{\bar{\rho}H^3}{\bar{\eta}}\right)_{i-1} \right] - \left[\frac{\partial\left(\frac{\bar{\rho}H^3}{\bar{\eta}}\right)_{i+1}}{\partial P_i} + 2\frac{\partial\left(\frac{\bar{\rho}H^3}{\bar{\eta}}\right)_i}{\partial P_i} + \frac{\partial\left(\frac{\bar{\rho}H^3}{\bar{\eta}}\right)_{i-1}}{\partial P_i} \right] P_i + \left[\frac{\partial\left(\frac{\bar{\rho}H^3}{\bar{\eta}}\right)_i}{\partial P_i} + \frac{\partial\left(\frac{\bar{\rho}H^3}{\bar{\eta}}\right)_{i-1}}{\partial P_i} \right] P_{i-1} \right\} \right.$$
$$\left. - \frac{12U^* E' R_x^3}{b^3 P_h \Delta X} \left\{ (1-\beta) \left[\frac{\partial(\bar{\rho}H)_{i+1}}{\partial P_i} - \frac{\partial(\bar{\rho}H)_i}{\partial P_i} \right] + \beta \left[\frac{\partial(\bar{\rho}H)_i}{\partial P_i} - \frac{\partial(\bar{\rho}H)_{i-1}}{\partial P_{i-1}} \right] \right\} \right]$$

(6.92)

(b) Previous Node Position

$$\bar{J}_{i,k-1} = \frac{\partial F_i}{\partial P_{i-1}} \tag{6.93}$$

Upon substitution into the residual equation:

$$= \frac{\partial}{\partial P_{i-1}} \left[\frac{1}{2\Delta X^2} \left\{ \left[\left(\frac{\bar{\rho}H^3}{\bar{\eta}}\right)_{i+1} + \left(\frac{\bar{\rho}H^3}{\bar{\eta}}\right)_i \right] P_{i+1} - \left[\left(\frac{\bar{\rho}H^3}{\bar{\eta}}\right)_{i+1} + 2\left(\frac{\bar{\rho}H^3}{\bar{\eta}}\right)_i + \left(\frac{\bar{\rho}H^3}{\bar{\eta}}\right)_{i-1} \right] P_i + \left[\left(\frac{\bar{\rho}H^3}{\bar{\eta}}\right)_i + \left(\frac{\bar{\rho}H^3}{\bar{\eta}}\right)_{i-1} \right] P_{i-1} \right\} \right.$$
$$\left. - \frac{12U^* E' R_x^3}{b^3 P_h \Delta X} \left\{ (1-\beta) \left[(\bar{\rho}H)_{i+1} - (\bar{\rho}H)_i \right] + \beta \left[(\bar{\rho}H)_i - (\bar{\rho}H)_{i-1} \right] \right\} \right]$$

(6.94)

Finally, by multiplying out brackets and upon collection of terms, the Jacobian becomes:

$$\bar{J}_{i,i\text{-}1} = \left[\frac{1}{2\Delta X^2} \left\{ \left[\frac{\P\left(\frac{\bar{\rho}H^3}{\bar{\eta}}\right)_{i+1}}{\P P_{i\text{-}1}} + \frac{\P\left(\frac{\bar{\rho}H^3}{\bar{\eta}}\right)_i}{\P P_{i\text{-}1}} \right] P_{i+1} - \left[\frac{\P\left(\frac{\bar{\rho}H^3}{\bar{\eta}}\right)_{i+1}}{\P P_{i\text{-}1}} + 2\frac{\P\left(\frac{\bar{\rho}H^3}{\bar{\eta}}\right)_i}{\P P_{i\text{-}1}} + \frac{\P\left(\frac{\bar{\rho}H^3}{\bar{\eta}}\right)_{i\text{-}1}}{\P P_{i\text{-}1}} \right] P_i + \left[\left(\frac{\bar{\rho}H^3}{\bar{\eta}}\right)_i + \left(\frac{\bar{\rho}H^3}{\bar{\eta}}\right)_{i\text{-}1} \right] + \left[\frac{\P\left(\frac{\bar{\rho}H^3}{\bar{\eta}}\right)_i}{\P P_{i\text{-}1}} + \frac{\P\left(\frac{\bar{\rho}H^3}{\bar{\eta}}\right)_{i\text{-}1}}{\P P_{i\text{-}1}} \right] P_{i\text{-}1} \right\} \right.$$
$$\left. - \frac{12U^* E' R_x^3}{b^3 P_h \Delta X} \left\{ (1\text{-}\beta) \left[\frac{\P(\bar{\rho}H)_{i+1}}{\P P_{i\text{-}1}} - \frac{\P(\bar{\rho}H)_i}{\P P_{i\text{-}1}} \right] + \beta \left[\frac{\P(\bar{\rho}H)_i}{\P P_{i\text{-}1}} - \frac{\P(\bar{\rho}H)_{i\text{-}1}}{\P P_{i\text{-}1}} \right] \right\} \right]$$

(6.95)

(c) Following Node Position:

$$\overline{J}_{i,k+1} = \frac{\partial F_i}{\partial P_{i+1}} \tag{6.96}$$

Upon substitution into the residual equation:

$$= \frac{\P}{\P P_{i+1}} \left[\frac{1}{2\Delta X^2} \left\{ \left[\left(\frac{\bar{\rho} H^3}{\bar{\eta}} \right)_{i+1} + \left(\frac{\bar{\rho} H^3}{\bar{\eta}} \right)_i \right] P_{i+1} - \left[\left(\frac{\bar{\rho} H^3}{\bar{\eta}} \right)_{i+1} + 2 \left(\frac{\bar{\rho} H^3}{\bar{\eta}} \right)_i + \left(\frac{\bar{\rho} H^3}{\bar{\eta}} \right)_{i-1} \right] P_i + \left[\left(\frac{\bar{\rho} H^3}{\bar{\eta}} \right)_i + \left(\frac{\bar{\rho} H^3}{\bar{\eta}} \right)_{i-1} \right] P_{i-1} \right\} \right.$$
$$\left. - \frac{12 U^* E' R_x^3}{b^3 P_h \Delta X} \left\{ (1-\beta) \left[(\bar{\rho} H)_{i+1} - (\bar{\rho} H)_i \right] + \beta \left[(\bar{\rho} H)_i - (\bar{\rho} H)_{i-1} \right] \right\} \right] \tag{6.97}$$

Finally, by multiplying out brackets and upon collection of the terms:

$$\overline{J}_{i,i+1} = \left[\frac{1}{2\Delta X^2} \left\{ \left[\left(\frac{\bar{\rho} H^3}{\bar{\eta}} \right)_{i+1} + \left(\frac{\bar{\rho} H^3}{\bar{\eta}} \right)_i \right] + \left[\frac{\partial \left(\frac{\bar{\rho} H^3}{\bar{\eta}} \right)_{i+1}}{\partial P_{i+1}} + \frac{\partial \left(\frac{\bar{\rho} H^3}{\bar{\eta}} \right)_i}{\partial P_{i+1}} \right] P_{i+1} - \left[\frac{\partial \left(\frac{\bar{\rho} H^3}{\bar{\eta}} \right)_{i+1}}{\partial P_{i+1}} + 2 \frac{\partial \left(\frac{\bar{\rho} H^3}{\bar{\eta}} \right)_i}{\partial P_{i+1}} + \frac{\partial \left(\frac{\bar{\rho} H^3}{\bar{\eta}} \right)_{i-1}}{\partial P_{i+1}} \right] P_i + \left[\frac{\partial \left(\frac{\bar{\rho} H^3}{\bar{\eta}} \right)_i}{\partial P_{i+1}} + \frac{\partial \left(\frac{\bar{\rho} H^3}{\bar{\eta}} \right)_{i-1}}{\partial P_{i+1}} \right] P_{i-1} \right\} \right.$$
$$\left. - \frac{12 U^* E' R_x^3}{b^3 P_h \Delta X} \left\{ (1-\beta) \left[\frac{\partial (\bar{\rho} H)_{i+1}}{\partial P_{i+1}} - \frac{\partial (\bar{\rho} H)_i}{\partial P_{i+1}} \right] + \beta \left[\frac{\partial (\bar{\rho} H)_i}{\partial P_{i+1}} - \frac{\partial (\bar{\rho} H)_{i-1}}{\partial P_{i+1}} \right] \right\} \right] \tag{6.98}$$

6.5.1.3 Simplification of the Jacobian Terms

By examining the Jacobian terms, it can be noted that it is possible to solve for a particular term once, and then make use of it repeatedly in each of the Jacobian values for a given node. This is beneficial for the calculations rather than having to calculate the same terms repeatedly. Therefore, two additional terms B_k^i and C_k^i were utilised, where:

$$B_k^i = \frac{\partial\left(\frac{\overline{\rho}H^3}{\overline{\eta}}\right)_i}{\partial P_k} = \left(\frac{H^3}{\overline{\eta}}\right)_i \frac{\partial\left(\overline{\rho}\right)_i}{\partial P_k} + \left(\frac{\overline{\rho}_i}{\overline{\eta}}\right)_i \frac{\partial\left(H^3\right)_i}{\partial P_k} + \left(\overline{\rho}_i H^3\right)_i \frac{\partial\left(\overline{\eta}^{-1}\right)_i}{\partial P_k} \qquad (6.99)$$
$$= \left(\frac{H^3}{\overline{\eta}}\right)_i \frac{\partial\left(\overline{\rho}\right)_i}{\partial P_k} - \left(\frac{\overline{\rho}_i H^3}{\overline{\eta}^2}\right)_i \frac{\partial\overline{\eta}_i}{\partial P_k} + 3\left(\frac{\overline{\rho}_i H^2}{\overline{\eta}}\right)_i \frac{\partial H_i}{\partial P_k}$$

And:

$$C_k^i = \frac{\partial\left(\overline{\rho}H\right)_i}{\partial P_k} = \overline{\rho}_i \frac{\partial H_i}{\partial P_k} + H_i \frac{\partial\overline{\rho}_i}{\partial P_k}$$

(6.100)

Furthermore, letting:

$$Ro_k^i = \frac{\partial\overline{\rho}_i}{\partial P_k}$$
$$Et_k^i = \frac{\partial\overline{\eta}_i}{\partial P_k} \qquad (6.101)$$
$$Lu_k^i = \frac{\partial H_i}{\partial P_k}$$

yields:

$$B_k^i = \left(\frac{H^3}{\overline{\eta}}\right)_i Ro_k^i - \left(\frac{\overline{\rho}_i H^3}{\overline{\eta}^2}\right)_i Et_k^i + 3\left(\frac{\overline{\rho}_i H^2}{\overline{\eta}}\right)_i Lu_k^i \qquad (6.102)$$

and:

$$C_k^i = \bar{\rho}_i Lu_k^i + H_i Ro_k^i \tag{6.103}$$

6.5.2 Transforming the general form to that of the inhaler contact

Thus far, Reynolds equation has been discretised for a general case with film thickness, density and viscosity variation with pressure. However, in the case of the initial model, neither fluid density nor viscosity were deemed to vary mainly due to the low pressures of the inhaler system.

Therefore:

$$\begin{aligned}
&\frac{\partial(\bar{\rho})_i}{\partial P_k} = 0 \\
&\bar{\rho}_i = \bar{\rho}_0 \\
&\frac{\partial(\bar{\eta}^{-1})_i}{\partial P_k} = 0 \\
&\bar{\eta}_i = \bar{\eta}_0
\end{aligned} \tag{6.104}$$

As these terms are now constant, they can also be moved outside of the differential terms within the Reynolds equation. This gives:

$$F_i^R = \left[\begin{array}{c} \frac{1}{2\Delta X^2}\left\{\left[\left(\frac{\bar{\rho}_0 H^3}{\bar{\eta}_0}\right)_{i+1} + \left(\frac{\bar{\rho}_0 H^3}{\bar{\eta}_0}\right)_i\right]P_{i+1} - \left[\left(\frac{\bar{\rho}_0 H^3}{\bar{\eta}_0}\right)_{i+1} + 2\left(\frac{\bar{\rho}_0 H^3}{\bar{\eta}_0}\right)_i + \left(\frac{\bar{\rho}_0 H^3}{\bar{\eta}_0}\right)_{i-1}\right]P_i + \left[\left(\frac{\bar{\rho}_0 H^3}{\bar{\eta}_0}\right)_i + \left(\frac{\bar{\rho}_0 H^3}{\bar{\eta}_0}\right)_{i-1}\right]P_{i-1}\right\} \\ -\frac{12U^* E' R_x{}^3}{b^3 P_h \Delta X}\left\{(1-\beta)\left[(\bar{\rho}_0 H)_{i+1} - (\bar{\rho}_0 H)_i\right] + \beta\left[(\bar{\rho}_0 H)_i - (\bar{\rho}_0 H)_{i-1}\right]\right\} \end{array} \right] \tag{6.105}$$

which results in:

$$F_i^R = \left[\begin{array}{c} \frac{\bar{\rho}_0}{2\Delta X^2 \bar{\eta}_0}\left\{\left[\left(H^3\right)_{i+1} + \left(H^3\right)_i\right]P_{i+1} - \left[\left(H^3\right)_{i+1} + 2\left(H^3\right)_i + \left(H^3\right)_{i-1}\right]P_i + \left[\left(H^3\right)_i + \left(H^3\right)_{i-1}\right]P_{i-1}\right\} \\ -\frac{12U^* E' R_x{}^3 \bar{\rho}_0}{b^3 P_h \Delta X}\left\{(1-\beta)\left[(H)_{i+1} - (H)_i\right] + \beta\left[(H)_i - (H)_{i-1}\right]\right\} \end{array} \right] \tag{6.106}$$

The Jacobian values can then be adjusted as given below, starting with the current node position:

$$\overline{J}_{i,k} = \frac{\partial F_i}{\partial P_i} \tag{6.107}$$

$$\overline{J}_{i,i} = \left[\frac{\bar{\rho}_0}{2\Delta X^2 \bar{\eta}_0} \left\{ \left[\left(H^3\right)_{i+1} + \left(H^3\right)_i \right] + \left[\frac{\partial\left(H^3\right)_{i+1}}{\partial P_i} + \frac{\partial\left(H^3\right)_i}{\partial P_i} \right] P_{i+1} - \left[\frac{\partial\left(H^3\right)_{i+1}}{\partial P_i} + 2\frac{\partial\left(H^3\right)_i}{\partial P_i} + \frac{\partial\left(\frac{\bar{\rho}H^3}{\bar{\eta}}\right)_{i-1}}{\partial P_i} \right] P_i + \left[\frac{\partial\left(H^3\right)_i}{\partial P_i} + \frac{\partial\left(H^3\right)_{i-1}}{\partial P_i} \right] P_{i-1} \right\} \right.$$
$$\left. - \frac{12U^* E' R_x{}^3 \bar{\rho}_0}{b^3 P_h \Delta X} \left\{ (1-\beta) \left[\frac{\partial(H)_{i+1}}{\partial P_i} - \frac{\partial(H)_i}{\partial P_i} \right] + \beta \left[\frac{\partial(H)_i}{\partial P_i} - \frac{\partial(H)_{i-1}}{\partial P_i} \right] \right\} \right] \tag{6.108}$$

$$= \frac{\partial}{\partial P_i} \left[\frac{\bar{\rho}_0}{2\Delta X^2 \bar{\eta}_0} \left\{ \left[\left(H^3\right)_{i+1} + \left(H^3\right)_i \right] P_{i+1} - \left[\left(H^3\right)_{i+1} + 2\left(H^3\right)_i + \frac{\bar{\rho}_0}{\bar{\eta}_0} \left(H^3\right)_{i-1} \right] P_i + \left[\left(H^3\right)_i + \left(H^3\right)_{i-1} \right] P_{i-1} \right\} \right.$$
$$\left. - \frac{12U^* E' R_x{}^3 \bar{\rho}_0}{b^3 P_h \Delta X} \left\{ (1-\beta) \left[(H)_{i+1} - (H)_i \right] + \beta \left[(H)_i - (H)_{i-1} \right] \right\} \right] \tag{6.109}$$

For the previous node position:

$$\overline{J}_{i,k+1} = \frac{\partial F_i}{\partial P_{i-1}} \tag{6.110}$$

$$\overline{J}_{i,i+1} = \left[\frac{\bar{\rho}_0}{2\Delta X^2 \bar{\eta}_0} \left\{ \left[\left(H^3\right)_{i+1} + \left(H^3\right)_i \right] + \left[\frac{\partial\left(H^3\right)_{i+1}}{\partial P_{i-1}} + \frac{\partial\left(H^3\right)_i}{\partial P_{i-1}} \right] P_{i+1} - \left[\frac{\partial\left(H^3\right)_{i+1}}{\partial P_{i-1}} + 2\frac{\partial\left(H^3\right)_i}{\partial P_{i-1}} + \frac{\partial\left(\frac{\bar{\rho}H^3}{\bar{\eta}}\right)_{i-1}}{\partial P_{i-1}} \right] P_i + \left[\frac{\partial\left(H^3\right)_i}{\partial P_{i-1}} + \frac{\partial\left(H^3\right)_{i-1}}{\partial P_{i-1}} \right] P_{i-1} \right\} \right.$$
$$\left. - \frac{12U^* E' R_x{}^3 \bar{\rho}_0}{b^3 P_h \Delta X} \left\{ (1-\beta) \left[\frac{\partial(H)_{i+1}}{\partial P_{i-1}} - \frac{\partial(H)_i}{\partial P_{i-1}} \right] + \beta \left[\frac{\partial(H)_i}{\partial P_{i-1}} - \frac{\partial(H)_{i-1}}{\partial P_{i-1}} \right] \right\} \right] \tag{6.111}$$

$$=\frac{\partial}{\partial P_{i-1}}\left[\begin{array}{c}\frac{\bar{\rho}_0}{2\Delta X^2\bar{\eta}_0}\left\{\left[\left(H^3\right)_{i+1}+\left(H^3\right)_i\right]P_{i+1}-\left[\left(H^3\right)_{i+1}+2\left(H^3\right)_i+\frac{\bar{\rho}_0}{\bar{\eta}_0}\left(H^3\right)_{i-1}\right]P_i+\left[\left(H^3\right)_i+\left(H^3\right)_{i-1}\right]P_{i-1}\right\}\\ -\frac{12U^*E'R_x{}^3\bar{\rho}_0}{b^3P_h\Delta X}\left\{(1-\beta)\left[(H)_{i+1}-(H)_i\right]+\beta\left[(H)_i-(H)_{i-1}\right]\right\}\end{array}\right] \tag{6.112}$$

For the following node position:

$$\bar{J}_{i,k+1}=\frac{\partial F_i}{\partial P_{i+1}} \tag{6.113}$$

$$\bar{J}_{i,i+1}=\left[\begin{array}{c}\frac{\bar{\rho}_0}{2\Delta X^2\bar{\eta}_0}\left\{\left[\left(H^3\right)_{i+1}+\left(H^3\right)_i\right]+\left[\frac{\partial\left(H^3\right)_{i+1}}{\partial P_{i+1}}+\frac{\partial\left(H^3\right)_i}{\partial P_{i+1}}\right]P_{i+1}-\left[\frac{\partial\left(H^3\right)_{i+1}}{\partial P_{i+1}}+2\frac{\partial\left(H^3\right)_i}{\partial P_{i+1}}+\frac{\partial\left(\frac{\bar{\rho}H^3}{\bar{\eta}}\right)_{i-1}}{\partial P_{i+1}}\right]P_i+\left[\frac{\partial\left(H^3\right)_i}{\partial P_{i+1}}+\frac{\partial\left(H^3\right)_{i-1}}{\partial P_{i+1}}\right]P_{i-1}\right\}\\ -\frac{12U^*E'R_x{}^3\bar{\rho}_0}{b^3P_h\Delta X}\left\{(1-\beta)\left[\frac{\partial(H)_{i+1}}{\partial P_{i+1}}-\frac{\partial(H)_i}{\partial P_{i+1}}\right]+\beta\left[\frac{\partial(H)_i}{\partial P_{i+1}}-\frac{\partial(H)_{i-1}}{\partial P_{i+1}}\right]\right\}\end{array}\right] \tag{6.114}$$

$$=\frac{\partial}{\partial P_{i+1}}\left[\begin{array}{c}\frac{\bar{\rho}_0}{2\Delta X^2\bar{\eta}_0}\left\{\left[\left(H^3\right)_{i+1}+\left(H^3\right)_i\right]P_{i+1}-\left[\left(H^3\right)_{i+1}+2\left(H^3\right)_i+\frac{\bar{\rho}_0}{\bar{\eta}_0}\left(H^3\right)_{i-1}\right]P_i+\left[\left(H^3\right)_i+\left(H^3\right)_{i-1}\right]P_{i-1}\right\}\\ -\frac{12U^*E'R_x{}^3\bar{\rho}_0}{b^3P_h\Delta X}\left\{(1-\beta)\left[(H)_{i+1}-(H)_i\right]+\beta\left[(H)_i-(H)_{i-1}\right]\right\}\end{array}\right] \tag{6.115}$$

where, once again, the repeated terms can be grouped as:

$$B_k^i=3\left(H^2\right)_i\frac{\partial H_i}{\partial P_k}=3\left(H^2\right)_i Lu_k^i$$

$$C_k^i=\frac{\partial\left(H\right)_i}{\partial P_k}=Lu_k^i \tag{6.116}$$

As previously described, deflection was initially considered as that arising from a series of individual pressure columns with neighbouring columns having no influence at a particular point in the computational grid.

However, this was replaced by an influence matrix derived from the enhanced deflection model (See section 6.4), as such when the i and k indices are aligned maximum influence will occur, with a lesser degree of influence on the surrounding nodes. This yields:

if $i = k$

$$Lu_k^i = \frac{\partial H_i}{\partial P_k} = D_{i,k}$$

Or if $i \neq k$

$$Lu_k^{i+1} = \frac{\partial H_{i+1}}{\partial P_k} = D_{i+1,k} \tag{6.117}$$

$$Lu_k^{i-1} = \frac{\partial H_{i-1}}{\partial P_k} = D_{i-1,k}$$

....and so forth.

6.5.3 Boundary Conditions of the Contact

In order for the Reynolds equation to be solved, boundary conditions must be imposed for both the inlet and outlet of the contact. For simplicity both inlet and exit boundary pressure values were set to zero, giving:

$$P_{Inlet} = P_s = 0 \qquad \frac{\partial P_{Inlet}}{\partial X} = 0$$

And: (6.118)

$$P_{Outlet} = 0 \qquad \frac{\partial P_{Outlet}}{\partial X} = 0$$

The second boundary condition marks the film rupture position at the contact exit. This is due to Reynolds and Swift-Steiber.

The loading from the canister pressure is included within the fitment routine so that in the case of the inhaler contact while the boundaries may vary during actuation, the conjunctional pressure is represented by these set conditions. The fitment loading accounts for the pressure boundary differences.

6.5.4 Computational Flow Chart

The overall program flowchart is provided in Figure 6.39 and 6.40. The important part is the way that convergence is achieved for both contact pressures and load. Convergence is achieved by comparison of the errors in either pressure or load to a predetermined allowable error. Once the calculation error is within the set condition, the solution is deemed to have converged. In this manner, the routine begins with the hydrodynamic pressure distribution of a dry contact from the load pair routine, and adjusts it into an EHL case, based on the resulting deflection and so forth. In order for a solution to be accepted, firstly the correct (converged) pressure distribution must be obtained. Following that, convergence for contact load is checked. Should the load be deemed to have not converged, H_0 is adjusted and the pressure convergence is carried out again until finally both are criteria are met. In order for pressure convergence to be achieved, the error is calculated as shown below:

$$P_{ERR} \le \frac{\sum_{i=1}^{nx} \left| \bar{P}_i^n - \bar{P}_i^{n-1} \right|}{\sum_{i=1}^{nx} \bar{P}_i^n} \tag{6.119}$$

If the calculated error is below that of the allowable error (P_{ERR}), then the routine is said to have converged on the correct pressure distribution for a given value of H_0. Should convergence remain unachieved, the pressure is updated using a relaxation factor. If converged, the load will then be calculated to check for overall routine convergence. The error within the load is calculated as:

$$W_{ERR} \le \frac{\left| W_{Contact} - W_{Calculated} \right|}{W_{Contact}} \tag{6.120}$$

Should convergence not be achieved, the H_0 value is adjusted based upon a second relaxation factor, usually referred to as a damping factor and the size of the load error as shown below:

$$H_0^n = H_0^{n-1} - \left(\alpha \frac{W_{Contact} - W_{Calculated}}{W_{Contact}} \right) \tag{6.121}$$

In each case, the dampening factor is used to prevent sudden changes in film thickness creating numerical errors that result in convergence failures.

The code is then used to obtain converged fitment and fluid entrainment results, each detailing the pressure profile, film profile and overall conjunctional load. These results are presented in Chapter 7 of this thesis.

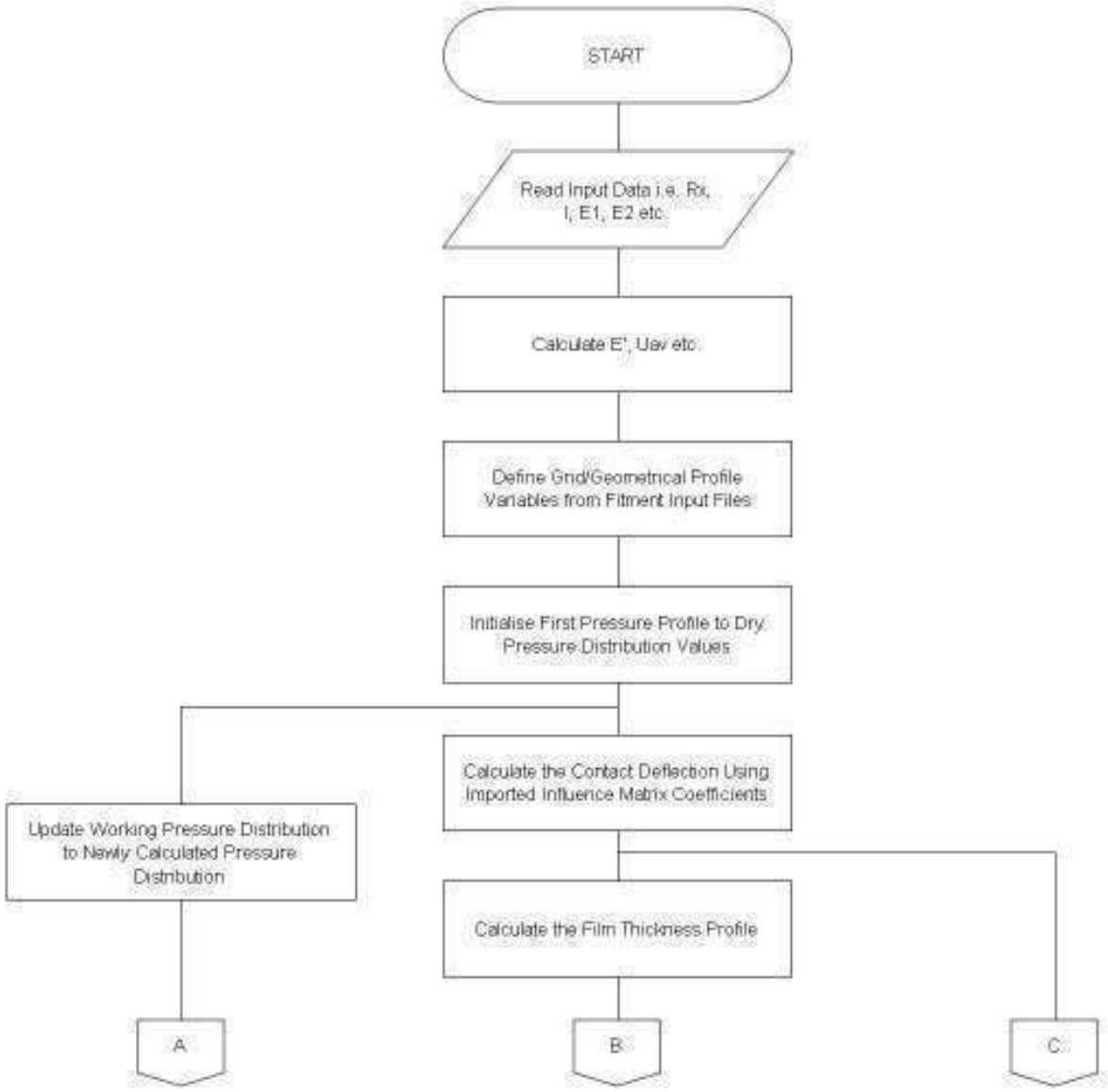

Figure 6.39: Program flowchart part 1

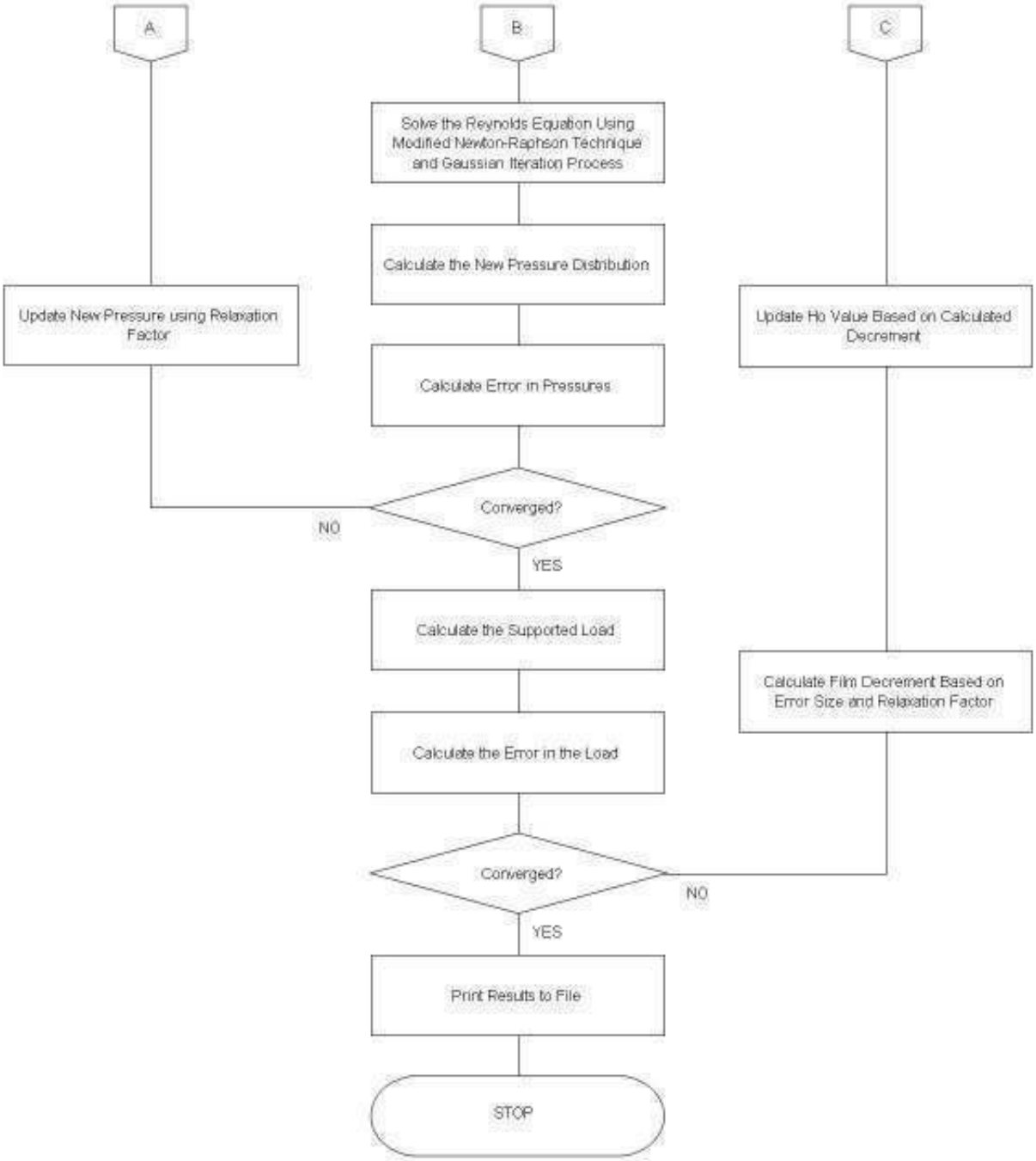

Figure 6.40: Program flowchart part 2

7.0 Results and Discussion

7.1 Introduction

This chapter aims to compare the results of the final code developed in this thesis with those of Karaszkiewicz (1979, 1985, 1987 and 1990). It is intended to show why the additional computation adds to the accuracy and level of detail. Table 7.1 details the model parameters used throughout the verification and testing of the developed numerical program and virtual prototype unless otherwise stated.

Parameter	Value
Seal Cross-sectional Diameter (1)	1.61mm
Seal Radial Diameter (1)	6 mm
Groove Width (1)	1.36 mm
Equivalent Radius	0.805 mm
Entrainment Velocity	10 mm/min
Greenwood and Tripp Product ($\varsigma\beta_{GWT}\sigma$)	0.1289
Stem Modulus of Elasticity (1)	2.6 GPa
Seal Modulus of Elasticity (1)	2.5 MPa
Stem Poisson's Ratio (1)	0.35
Seal Poisson's Ratio (1)	0.49
Nominal Canister Pressure (1)	0.55 MPa
Pressure-Viscosity Coefficient (2)	2.8×10^{-9} Pa-1
Ambient Viscosity (2)	0.211×10^{-3} Pa.S
Eyring Shear Strength (3)	3.5 Mpa
Hamaker Constant (4)	1.35×10^{-19}

(1) Obtained from 3M data
(2) Solvay Fluor Datasheet (www.solvaychemicals.com)
(3) Roberts (1992)
(4) Israelachvili (1992)

Table 7.1: Model parameters

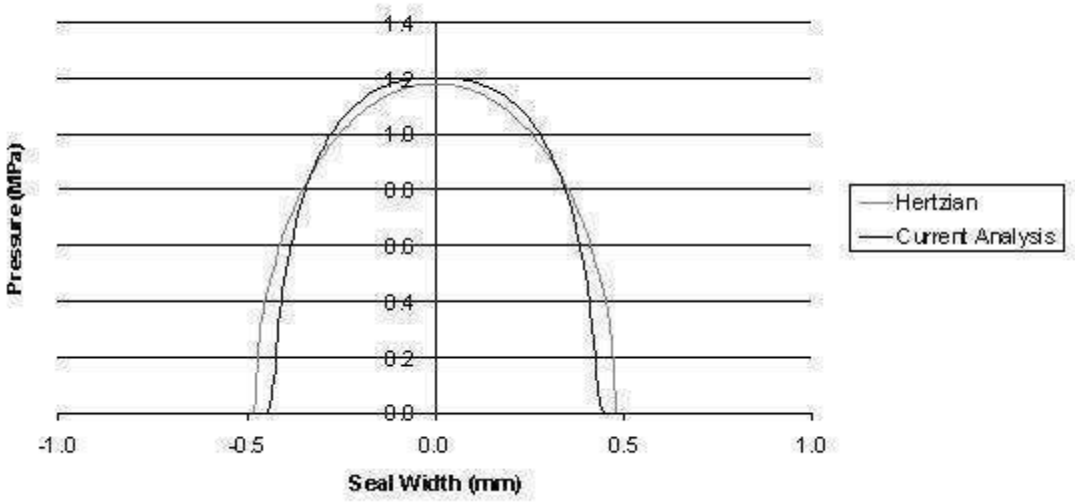

Figure 7.1: Comparison of typical pressure distributions for Hertzian contact and for the current analysis

Figure 7.1 shows a typical pressure distribution across the seal contact region. As it can be seen, the classical Hertzian pressure profile differs to that predicted by the current analysis in that a larger contact width and thus lower peak contact pressures are predicted. This highlights the fact that Hertzian conditions cannot be assumed entirely. For one thing the contact is at least partially conforming. Hertzian assumption may only be made as a first approximation. With no account being taken of the effects of load on the opposing side of the seal, the classical elastic line contact Hertzian approach predicts greater deformation due to load. Karaszkiewicz's (1979, 1985, 1987 and 1990) approach, based on Hertzian theory was developed for hydraulic O-ring seals and thus predicts an increased contact load and greater contact width to that of the current model (see Chapter 6), as indicated in Figure 7.2. As a result, greater minimum film thickness is also predicted, as shown in Figure 7.3, where it is also clear that Karaszkiewicz's approach does not include the level of detail in film variation as found with the current analysis. Karaszkiewicz's approach giving just the one calculated film thickness value which is then assumed across the entire contact width rather than a varying profile with inlet and exit minima for example as shown by the current analysis in Figure 7.3.

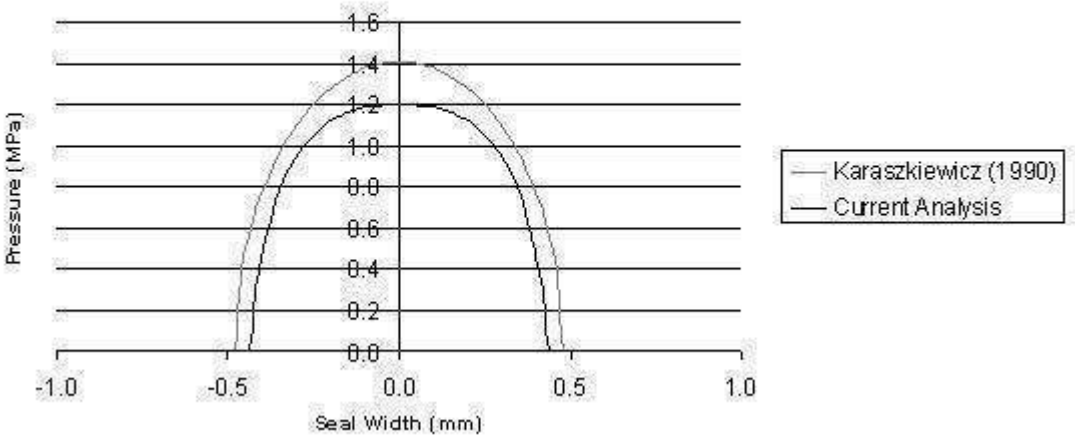

Figure 7.2: Comparison of typical pressure distributions for the current analysis and for Karaszkiewicz

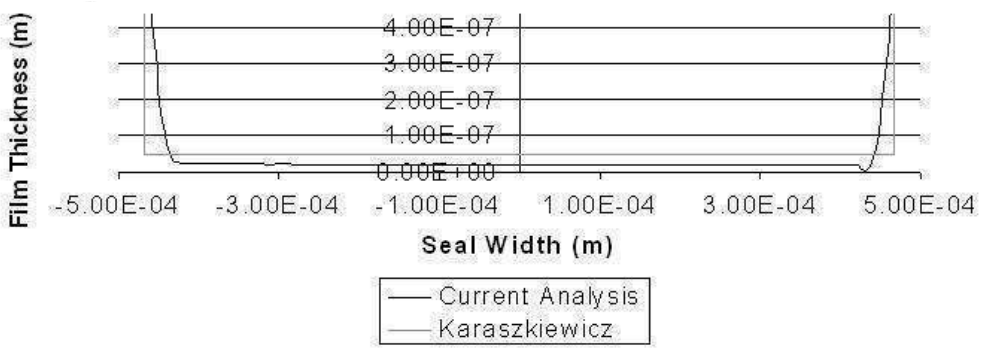

Figure 7.3: Typical contact film thickness/seal profile

7.2 Effect of Variation in Seal Geometry

During manufacture of the seal components, variation in geometry can occur (piece-to-piece variations). It may also be desired to promote increased lubrication by manipulating the seal geometry (Nikas, 2003). This can, however, have the converse effect of resulting in leakage. Nevertheless, some degree of edge profiling of the seal face-width would alter the wedge shape and can encourage lubrication. Therefore, it is of interest to the designer of the inhaler to have an indication of the contact condition that such variations would provide. As previously stated in Chapter 1 the canister pressure must be able to overcome the friction forces preventing actuation, namely those of the seals against the housing bore in order for the device to operate smoothly. As in the new design (see Chapter 1), the pressure operated piston is the only moving component. With no requirement for a spring or other return mechanisms, an acceptable leakage rate must be achieved and so appropriate sealing must also be maintained in order to prevent leakage of formulation throughout the life

of the device. In order to optimise the inhaler design efficiently and cost effectively, a representative computer model is certainly required.

7.2.1 Inner Diameter Variation

Following a review of data provided by 3M on the manufacture of seals it was decided that the variation of the inside diameter of the O-ring would be modelled to review its effect on the contact conditions.

As such, the inner diameter was varied from 2.82 mm to 2.86 mm as can be seen in Table 7.2. A value of 2.84 mm was used for the majority of the analyses in this thesis, so this range provides an effective high and low band of possible sizes based on the typical 3M tolerance and seal data.

Seal Dimensions (Inner Diameter) (mm)	2.82		2.84		2.86	
Deflection Approach	Karaszkiewicz	Current Analysis	Karaszkiewicz	Current Analysis	Karaszkiewicz	Current Analysis
Contact Width (m)	9.567E-04	8.886E-04	9.567E-04	8.886E-04	9.567E-04	8.886E-04
Normal Load (N)	14.714	12.271	14.781	12.395	14.847	12.520
Peak Contact Pressure (Pa)	1407084.8	1189737.8	1407084.8	1197543.7	1407084.8	1205035.1

Table 7.2: Inner diameter variation results

With only the inner seal diameter varied, the predictions based on the work of Karaszkiewicz (1979, 1985, 1987 and 1990) do not show any variation in any of the contact mechanics characteristics other than the total load around the seal itself. The method developed in this thesis however shows a small increase in both peak pressure and overall load would be expected, as well as a marginal increase in the resulting contact width. This is due to the current method taking a more accurate account of the fitment of the seal, including fitting over the stem dimensions. Karaszkiewicz (1979, 1985, 1987 and 1990), on the other hand, relies on the seal simply being squeezed at its cross-section, meaning that the overall seal dimensions are not taken into account. Although, it is accepted that the variation due to the inner diameter changes are quite small, it is still felt that as part of the overall analysis, it is a worthwhile exercise.

Figure 7.4 shows the resulting pressure profile changes as predicted by the current method.

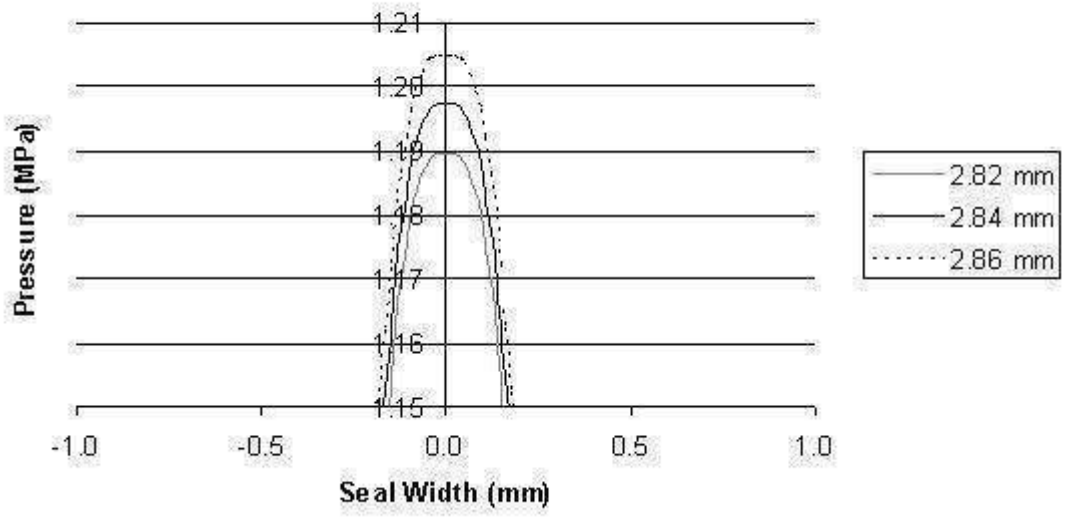

Figure 7.4: Contact pressure profile variation with inner diameter alteration

As can be seen, although the variation is not excessive, this is as the result of purely manufacturing piece-to-piece variations. Any designer considering more substantial changes to the seal geometry must therefore consider the effect of the inner seal diameter. It is, therefore, felt that although more computationally intensive than simply a Hertzian elastic line, the current model is firstly more fundamental and secondly more appropriate given the conforming nature of the contact.

7.2.2 Cross-Sectional Diameter Variation

Following the variation of the inner diameter, the cross section of the seal was also varied. This is thought to be influential in the formation of the contact patch. The results are shown in Table 7.3, the chosen cross-sectional dimensions representing the piece-to-piece variation of manufactured seals. These values represent a mean value, and both an upper and lower extreme case, based upon data from 3M reports. Under these circumstances Karaszkiewicz's approach also shows a variation in the contact load, contact width and the peak pressure. As expected, as the cross-sectional diameter is increased all the contact characteristics are also increased accordingly. This makes sense as the level of squeeze within the contact groove is increased due to a larger cross-sectional diameter.

Seal Dimensions (Cross section) (mm)	1.59		1.61		1.63	
Deflection Approach	Karaszkiewicz	Current Analysis	Karaszkiewicz	Current Analysis	Karaszkiewicz	Current Analysis
Contact Width (m)	9.160E-04	8.543E-04	9.567E-04	8.886E-04	9.976E-04	8.996E-04
Normal Load (N)	13.733	11.611	14.781	12.395	15.861	13.181
Peak Contact Pressure (Pa)	1371666.7	1163127.0	1407084.8	1197543.7	1441633.6	1230639.8

Table 7.3: Cross section diameter variation results

The pressure profile variation is shown in Figure 7.5. It is observed that even simple manufacturing differences have a noticeable effect on the contact pressure within the inhaler assembly and, therefore, these must be taken into account in any modelling work carried out.

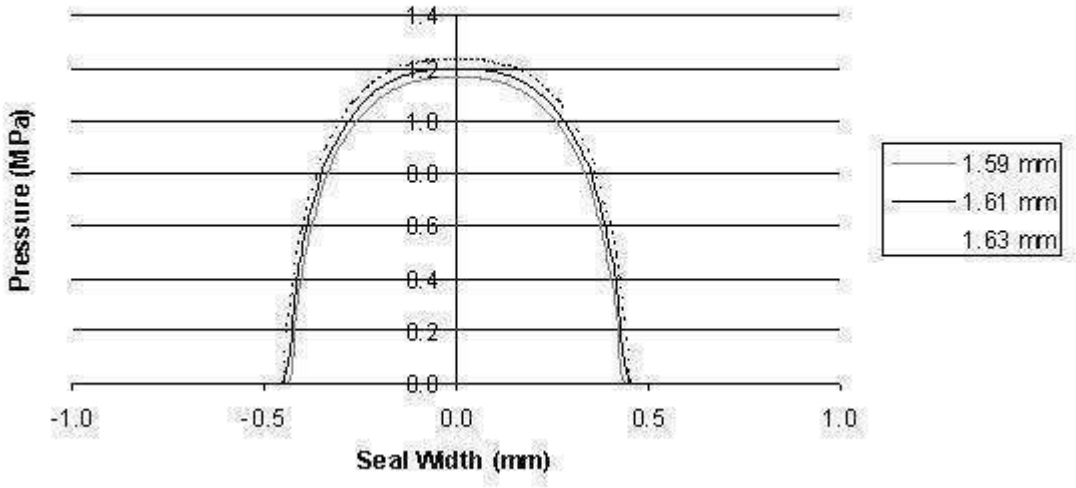

Figure 7.5: Contact pressure profile variation with cross section diameter alteration

7.3 Effect of Changing Canister Pressure Condition on Fitment

A key feature of the inhaler design is the canister pressure. During actuation the pressure boundaries not only change, but also differ according to the contained formulation. This is because of the requirement for atomisation prior to spraying of the mixture through the inhaler nozzle. Table 7.4 shows the resulting effect of varying the canister pressure.

Pressure Loading (Mpa)	0		0.29		0.55	
Deflection Approach	Karaszkiewicz	Current Analysis	Karaszkiewicz	Current Analysis	Karaszkiewicz	Current Analysis
Contact Width (m)	7.093E-04	5.900E-04	8.700E-04	7.682E-04	9.567E-04	8.886E-04
Normal Load (N)	5.719	4.371	10.403	8.469	14.781	12.395
Peak Contact Pressure (Pa)	734265.0	637195.3	1089024.5	942625.8	1407084.8	1197543.7

Table 7.4: Canister pressure variation results

Figure 7.6 shows the variation in pressure profile as a result of canister pressure changes. It is clear that the influence of canister loading is substantial and increases the load to be supported by the seal contact in a significant manner.

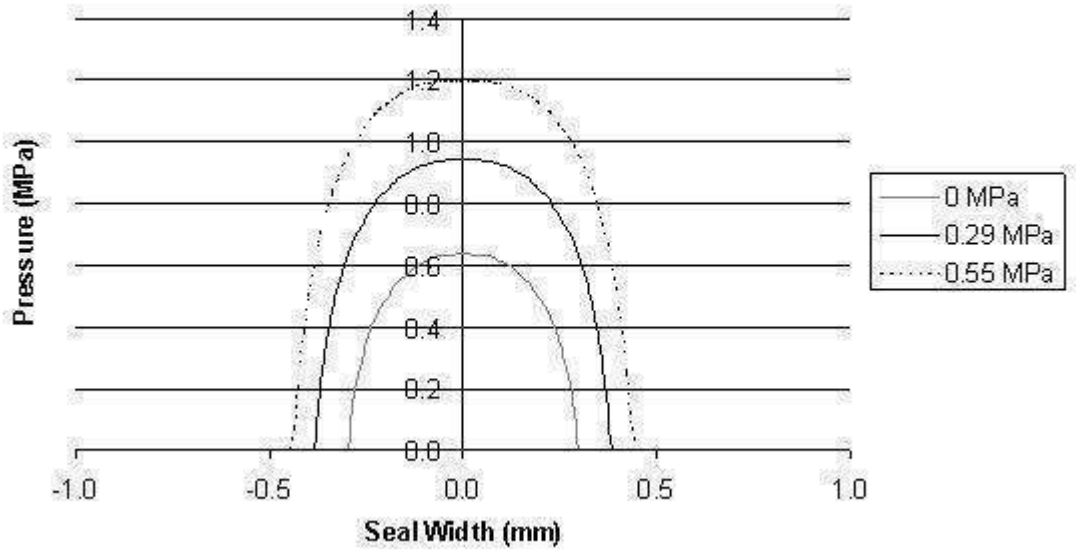

Figure 7.6: Contact pressure profile variation with canister pressure alteration

Between the unpressurised case and the fully pressurised, the load is increased by almost 200%, with an almost 100% rise in the peak contact pressure. This highlights the effect of canister pressure both within the current model and also within the ADAMS numerical model (see Chapter 4), which accounts for the variation of pressure boundary conditions during each time step of actuation.

7.4 Effect of Sliding Velocity Changes on Contact Conditions

Table 7.5 shows the key parameters for the contact conditions for differing sliding velocities. The velocities were chosen in order to provide a considerable range of actuation speeds and ascertain the effect of velocity change. It should be noted, however, that actuation occurs in the region of the slowest speed in normal use.

Sliding Velocity (m/s)	0.03		0.1		0.5	
Deflection Approach	Karaszkiewicz	Current Analysis	Karaszkiewicz	Current Analysis	Karaszkiewicz	Current Analysis
Contact Width (m)	9.567E-04	8.886E-04	9.567E-04	8.886E-04	9.567E-04	8.886E-04
Normal Load (N)	14.761	12.395	14.761	12.395	14.761	12.395
Minimum Film Thickness (m)	4.8622E-08	2.3986E-09	1.0676E-07	2.0728E-08	4.7696E-07	6.7319E-08
Peak Contact Pressure (Pa)	1407084.8	1197543.7	1407084.8	1197541.0	1407084.8	1197317.7

Table 7.5: Sliding velocity variation results

The main point of interest is that of the minimum film thickness and the film thickness shape. As expected, higher sliding velocities develop thicker minimum films. Karaszkiewicz's (1979, 1985, 1987 and 1990) proposed an extrapolated fluid film formula, predicting the film thickness which is an entire order of magnitude larger than that of the current numerical model, whose prediction is in line with that initially anticipated, in that a nano-scale film would normally exist, if any at all (in fact the predicted films can be considered as adsorbed surface films). Figure 7.7 shows the pressure profile in the contact, which varies little with differing velocities, with the only significant difference being visible at the inlet to the contacting region (similar to an increasing hydrodynamic trail with increasing surface velocities). This is expected as the condition, in lubrication terms, is elastohydrodynamic, in which the film thickness is rather insensitive to load. Whilst usually an increase in the speed of entraining motion of fluid under EHL conditions, markedly increases the film thickness. However, this is not usually the case in largely starved contacts, as in this case. In fact increasing surface velocities can have the adverse effect of increasing the level of starvation (not evident here). Therefore, predictions by Karaszkiewicz's approach are unrepresentative. In such conjunctions any small changes are only noted in the inlet trail. As the velocity is reduced the overall profile rapidly approaches that of a stationary contact (i.e. dry elastostatic case, see Figure 7.6), and indeed, below the velocity of 30 mm/s numerical convergence has proved unachievable, despite utilising a greatly refined mesh in an attempt to improve stability. It is, therefore, concluded that at velocities below this range, the speed of entrainment is so low that a coherent uninterrupted film cannot be achieved. Certainly, at 30 mm/s the film thickness falls to just 2.4 nm, the prospect of the film collapsing at velocities below this seems highly likely.

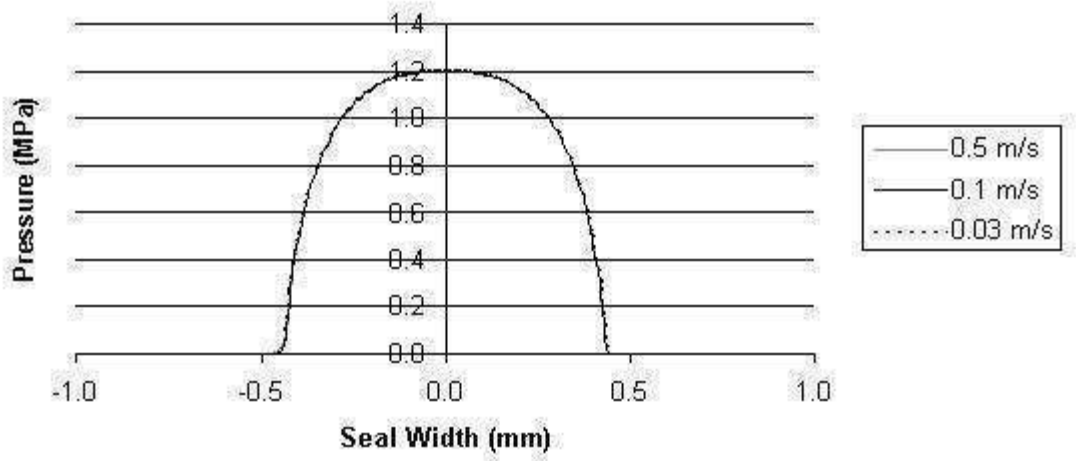

Figure 7.7: Variation of contact pressure profile due to sliding velocity

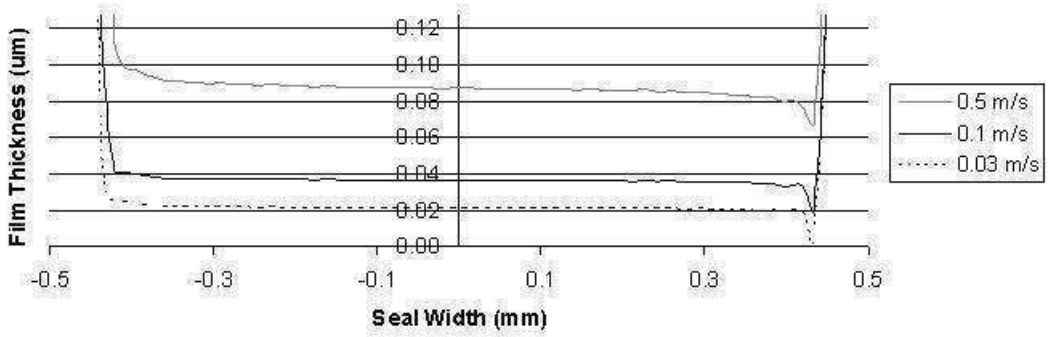

Figure 7.8: Variation of film thickness with sliding velocity

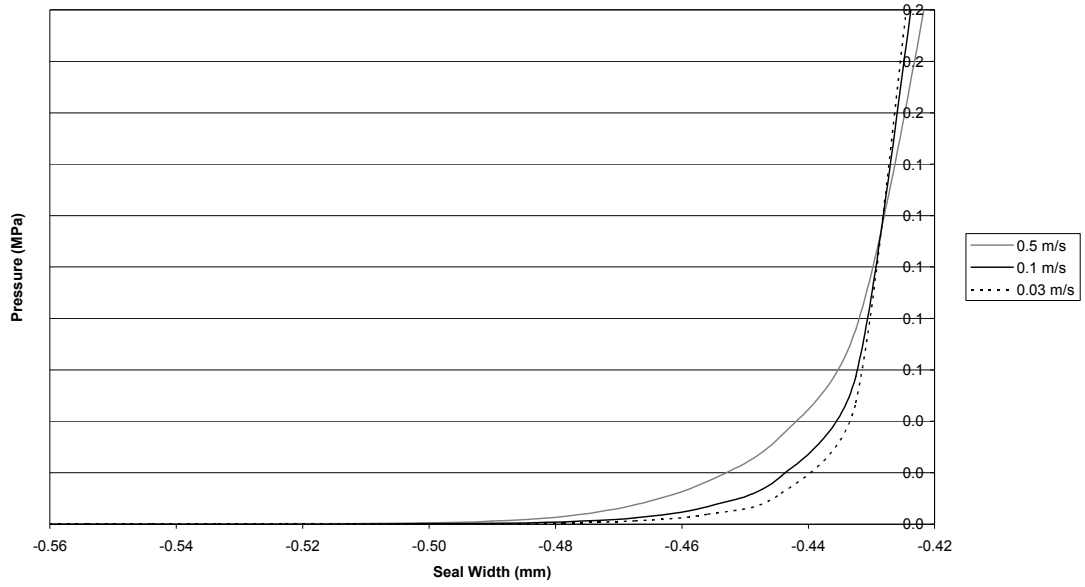

Figure 7.9: Zoomed inlet plot of contact pressure variation with sliding velocity

The pressure distributions in Figure 7.7 correspond to the film shapes in Figure 7.8. These distributions differ from those due to the fitment of the seal without application

of canister pressure and sliding motion (see for example Figure 7.2). The difference is the inlet trail and in the vicinity of the exit. However, the usual pressure spike at the exit is not noted, because of two reasons. Firstly, the pressure spike in EHL diminishes as contact becomes starved, which is the case here. Secondly, the conditions here are soft EHL, where presence of a pressure spike is not usual (see for example Hamrock and Dowson, 1978).

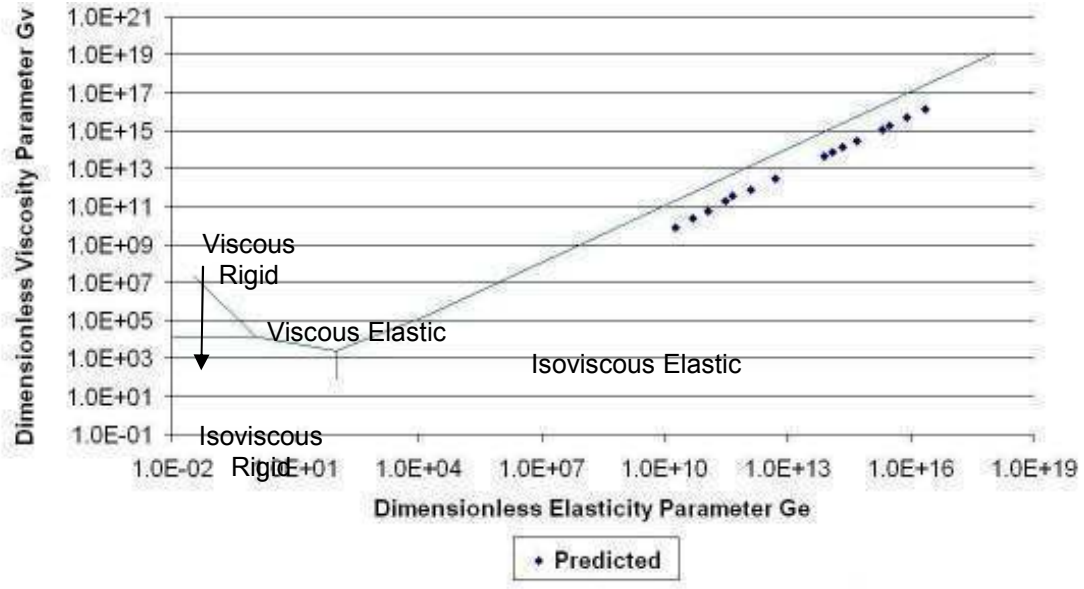

Figure 7.10: Greenwood chart (Greenwood, 1969)

Figure 7.10 shows a plot of the dimensionless Greenwood parameters, related to the conditions described above upon the Greenwood chart (Greenwood, 1969). It can be seen that, although off the traditional scale due to the primary application of the Greenwood chart to hard contacts, when extended the inhaler-seal contact falls within the iso-viscous elastic region (i.e. soft EHL), which would agree with the lack of a pressure spike that has been found in the current results. It should also be noted that whilst the pressure profile variation is relatively small, the effect on the film thickness is noticeable. The film at 0.03 m/s being basically a tenth of that at 0.1 m/s (see Figure 7.8).

7.5 Effect of Lubricant Viscosity Changes on Contact Conditions

The effect of lubricant viscosity was analysed by utilising the viscous properties of silicone oil, to represent the siliconisation of the inhaler bore boundary. This is sometimes performed to improve tribological performance the contacts. While it is accepted that in truth, degradation by the HFA of any surface silicone film would

reduce its viscosity to some extent from an initial value, it was felt the result provided a clear illustration of the potential for an additional silicone layer acting as a lubricant. A full Reynolds analysis was performed using the fitment and fluid entrainment model, highlighted in Chapter 6.

Lubricant	HFA (1)	Siliconised (2)
Viscosity (Pa.s)	2.09×10^{-4}	9.14×10^{-4}
Pressure-Viscosity Coefficient (Pa^{-1})	2.80×10^{-7}	9.53×10^{-9}
Density (Kg/m^3)	1226	820

(1)Solvay Fluor Datasheet (www.solvaychemicals.com)
(2) King *et al.* (1991)

Table 7.6: Comparison of HFA and Silicon tribological properties

Table 7.6 provides the tribological data required while Table 7.7 shows how the improvement to the fluid film viscosity due to silicone oil has resulted in a considerable improvement in the minimum film thickness for the same contact parameters of load and fitment.

Lubricant	HFA	Siliconised
Contact Width (m)	8.886E-04	8.886E-04
Normal Load (N)	12.395	12.395
Minimum Film Thickness (m)	2.3986E-09	2.8559E-08
Peak Contact Pressure (Pa)	1197543.7	1197625.2

Table 7.7: Viscosity variation results

Figure 11 further illustrates the improvement in pressure build up (hydrodynamic lift) due to entrainment of a more viscous fluid at inlet wedge, while the overall pressure profile (See Figure 7.12) remains fundamentally unchanged elsewhere in the contact as would be expected. Finally, Figure 7.13 shows the increase in film thickness across the contact face-width.

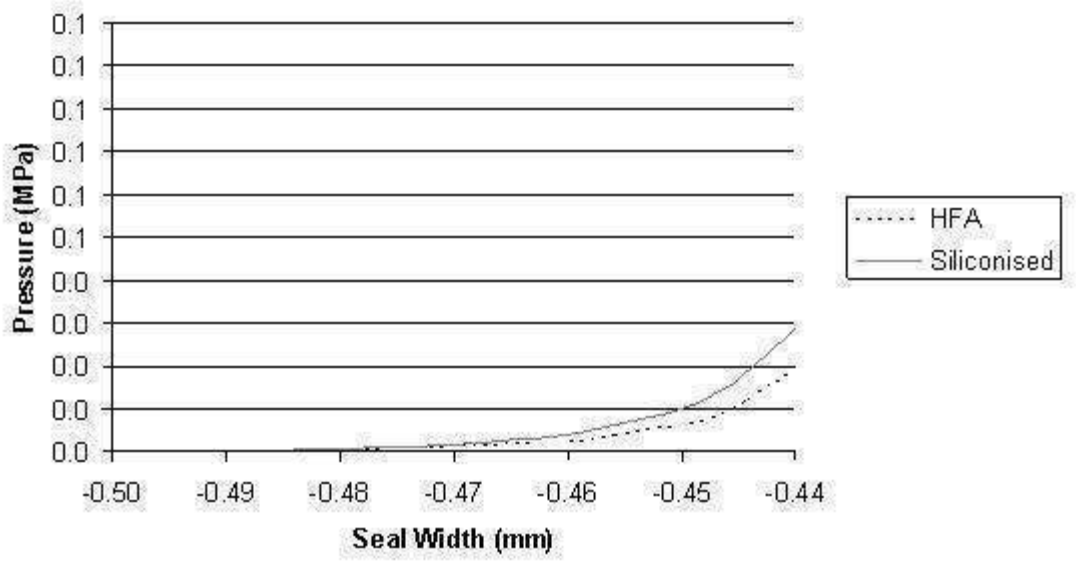

Figure 11: Contact pressure ramp comparison for HFA and Siliconised lubricant

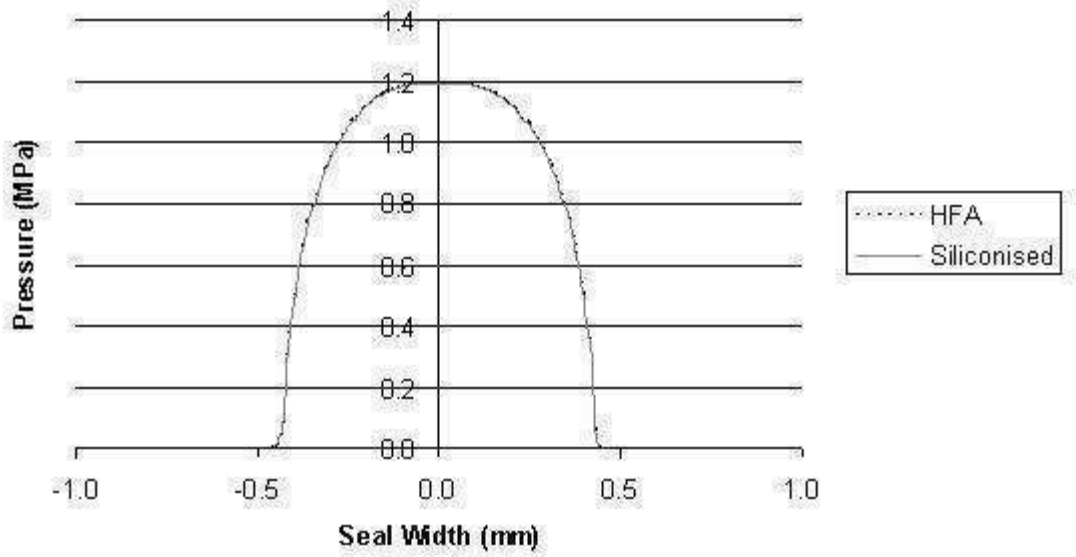

Figure 7.12:Contact pressure comparison for HFA and Siliconised lubricant

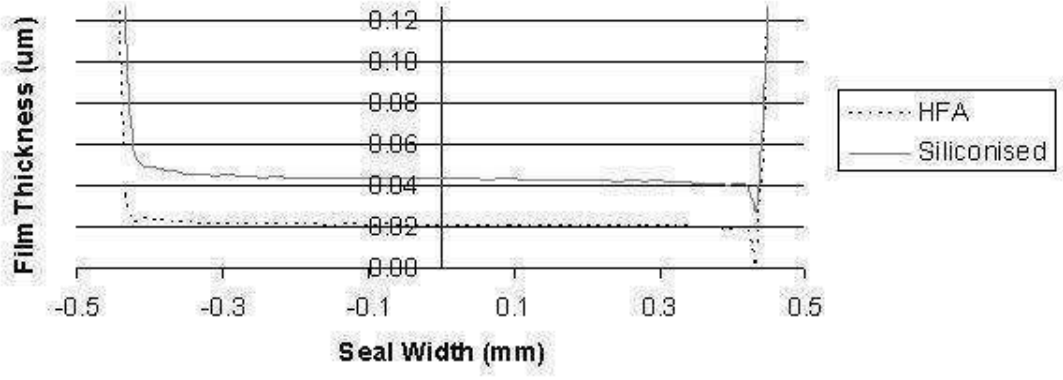

Figure 7.13: Film thickness comparison for HFA and Siliconised lubricant

7.6 Effects of Asperity Height on Overall Device Friction

Finally, asperity interaction was explored using the Karaszkiewicz approach in the devised ADAMS multi-body model. This was carried out in order to view the effect of a potentially roughened seal due to manufacturing variations, but also to see the effect of the so-called 'running-in' seal wear on friction within the contact conjunction.

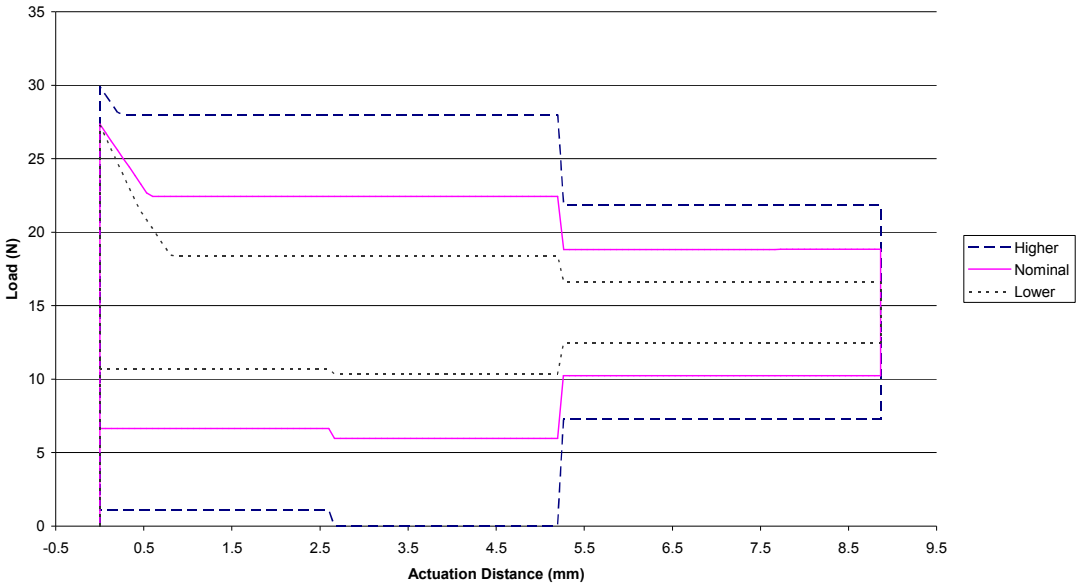

Figure 7.14: Effect of surface roughness variation on overall system friction

Surface roughness was varied by ±30% from the nominally determined value. As is shown in Figure 7.14, the variation of surface roughness has a marked effect on the actuation of the valve. In each case the initial dry static coefficient of friction was kept the same. For the roughened case, the model shows that the device is very likely to fail to actuate. The return force being so low that it would take very little variance in the device or conditions for the actuation to fail altogether. For the nominal surface roughness however, the resulting coefficient of friction was compared to that which was determined in Chapter 3 (See section 3.4.3), the results of which are shown in Table 7.8. The result is reasonable, the likely reasons for the discrepancy being explained in Chapter 8 (See section 8.4).

	Dynamic Coefficient of Friction
Experimental Results	0.51
Predicted Results	0.4

Table 7.8: Comparison of experimental and predicted coefficient of friction Values

7.7 Extrapolated Equation

Using the numerical data, the effect of dimensionless load and speed was tabulated using the following non-dimensional groups:

$$U^* = \frac{\eta_0 \tilde{u}}{E' R_x}$$

$$W^* = \frac{w}{E' R_x} \qquad (7.1)$$

$$H^* = \frac{H_c}{R_x}$$

7.7.1 The effect of Load Parameter

Table 7.9 shows the variation of dimensionless film thickness in the O-ring elastohydrodynamic contact for five values of dimensionless load. Load variation was achieved by altering the canister pressure in order to vary the contact load for a given geometry. This range of values covers both upper and lower extremes of the likely pressure conditions a seal would encounter during operation of the pMDI device.

Velocity u	Pressure CP	Dimensionless Load Parameter W*=wz / E'Rx	Dimensionless Speed Parameter U=EtA0u / E'Rx	Dimensionless Film Thickness H*=Hc/Rx
8	0.7	0.19055	8.72504E-09	0.000461178
8	0.55	0.16074	8.72504E-09	0.000503025
8	0.29	0.10962	8.72504E-09	0.000562263
8	0.13	0.07981	8.72504E-09	0.000618079
8	0	0.05667	8.72504E-09	0.000657335

Table 7.9: Effect of dimensionless load

From these results, a natural logarithm plot was formed, as shown in Figure 7.15, from which a linear trend line was used to extract the gradient of the line.

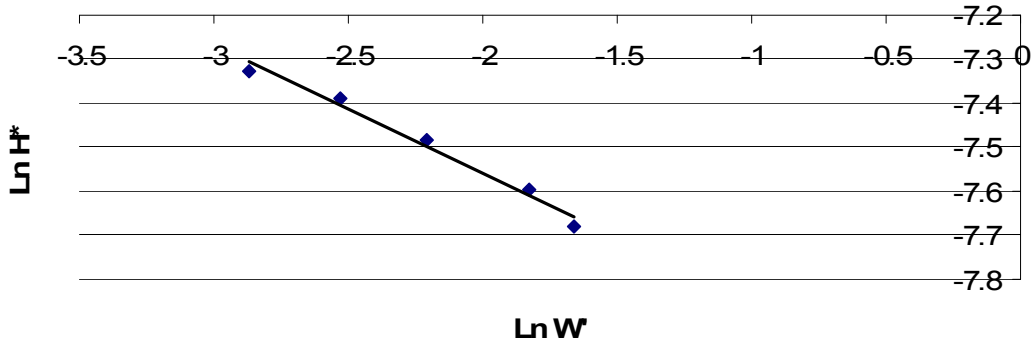

Figure 7.15: Log plot of dimensionless load and film variation

Now, the relationship is such that:

$$H^* \propto W^*$$

$$LnH^* \propto LnW^*$$

Whereby:

$$H^* = KW^{*\alpha}$$

$$LnH^* = LnK + \alpha LnW^* \tag{7.2}$$

Once α has been found it is then necessary to look at the variation of dimensionless film thickness with speed of entraining motion (speed parameter).

7.7.2 The effect of Speed Parameter

Table 7.10 shows the variation of dimensionless film thickness in the O-ring elastohydrodynamic contact for twelve values of dimensionless speed. Speed variation was achieved by altering the sliding velocity of the actuation for a given geometry. This range of values covers the likely extremes of the conditions a seal would encounter during operation of the pMDI device by a range of potential users.

Velocity u	Pressure CP	Dimensionless Load Parameter W*=w'z / E'Rx	Dimensionless Speed Parameter U=EtA0u / E'Rx	Dimensionless Film Thickness H*=Hc/Rx
8	0.55	0.16071	1.57994E-07	0.000506358
7	0.55	0.16071	1.38244E-07	0.000464685
4	0.55	0.16071	7.89968E-08	0.000345217
2	0.55	0.16071	3.94984E-08	0.000236497
0.5	0.55	0.16071	9.87460E-09	0.000108488
0.4	0.55	0.16071	7.89968E-09	9.0625E-05
0.3	0.55	0.16071	5.92476E-09	7.47514E-05
0.2	0.55	0.16071	3.94984E-09	6.36587E-05
0.1	0.55	0.16071	1.97492E-09	4.53934E-05
0.08	0.55	0.16071	1.57994E-09	3.85129E-05
0.05	0.55	0.16071	9.87460E-10	3.33181E-05
0.03	0.55	0.16071	5.92476E-10	2.56682E-05

Table 7.10: Effect of dimensionless speed

From these results, a natural logarithm plot was formed, as shown in Figure 7.16, again, from which a linear trend line was used to extract the gradient of the line.

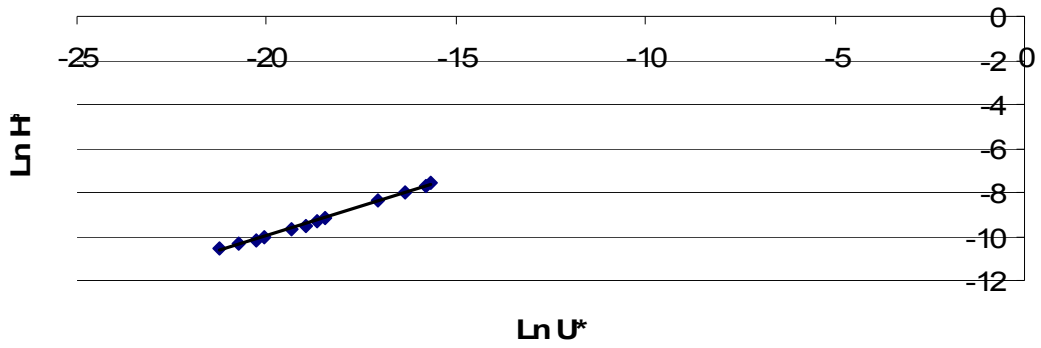

Figure 7.16: Log plot of dimensionless load and film variation

Now, the relationship is such that:

$$H^* \propto U^*$$

$$LnH^* \propto LnU^*$$

Whereby:

$$H^* = JU^{*\beta}$$

$$LnH^* = LnJ + \beta LnU^* \qquad (7.3)$$

Once β has been found it is then the relationships for both speed and load can be combined in order to extract the final equation.

7.7.3 Method of Extrapolation and Results

Overall, the following relationship exists:

$$H^* = kU^{*\beta} W^{*\alpha} \qquad (7.4)$$

Where k is a constant.

From the previous data and extrapolation steps the only remaining unknown is k. This is obtained by using the previous data and taking an average of the calculated values of k. Finally, the extrapolated equation becomes:

$$H^* = 1.492U^{*0.5434} W^{*-0.2893} \qquad (7.5)$$

Also recall the extrapolated equation stated by Karaszkiewicz (1987), which he received via a communication with Prof. Duncan Dowson. Karaszkiewicz (1987) does not refer to the originating source of his equation, but states that to was modified to suit the o-ring contacts that were being investigated. Upon reflection and restating this

equation in the following form, it is clear that the equation is that obtained by regression analysis of numerical results for materials of low elastic modulus in concentrated counterforming contact by Hamrock and Dowson (1978):

$$H^* = 4.4U^{*0.65} W^{*-0.21} \quad (7.6)$$

It is not quite clear what exact modifications Karaszkiewicz has carried out, aside from the removal of the governing parameter G^*. There are two problems with the use of this equation in the conforming contact of o-rings and seals. Firstly, it was obtained for counterforming concentrated contacts by Hamrock and Dowson (1978) and secondly, the kinematic conditions assumed in the pursuance of this equation were largely due to pure rolling conditions. Both these assumptions are rather tenuous when dealing with seals and o-rings.

A comparison of Equations (7.5) and (7.6) show that the dependence of the lubricant film thickness on speed of entraining motion is enhanced in (7.6) precisely because of more favourable kinematic conditions under rolling contacts assumed, when compared with the poorer lubricant entrainment under sliding condition underlying (7.6).

As far as the power index of the load parameter is concerned, both equations show less dependence of lubricant film thickness with this than with the speed parameter. This is expected as the conditions are soft EHL and film thickness insensitivity with load is a characteristic of EHL films. However, with soft EHL this insensitivity is somewhat reduced. For example, Gohar and Rahnejat (2008) shows that for Hard EHL the power index of the load parameter is -0.037 for the minimum film thickness in finite line contact conditions. This insensitivity to load is considerably reduced with power indices of -0.21 (Equation (7.6)) and nearly -0.29 (Equation (7.5)). The difference means that in the case of the former, load has a greater effect (causing larger localised elastic deformation) which is expected as the underlying assumption by Hamrock and Dowson (1978) has been Hertzian-type deformation. However, in the case of Equation (7.5) the deformation of the seal is as the result of global elastic response due to fitment and application of pressure and any local pressure distribution. The contact area is therefore larger and more realistic, reducing the effect

of load. However, variations of film due to load changes would be more noticeable as discussed below.

Dimensionless Load Parameter W*=w'z / E'Rx	Dimensionless Speed Parameter U=EtA0u / E'Rx	Dimensionless Film Thickness H*=Hc/Rx	Extrapolated H*	ERROR %
0.16071	1.57994E-07	0.00050636	0.00050993	-0.69971
0.16071	1.36244E-07	0.00046489	0.00047423	-1.97129
0.16071	7.89968E-08	0.00034522	0.00034989	-1.33437
0.16071	3.94984E-08	0.00023650	0.00024007	-1.49002
0.16071	9.87460E-09	0.00010849	0.00011303	-4.01705
0.16071	7.89968E-09	0.00009062	0.00010012	-9.48495
0.16071	5.92476E-09	0.00007475	0.00008563	-12.70605
0.16071	3.94984E-09	0.00006366	0.00006870	-7.33610
0.16071	1.97492E-09	0.00004539	0.00004714	-3.70035
0.16071	1.57994E-09	0.00003851	0.00004175	-7.76428
0.16071	9.87460E-10	0.00003332	0.00003234	3.01294
0.16071	5.92476E-10	0.00002567	0.00002450	4.75134
0.19055	1.57994E-07	0.00046118	0.00048541	-4.99150
0.16074	1.57994E-07	0.00050303	0.00050990	-1.34813
0.10962	1.57994E-07	0.00056226	0.00056931	-1.23727
0.07981	1.57994E-07	0.00061808	0.00062438	-1.00952
0.05667	1.57994E-07	0.00065734	0.00068938	-4.64841

Table 7.11: Extrapolated results comparison

The numerical results can now be compared with these equations, particularly that of Karaszkiewicz (See Chapter 5, Equation 5.6) in order to see the difference in influence of each of the governing parameters on the dimensionless film thickness. As seen in Table 7.11 a degree of variance between that of the full numerical result and the extrapolated Equation (7.5) also exists. This is to be expected, however, and although the peak error percentage is some 12%, this could be further improved by using a larger data set or a more in-depth curve fitting approximation. Nevertheless, it is felt that a good level of agreement is shown with that of the much more computationally intensive full numerical method. While at the same time the extrapolated equation represents a more pertinent formula than that of Karaszkiewicz (1987).

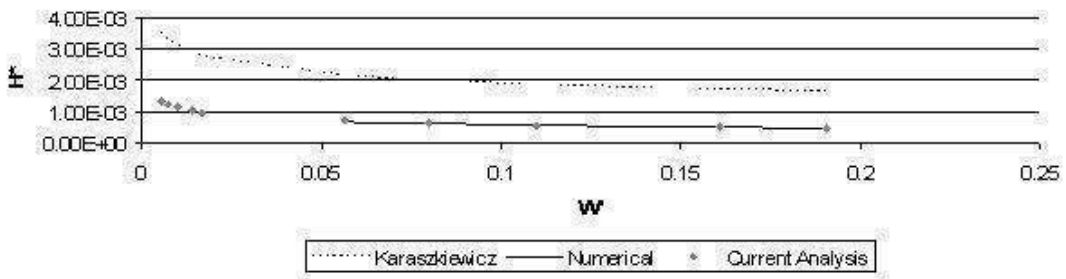

Figure 7.17: Comparison of dimensionless load influence

In comparing the dimensionless group results of Karaszkiewicz and the current analysis it is clear that for given conditions, the influence of dimensionless load and speed, as noted above, are different. In the case of the current analysis the load variation gives approximately a 40% reduction in the H* value for the given load conditions. Karaszkiewicz's extrapolated film thickness equation, on the other hand, shows only around a 20% drop in H* for a similar variation in load. This indicates how the current analysis is more sensitive to the effects of load on the contact despite the physically predicted H* value being overall smaller for the case of the current analysis, a plot of which is shown in Figure 7.17.

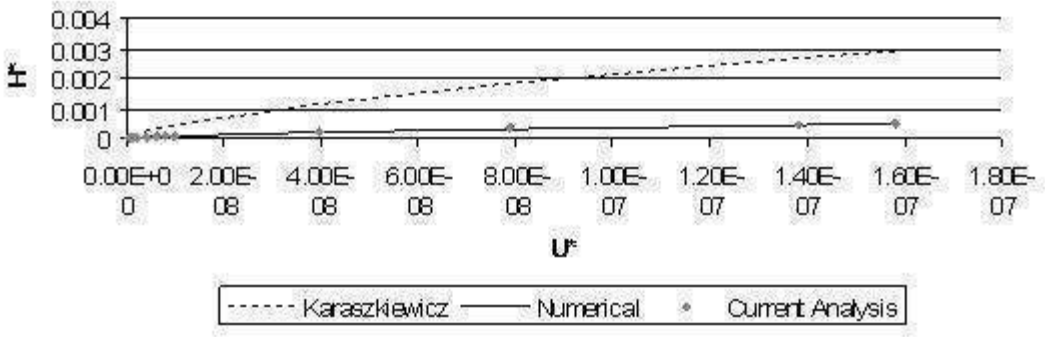

Figure 7.18: Comparison of dimensionless speed influence

In the case of variations in the speed parameter, it is shown that the opposite effect results, with the current analysis being less sensitive to this compared with that of Karaszkiewicz's equation. Overall suggesting that contact load is of more importance with regard to the final film thickness within the conjunction as in the case of inhaler valves with standard tests the speed variation is quite small. This would make sense in reality where the load resulting from geometry and pressure loading plays a vital part in determining whether the valve actuates successfully or not. In both Figure 7.17 and Figure 7.18 it can again be seen that the extrapolated equation matches well with the results of the full numerical solution.

7.7.4 Results of Extrapolated Equation and Inhaler Leakage

The results of the extrapolated equation were then compared with Karaszkiewicz's approach over the given range in speed, and finally implemented within the ADAMS multi-body dynamics model.

	Predicted Minimum Film	
Sliding Velocity	Karaszkiewicz	Current Analysis
0.3333 mm/s	2.61E-09	2.69E-09
0.5 mm/s	3.39E-09	3.35E-09
10 mm/s	2.38E-08	1.71E-08
500 mm/s	3.02E-07	1.43E-07

Table 7.12: Comparison of minimum film trend between Karaszkiewicz and the current analysis

As shown in Table 7.12, the results using Karaszkiewicz's approach and those employing the current study eventually converge as the testing actuation speed is reached. However, at higher speeds (such as an entirely plausible 10 mm/s) where operation is likely to take place with a patient, the current analysis predicts a thinner film thickness compared with that of Karaszkiewicz's equation.

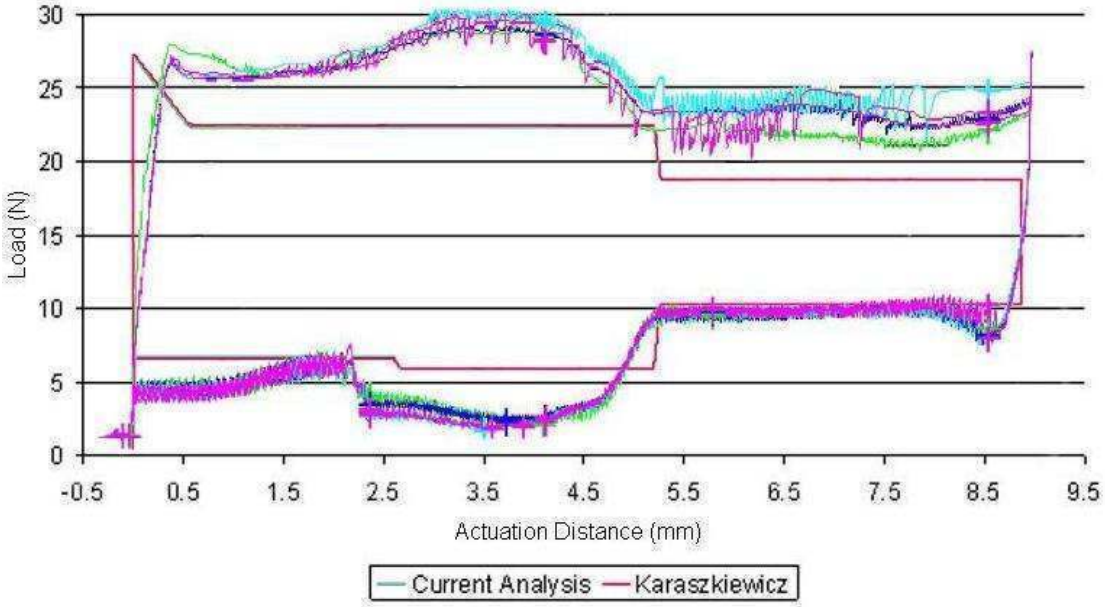

Figure 7.19: Comparative hysteresis curve of Karaszkiewicz and current analysis

At the standard test speed used by 3M currently (0.333 mm/s), the difference in result between Karaszkiewicz and the current analysis is negligible when compared with typical 3M test data (See Figure 7.19). It must still be noted though that the numerical method employed to extrapolate the current analysis equation does provide greater detail on the characteristic behaviour of the contact conjunction. As such it is able to allow the future introduction of further physical phenomena and interactions.

Dimensionless Load Parameter W*=wz / E'Rx	Dimensionless Speed Parameter U=EtA0u / E'Rx	Dimensionless Film Thickness H*=Hc/Rx	Leakage (ml for 400 Actuations)
0.16071	1.57994E-07	0.00050636	1.01E-02
0.16071	1.38244E-07	0.00046489	9.31E-03
0.16071	7.89968E-08	0.00034522	6.92E-03
0.16071	3.94984E-08	0.00023650	4.74E-03
0.16071	9.87460E-09	0.00010849	2.17E-03
0.16071	7.89968E-09	0.00009062	1.82E-03
0.16071	5.92476E-09	0.00007475	1.50E-03
0.16071	3.94984E-09	0.00006366	1.28E-03
0.16071	1.97492E-09	0.00004539	9.09E-04
0.16071	1.57994E-09	0.00003851	7.71E-04
0.16071	9.87460E-10	0.00003332	6.67E-04
0.16071	5.92476E-10	0.00002567	5.14E-04
0.19055	1.57994E-07	0.00046118	9.24E-03
0.16074	1.57994E-07	0.00050303	1.01E-02
0.10982	1.57994E-07	0.00056226	1.13E-02
0.07981	1.57994E-07	0.00061808	1.24E-02
0.05667	1.57994E-07	0.00065734	1.32E-02

Table 7.13: Leakage calculation results

Finally, using the new extrapolated equation, calculation of seal leakage is made over a time period of 400 actuations. Table 7.13 shows the predicted leakage, the calculation for which is shown in Chapter 5.

8.0 Conclusions and Suggestions for Future Work

8.1 Overall Conclusions

- It was found that the dominant regime of lubrication is that of boundary lubrication in the seal conjunctions of an inhaler valve. Analysis has shown that an insignificant film thickness is predicted when using HFA as lubricant, although a small absorbed film may exist at the asperity tip. Ultra-thin films of the order of nanometres are predicted at best. Due to the properties of HFA and its inert characteristics, it is most likely that such thin films would be interrupted formulation deposits, which are observed in practice.
- It has been shown that siliconisation of the contact can produce thicker films within the conjunction. However, these are still small, when compared with the surface roughness of solid surfaces in contact. Therefore, the boundary regime of lubrication prevails.
- Friction within the conjunction is dominated by adhesive friction. With such ultra-thin films the viscous shear is very low as no coherent film forms within the conjunction.
- Due to the asperity profile the contribution to deformation friction is relatively low. The asperity slope is rather shallow. The large asperity tip radius and shallow asperity slope are the reasons for insignificant contribution from deformation friction. The hysteresis predictions based on this approach of low deformation friction and high adhesive friction were found to offer reasonable agreement with those of experimental findings.
- It is inappropriate, as expected, to assume Hertzian contact conditions as has been suggested by other research workers in the field in the case of this elastomeric seal. This is corroborated by the deformation results arising from assuming a Hertzian contact compared with that of global deformation arising from fitment of seal (see Chapter 6). This has shown that normal force and film thickness within the conjunction are not as insensitive to one another as the formula proposed by Karaszkiewicz (1987) would suggest. If it were possible for a coherent film to be formed, it would be in line with that of a soft elastohydrodynamic contact. This is highlighted by the extrapolated W* power being approximately -0.29 as opposed to Karaszkiewicz' -0.21 or that of a

hard elastohydrodynamic contact which is considerably lower, such as that of Dowson and Higginson (1966), being -0.13 or Gohar and Rahnejat (2008) at -0.037.

- The discretised generalised elasticity approach is much more appropriate to the contact conditions, being at least partially conforming and fits the seal shape to the conjunction boundary rather than relying on an empirical squeeze ratio, proposed by Karaszkiewicz (1990). This allows for parametric analysis of seal fitment and dimensional control studies to be undertaken. Additionally, evaluation of leakage can be performed, as once fitted, the conditions of the film gap can be determined for the entire contact width in some detail. This will allow determination of the primary function of the seal.
- Analysis of lubrication and leakage shows that knowledge of one phenomenon is usually required to determine the outcome of another as the problem is very multi-disciplinary.

8.2 Achievement of Aims

The overall aim of this research was to:

"Develop a fundamental understanding of the seal and formulation interactions with emphasis on system dynamics and physical effects within the mechanism."

This was broken down into two key areas:

1. A fully-parameterised numerical model to simulate the system and allow parametric studies of key design variables.

This has been achieved through the analysis of:

- Seal material changes
- Seal dimensional changes and any piece-to-piece variations
- Surface modification effects
- Lubricant rheology and in fact the type of fluid considered as the lubricant
- Prediction of friction

2. Graphical output from the model to aid with communication of results, to include but not necessarily limited to graphs, diagrams and animations.

This has been achieved by the production of:

- Hysteresis curve outputs from ADAMS software
- Actuation animations of valve CAD geometrical components
- Data charts to represent the findings of the parametric studies
- Diagrams of seal deformation and fitment

8.3 Contributions to Knowledge

- There is a dearth of fundamental science investigations of elastomeric seals in inhalation devices, especially those providing a multi physics, multi scale solution, which includes the rigid multi-body dynamics at the *macro-sliding* scale, the global deformation of the seal and the asperity interactions at the *micro-scale*, whilst also taking into account the absorbed film formation at the *nano-scale*. The problem is of a multi physics' nature due to rigid body inertial dynamics, elasticity, surface interactions such as adhesion, hydrodynamics and intermolecular surface interactions such as Van der Waals forces.
- This analysis is different to that of general O-ring and hydraulic analysis in that:
    - The roughness to film ratio is very poor compared with other seals in operation. At best the conjunction approaches the mixed regime of lubrication and not hydrodynamic conditions predicted in other cases.
    - The physical component scale is much smaller than the general hydraulic seals.
    - The seals are relatively lightly loaded.
    - The lubricant is a much more complex fluid than a typical hydraulic oil.
    - Gross global deformation is allowed for without the need for assuming an empirical approach for fitment of the seal *in-situ*.
    - In the case of hydraulic seals hydrodynamic conditions mean that adhesive friction is not an important issue. The converse is true in inhaler seals.

The above constitute contributions to knowledge and have not hitherto been reported in literature. Additionally, the friction model, although not novel (see for example, Greenwood and Tripp, 1971, Fuller and Tabor, 1975, Gohar and Rahnejat, 2008, Bhushan, 1999 among others), shows good agreement with experimental work and therefore describes the phenomena involved in the actuation of the inhaler and operation of the valve.

8.4 Critical Assessment of Current Approach

- Viscoelastic behaviour could have been included at the fitment stage of the seal within the device. This would allow for some degree of stress relaxation which clearly takes place over time, therefore expanding the contact width of conjunction.
- When the device is stationary, adsorption of the drug to rough asperity contacts can be quantified, as well as ingestion of the same into the porous elastomeric material. Currently geometry and material adjustments allow a degree of swell to be allowed for, but no automatic calculation is included, as swell can account for up to 20% increase in volume and a corresponding change in elastomer properties by as much as 60% (Westbrook and French, 1999) this would be a beneficial inclusion on the fundamental science level.
- The current model of asperity interaction refers to elastic deformation of asperity pairs, it does not allow for viscoelastic deformation of asperity contacts, producing enlarged contact areas and reducing peak pressures at the asperity tips. The Greenwood and Tripp (1971) model utilised does not allow for this aspect. Therefore this aspect did not form a part of the current study.
- Adhesion force was not taken into account in terms of increasing the contact force, and energy dissipation due to a required pull-off force. This can account for some differences between the measured hysteresis loop and the predicted ones. Either the JKR (Johnson, 1985) model or DMT (Derjaguin *et al*., 1971) model would be of benefit in taking such issues into account.
- No thermodynamic effects have been taken into account due to areolisation or adhesive bonds being broken, therefore the current study is under isothermal conditions.

8.5 Future Work

- The points raised in section 8.4 can be included at the basic science level. For instance, the asperity interaction model can be expanded to allow for the stretch portion (pull-off of asperity pairs) before release takes place, further increasing hysteresis effect (the area within the curve is increased, representing higher losses) and can account for the current differences between predicted and experimental results.
- Asperity contact can be enhanced to include viscoelastic relaxation both in asperity pair contacts and on the overall contact level. For the latter works of Naghieh *et al* (1998) can form the initial basis for the necessary approach.
- Further studies on the effects of formulation sedimentation and adsorption on surfaces of canister and seals may be beneficial. This brings the inclusion of action of surfactant, present in the formulation, into play . Such a study would be critical in the understanding of the loss of prime in inhalation devices. Although the need for a primed dose is somewhat eliminated in some modified inhaler valve designs, it is still a feature of many current devices.
- At the component level, the macroscopic device assembly issues can be investigated. The assembly of the seal can have a crimp-like effect on the o-ring seal, or in a traditional design the seal is deliberately crimped in place. In either instance further deformation may take place than has been allowed for at the fitment level.
- It is assumed in testing and by industry that uniform motion takes place during actuation although this is not the case. Forces in the axial direction should be taken into account, which result in out-of-plane deformation of seals in the axial direction of travel. In order to do this, however, it is acknowledged that an approach of greater complexity would be required, such as that of a full finite element analysis. Again, such motions and deformations can further account for the differences between the experimental and numerical hysteresis curves.
- Deformation of the seal can be expanded to include deformation due to dragging of the seal across the bore surface, this would provide leading and

trailing edges and further increase the representation of the actual conditions within the inhaler valve.

- Currently the phenomena of swell is handled through means of geometrical modification and the manual adjustment of elastomer material properties. Automatic calculation of the phenomena over time would be a beneficial inclusion on the fundamental science level and also provide a more detailed (and therefore accurate) picture of seal functionality throughout the life of the inhaler.

References

Akalin O and Newaz G M (2001), *Piston Ring-Cylinder Bore Friction Modelling in Mixed Lubrication Regime: Part 1 – Analytical Results*, Journal of Tribology, Vol. 123 211-218

Al-Ghathian, Faisal M M, Tarawneh, Muafag S (2005), *Friction Forces in O-ring Sealing*, American Journal of Applied Sciences 2(3): 626-632

Almqvist T and Larsson R (2002), *The Navier-Stokes Approach for Thermal EHL Line Contact Solutions*, Tribology International 35 163-170

Balakrishnan, S. and Rahnejat, H. (2005), *Isothermal Transient Analysis of Piston Skirt-to-Cylinder Wall Contacts under Combined Axial-Lateral-Tilting Motion*, J. Phys., Part D: Appl. Phys., 38, pp.787-799.

Barquins M (1993), *Friction and Wear of Rubber-like Materials*, Wear 160, 1-11

Barquins M, Courtel R (1975), *Rubber Friction and the Rheology of Viscoelastic Contact*, Wear 32, 133-150

Barquins M, Roberts A D (1986), *Rubber Friction Variation with Rate and Temperature: Some new Observations*, J. Phys. D: Appl. Phys. 19 547-563

Berry J, Heimbecher S, Hart J L and Sequeira J (2003), *Influence of the Metering Chamber Volume and Actuator Design on the Aerodynamic Particle Size of a Metered Dose Inhaler*, Drug Development and Industrial Pharmacy, Vol. 29, No. 8.

Berry J, Kline L C, Hart J L and Sequeira J (2003), *Influence of the storage orientation on the aerodynamic particle size of a suspension metered dose inhaler containing propellant HFA-227*, Drug Development and Industrial Pharmacy, Vol. 29, No.6.

Bespak Corporate Website,
http://www.bespak.co.uk/site/ProductInno/valvesactuators.html

Best B, Meijers P, Savkoor A R (1981), *The Formation of Schallamach Waves*, Wear 65 385-396

Bhushan B. (1999), *Handbook of Micro/Nanotechnology*, 2nd Ed., CRC Press, Boca Raton, Florida.

Bou-Said B, Fantino B (2001), *Hellinger-Reissner Model and its Application to Elastomeric Materials in Contact Situations*, 2nd World Tribology Conference. F. Franek, W.J. Bartz, A.Pauschitz Vienne (Autriche), 3/9/2001 0-7/9/2001 0160

Bouvier J.M, Gelus M (1986), *Diffusion of Heavy Oil in a Swelling Elastomer*, Rubber Chemistry and Technology, Vol 59, 233-240

Briggs G A D, Briscoe B J (1979), *Surface Roughness and the Friction and Adhesion of Elastomers*, Wear 57 269-280

Briscoe B.J, Scruton B and Willis F.R (1973), *The Shear Strength of Thin Lubricant Films*, Proc. R. Soc. Lond. A., Vol 333, 99-114

Byron P R, *Drug Delivery Devices – Issues in Drug Development*

Calladine C.R, Greenwood J.A (1978), *Line and Point Loads on a Non-Homogeneous Incompressible Elastic Half-space*, Journal of Mechanical Applied Mathematics, Vol 31, Pt. 4, 507-529
Cambridge Consultants Company presentation, *New Concepts for pMDIs*

Cameron A (1976), *Basic Lubrication Theory*, Ellis Horwood series in engineering science.

Chandrasekanren M, Batchelor A W (1997), *In situ Observation of Sliding wear Tests of Butyl Rubber in the Presence of Lubricants in an X-ray Microfocus Instrument*, wear 211, 35-43

Chang L (1995), *A deterministic Model for Line-Contact Partial Elasto-Hyrdodynamic Lubrication*, Tribology International, Vol 28, No 2, 75-84

Cheng H. S and Sternlicht B (1965), *A Numerical Solution for the Pressure, Temperature, and Film Thickness Between Two Infinately Long, Lubricated Rolling and Sliding Cylinders, Under Heavy Loads*, Journal of Basic Engineering (Transactions of the ASME), September, 695-707

Colthorpe P (2003), *Industry experiences of the HFA transition*, Drug delivery systems and sciences

Crowder T M, Louey M D, Sethuraman V V, Smyth H D C and Hickey A J (2001), *2001: An odyssey in inhaler formulation and design*, Pharmaceutical Technology, July.

Derjaguin K., Muller V. and Toporov Y. (1971), *Effect of Contact Deformation on the Adhesion of Particles*, J.Colloid Interface Sci., Vol. 53, No. 2, 314-326.

Dowson D (1998), *Modelling of Elastohydrodynamic Lubrication of Real Solids by Real Lubricants*, Meccanica 33: 47-58

Dowson D Ehret P (1999), *Past, Present and Future Studies in Elastohydrodynamics*, Proc Instn Mech Engrs Part J Vol 213, 317-333

Dowson D, Ruddy B L and Economou P N (1983), *The Elastohydrodynamic Lubrication of Piston Rings*, Proc. R. Soc. Lond., A 386, 409-430

Dowson D. and Higginson G.R. (1966), *Elasto-hydrodynamic lubrication: The fundamentals of roller and gear lubrication*, Pergamon, Oxford.

Dowson D. and Higginson G.R. (1966), *Elasto-hydrodynamic lubrication: The fundamentals of roller and gear lubrication*, Pergamon, Oxford.

Dragoni E, Strozzi A (1988), *Analysis of an Unpressurised, Laterally Restrained, Elastomeric O-Ring Seal*, Journal of Tribology, Vol. 110, 193-200

Dragoni E, Strozzi A (1989), *Theoretical Analysis of an Un-pressurised Elastomeric O-ring Seal Inserted into a Rectangular Groove*, Wear 130 41-51

Elcoate C D, Evans H P and Hughes T G (1998), *On the Coupling of the Elastohydrodynamic Problem*, Proc. Instn Mech Engrs, Vol 212 Part C, 307-318

Evans C R and Johnson K L (1986), *The Rheological Properties of Elastohydrodynamic Lubricants*, Proc. Instn. Mech. Engrs., Vol. 200, 303-312

Faraon I C and Schipper D J (2007), *Stribeck Curve for Starve Line Contacts*, Journal of Tribology, Vol. 129 181-187

Field G J, Nau B S (1975), *Lubricant Behaviour in Loaded Rubber Contacts*, Wear 35 79-85

Fink J B (2000), *Metered-dose Inhalers, Dry powder Inhalers, and Transitions*, Respir Care.

Flamant (1892), Paris Compt. Rend., 114, 1465.

Flitney R K (1982), *Reciprocating Seals*, Tribology International, August, 219-226

Fuller K.N.G, Tabor D (1975), *The Effect of Surface Roughness on the Adhesion of Elastic Solids* , Proc. R. Soc. Lond. Series A: Math. And Phys. Sciences, Vol. 345, No. 1642, 327-342

Furuhama, S., and Sasaki, S. (1983), *New Device for the Measurement of Piston Frictional Forces in Small Engines*, SAE Paper 831284

George A F, Strozzi A, Rich A J (1987), *Stress fields in a Compressed Unconstrained Elastomer O-ring Seal and a Comparison of Computer Predictions and Experimental Results*, Tribology International, October, Vol 20, No 5 237-247

George A.F, Strozzi A, Rich J.I (1987), *Stress Fields in a Compressed Unconstrained Elastomeric O-Ring Seal and a Comparison of Computer Predictions and Experimental Results*, Tribology International, Vol 20, No. 5, 237-247

Gillen K T, Bernstein Wilson M H (2005), *Predicting and Confirming the Lifetime of O-rings*, Polymer Degradation and Stability 87 257-270

Gohar R. (2001), *Elastohydrodynamics*, Imperial College Press, 2nd Ed.

Gohar, R. and Rahnejat, H (2008), *Fundamentals of tribology*, World Scientific Publishing Uk, ISBN:1848161840.

Gohar, R. and Rahnejat, H. (2008), *Fundamentals of tribology*, Imperial College Press, London.

Green A P (1954), *The Plastic Yielding of Metal Junctions due to Combined Shear and Pressure*, J.Mech. Phys. Sol. 2 197-201

Green I, English C (1992), *Analysis of Elastomeric O-Ring Seals in Compression Using the Finite Element Method*, Tribology Transactions, Vol 35, 83-88

Green I, English C (1994), *Stresses and Deformation of Compressed Elastomeric O-Ring Seals*, 14th International Conference on Fluid Sealing, BHR Group Cranfield,6-8th April

Greenwood J A (1969) *Presentation of elastohydrodynamic film thickness results,* J. Mech. Sci. 11 128–32

Greenwood J.A and Tripp J.H (1971), *The Contact of Two Nominally Flat Rough Surfaces*, Proc. Instn Mech Engrs, Vol. 185, 625-633

Greenwood J.A. and Williamson J.B.P (1966), *Contact of Nominally Flat Surfaces*, Proc. R. Soc. Lond. A, Mathematical and Physical Sciences, Vol. 295, No. 1442, 300-319

Grimble D.W., Theodossiades S., Rahnejat H., and Wilby M. (2008), *Tribology of rough ultra-film contacts in drug delivery devices,* Proc. IMechE Part C: J. Mech. Eng. Sci., Vol. 222, pp. 2209-2216

Grosch K A (1963), Proc. R, Soc. A, 274 21-39

Hamilton G M (1980), *The Hydrodynamics of a Cam Follower*, Tribology International, June, 113-119

Hamrock B (1994), *Fundamentals of Fluid Film Lubrication*, McGraw-Hill series in mechanical engineering, pg's 2-11, ISBN 0-07-025956-9

Hamrock B J and Dowson D (1978), *Elastohydrodynamic Lubrication of Elliptical Contacts for Materials of Low Elastic Modulus I – Fully Flooded Conjunction*, Trans. ASME, Vol. 100, 236-245

Hamrock B J and Dowson D (1979), *Elastohydrodynamic Lubrication of Elliptical Contacts for Materials of Low Elastic Modulus II – Starved Conjunction*, Trans. ASME, Vol. 101, 92-98

Hamrock B.J. and Dowson D (1976), *Isothermal Elastohydrodynamic Lubrication of Point Contacts Part 1 – Theoretical Formulation*, Journal of Lubrication Tech., April, 223-229

Hamrock B.J. and Dowson D (1976), *Isothermal Elastohydrodynamic Lubrication of Point Contacts Part 2 – Ellipticity Parameter Results*, Journal of Lubrication Tech., July 375-383

Hamrock B.J. and Dowson D (1976), *Isothermal Elastohydrodynamic Lubrication of Point Contacts Part 1 – Theoretical Formulation*, Journal of Lubrication Tech., April, 223-229

Hamrock B.J. and Dowson D (1977), *Isothermal Elastohydrodynamic Lubrication of Point Contacts Part 3 – Fully Flooded Results*, Journal of Lubrication Tech., April, 264-276

Herreburgh K (1968), *Solving the Incompressible and Isothermal Problem in Elastohydrodynamic Lubrication Through an Integral Equation*, Transactions of the ASME, January 262-270

Hooke C.J, Lines D.J and O'Donoghue J.P (1966-67), *Elastohydrodynamic Lubrication of O-Ring Seals*, Proc. Instn Mech Engrs, Vol. 181, Pt 1, No 9, 205-210

Houpert L.G, Hamrock B.J (1986), *Fast Approach for Calculating Film Thicknesses and Pressures in Elastohydrodynamically Lubricated Contacts at High Loads*, Journal of Tribology, Vol. 108, 411-420

Hsu S H (1997), *Boundary Lubrication: Current Understanding*, National Institute of Standards and Technology, Tribology Letters 3, 1-11

Hsu S H, Gates R S (2005), *Boundary Lubricating Films: Formation and Lubrication Mechanism*, Nat. Inst, of Standards and Technology, Tribology International 38 305-312

Hu Y and Zhu D (2000), *A Full Numerical Solution to the Mixed Lubrication in Point Contacts*, Journal of Tribology, Vol. 122 1-9

Hu Y, Hui W, Whang W, Zhu D (2001), *A Computer Model of Mixed Lubrication in Point Contacts*, Tribology International 34 65-73

Hui C Y, Lin Y Y, Baney J M (2000), *The Mechanics of Tack: Viscoelastic Contact on a Rough Surface*, J. Polymer Science: Part B Polymer Phys., Vol 38, 1485-1495

Ibiapina C C, Cruz A A, Camargos A M (2004), *HFA as a propellant for pressuized metered-dose inhalers: history, pulmonary deposition, pharmacokinetics, efficacy and safety*, Journal de Pediatria.

Israelachvili, J.N. (1992), *Intermolecular and Surface Forces*, 2nd ed edition, Academic Press, London.

Jalali-Vahid D, Rahnejat H, Gohar R and Jin Z M (1998),, *Comparison Between Experiments and Numerical Solutions for Isothermal Elastohydrodynamic Point Contacts*, J. Phys. D: Appl. Phys. 31 2725-2732

Jalali-Vahid D. (2000), Transient Analysis of Isothermal Elastohydrodynamic Point Contact, PhD. Thesis, University of Bradford.

Jalali-Vahid D., Rahnejat H., Gohar R. and Jin Z.M. (2000), *Prediction of Oil-film Thickness and Shape in Elliptical Point Contacts Under Combined Rolling and Sliding Motion*, Proceedings of the Institution of Mechanical Engineers, Part J: Journal of Engineering Tribology, 214 (5), pp. 427-437.

Jeng Y (1992),, *Theoretical Analysis of Piston-Ring Lubrication Part 1 – Fully Flooded Lubrication*, Tribology Transactions, Vol 35 No 4, 696-706

Jin Z M Dowson D (2005), *Elastohydrodynamic Lubrication in Biological Systems*, Proc. IMechE Part J ,Vol. 219, 367-380

Johns P M and Gohar R (1981), *Roller Bearings Under Radial and Eccentric Loads*, Tribology International, June, 131-136

Johnson K.L. (1985), *Contact Mechanics*, Cambridge University Press.

Karaszkiewicz A (1979), *Contact Width and Contact Pressure of O-seals*. Przeglad Mechaniczny, 7, 14-16

Karaszkiewicz A (1985), *Hydrodynamic Lubrication of Rubber Seals for Reciprocating Motion; Leakage of Seals with an O-ring*, Tribology International, Vol 21 No 6

Karaszkiewicz A (1987), *Hydrodynamics of Rubber Seals for Reciprocating Motion, Lubricating Film Thickness, and Out-Leakage of O-seals*, Ind Eng Chem Res, Vol 26 No. 11.

Karaszkiewicz A (1990), *Geometry and Contact Pressure of an O-ring Mounted in a Seal Groove*, Ind Eng Chem Res, 29 pg 2134-2137

Keller M, *Innovations and perspectives of metered dose inhalers in pulmonary drug delivery*, International Journal of Pharmaceuticals

Kim H, Park S, Lee H, Kim D and Lee Y (2007), *Approximation of contact stress for a compressed and laterally one side restrained O-ring*, Engineering Failure Analysis, Vol 14, 1680-1692.

Koudine A A, Lambert M, Barquins M (1997), *Some New Experimental Results on the Schallamach Waves Propagation by Space-time Analysis*, Int. J. Adhesives Vol 17 Number 4 359-363

Kuran S, Gracie B.J, Metcalfe R (1995), *Low Pressure Sealing Integrity of O-Rings Based on Initial Squeeze and Counterface Finish*, Tribology Transactions, Vol 38, No 2, 213-222

Kushwaha M. and Rahnejat H. (2002), *Transient elastohydrodynamic lubrication of finite line conjunction of cam to follower concentrated contact*, J. Phys. D: Appl.

Kushwaha, M., Rahnejat, H. and Jin, Z.M. (2000), *Valve-train Dynamics: A Simplified Tribo-elasto-multi-body Analysis*, Proceedings of the Institution of Mechanical Engineers Part K: Journal of Multi-body Dynamics, 214, pp 95-110.

Le Guen J, Thouverez F, Demoulin G, Jezequel L (2001), *Time Model of Rubber Deformation*, Journal of Engineering Materials and Technology, January, Vol 123 36-44

Lindley P B (1967), *Compression Characteristics of Laterally-unrestrained Rubber O-rings*, Journal of the I.R.I, July/August.

Luo J B, Liu S (2006), *The Investigation of Contact Ratio in Mixed Lubrication*, Tribology International 39, 409-416

Massey B S (2001), *Mechanics of Fluids*, Spon Press, ISBN 0415362067

Mavros G., Gnanakumarr M., Homer Rahnejat H. and Bouazza-Marouf K. (2003), Loughborough University Internal Reports for 3M.

McDonald K J and Martin G P, *Transition to CFC-free metered dose inhalers – into the new millennium*, International Journal of Pharmaceuticals

MeRec *Briefing for the NHS*, National Prescribing Centre, issue 18, 2002
Milne-Thomson, L.M (1960), *Plane Elastic Systems*, 117.

Mishra P.C., Rahnejat H. and King P.D. (2008), *Tribology of the ring–bore conjunction subject to a mixed regime of lubrication*, Proc. IMechE Part C: J. Mechanical Engineering Science, Vol. 223, p987-998

Moore D F, Geyer W (1972), *A Review of Adhesion Theories for Elastomers*, Wear 22, 113-141

Mostofi A and Gohar R (1982), *Oil Film Thickness and Pressure Distribution in Elastohydrodynamic Point Contacts*, Journal of Mechanical Engineering Science, Vol. 24, No. 4, 173-182

Muskhelishvili N.I. (1963), *Some Basic Problems of the Mathematical Theory of Elasticity: Fundamental Equations, Plane Theory of Elasticity, Torsion and Bending*. (2nd Edn. ed.), Noordhoff, Groningen.

Naghieh, G. R. , Rahnejat, H. and Jin, Z.M. (1998), "*Characteristics of Frictionless Contact of Bonded Elastic and Viscoelastic Layered Solids*", Wear, 232, pp. 243-249.

Nau B S (1999), *An Historical Review of Studies of Polymeric Seals in Reciprocating Hydraulic Systems*, Proc Instn Mech Engrs Part J, Vol 213, 215-226

Nikas G K (2003), *Elastohydrodynamics and Mechanics of Rectangular Elastomeric Seals for Reciprocating Piston Rods*, Transactions of the ASME (Journal of Tribology), Jan Vol. 125 pg 60-69

Nikas G K (2003), *Transient Elastohydrodynamic Lubrication of Rectangular Elastomeric Seals for Linear Hydraulic Actuators*, Proc. Instn Mech. Engrs Vol. 217 Part J, 461-473

Nikas G K (2004), *Theorectical Study of Solid Back-up Rings for Elastomeric Seals in Hydraulic Actuators*, Tribology International 37 689-699

Nikas G K, Sayles R S (2005), *Computational Model of Tandem Rectangular Elastomeric Seals for Reciprocating Motion*, Tribology International, 1-13

Nikas G K, Sayles R S (2005), *Nonlinear Elasticity of Rectangular Elastomeric Seals and its Effect on Elasto-hydrodynamic Numerical Analysis*, Sealing Technology, March

Nikas G K, Sayles R S (2005), *Study of Leakage and Friction of Flexible Seals for Steady Motion via a Numerical Approximation Method*, Tribology International September

Noakes T, *Medical Aerosol Propellants*, Journal of Fluorine Chemistry

Nogueira I, Dias A M, Gras R, Progri R (2002), *An Experimental Model for Mixed Friction During Running-in*, Wear 253, 541-549

Öngün Y, André M, Bartel D and Deters L (2008), *An Axisymmetric Hydrodynamic Interface Element for Finite-Element Computations of Mixed Lubrication in Rubber Seals*, Proc. IMechE, Vol. 222, Part J: Engineering Tribology, 471-481

Park T and Kim K (1998), *Elastohydrodynamic Lubrication of a Finite Line Contact*, WEAR, Vol. 223, 102-109

Patir, N. and Cheng, H. S. (1979), "Application of Average Flow Model to Lubrication between Rough Sliding Surfaces", *Trans. ASME, J. Lubn. Tech., **101**, pp.221-230*

Peng W, Bhushan B (2001), *A Numerical Three-dimensional Model for the Contact of Layered Elastic/Plastic Solids with Rough Surfaces by a Variational Principle*, Journal of tribology, April, Vol 123 330-342

Persson B N J (2000), *Sliding Friction: Physical Principles and Applications,* Nano Science and Technology, Springer, pg 102-110, ISBN 3-540-67192-4
Phys. 35, pp. 2872–2890

Pinkus & Sternlicht (1961), *Theory of Hydrodynamic Lubrication*, McGraw-Hill Book Company.

Purewal T S, Grant D J W (1998), *Metered Dose Inhaler Technology,* Interpharm Press Inc, Buffalo Grove, Ill

Rahnejat, H. (1998), *Multi-body Dynamics: Vehicles, Machines and Mechanisms*, Professional Engineering Publications (IMechE).

Rahnejat H. (2000), *Multi-body dynamics: historical evolution and Application*, Proc Instn Mech Engrs Part C, Vol 214, p149-173

Rana A Sayles R Nikas G Jalisi I (2001), *An Experimental Technique for Investigating the Sealing Principles of Reciprocating Elastomeric Seals for use in Linear Hydraulic Actuator Assemblies*, Proceedings of 2nd World Tribology Congress, Vienna, Austria.

Rana A, Sayles R, Nikas G and Jalisi I (2001), *An Experimental Technique for Investigating the Sealing Principles of Reciprocating Elastomeric Seals for Use in Linear Hydraulic Actuator Assemblies*, Proceedings of the 2nd World Tribology Congress, Vienna, Austria

Rhoads Stephenson R and Fletcher Osterle J (1962), *A Direct Solution of the Elasto-Hydrodynamic Lubrication Problem*, ASLE Transactions, Vol 5, 365-374.

Roberts A (1992), *A Guide to Estimating the Friction of Rubber*, Rubber and Chemistry Technology, Vol 65, 673-686

Roberts A D, Tabor D (1968), *Fluid Film Lubrication of Rubber – an Interferometric Study*, Wear II

Roberts A D, Thomas A G (1974), *The Adhesion and Friction of Smooth Rubber Surfaces*, Wear 33 45-64

Rubin B K and Durotoye L, *How do patients determine that their metered-dose inhaler is empty?*, CHEST Journal.

Ruskell L.E.C (1980), *A Rapidly Converging Theorectical Solution of the Elastohydrodynamic Problem for Rectangular Rubber Seals*, Journal of Mechanical Engineering Science, Vol 22, No 1, 9-16

Schallamach A (1971), *How Does Rubber Slide*, Wear 17 301-312

Shen D, Salant R.F (2007), *An Unsteady Mixed Soft EHL Model, with Application to a Rotary Lip Seal*, Tribology International, Vol. 40, 646-651

Solvay Fluor Website,
http://www.solvaychemicals.com/product/datasheet/0,0,-_EN-1000700,00.html

Stribeck R. (1907), *Die Wesentliechen ichen Eigenschaften Gleit und Rollen Lager* OR: *Ball Bearings for Various Loads*, Trans. ASME, Vol 29, pp. 420-463.

Stupkiewicz S, Marcinisyn A (2008), *Elastohydrodynamic Lubrication and Finite Configuration Changes in Reciprocating Elastomeric Seals*, Tribology International

Theodossiades S Gnanakumarr M Rahnejat H and Menday M (2004), *Mode identification in impact-induced high-frequency vehicular driveline vibrations using an elasto-multi-body dynamics approach*, Proc. Instn Mech. Engrs Vol. 218 Part K: J. Multi-body Dynamics, 81-94

Timoshenko S (1965), *Strength of Materials*, D.Van Nostrand Company, Third Edition

Torrence A A (2005), *A Method for Calculating Boundary Friction and Wear*, Department of Mechanical and Manufacturing Engineering, Trinity College, Dublin 2, Ireland, Elsevier Wear 258, 924-934

United Sates Patent, Glaxo Group Limited, US6,926,178 B1

United States Patent, Virginia Commonwealth University, US5,190,029

University of Maryland School of Pharmacy Presentation*, Introduction to pressurised metered dose inhaler formulation*,

http://www.pharmacy.umaryland.edu/faculty/rdalby/Teaching%20Web%20Pages/Pressurized%20Metered%20Dose%20Inhaler%20Formulation.pdf

Venner C.H. and Lubrecht A.A. (2000), Multilevel Methods in Lubrication, Tribology Series 37, Elsevier.

Vervaet C and Byron P.R (1999), *Drug-Surfactant-Propellant Interactions in HFA-Formulations*, International Journal of Pharmaceuticals, Vol. 186, 13-30

Wang W, Hu Y, Liu Y, Wang H (2005), *Deterministic Solutions and Thermal Analysis for Mixed Lubrication in Point Contacts*, Tribology International.

Westbrook P.A, French R.N (1999), *Elastomer Swelling in Mixed Solvents*, Rubber Chemistry and Technology, Vol 72, 74-90

Wilby M (2005), *Increasing Performance Consistency of pMDIs*, DRUG Delivery Technology, Vol 5, Issue 9, 56-63 October

Wright J, Brocklebank D and Ram F*, Inhaler devices for the treatment of asthma and chronic obstructive airways disease (COPD)*, QSHC Online

Young P M, Price R, Lewis, Edge S and Traini D (2003), *Under Pressure: Predicting pressurised metered dose inhaler interactions using the atomic force microscope*, Journal of Colloid and Interface Science.

Young W, Budynas R (2001), *Roarks Formula's for Stress and Strain*, McGraw-Hill Professional, 7 edition.

Yujin F and Linqing Z (1993), *A Study on the Limit Criterion of Full and Partial Lubrication*, Wear, 143, 221-229

Appendices

Grimble D.W., Theodossiades S., Rahnejat H., and Wilby M. (2008), *Tribology of rough ultra-film contacts in drug delivery devices,* Proc. IMechE Part C: J. Mech. Eng. Sci., Vol. 222, pp. 2209-2216